LASI Laboratory for Advanced Subsurface Imaging

The University of Arizona

GEOPHYSICAL INVESTIGATION OF SUBSIDENCE FISSURES NEAR WILLCOX, ARIZONA

GEOPHYSICS FIELD CAMP 2009
LASI-09-1
May 14, 2009

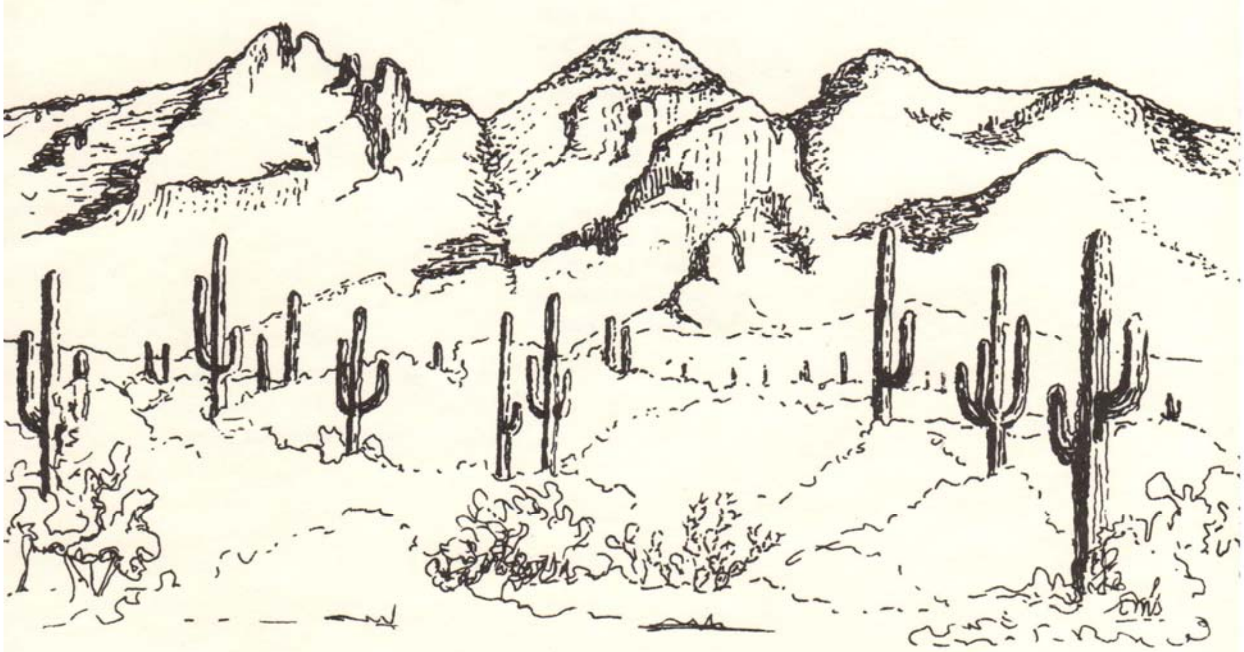

GEOPHYSICAL INVESTIGATION OF SUBSIDENCE FISSURES NEAR WILLCOX, ARIZONA

GEOPHYSICS FIELD CAMP 2009
LASI-09-1
May 14, 2009

Nicholas A. Barbato
Peter D. Bingham
Michael C. Conley
Makko A. DeFilippo
Elizabeth M. Desser
Christina A. King
Benjamin J. Lewis
Emily S. McCarthy
Nirio Mendoza
Michael L. Rucker[1]
Whitney K. Rutherford
Ben K. Sternberg
Philip J. Stokes
Ralph E. Weeks[2]

[1] AMEC Earth & Environmental, Inc.
[2] GeoSouthwest, LLC
All other authors are with the University of Arizona

ABSTRACT

An interdisciplinary survey consisting of four geophysical methods was conducted on the western edge of the Apache Generating Station's property in Willcox, Arizona. The aim of the survey was to apply various methods for the detection of earth fissures and desiccation cracks. The geophysical methods used were static magnetic field measurements, frequency domain electromagnetics (FEM), ground penetrating radar (GPR), and seismic. Two grids were delineated and surveyed by each method. Grid 1 was set up at a site containing a fissure with visible surface expression over some parts of the grid, and Grid 2 was set up at a site with little visible surface expression of the fissure, but was suspected to contain a fissure in the subsurface. At another location, northwest of the Apache Generating Station, three lines were surveyed in an area of known desiccation cracks. All of the methods showed an anomaly associated with the fissure in Grid 1. Furthermore, at locations where the fissure is not visible in Grid 1, there were still strong anomalies in line with the suspected location of the fissure extending below the surface. Magnetic data from Grid 2 suggests that magnetics may not be a useful method in subsurface earth fissure detection at this site, where we believe that the fissure is only a very small crack with small aperture at depth. The electromagnetic results from Grid 2 show anomalies extending from lines 1 through 5 where there is only minimal surface expression in lines 1 and 2 and no surface expression in lines 3-5. No anomaly was seen in the northern end of Grid 2. It was found that GPR in Grid 2 did not display conclusive results in distinguishing subsurface earth fissure anomalies from other anomalies, such as roots. Seismic lines in Grid 2 show anomalies in the profiles that could indicate the presence of earth fissures; however a thin high velocity horizon may appear as a subsurface fissure, and this made interpretations more challenging. At the desiccation crack

site, there is evidence of a shallow feature, which we interpret to be a dessication crack and not an earth fissure. A dirt road was present at the desiccation crack site, and it is possible that the road may have produced some of the observed anomalies due to rain-water channeling effects. The locations of fissures were confirmed by trenches excavated at the locations where anomalies were visible in the geophysical data, but where the fissures were not exposed at the surface.

ACKNOWLEDGEMENTS

The University of Arizona Geophysics Field Camp Class, GEN/GEOS 416/516, would like to thank the United States Geological Survey (USGS), Water Resources Division, Tucson, Arizona, for their financial support of this project, and for allowing the use of their equipment during field surveys.

James Callegary, USGS Hydrologist, Tucson Arizona, was with the field team during all of the surveys. His expertise, guidance, and experience with groundwater in the area was instrumental in conceptualizing the problem, and was an extraordinary benefit for the students.

Michael Rucker, P.E. Sr. Engineer, AMEC Earth and Environmental, Tempe Arizona, gave the field class countless hours of guidance, explanation, and review. The students of this geophysics field camp would like to extend a special acknowledgement for offering his expertise in and knowledge of using seismic data and interpretation to locate earth fissures. This was instrumental in quantifying and achieving the goals for this project.

Ralph Weeks, GeoSouthwest, LLC, collaborated with Mike Rucker on the seismic data acquisition and the trenching, and was at our field location on one of our field survey days to provide additional assistance. Mr. Weeks also logged test trenches across the fissure or fissure alignment to confirm the nature of the fissure features targeted by the geophysics.

Arizona Electric Power Cooperative, Inc. (AEPCO) Apache Generation Plant, Cochise, Arizona provided access to their property, and provided the backhoe and operator used to excavate test trenches across the fissure features. They also provided the necessary safety training to allow access to their property.

Mickey Reed, GIS Analyst, University of Arizona RNR Department, provided his advice, guidance, and expertise using GIS software for acquiring aerial photos of the survey area.

Philip J. Stokes, Graduate Assistant/Associate, University of Arizona MGE Department, was an integral part of the GPR data collection and interpretation. His experience with GPR equipment, data collection, and data processing was essential to this project. Philip's out-of-class consultations, multiple trips to the field, and good-natured attitude were of great benefit to this year's class.

TABLE OF CONTENTS

1.0 INTRODUCTION

1.1. Background

The Willcox Basin, and in particular the areas immediately surrounding Kansas Settlement, Willcox, and the Willcox Playa have experienced substantial groundwater depletion due to increased groundwater use. Earth fissures have been documented in the Willcox Basin and nearby Bowie areas for decades (Holzer, 1980). Groundwater depletion is believed to be the primary cause for large-scale surface subsidence in the area, which has led to regions of tension in the subsurface. Figure 1.0 (ADWR, 2009) presents current subsidence in the region as imaged using InSAR technology. Local tensional stresses caused by surface subsidence have led to the development of earth fissures, especially around the edges of major subsidence features, while other mechanisms contribute to prolific desiccation cracking in the area.

Earth fissures can be damaging to roads, buildings, and other infrastructure (ALSG, 2007). While earth fissures are exposed at the surface in some areas, the tension-induced ground cracking necessary to develop fissures may be present beneath the surface without surface expression. Once a tension crack reaches the surface and becomes exposed to significant erosion, that surface expression may develop into a large surface feature. A visible, large earth fissure that has been enhanced by significant erosion is properly termed a fissure gully. Methods are needed to detect incipient earth fissures that are not yet exposed at the surface so that they can be effectively mapped.

The Apache Generating Station, owned and operated by the Arizona Electric Power Cooperative (AEPCO), has experienced earth fissuring in some areas of the facility, including a fissure at the Combustion Waste Disposal Facility northwest of the power plant. The Apache Generating Station is a coal-fired power plant that supplies 520 megawatts of electricity to Arizona and parts of Mew Mexico and California. Interest in earth fissures has been driven by the potential high cost of mitigating fissure damage at the existing facility, and potential impacts of fissuring on future land use in the area.

1.2 Project Overview

Geophysical methods have had moderate success in determining the location of earth fissures in the greater desert southwest. Michael Rucker of AMEC Earth and Environmental, Inc., has demonstrated the success to which small-scale seismic surveys can be used to detect earth fissures (Rucker et. al. 2009). In this study, a variety of geophysical methods were used to assess their effectiveness in determining the location of a known earth fissure. Geophysical surveys used in this project are as follows: Magnetic, EM31, EM34, EM38, Ground Penetrating Radar (GPR), and Seismic Surveys. At least two LIDAR surveys are necessary to observe changes in topography. Typically, these would be separated by a minimum of a few months unless changes are expected to be rapid relative to this time scale. One LIDAR survey was carried out, but it was expected that there was an insufficient time delay to carry out a second survey and obtain useful results for this report. The USGS plans on carrying out a second LIDAR survey at a future date and will be publishing these results separately.

Figure 1.0 presents project area Satellite Interferometry by Synthetic Aperture Radar (InSAR) that was taken near the Willcox Playa. Each complete cycle of color bands (ie. blue to blue, red to red, etc.) represents about 2.8 cm of differential subsidence. The Willcox Playa is a de-correlated area shown in black. Ground surface tension due to subsidence tends to be at a maximum at the edge of subsidence bowls. Earth fissures are most likely to develop in these areas of maximum tension.

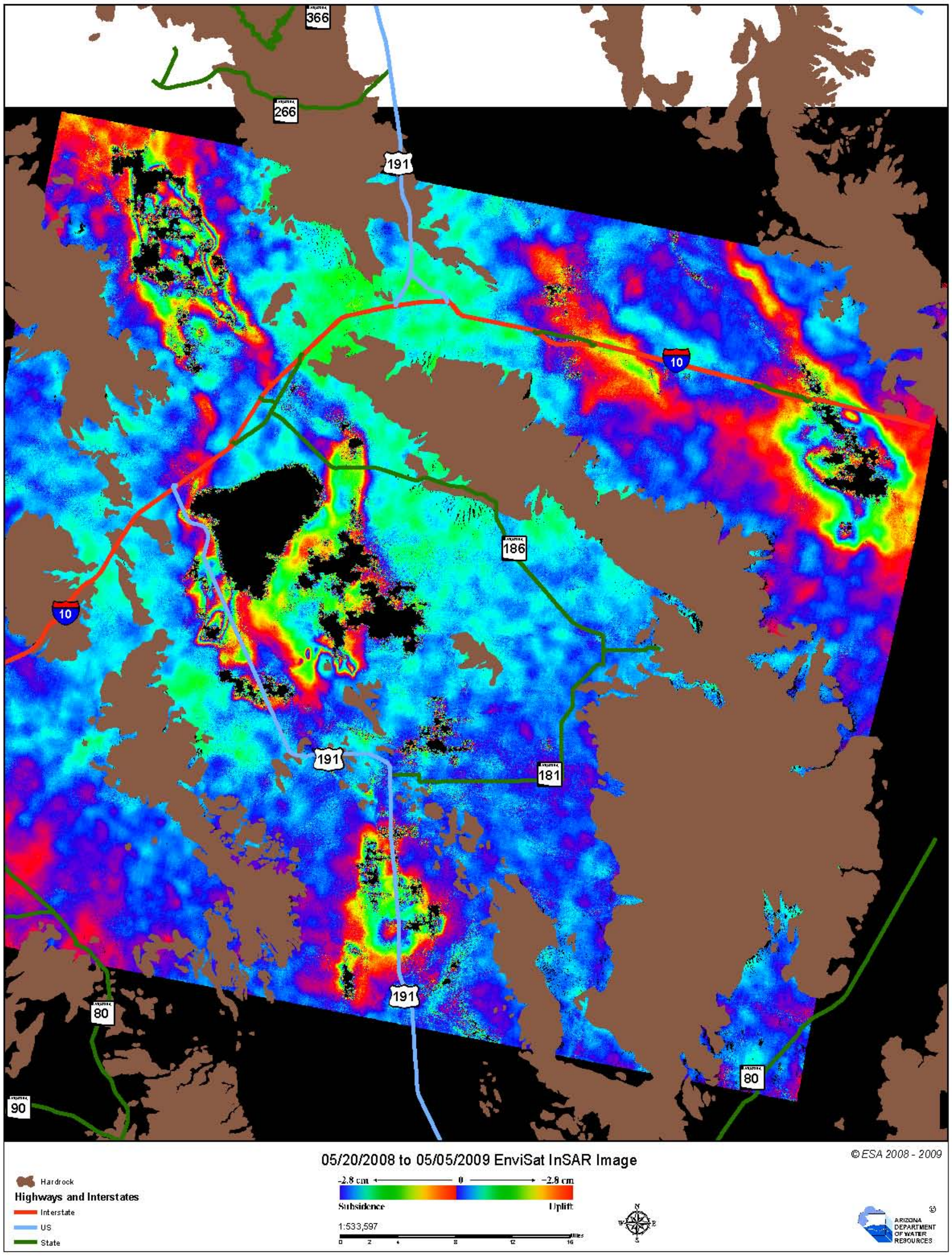

Figure 1.0 Satellite Interferometry by Synthetic Aperture Radar (InSAR) image showing subsidence in Willcox area from May 2008 to May 2009 (ADWR, 2009). Figure provided by Brian D. Conway, Supervisor, Geophysics/Surveying Unit, Arizona Department of Water Resources.

1.3 Project Location

Geophysical Surveys took place within northern Cochise County, approximately 19 miles southwest of Willcox Arizona. Figure 1.1 shows the state of Arizona with Figure 1.2 inset outlined in red.

Figure 1.1 Arizona Map with Figure 1.2 Inset outlined in red. Photo courtesy of Cochise County.

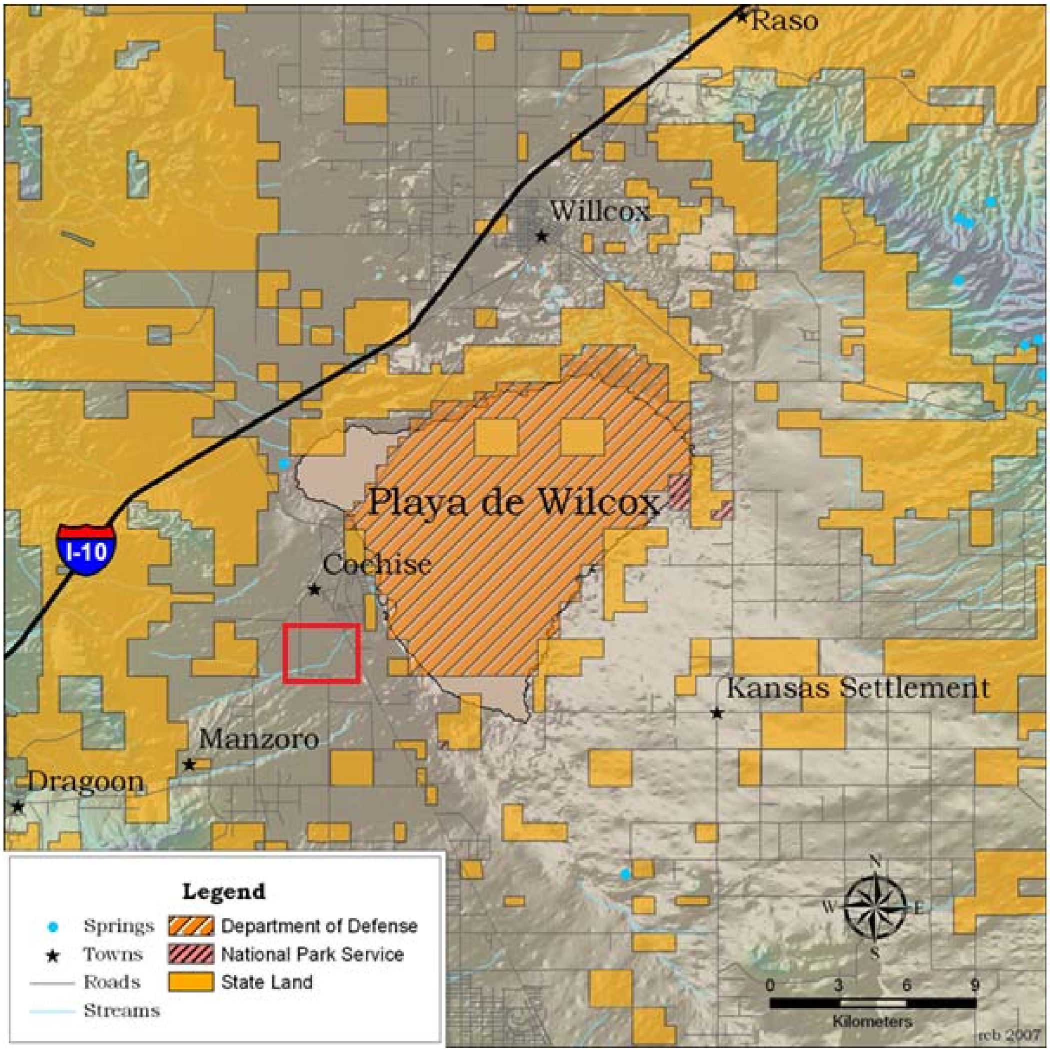

Figure 1.2 Inset from Figure 1. Willcox Survey area (Figure 1.3) outlined in red. Photo courtesy of Cochise County.

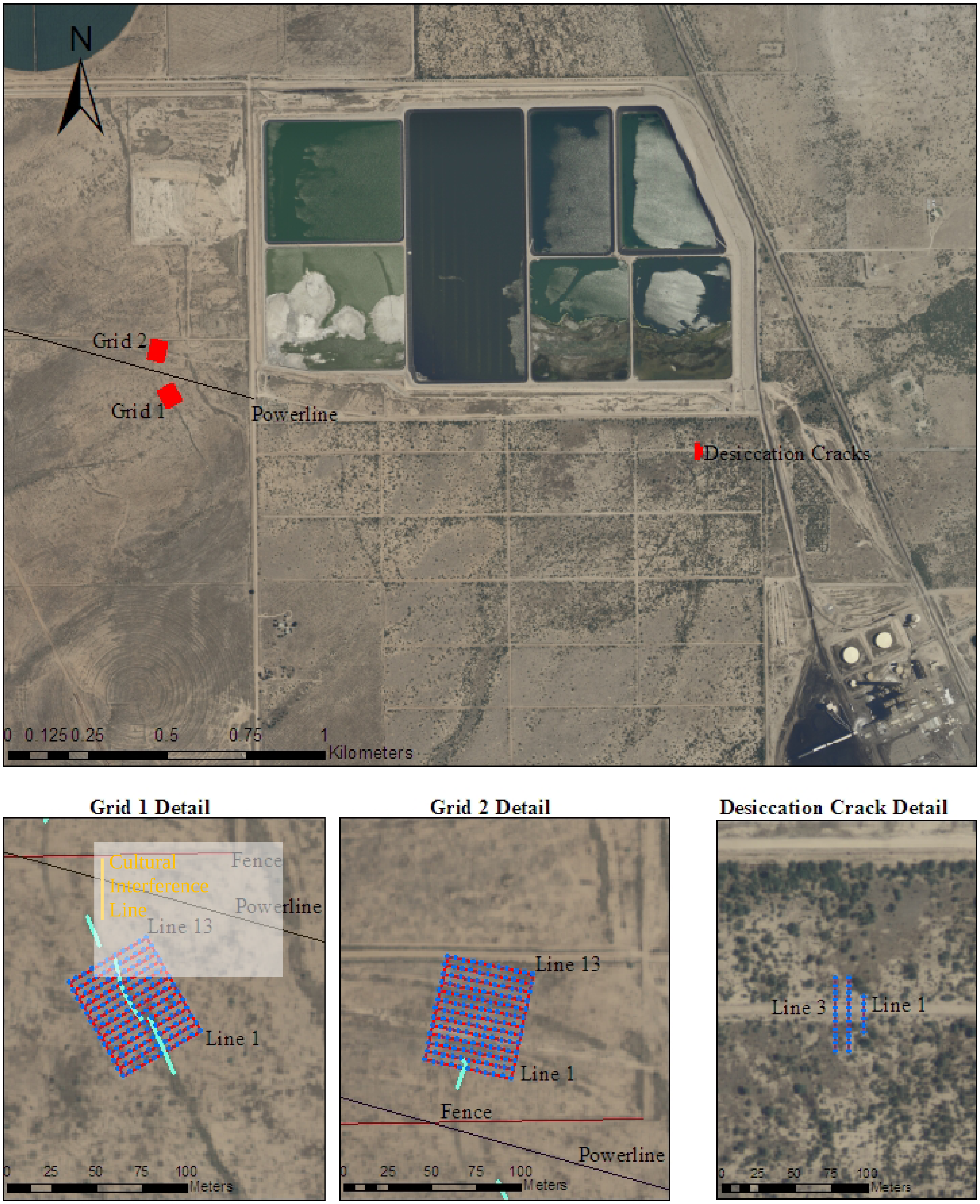

Figure 1.3 Willcox survey area aerial photo with mapped survey locations, local features, and approximate visible fissure locations. Photos courtesy of AEPCO.

Figure 1.3 shows the survey areas consisting of two grids situated West of the power plant Combustion Waste Disposal Facility, and the desiccation crack site to the South of the ponds. The sites were selected on the basis of being over, or on the projection of known fissure trends. The two grids each consist of 13 parallel lines at 50 meters length, with 5 meter spacing between lines. Grid 1 was located to the south of Grid 2, and was set up with the lines running perpendicular to a visible earth fissure that had an aperture ranging from 0.1-1m. Grid 2, was set up with lines running perpendicular to a suspected fissure that had no surface expression.

Grid 1 lines were oriented at S60W, with the (0,0) reference point situated at the southwest corner of the grid. Grid 2 lines were oriented approximately N78W, which ran east-west when considering the magnetic declination in the area, with the (0,0) reference point situated at the southwest corner of the grid. The grid orientations were chosen because they were believed to be the closest to perpendicular to approximate fissure locations.

The three lines to the south of the evaporation ponds were run N-S over a desiccation crack identified in 2005, but subsequently covered, that had formed parallel to the road. Line 1 was slightly shorter due to vegetation interference, and is the easternmost line, with lines 2 and three to its West. The (0,0) reference point for the desiccation crack lines is at the NE corner of the lines. The detail view of all lines is shown in Figure 1.3.

In addition, Figure 1.3 shows the approximate location of visible earth fissures (cyan color). Coordinates were taken with by GPS which could introduce approximately 3 meters of error in the actual location.

There are two survey sites not shown in Figure 1.3: the cultural interference test line, and one of the seismic lines that was run off the grids. Locations of these lines are approximately 20 meters East of the fence-powerline crossing. The cultural interference line was run perpendicular to the fence and extending South 40 meters. The off-grid seismic line was run parallel to the fence.

1.4 Seismic Lines and Trench Locations

After the geophysical measurements were completed, three test trenches were excavated using AEPCO personnel and equipment under the direction of Ralph E. Weeks, RG of GeoSouthwest. Mr. Weeks performed geologic logging of the trenches. Logs of Test Trenches Nos. 1, 2 and 3 are included in Chapter 7. Trench No. 1 was located in an area on the fissure alignment 3 meters South of Seismic Line 1 and 6 meters South of the barbed wire fence. There was no fissure surface expression at Trench No. 1; the nearest surface exposure was about 7 to 8 meters to the South. Trench No. 2 was located in Grid 2 on the fissure alignment about 7 to 8 meters South of Seismic Line 1, between Lines 2 and 3 of Grid 2. Again, there was no fissure surface expression at Trench No. 2; the nearest surface exposure was to the South. Trench No. 3 was located in Grid 1 near the LiDAR instrument station. This trench crossed the visible fissure. Figures 1.4 and 1.5 show the locations of the seismic lines, as well as the trenches that were excavated.

These trenches (approximately 3-4 ft deep) were excavated using a Case 580C backhoe, owned by AEPCO and operated by Mr. Jerry Ennis of AEPCO. In two cases (Test Trench 4 and 5), the trenches were positioned in close proximity to ground markers indicating the presence of a seismic refraction anomaly, as staked by AMEC. The third excavation was placed in near proximity to a former LiDAR instrument station, located several hundred feet south of the area that received the bulk of the geophysical coverage. Each trench was positioned transverse to the trend of exposed fissures present in the locale, with each trench about 9 to 12 meters long and excavated first with a wide equipment pass to a depth of about 30 cm, followed by the completion of a narrow keyed trench in shallow, smoothed surface.

Each trench was then geologically logged by Ralph E. Weeks, and subsequently backfilled with the trench spoils. The test trench logs and selected photographs of the earth fissures exposed are attached to this report.

The shallow soil profile encountered by the excavation consisted of a surficial, ½ to 1-foot thick unit (A-1) consisting of slightly moist, soft sandy silt that is uncemented and cohesionless. This unit is underlain by a more cemented, firm to very firm clayed sand whose degree of cementation increases with depth. Units A-2 and A-3, as logged, are very similar, with the exception of the degree of calcareous soil development, with the stage of cementation increasing from Stage I-II to Stage II-II+ with depth.

Physical evidence of earth fissuring was detected in all three trenches, with the features of Trench 2 consisting of a zone of strain, with no definitive earth fissure exposed in the excavation. In contrast, the earth fissures present in Trench 1 and 3 were more organized, with segments where the fissuring is expressed as one fracture, with aperture. Descriptions of the earth fissure features observed in each trench are presented in Chapter 7, Trenching Report.

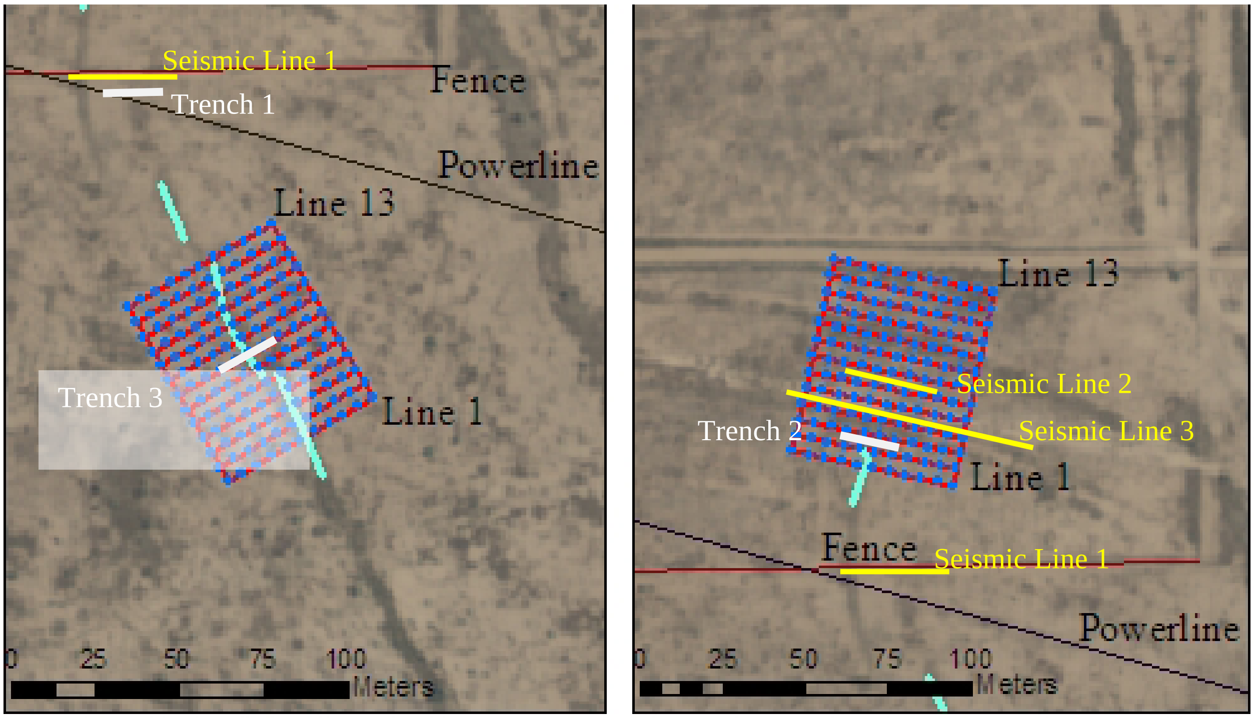

Figure 1.4 Approximate Seismic and trench locations shown on Grid 1 (Left), and Grid 2 (Right).

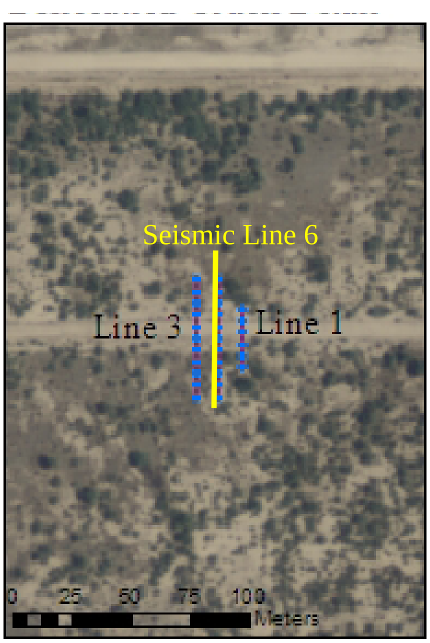

Figure 1.5 Approximate seismic line location shown on desiccation crack surveys.

1.5 Project Area Geologic and Hydrologic Setting

Little information is available concerning the geometry and geology of the immediate underlying basin and bedrock. About 2 kilometers northwest of the fissure, and closer to the Redbird Hills at the basin edge, Drewes (1980) reports a deep well encountering Paleozoic limestone at a depth of 698 feet. About 2 kilometers southeast of the fissure, Rucker and Keaton (1996) report borehole geophysical logs at several wells encountering interpreted bedrock at depths of about 1060 to 1080 feet. Descriptions of basin materials, based primarily on a few water well driller logs, are very limited. The fissure location is thought to be controlled by facies changes in the basin alluvium as it grades from mountain-derived stream alluvium to lacustrine clays in the basin center.

As documented in historic ADWR records, groundwater levels under the fissure have been dropping steadily over the decades. When water wells were drilled in the area in the 1950s, the water table was at a depth of about 100 feet. By the mid 1980’s, those levels had dropped to about 170 feet, and by the year 2000, groundwater levels had dropped to a depth of about 200 feet. Currently, groundwater levels are typically more than 250 feet in depth in the fissure area. The local fissuring is just a small feature of the regional Willcox Groundwater Basin (WGB).

The Willcox Groundwater Basin is approximately 90 miles long and ranges from 10 to 30 miles wide compromising approximately 1911 square miles (Towne and Freark 1999). Located roughly 80 miles east of Tucson Arizona, the WGB is bordered by the Dos Cabezas and Chiricahua Mountains to the east, the Pinaleño Mountains to the north, and the Dragoon Mountains to the west. The deep basin has long been a site of rural agricultural development. Recently, increased development has led to increased aquifer usage, which currently far exceeds groundwater recharge in the semi-arid basin. Monitoring wells south of the Willcox basin have seen groundwater depletion of more than 80 feet from 1990 to 2005 (ADWR 2009). Recharge in the area comes solely from precipitation which averages approximately 300 mm per year in the basin floor and 900 mm per year in the mountains (ADWR 2009). Figure 1.6 shows the Willcox Basin details.

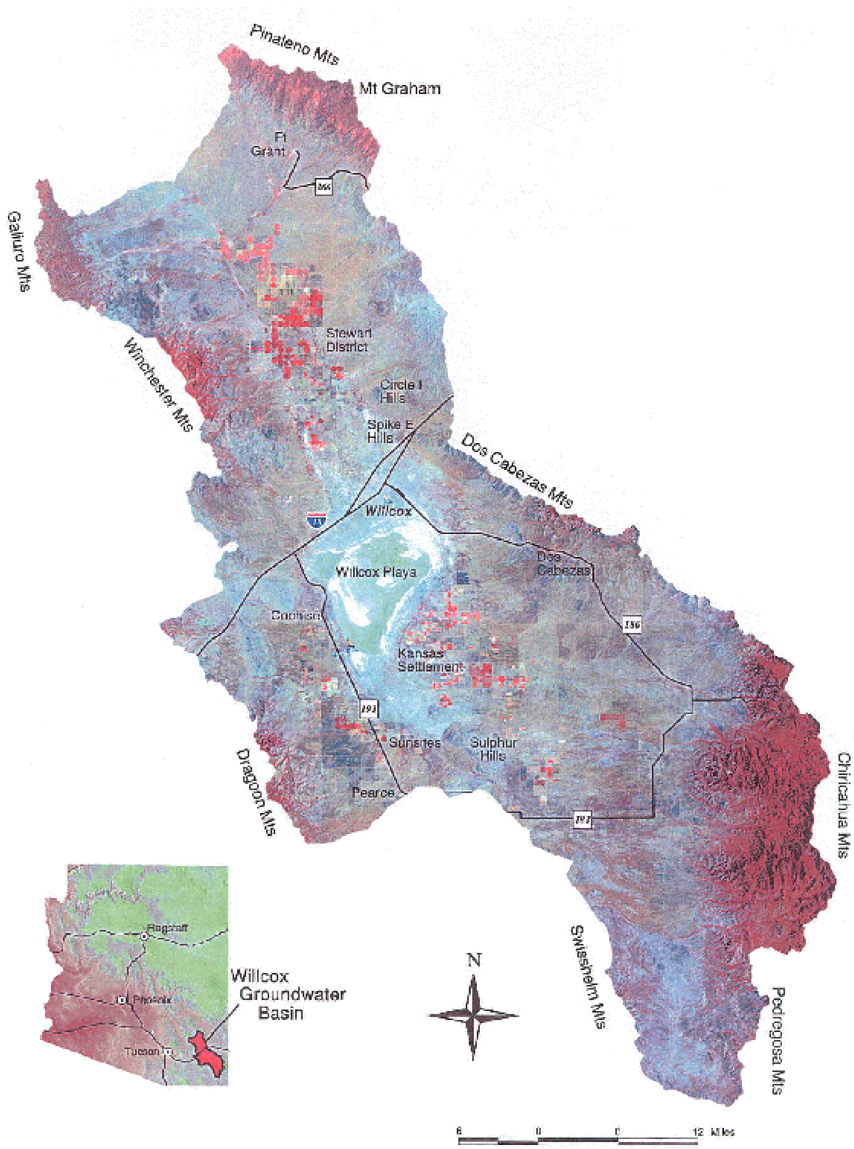

Figure 1.6 Willcox Groundwater Basin

The WGB is physically dominated by a basin and range structure which causes large variation in depth to bedrock. Although there is no active geologic activity, unevenness of the basin floor could be a factor in determining uneven settling with ground water removal. Figure 1.7 shows a graphical representation of the complex geometry of the Willcox Basin.

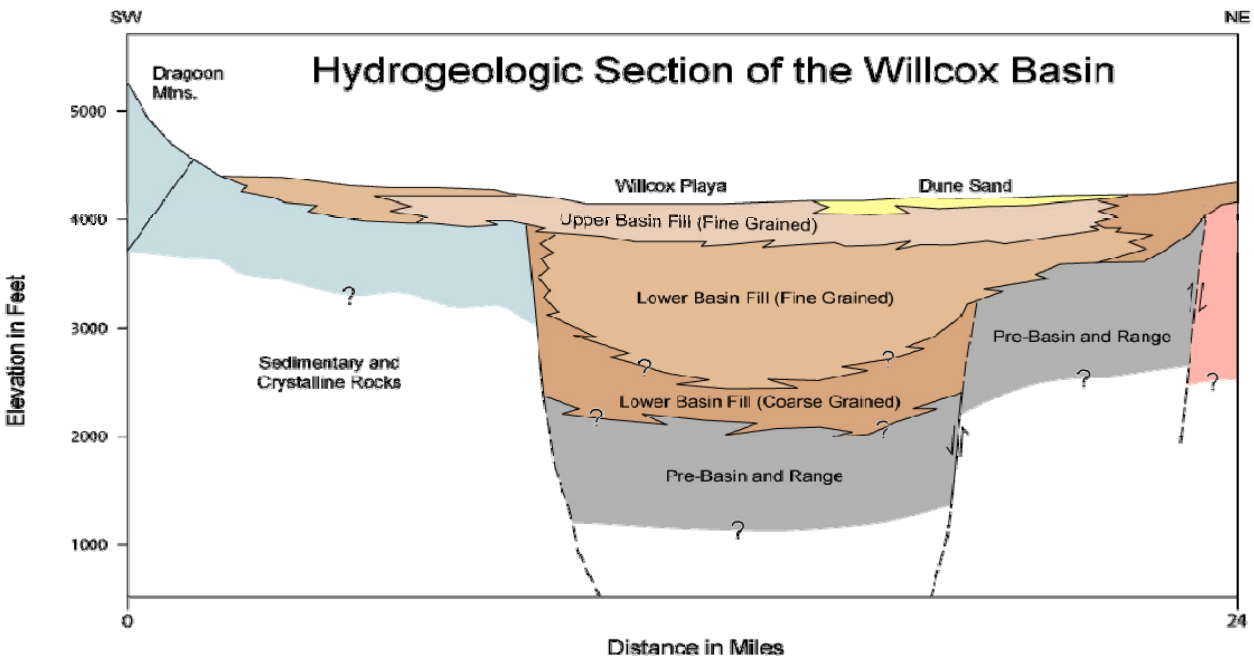

Figure 1.7 Willcox Basin Hydrogeologic Section (Anderson 2005).

Pre-development depth to groundwater was shallowest near the Willcox Playa at 34 feet below the surface, and ranged to 649 feet at its deepest (Towne and Freark 1999). The WGB has an estimated 45 million acre-feet of water stored to a depth of 1200 feet below land surface (Towne and Freark 1999), and in the year 2000 a total of 142,700 acre-feet was pumped to the surface for use (Tadayon 2009).

2.0 MAGNETICS

2.1 Technique

Static magnetic field surveys were carried out on the Apache Power plant property near Willcox Arizona. The instrument used was a GEM systems GSM-18 Overhauser magnetometer. In total, 29 lines were run on March 7, 8, 28 and 29 of 2009.

We used a handheld, staff-mounted magnetometer that was capable of measuring the total magnetic field as well as the magnetic gradient. During the first weekend of March 7-8, both total field and gradient were measured. After reviewing the data, the magnetic gradient data were determined to be inconclusive. Therefore, during the following weekend of March 28-29, only total field was measured.

In Grids 1 and 2, measurements were taken on each line every two meters while the desiccation crack line spacing was every one meter. Each measurement was recorded with a corresponding time, as well as an initial station recheck, to account for any drift over time due to the earth's magnetic field.

On April 19, 2009, tie lines were measured at grids one and two. These tie lines were perpendicular to the original lines. This helps eliminate any drift that may be present between individual survey lines in each grid.

2.2 Location

The magnetic surveys were conducted on Apache Power Plant property near Willcox, Arizona. For exact locations, refer to Section 1, Introduction. Surveys were completed in two grids and one desiccation crack area. All survey lines followed those of all the other test methods of Grid 1, Grid 2, and the Desiccation Crack Grid.

2.3 Data Processing

Two-dimensional, total-field plots were compiled for each line, while contour and surface plots were constructed for each grid (Figures 2.1-2.40). All plots were drift corrected using the initial base recheck and the tie-line surveys before interpretation was completed.

2.4 Data Description

At first glance, the individual line plots from the magnetic surveys of Grid 1 have an easily visible peak of some form or another. It is hard to say what the overall structure may look like until looking at the contour plots which show an overall high trend running north to south at about 20-25 meters distance (Figure 2.37).

2.5 Interpretation

As seen in Figure 2.37, the total magnetic field high at the 20-25 meter mark in Grid 1 correlates with the fissure which is visible at some places along the ground and with the other field techniques applied to the area. This can be interpreted to mean the magnetometer is successfully defining the location of the fissure. However, in Grid 2, (Figure 2.38) there is not the same type of consistent high values. Instead, the high that is visible in the contour plot runs east to west at approximately the same location as a known fiberglass water pipe.

When looking at the desiccation crack contours (Figures 2.39-2.40), a high is seen right where the road is. This anomaly could be due to the road and associated runoff or it could be showing the desiccation crack.

2.6 Cultural Interference

Cultural interference was also taken into consideration for the survey as the surrounding area had power lines and barbed wire fences present. A single test line was run to determine the affect of the cultural interference. This test line was run perpendicular to the barbed wire fence that separated Grid 1 from Grid 2. As seen in Figure 2.33, the fence had no effect on the instrument if kept at least 5 meters away. As seen in Figure 2.34, the power lines do not seem to affect the instrument at all at any distance that was measured. Based on these tests, the magnetometer was always kept at least 5 meters away from metal objects like the fence.

2.7 Graph Plots

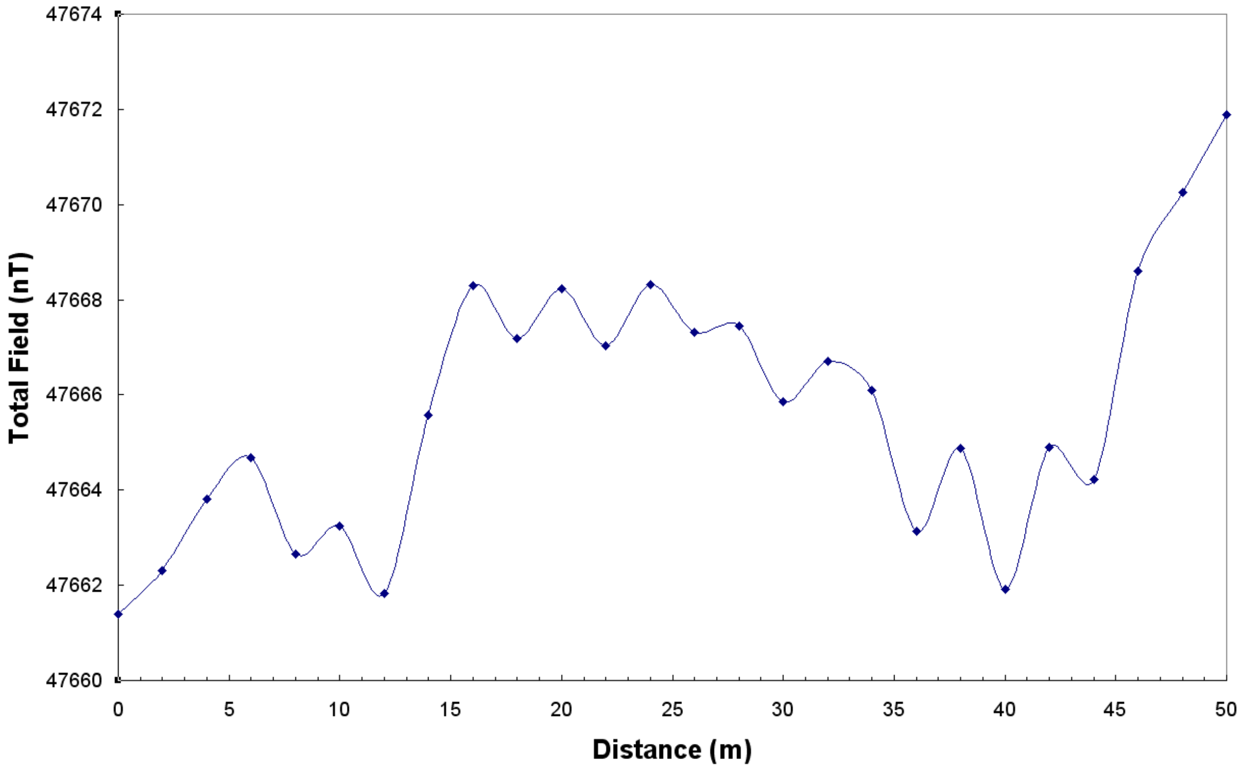

Figure 2.1. Grid 1 Line1 (0 meters). Plot runs E-W. Plot shows total magnetic field.

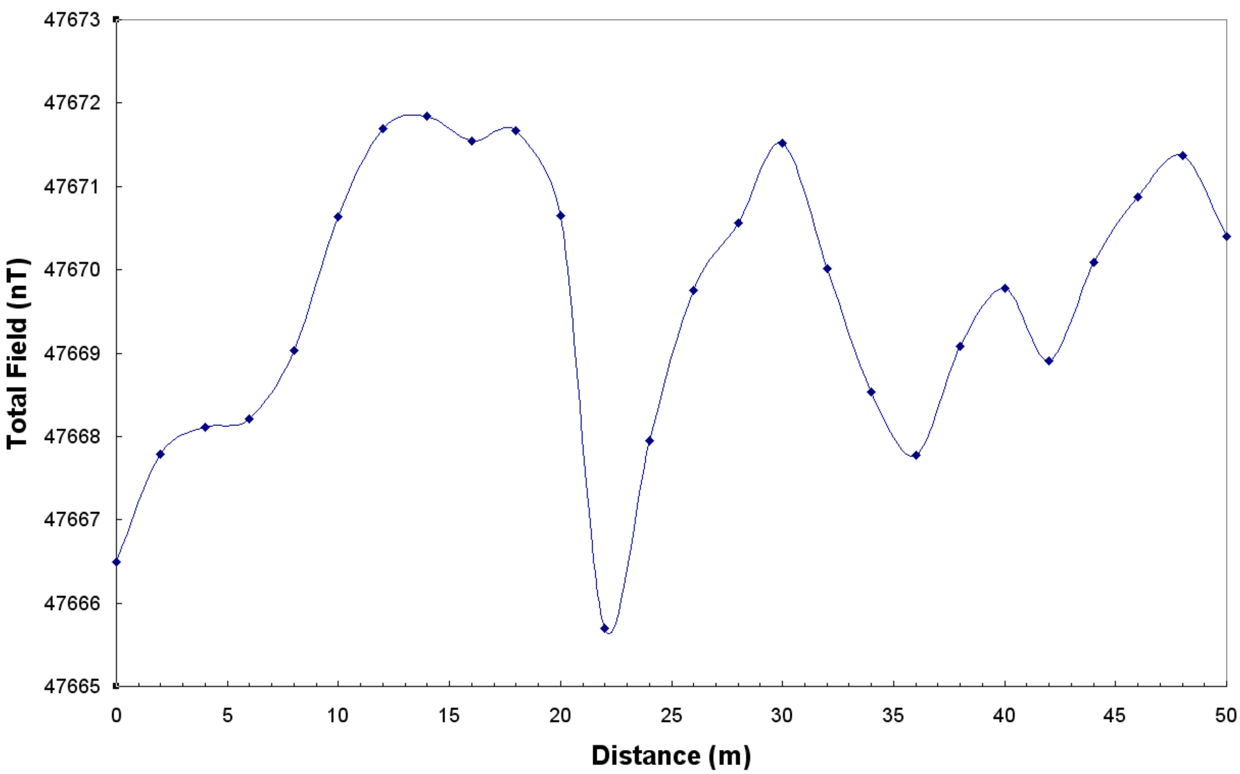

Figure 2.2. Grid 1 Line 2 (5 meters). Plot runs E-W. Plot shows total magnetic field.

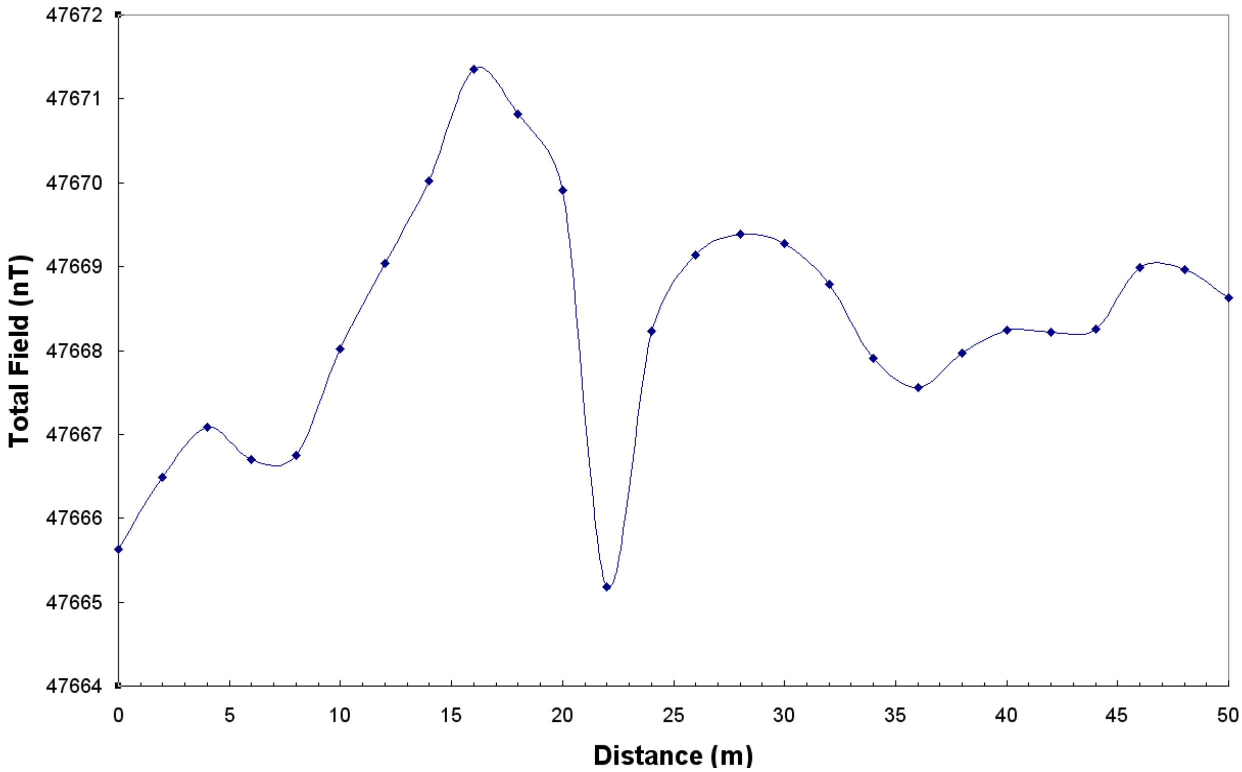

Figure 2.3. Grid 1 Line 3 (10 meters). Plot runs E-W. Plot shows total magnetic field.

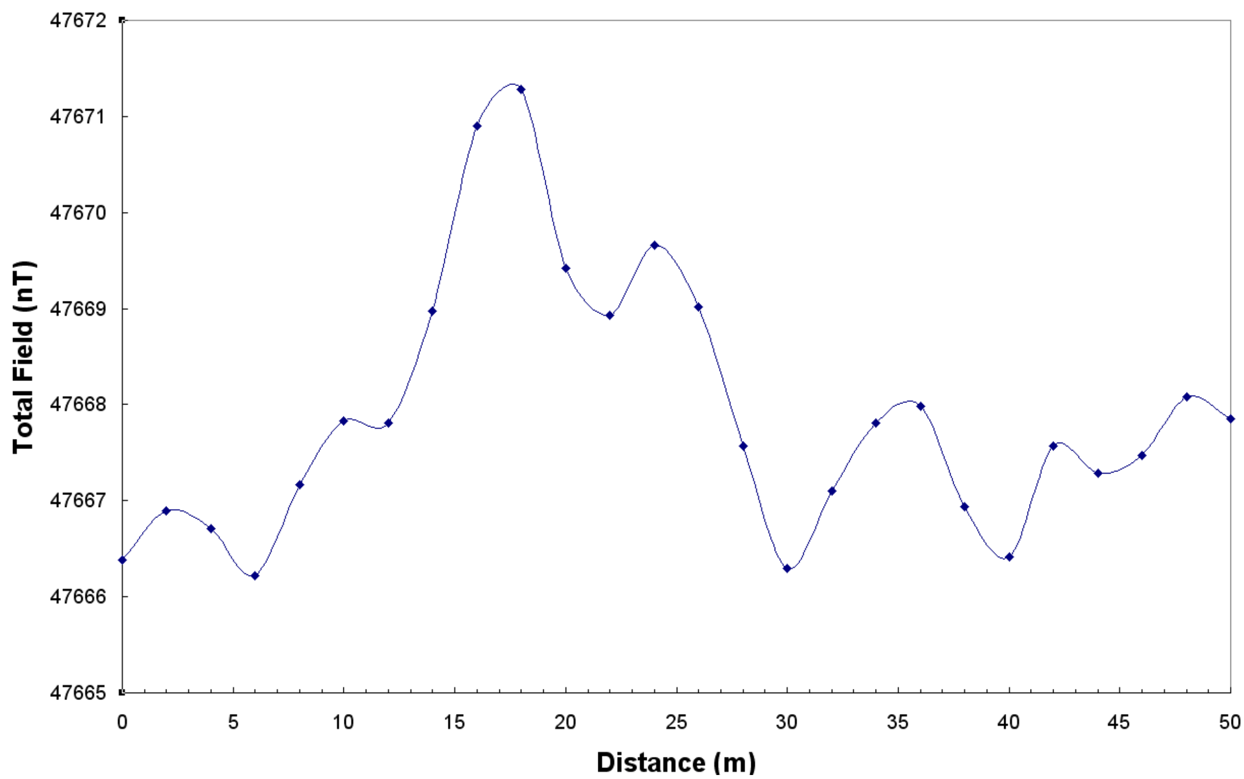

Figure 2.4. Grid 1 Line 4 (15 meters). Plot runs E-W. Plot shows total magnetic field.

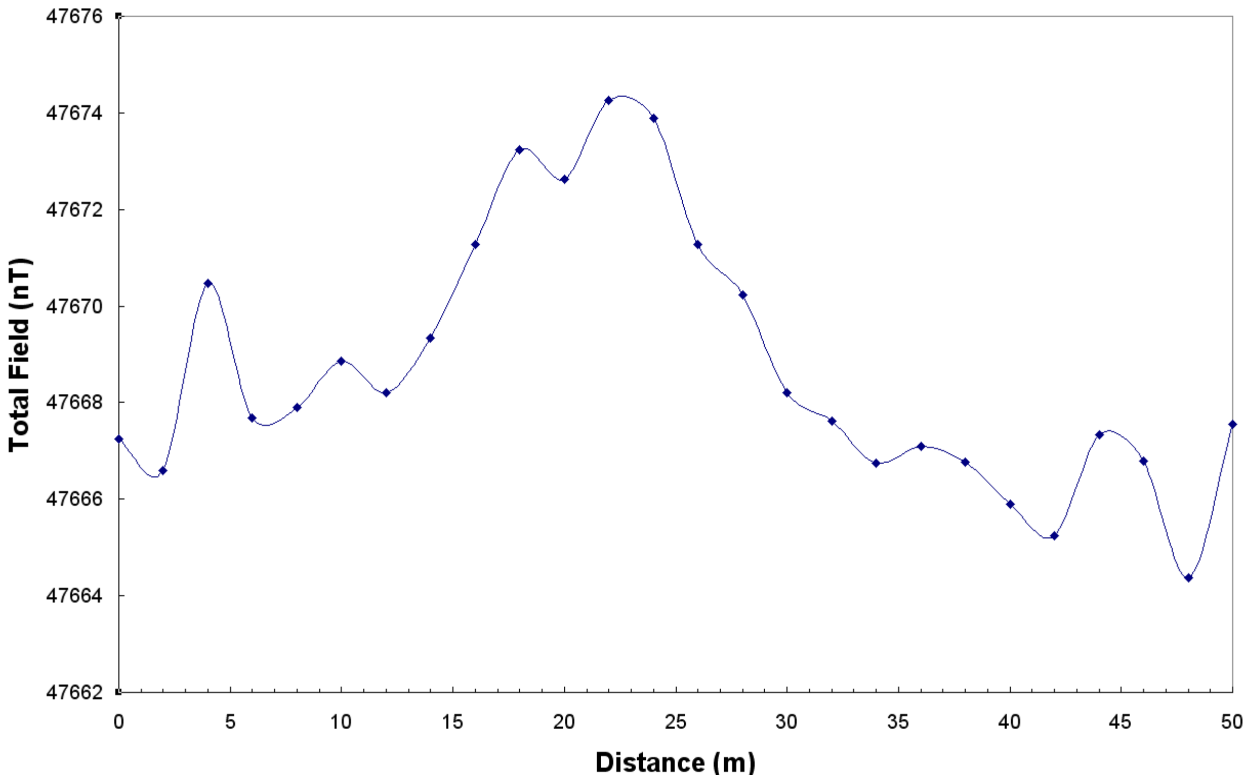

Figure 2.5. Grid 1 Line 5 (20 meters). Plot runs E-W. Plot shows total magnetic field.

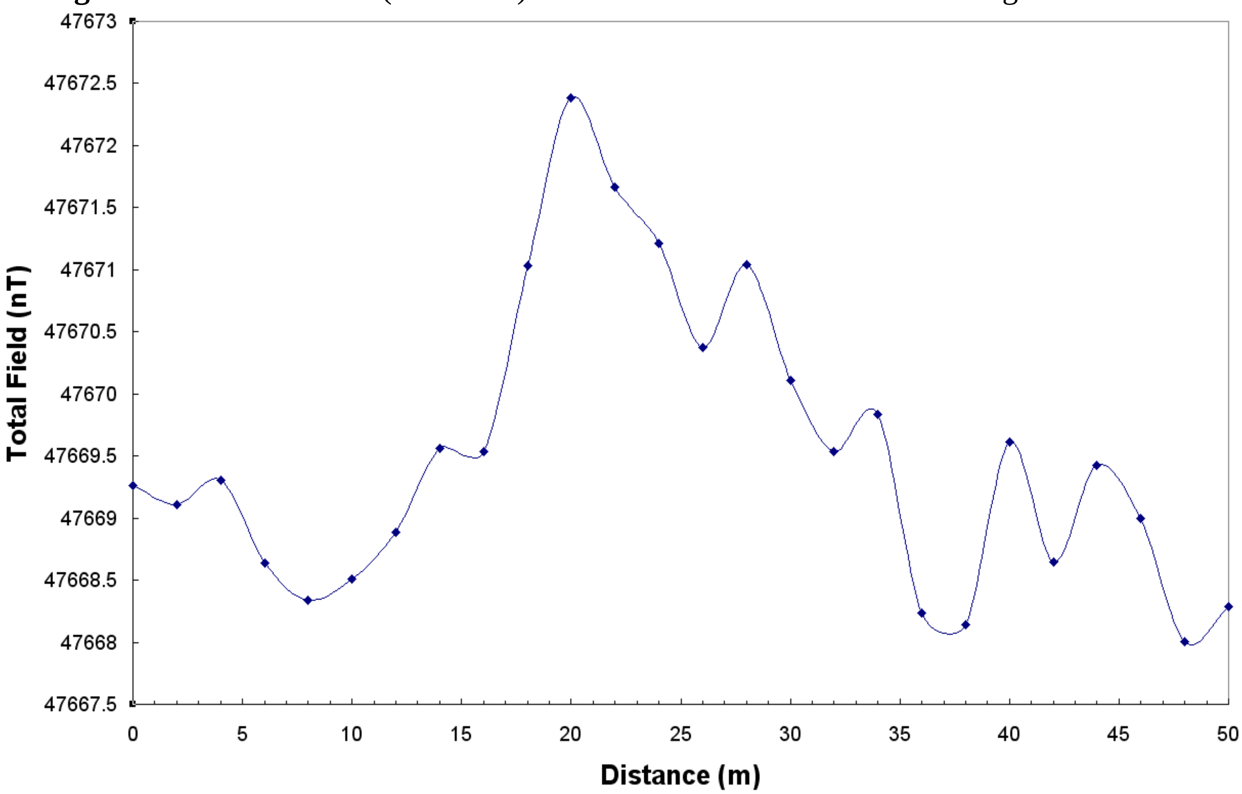

Figure 2.6. Grid 1 Line 6 (25 meters). Plot runs E-W. Plot shows total magnetic field.

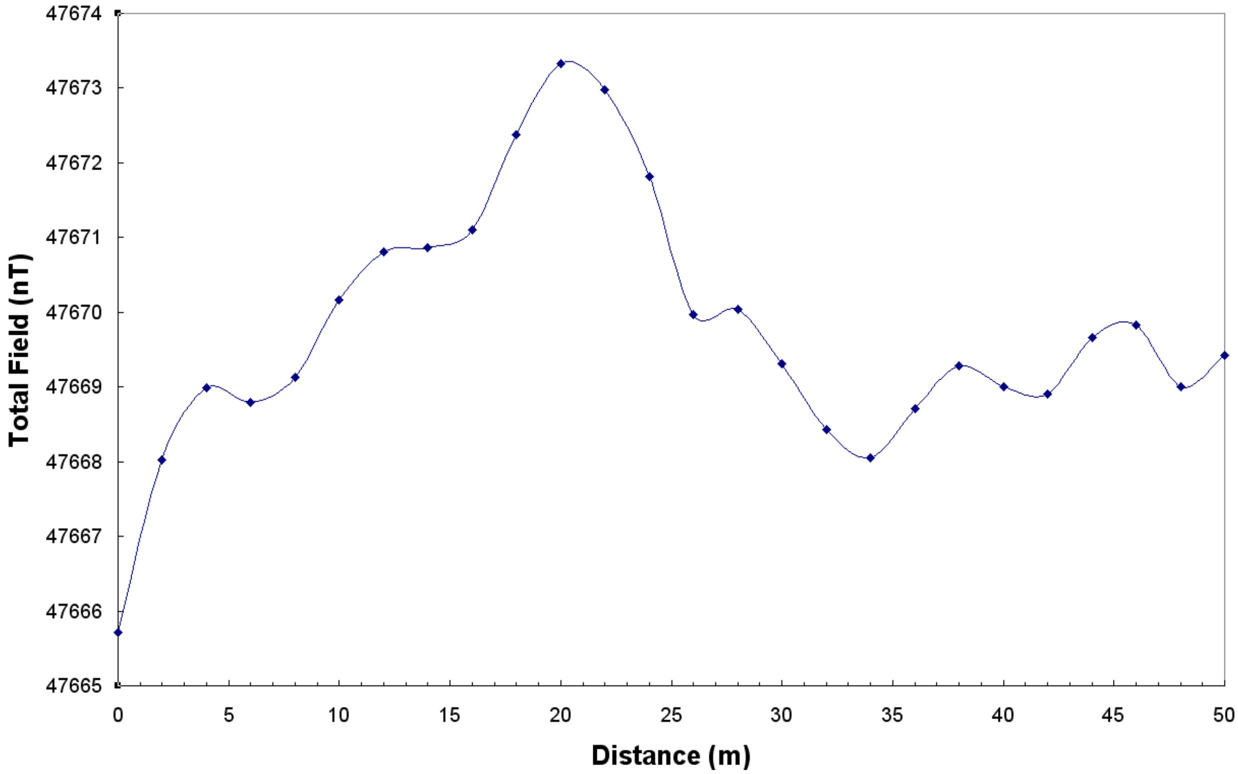

Figure 2.7. Grid 1 Line 7 (30 meters). Plot runs E-W. Plot shows total magnetic field.

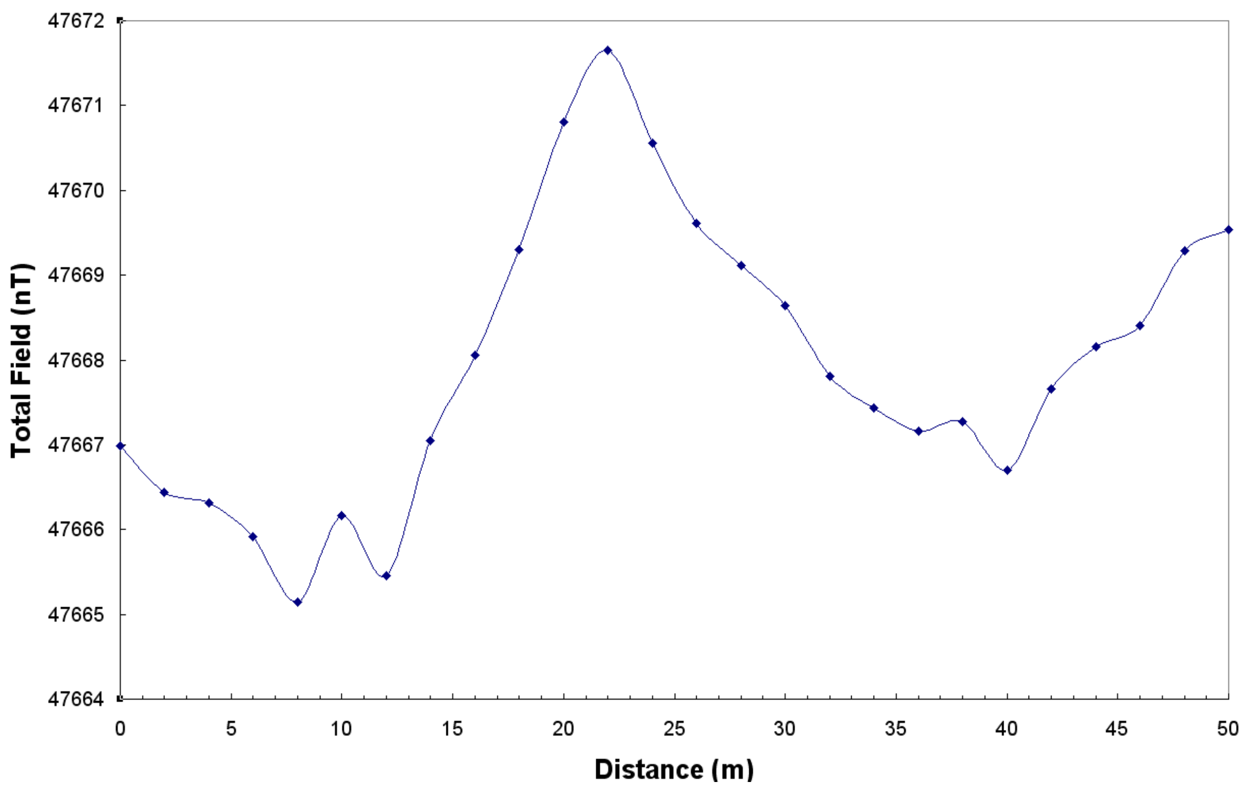

Figure 2.8. Grid 1 Line 8 (35 meters). Plot runs E-W. Plot shows total magnetic field.

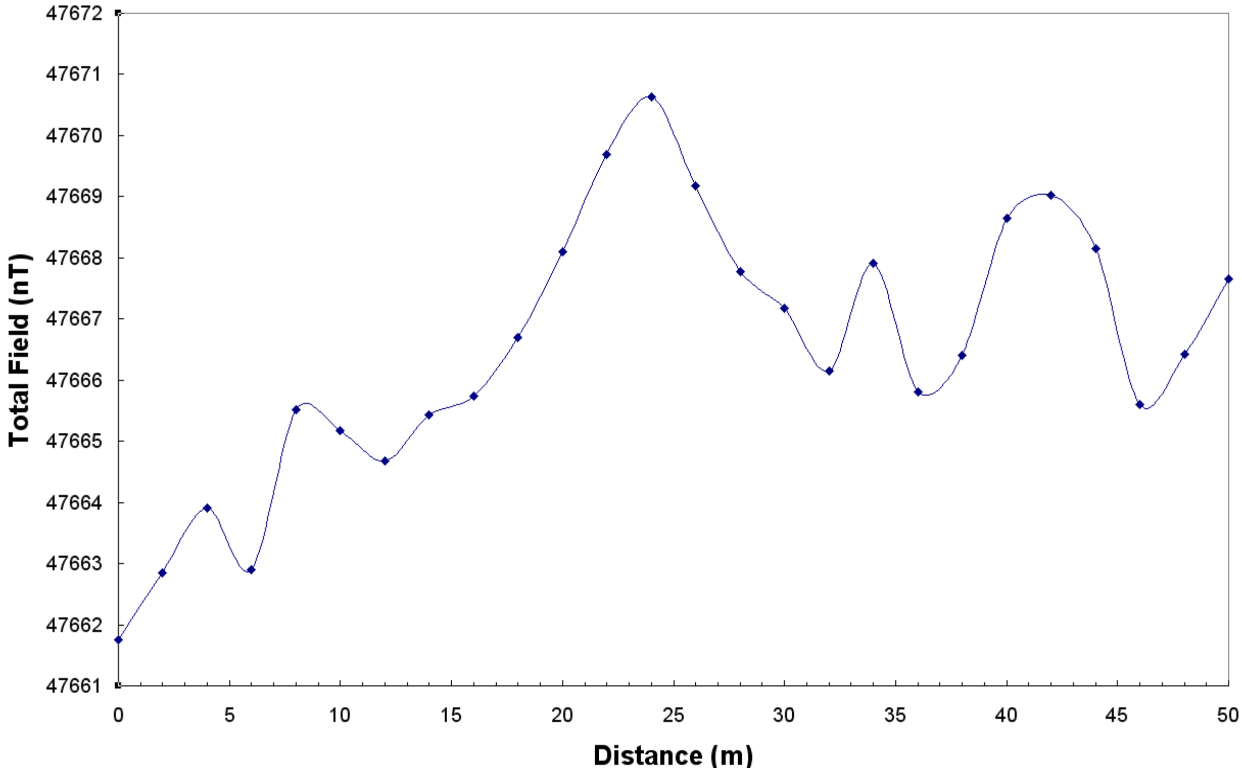

Figure 2.9. Grid 1 Line 9 (40 meters). Plot runs E-W. Plot shows total magnetic field.

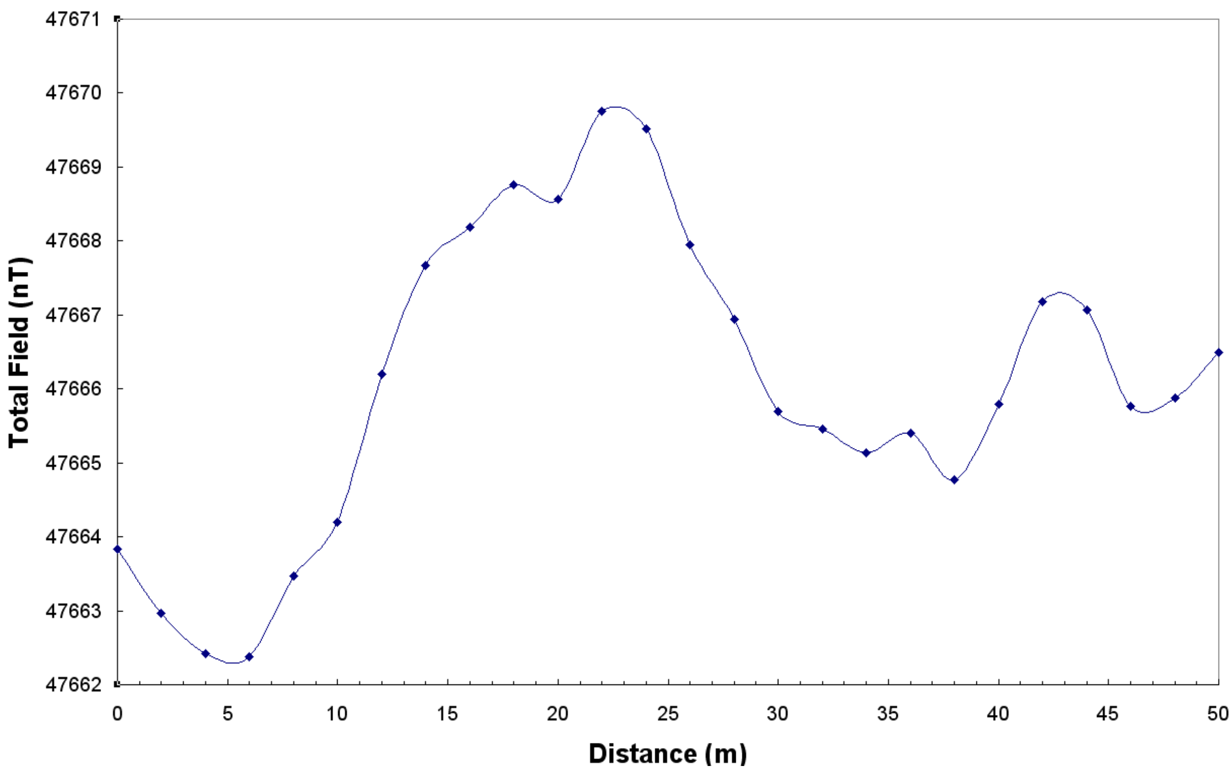

Figure 2.10. Grid 1 Line 10 (45 meters). Plot runs E-W. Plot shows total magnetic field.

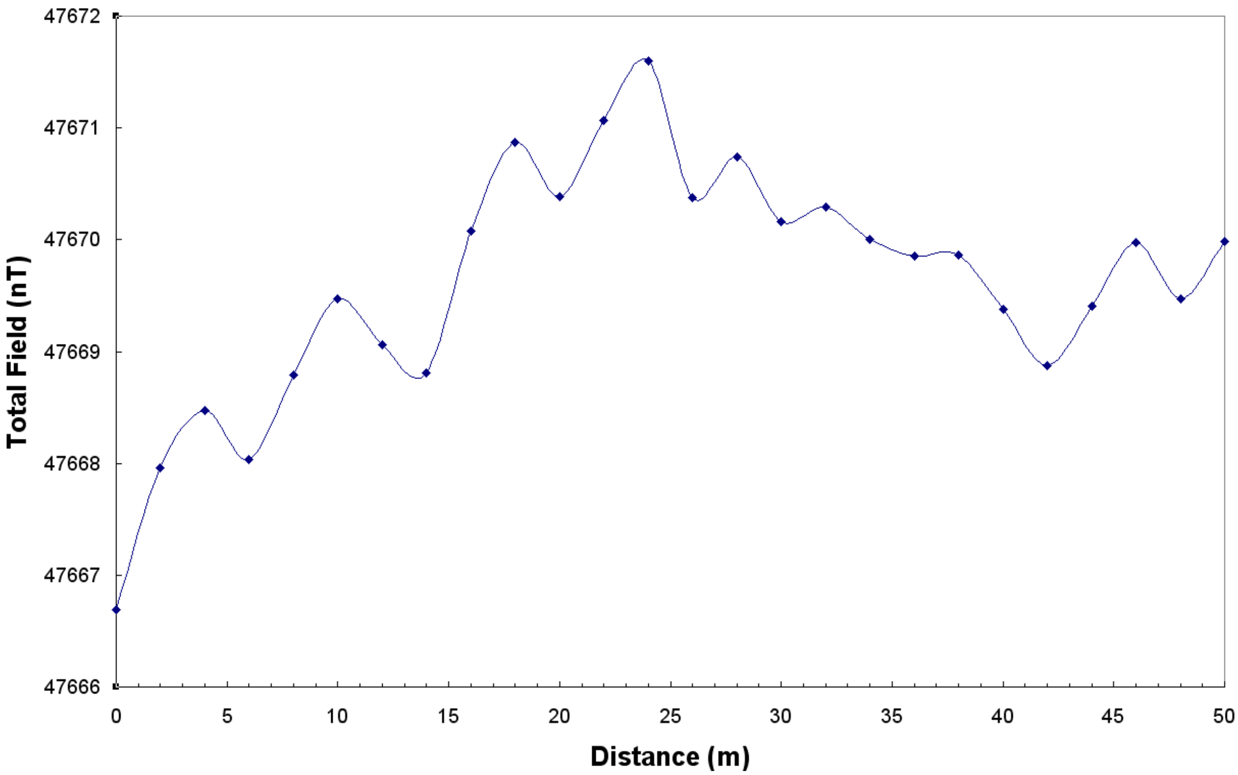

Figure 2.11. Grid 1 Line 11 (50 meters). Plot runs E-W. Plot shows total magnetic field.

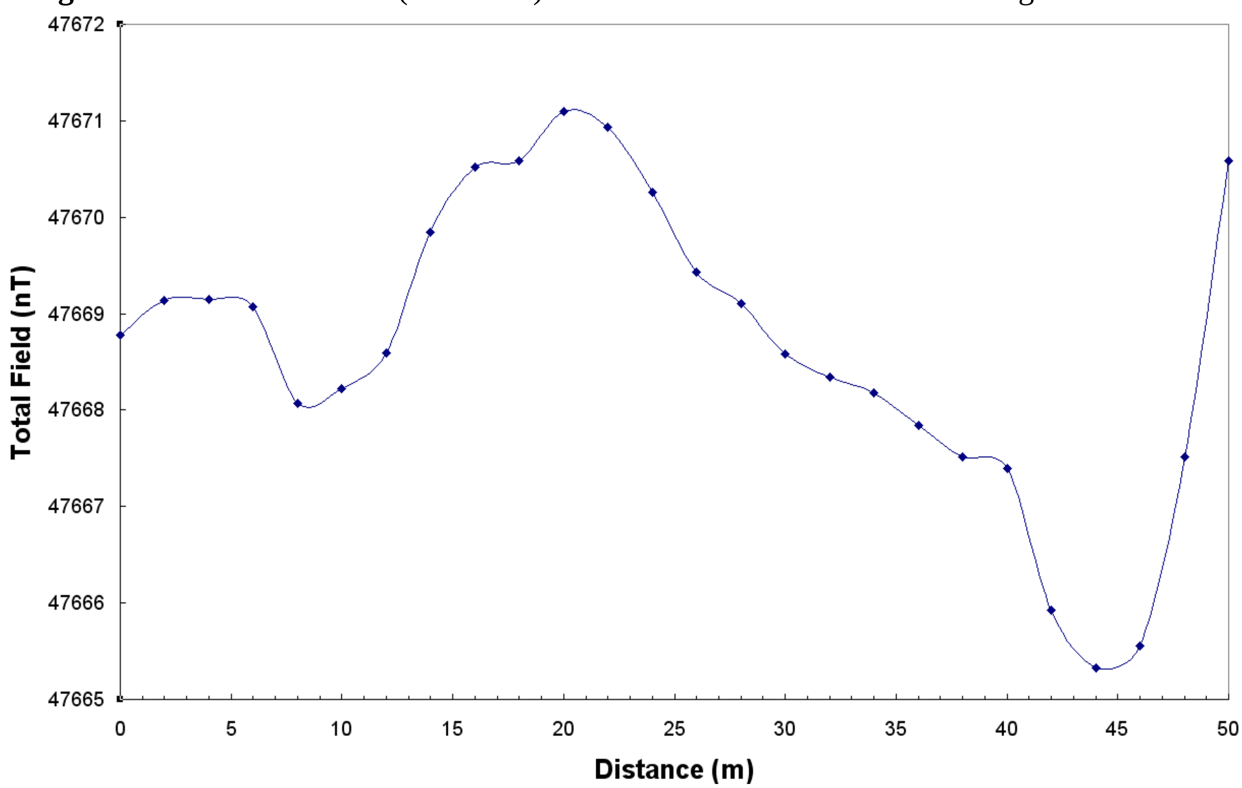

Figure 2.12. Grid 1 Line 12 (55 meters). Plot runs E-W. Plot shows total magnetic field.

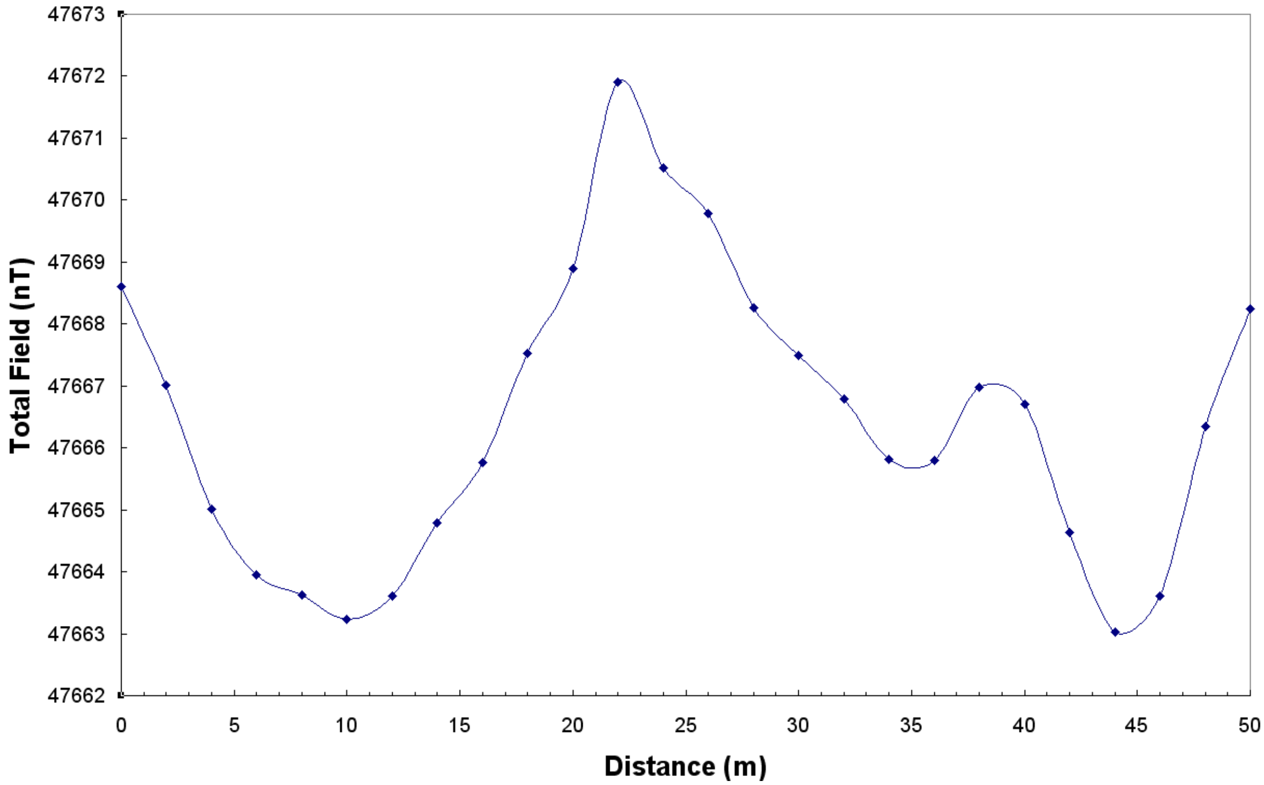

Figure 2.13. Grid 1 Line 13 (60 meters). Plot runs E-W. Plot shows total magnetic field.

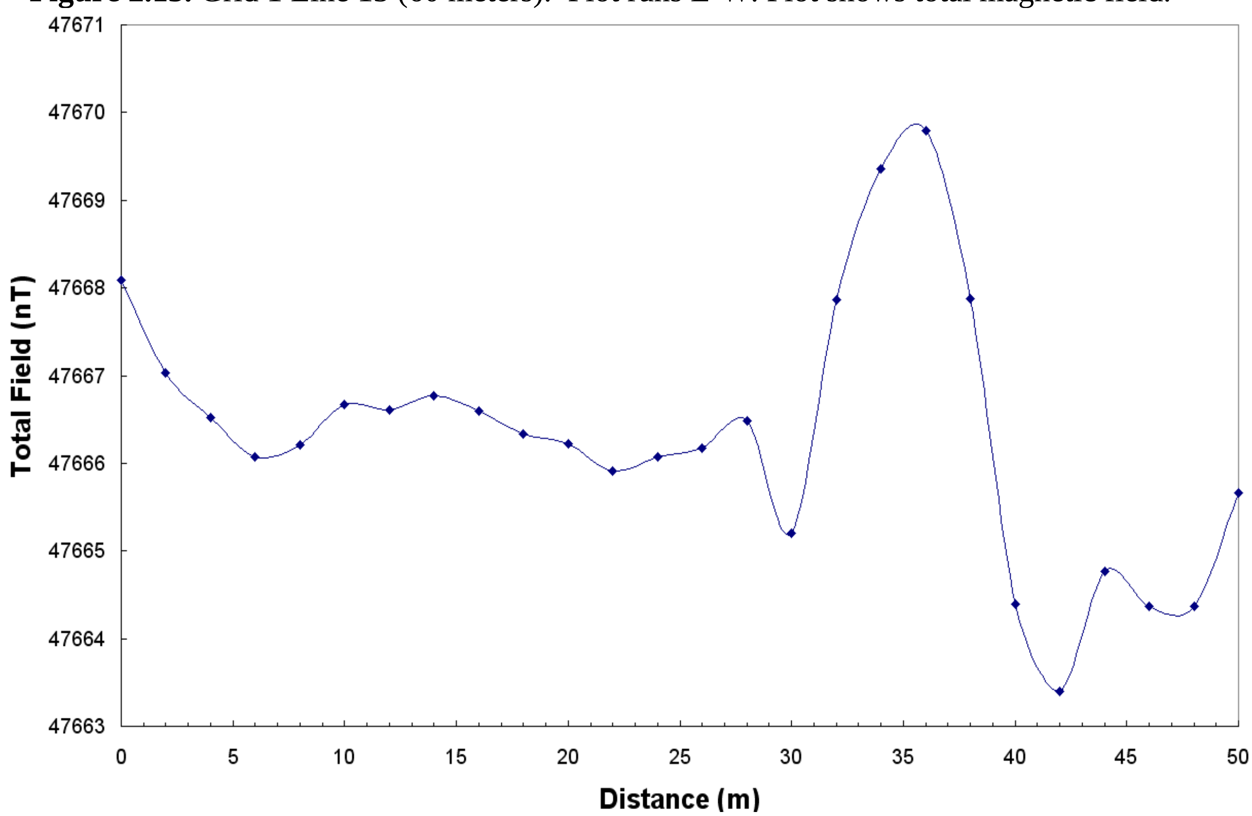

Figure 2.14. Grid 2 Line1 (0 meters). Plot runs E-W. Plot shows total magnetic field.

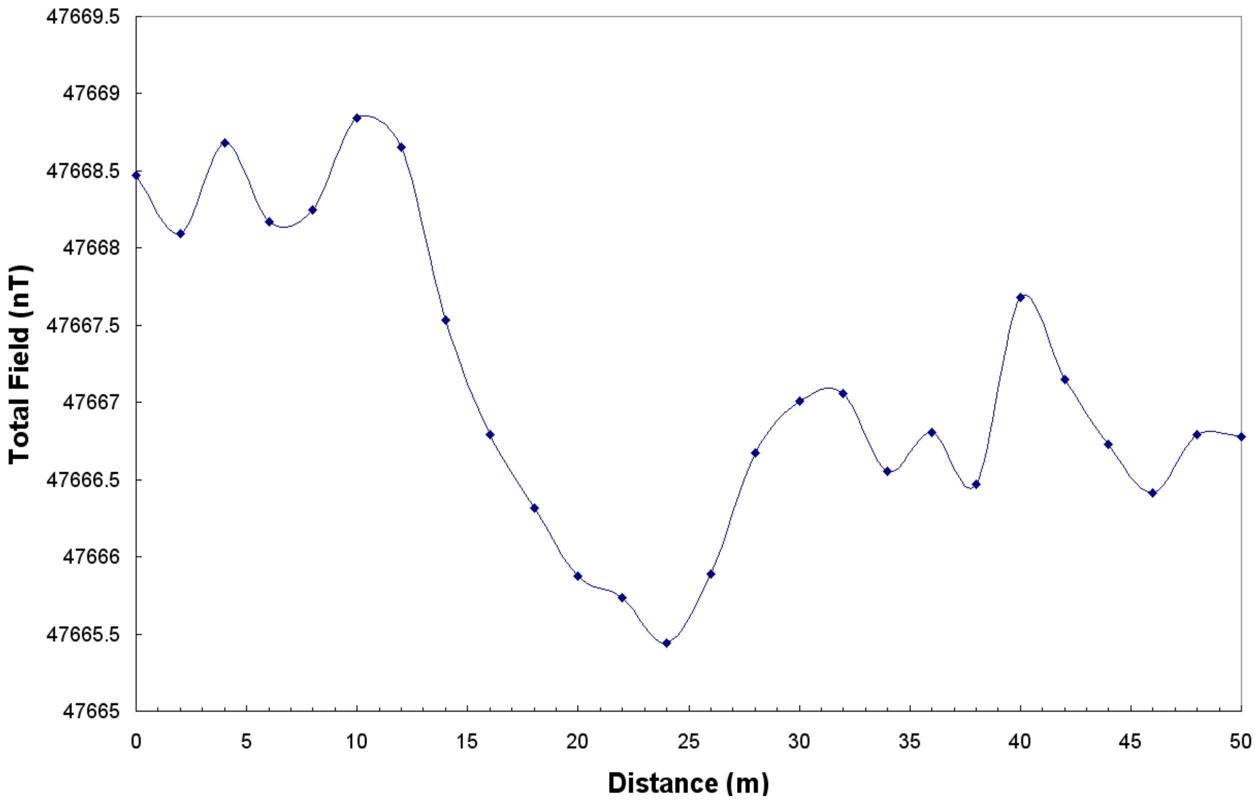

Figure 2.15. Grid 2 Line 2 (5 meters). Plot runs E-W. Plot shows total magnetic field.

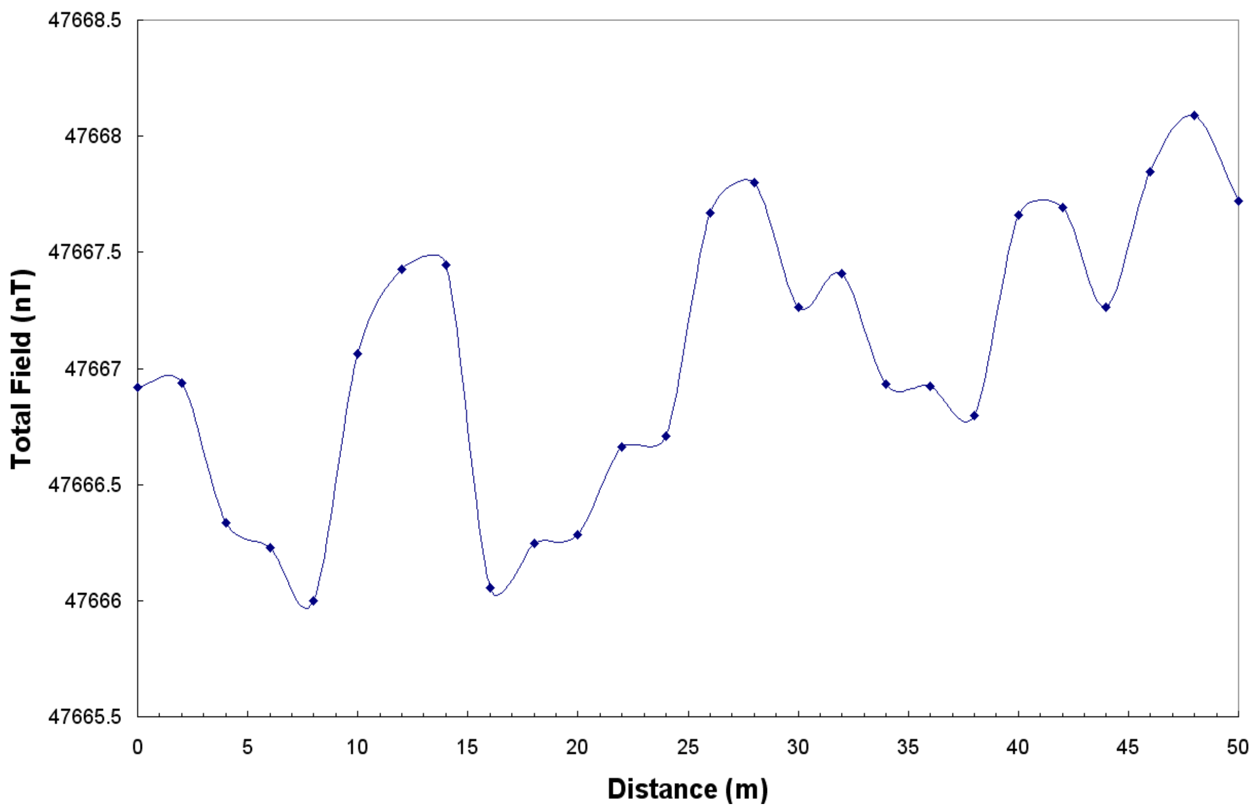

Figure 2.16. Grid 2 Line 3 (10 meters). Plot runs E-W. Plot shows total magnetic field.

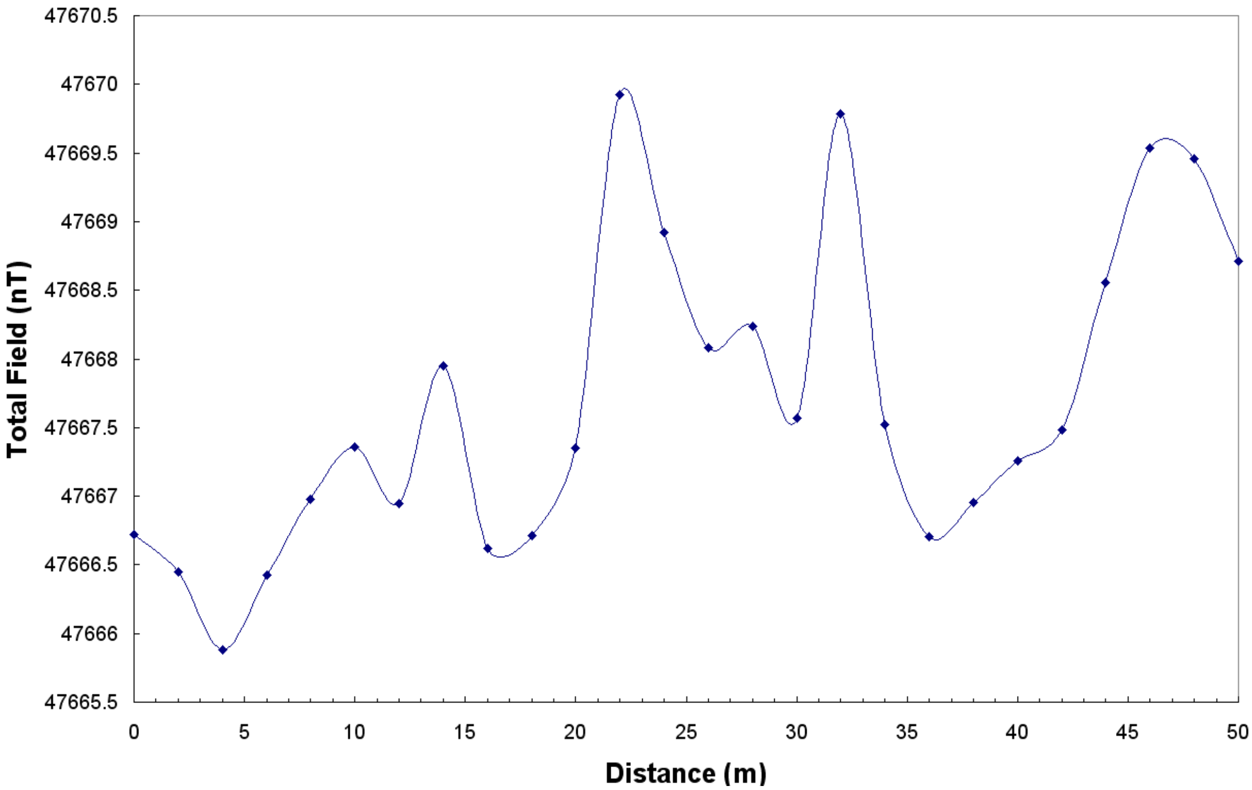

Figure 2.17. Grid 2 Line 4 (15 meters). Plot runs E-W. Plot shows total magnetic field.

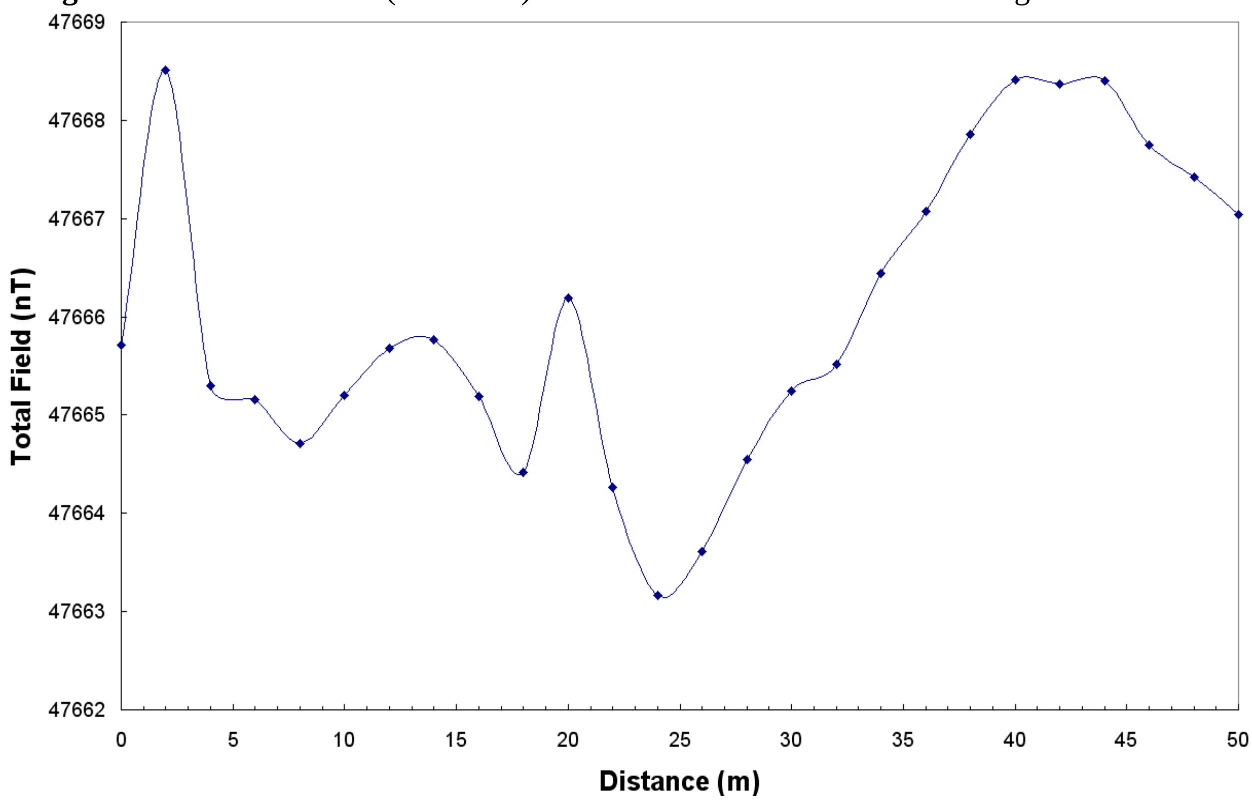

Figure 2.18. Grid 2 Line 5 (20 meters). Plot runs E-W. Plot shows total magnetic field.

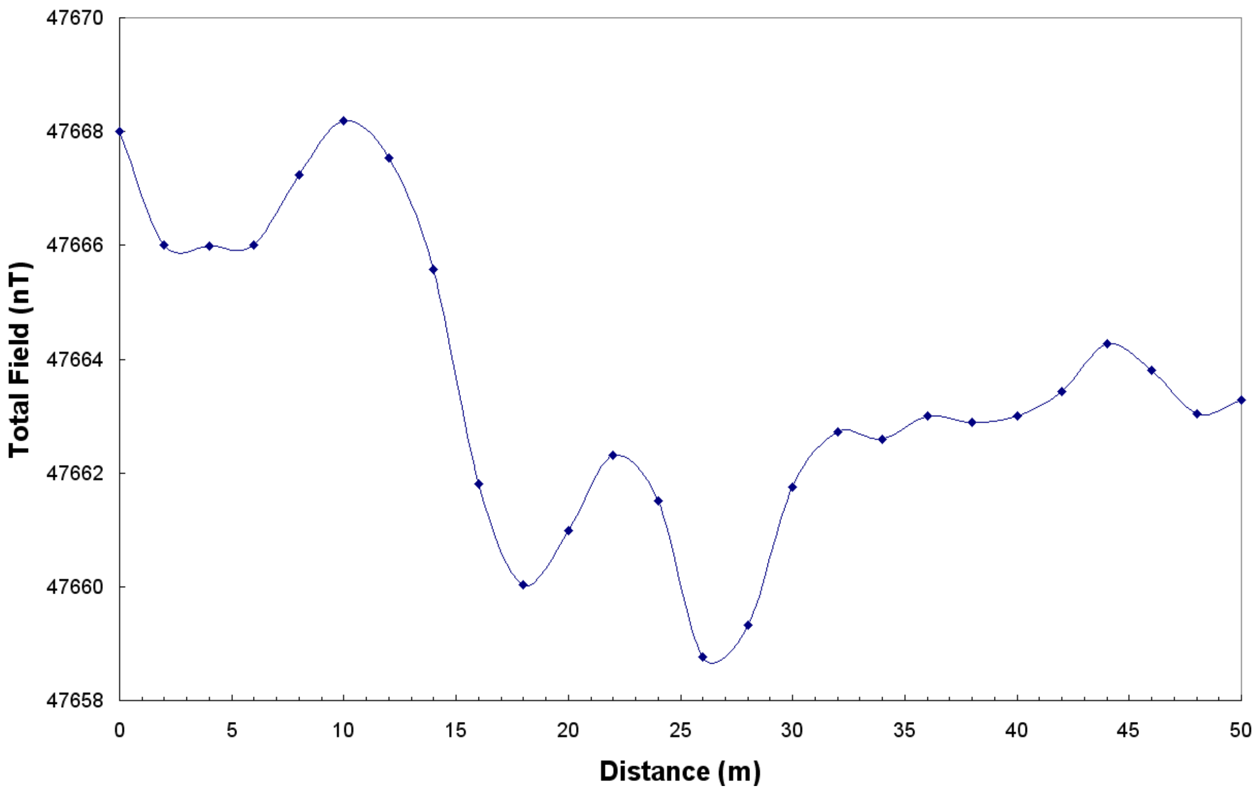

Figure 2.19. Grid 2 Line 6 (25 meters). Plot runs E-W. Plot shows total magnetic field.

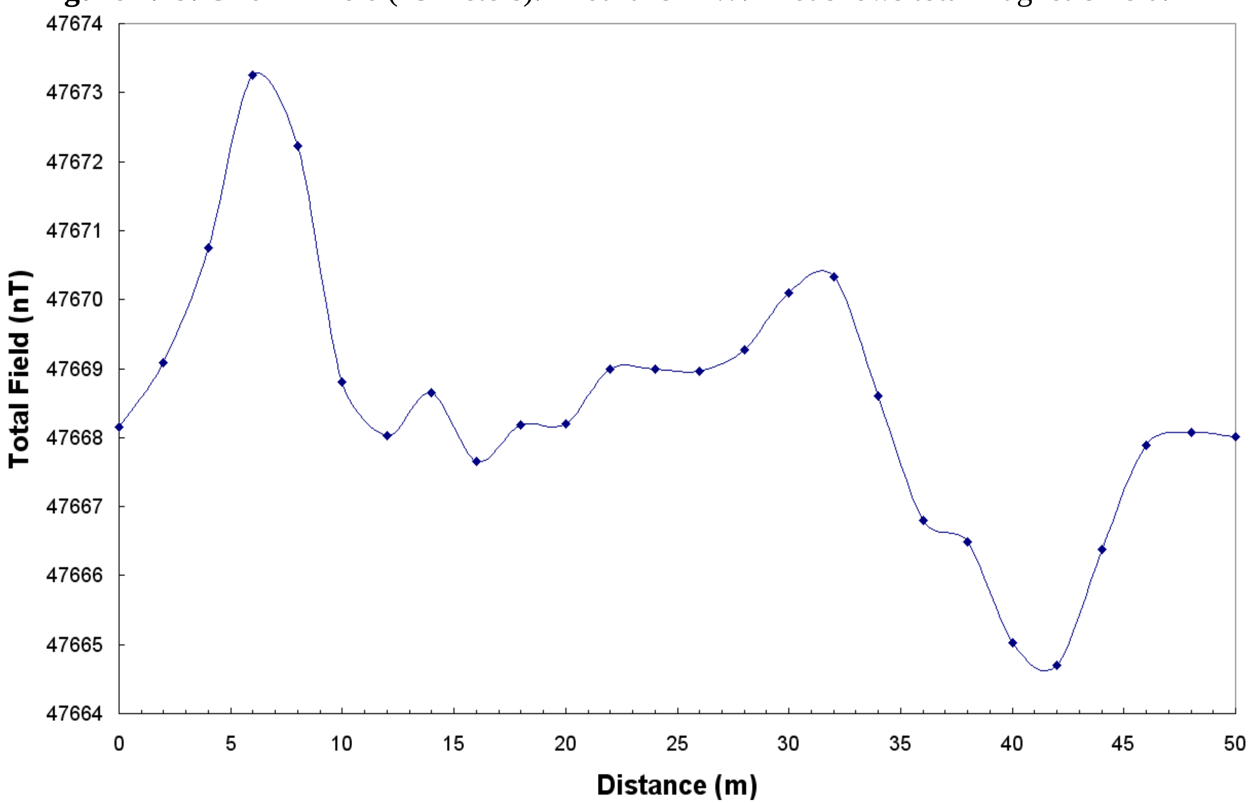

Figure 2.20. Grid 2 Line 7 (30 meters). Plot runs E-W. Plot shows total magnetic field.

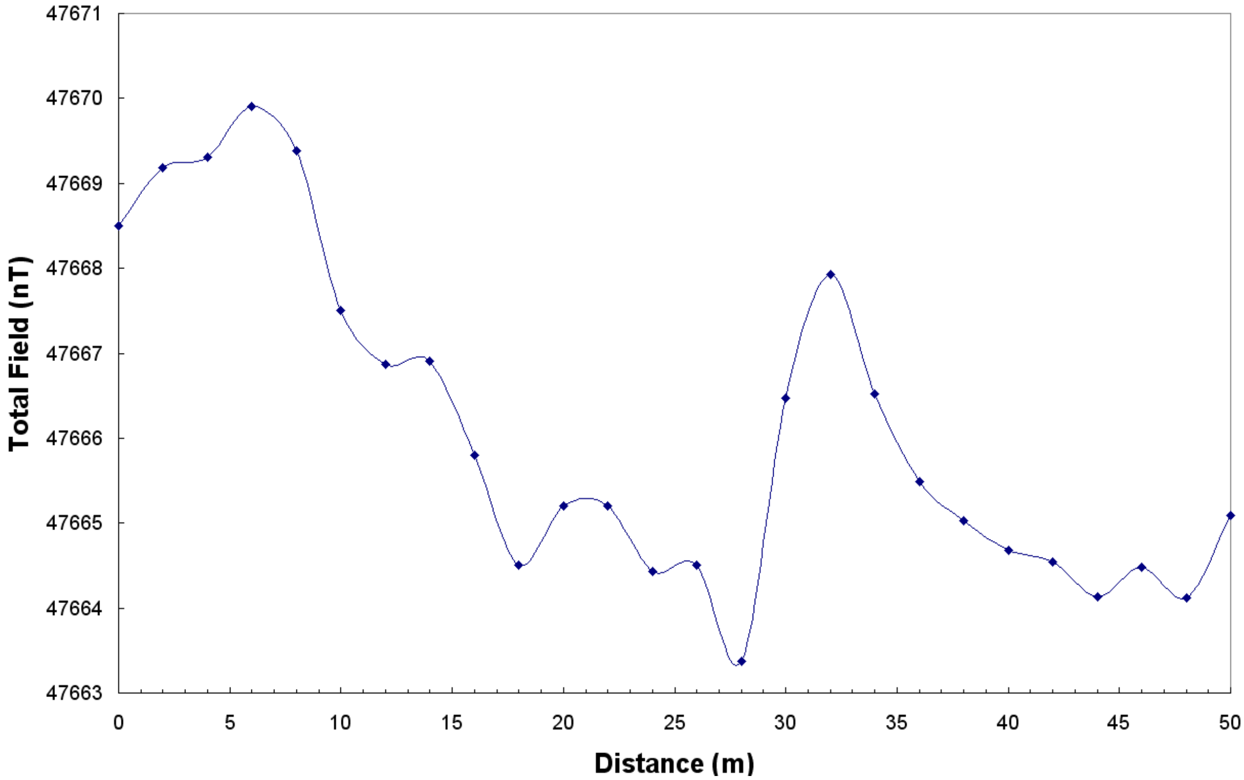

Figure 2.21. Grid 2 Line 8 (35 meters). Plot runs E-W. Plot shows total magnetic field.

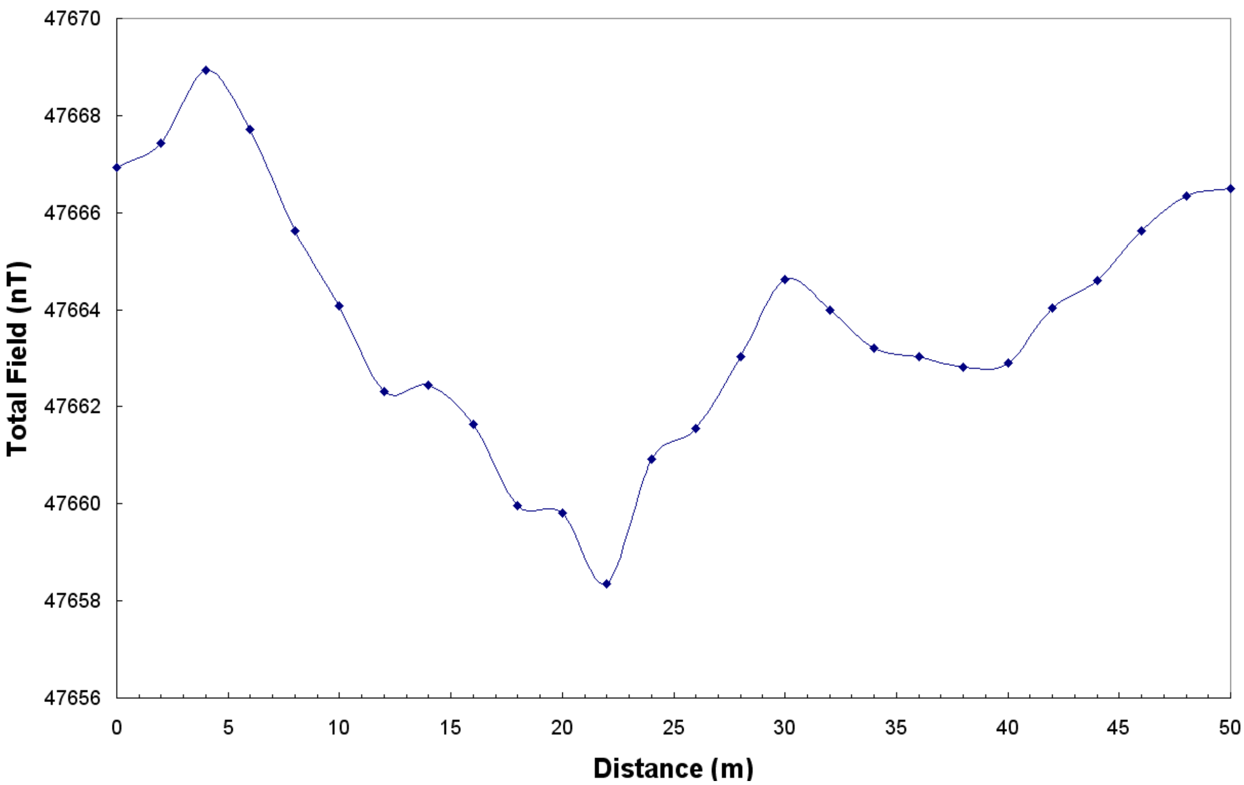

Figure 2.22. Grid 2 Line 9 (40 meters). Plot runs E-W. Plot shows total magnetic field.

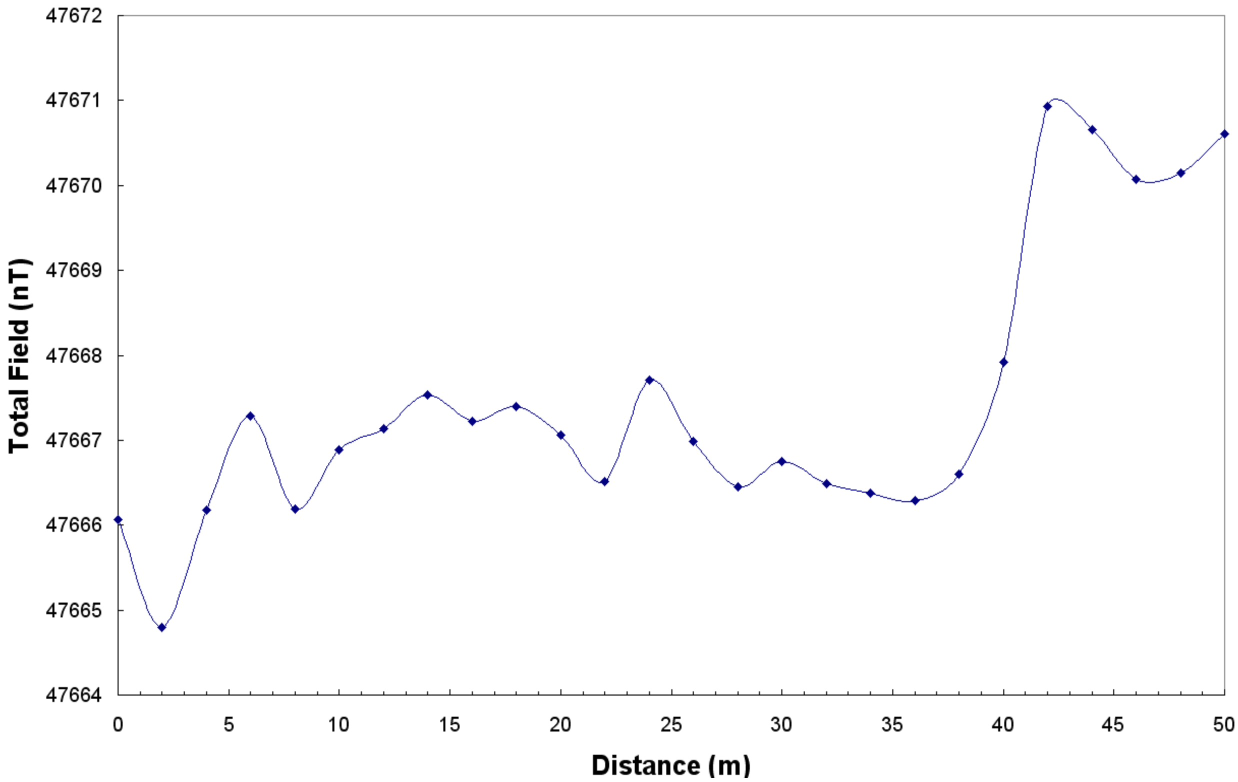

Figure 2.23. Grid 2 Line 10 (45 meters). Plot runs E-W. Plot shows total magnetic field.

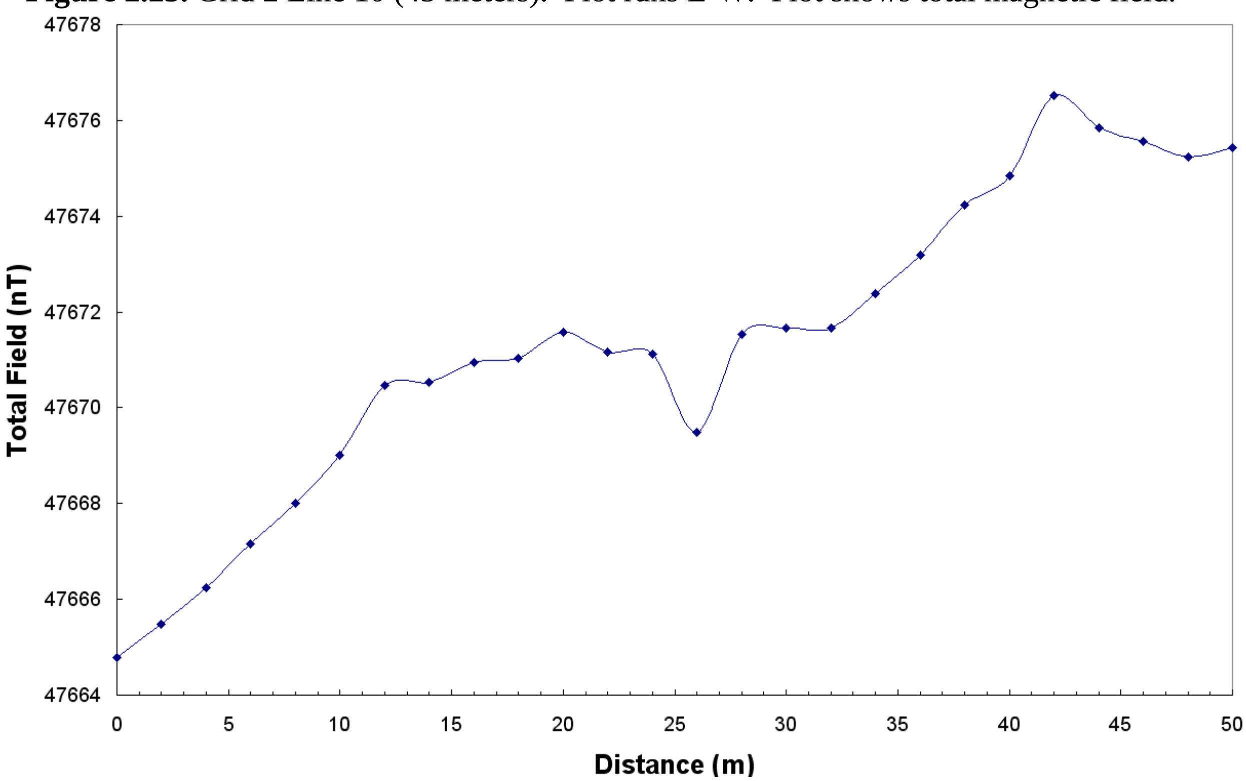

Figure 2.24. Grid 2 Line 11 (50 meters). Plot runs E-W. Plot shows total magnetic field.

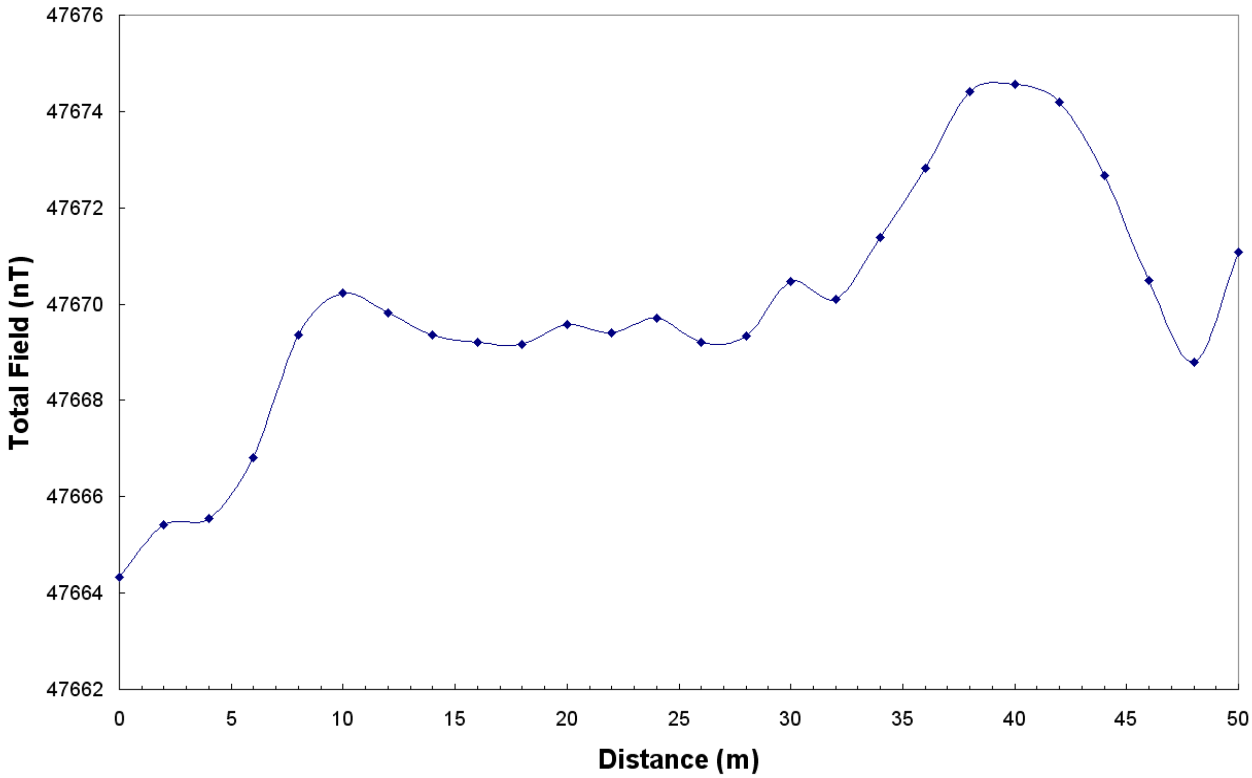

Figure 2.25. Grid 2 Line 12 (55 meters). Plot runs E-W. Plot shows total magnetic field.

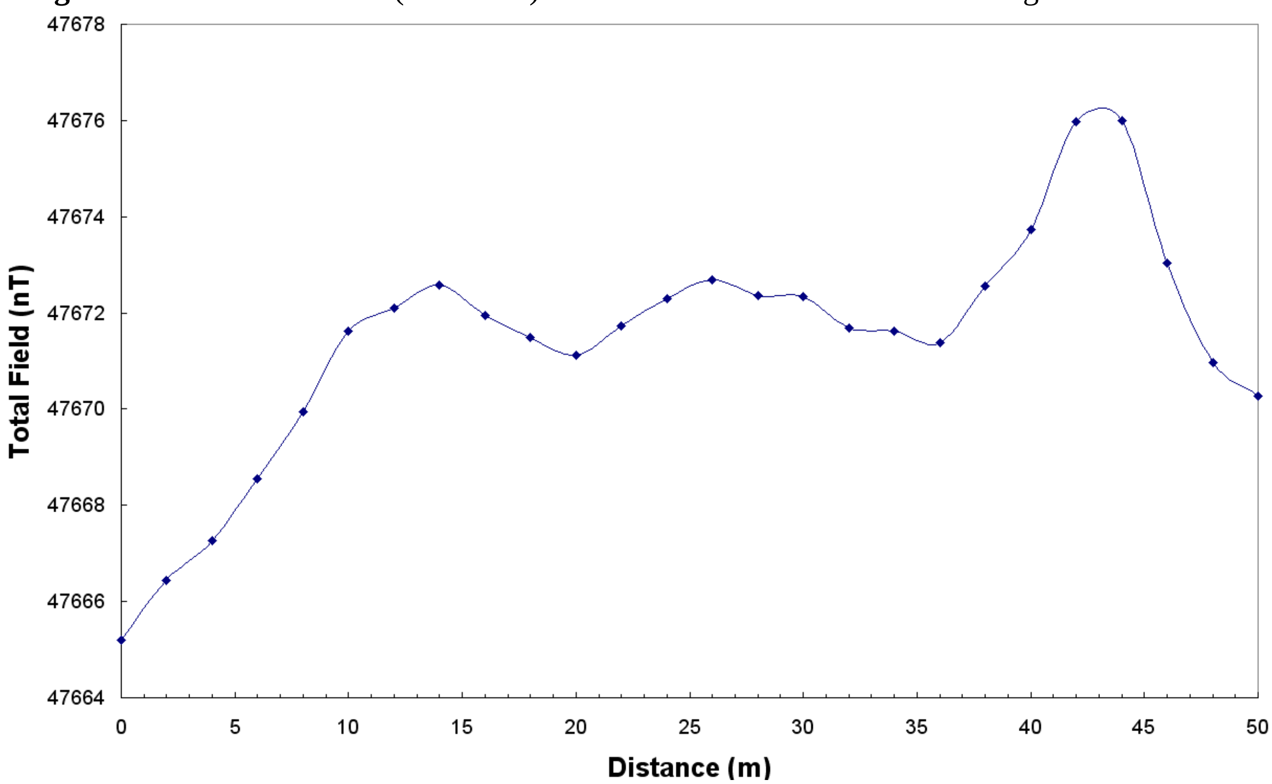

Figure 2.26. Grid 2 Line 13 (60 meters). Plot runs E-W. Plot shows total magnetic field.

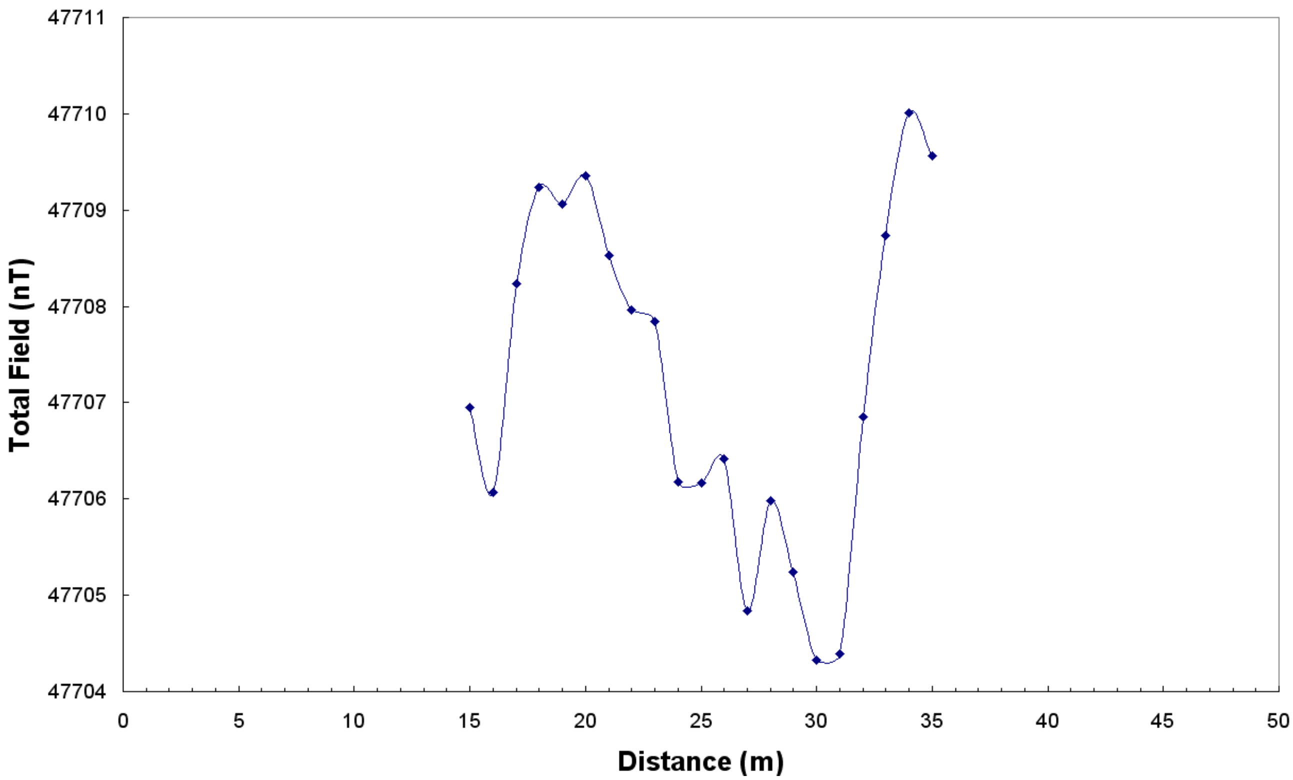

Figure 2.27. Desiccation Line 1 (0 meters). Plot runs N-S. Plot shows total magnetic field.

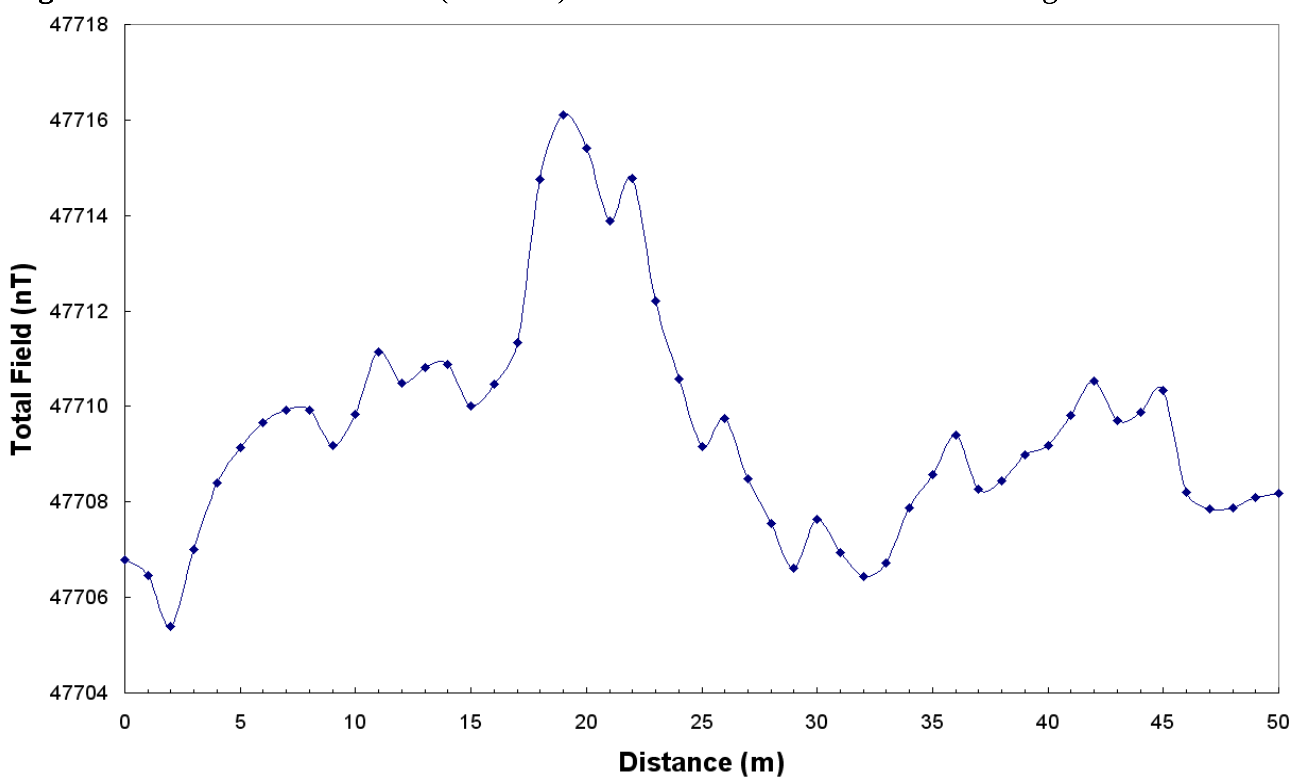

Figure 2.28. Desiccation Line 2 (10 meters). Plot runs N-S. Plot shows total magnetic field.

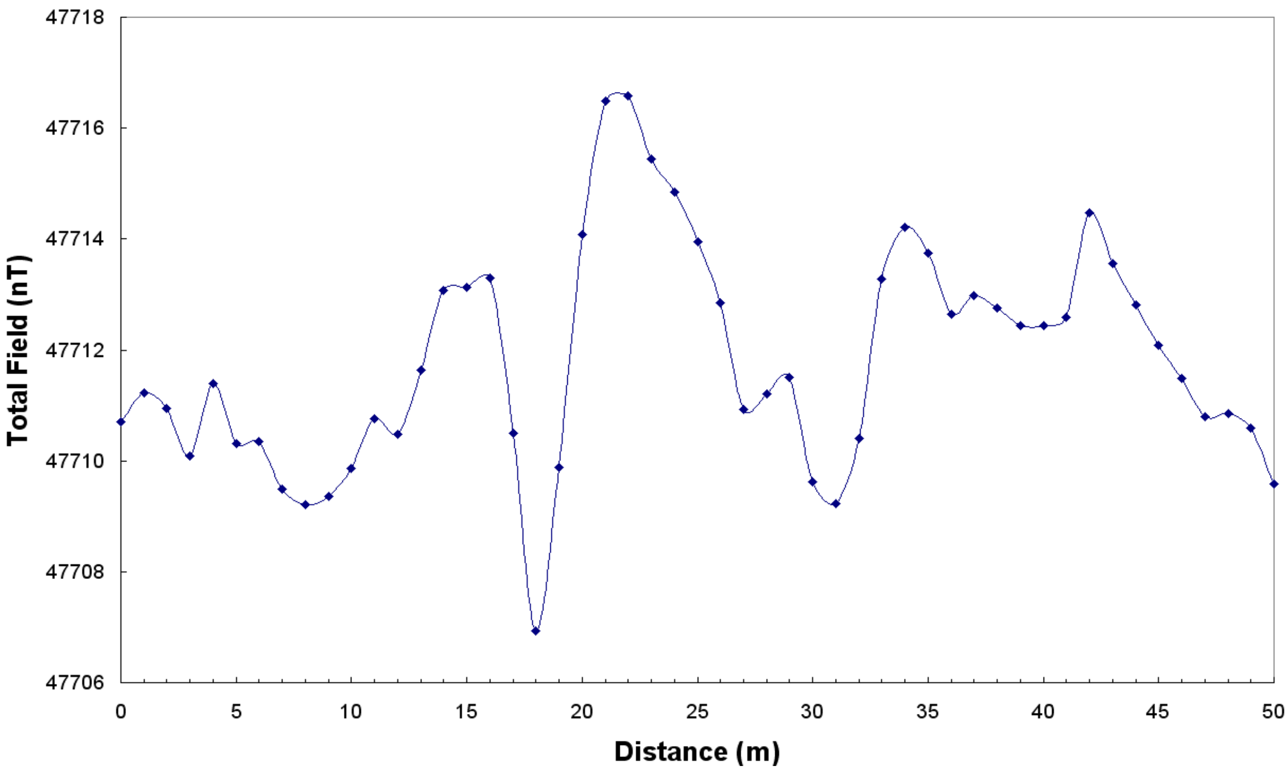

Figure 2.29. Desiccation Line 3 (20 meters). Plot runs N-S. Plot shows total magnetic field.

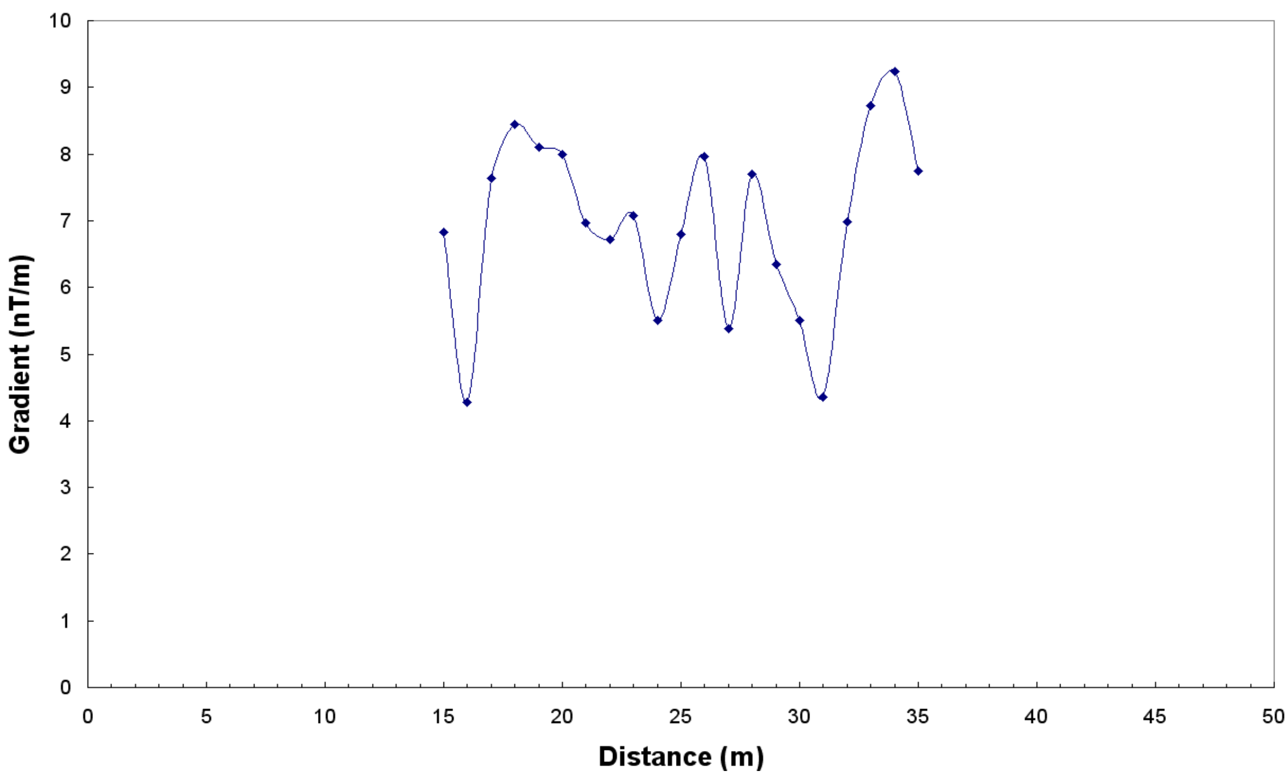

Figure 2.30. Desiccation line 1 (0 meters). Plot runs N-S. Plot shows gradient magnetic field.

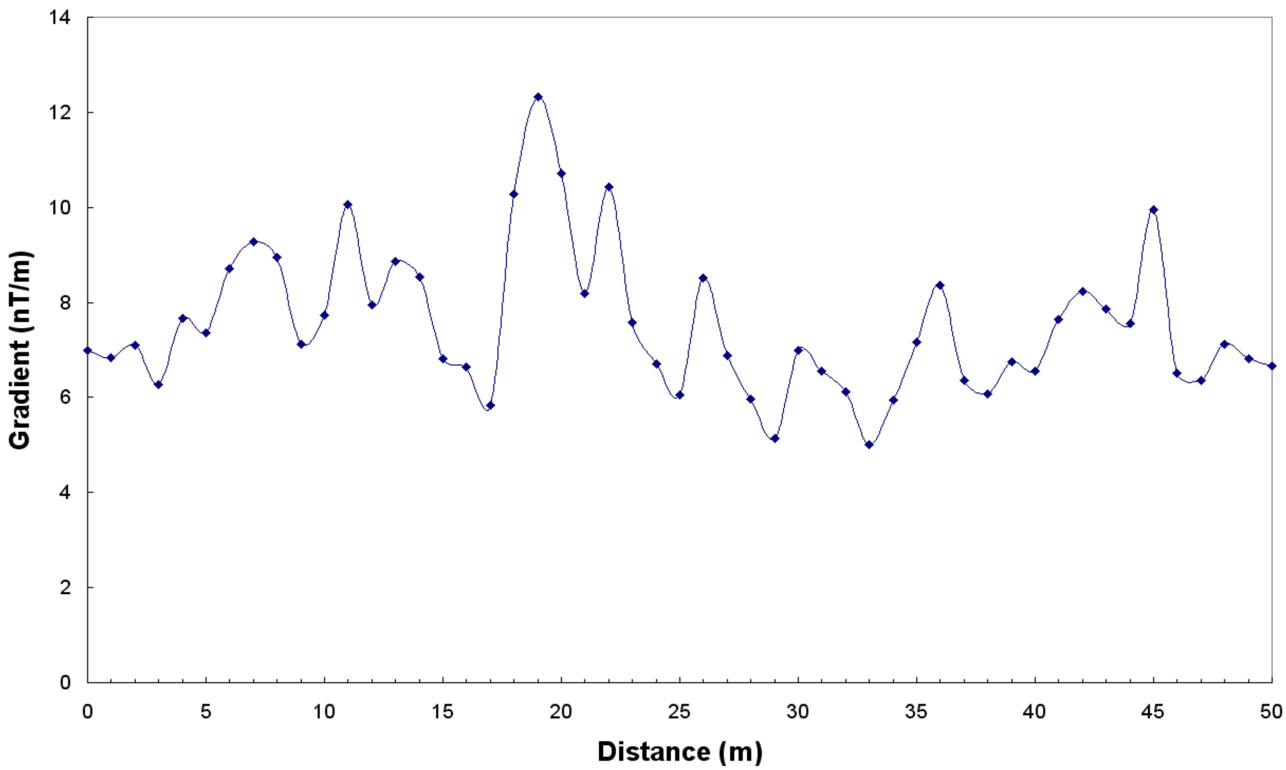

Figure 2.31. Desiccation line 2 (10 meters). Plot runs N-S. Plot shows gradient magnetic field.

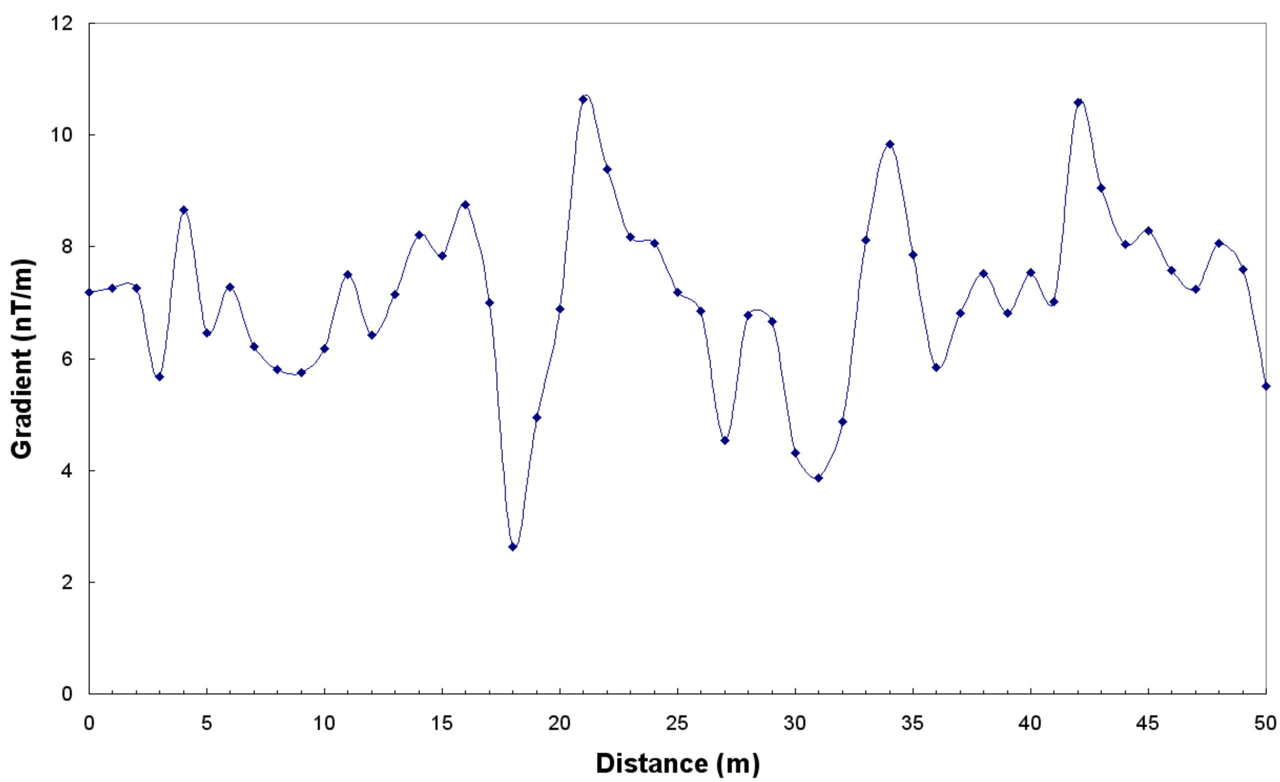

Figure 2.32. Desiccation line 3 (20 meters). Plot runs N-S. Plot shows gradient magnetic field.

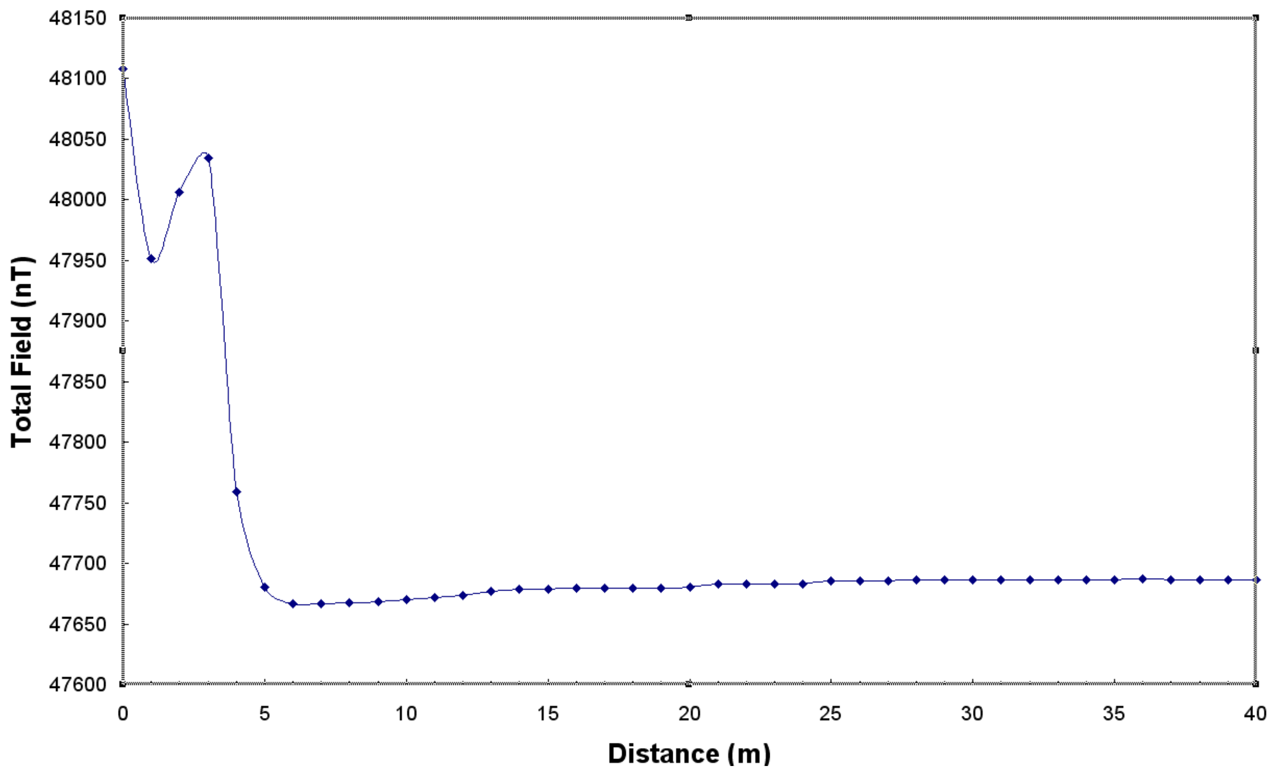

Figure 2.33. Cultural interference test line. Plot runs N-S. Plot shows total magnetic field.

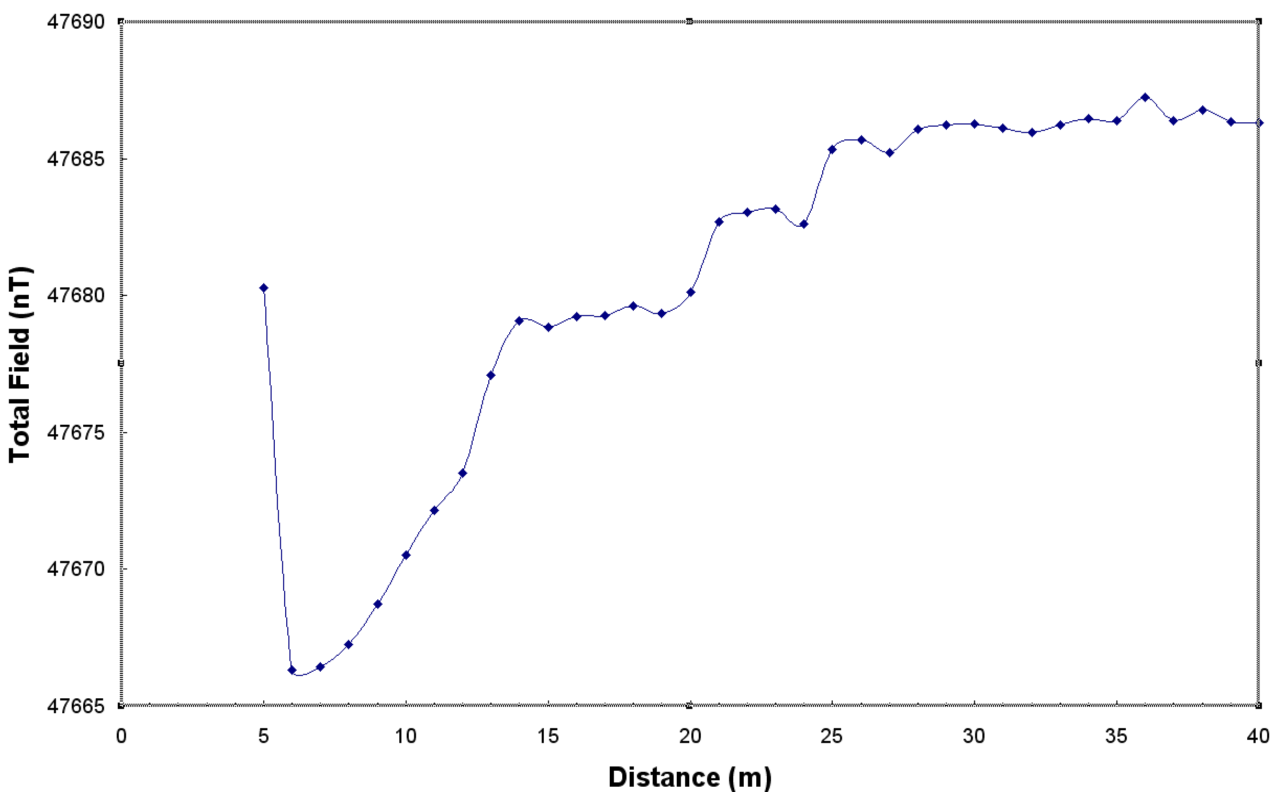

Figure 2.34. Cultural interference test line. Plot runs N-S. Plot shows total magnetic field. Notice the y-axis scale bar as compared to figure 2.33. This is the same plot as figure 2.33.

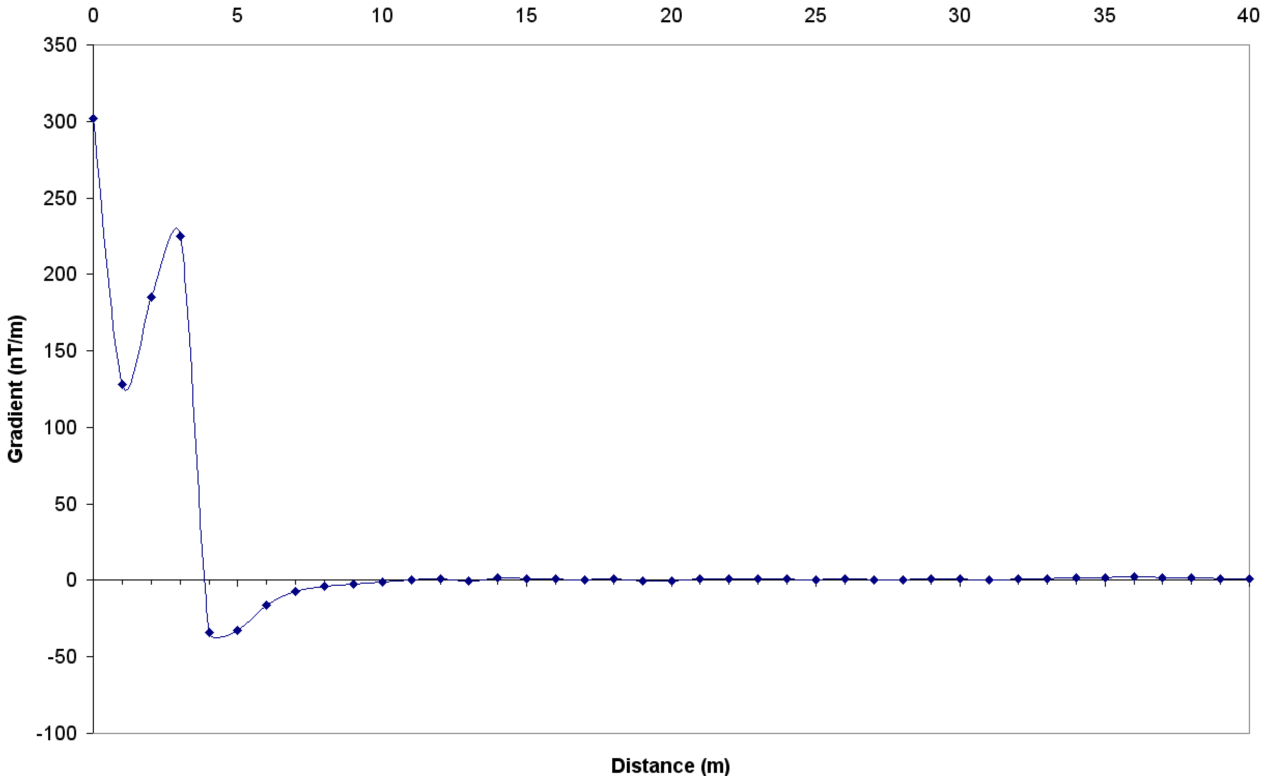

Figure 2.35. Cultural interference test line. Plot runs N-S. Plot shows gradient magnetic field.

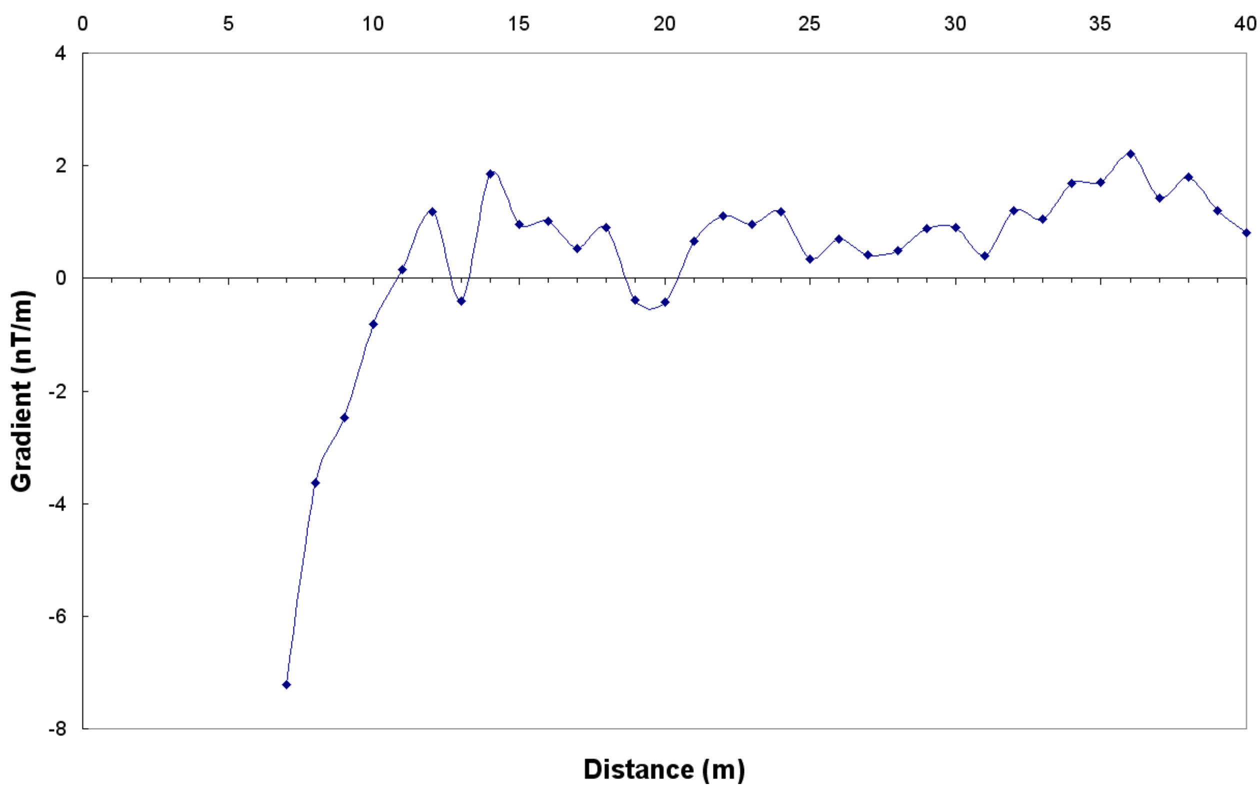

Figure 2.36. Cultural interference test line. Plot runs N-S. Plot shows gradient magnetic field. Notice the y-axis scale bar as compared to figure 2.35. This is the same plot as figure 2.35.

2.8 Contour plots

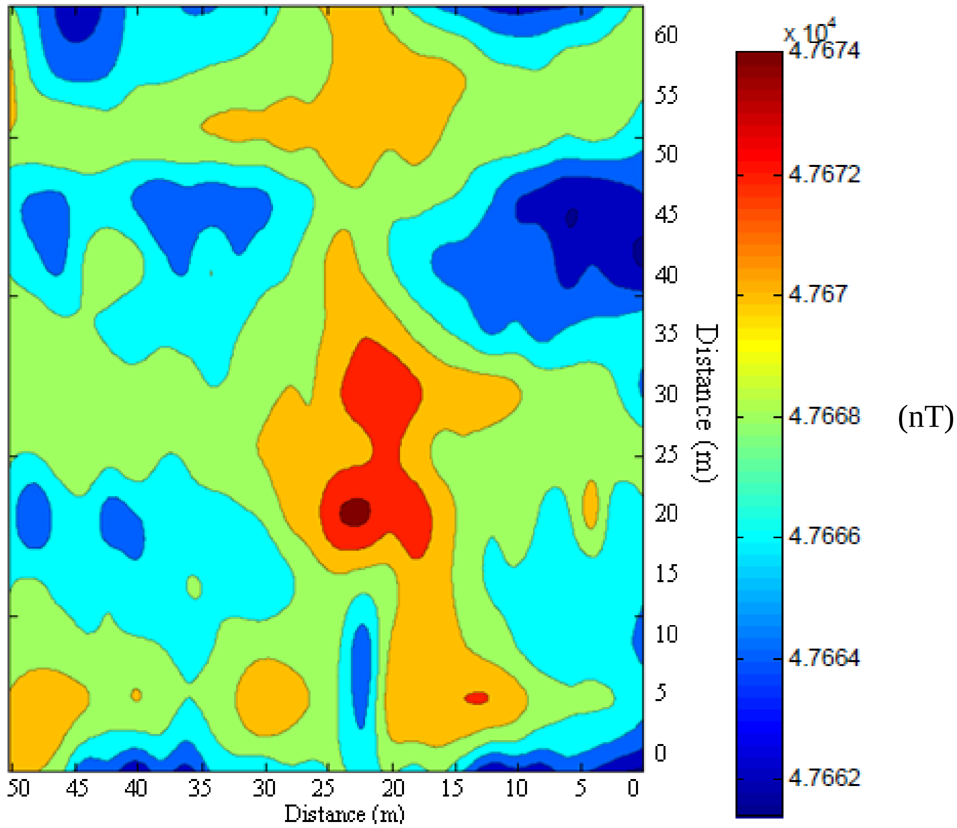

Figure 2.37. Grid 1 total magnetic field contour plot. North is up and east is to the right.

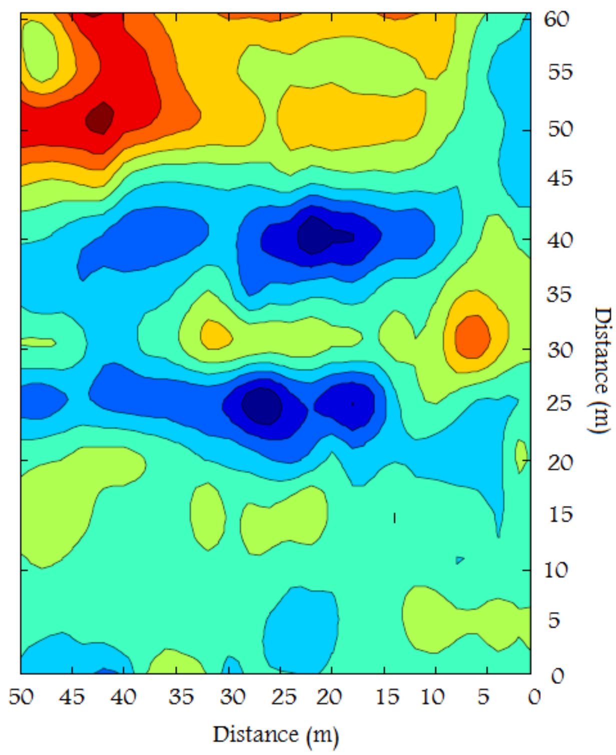

Figure 2.38. Grid 2 total magnetic field contour plot. North is up and east is to the right.

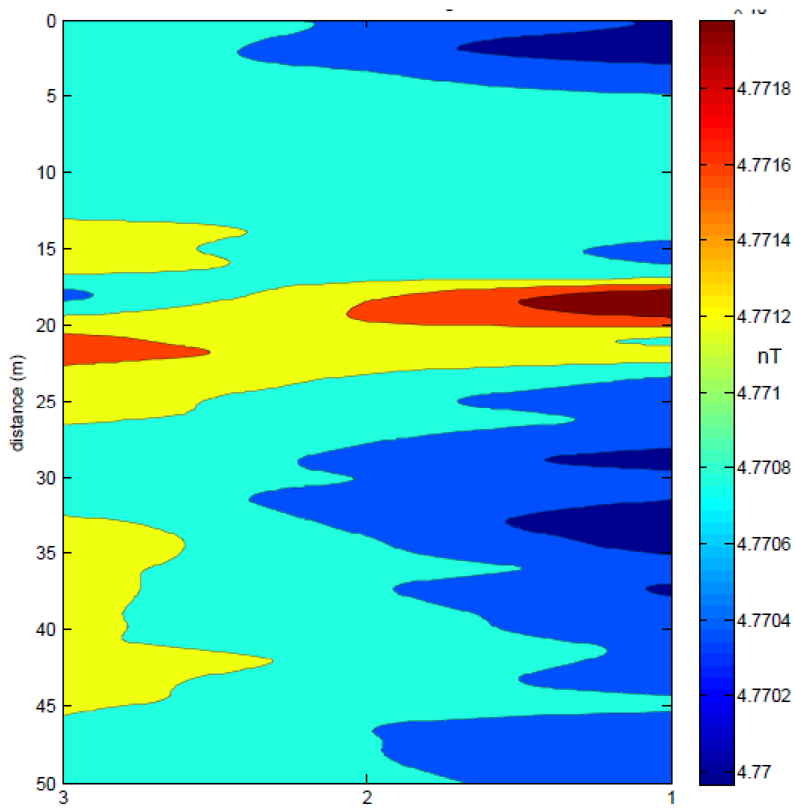

Figure 2.39. Desiccation Crack Contour of Total Magnetic Field. North is up.

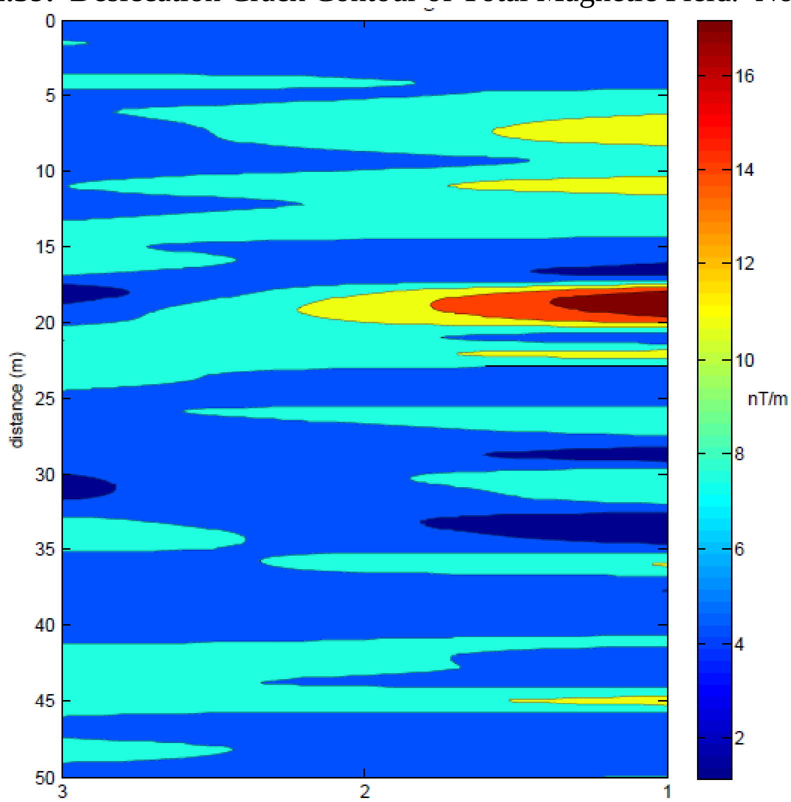

Figure 2.40. Desiccation Crack Contour of Gradient Magnetic field. North is up.

3.0 EM31

3.1 Introduction and Location

The Geonics EM31 is a useful tool for mapping "geologic variations, groundwater contaminants, or any shallow subsurface feature associated with changes in ground conductivity". In this study, we are using the EM31 to help locate possible earth fissures including those that may be forming beneath the surface. Our area of study is in southeastern Arizona near the town of Willcox. There are two areas in which we conducted our measurements. Two are in a pasture west of the AEPCO power plant where we set up two 50 by 60 meter grids with 5 meter interval spacing, each with 13 lines. Our measurements were taken in the East-West direction. All measurements were taken using the OPP function on the instrument. Notes were taken with respect to where open fissures were observed along the surveys so that they may be correlated with the data later on.

3.2 Overview and Technique

3.2.1 Grid 1

Surveys taken along the first grid in the pasture behind the AEPCO power plant on the southern side of the fence were conducted along lines #1, 3, 5, 7, 9, 11, and 13 at ten meter intervals. At each interval, measurements were made with the instrument running parallel and perpendicular to the survey line collecting the horizontal and vertical coplanar value from each interval. Around the 25-meter mark, there was an open fissure that was observed along our grid.

3.2.2 Grid 2

Grid 2 was located North of grid 1 and was set up with the same dimensions as Grid 1, but slightly angled. The grid had 13 lines which ran almost East-West that were each 50 meters long. Our grid, therefore, had the dimensions of a 50 by 60 meter rectangle. In this grid, there was a visible fissure that ran approximately from lines 1-3. The fissure was generally around the 25 meter mark on the lines. There was also a water line running through the grid along line 5, trending almost East-West. Data were collected with the EM31 at 5-meter intervals along each line and holding the instrument on the ground. We oriented the instrument both parallel and perpendicular to the lines, which are referred to as "parallel" and "perpendicular" in the data sets. We also took coplanar measurements oriented horizontally and vertically relative to the earth's surface. In total, this left us with four different measurements for each point. The data are shown in Figures 3.1 through 3.25**.** Contour plots for these measurements are displayed in Figures 3.26-3.28.

3.2.3 Desiccation Cracks

Measurements taken along the desiccation cracks were taken the same way as in Grids 1 and 2. The desiccation crack grid size was 20 meters by 50 meters. The lines are set 10 meters apart with line 1 only extending 20 meters, but centered along the grid. Running through the middle of the grid across the lines is a dirt road. The desiccation crack ran along the side of the road at about the 25-or 30-meter mark on the lines. Again, the EM31 was used at ground level both parallel and perpendicular to the lines. The measurements were again taken with the coplanar horizontal and vertical. The contours of the data are displayed in Figure 3.4 and the actual data are provided in Figures 3.21 through 3.23.

3.3 Data Processing

As mentioned above, measurements were taken along ten meter intervals in the first grid and five meter intervals in the second grid. We recorded values obtained from the vertical and horizontal coplanar orientations running both parallel and perpendicular to the survey lines. Once our data were recorded, we input the values into Microsoft Excel and we created charts showing the conductivity of the ground with respect to its location along the survey line. From these charts, we were then able to observe high and low peaks that were thought to be related to possible locations of fissures. To visualize the data in improved two dimensions, the grids were contoured. These contour plots are displayed in Figures 3.26-3.28.

3.4 Interpretation

3.4.1 Grid 1

In most of the charts for Grid 1, there appear to be peaks occurring around 20 to 25 meters. These peaks have been fairly consistent with peaks found with the other geophysical instruments used in this study. Figures for lines 1 through 11 all seem to display peaks in roughly the location where we noted the trend of the fissure at some locations on the surface. The fissure was mainly spotted along the 25 meter mark with a couple being noted along the 20 meter mark. Figure 3.11 displays the data for line 11. At this line, we took our measurements directly over the open fissure, whereas, most of the other measurements were taken near an open fissure. In Figure 3.13, the data for line 13 are displayed. In this figure, you can see that there is a relatively high value being shown around the 20 meter distance. It is important to note that the fissure was not visible near this line. Therefore, this high peak around 20 meters is indicative of ground disturbance beneath the surface.

The EM31 data are displayed as a contour plot in Figure 3.26 with the horizontal and vertical coplanar orientations, and the parallel and perpendicular orientations of the instrument displayed. In plots A and C there is a higher magnitude in the data than in plots B and D. This is related to the depth of penetration for the EM31 instrument. In plots B and D there is a high around distance 25 while in plots A and C there is a dispersive high above 30 and below 20. The open fissure corresponds to where we see the highs in plots A and C. The plots B and D could also be observing the fissure at a shallower depth or smoothing the effect between the offset near line position at 40 meters. The fissure is open along some of the lines in this grid.

3.4.2 Grid 2

Looking at Figure 3.27, the different orientations of the instrument are displayed for grid 2. In plot A, C, and D we see that there is a large high from lines 1 to almost 4 at the 25-meter distance. This is near where there is an open fissure. On all of the plots, there is a low, trending from line 5, distance 50 meters, to line 10, 0 meters. This is consistent through all of the plots and corresponds to an area North of the water line. It is hard to determine if the water line is causing this low or whether it is just a characteristic of the earth itself. It can also be seen that when the instrument is oriented vertical coplanar, plots B and D, the magnitude of the plots are much lower then if it is oriented with a horizontal coplanar. When the orientation is horizontal, the instrument is theoretically penetrating deeper, therefore, this change in magnitude is telling us about the change in properties at depth.

3.4.3 Desiccation Crack

The data in Figure 3.28 are for the desiccation crack. When the instrument is oriented vertically, and therefore has a shallower depth of penetration, a lower magnitude is observed. Through all four contour plots, a high occurs around 30 meters on all lines, and also another high around 15 and 5 near line 1 can be seen. In plots B and D, the highs are not as clear, and in plot D the high appears to be trending down the middle of the lines at distance 25 m. This high along the middle of the plots could be representing the desiccation crack. However, it is also possible that it is picking up a signal from the road as the highs are fairly centered along the plots where the road is located. The only plot that really picks up a signal where the desiccation crack is located is plot A, which is displaying measurements that were made parallel to the lines with a horizontal orientation.

3.5 Cultural Interference Test

In between grids one and two, there was a barbed wire fence as well as a power line. To see if these large quantities of metal had any effect on our data, we ran tests perpendicular to the power line and began at the fence.

3.6 Summary

The charts displaying peaks for fissures that were observed on the surface seem to be consistent with the charts that display peaks for areas where a fissure was not seen. Therefore, it may be interpreted that those peaks where a fissure was not seen on the surface may possibly be a location of other fissure locations where the ground has been altered.

3.7 EM31 Graph Plots

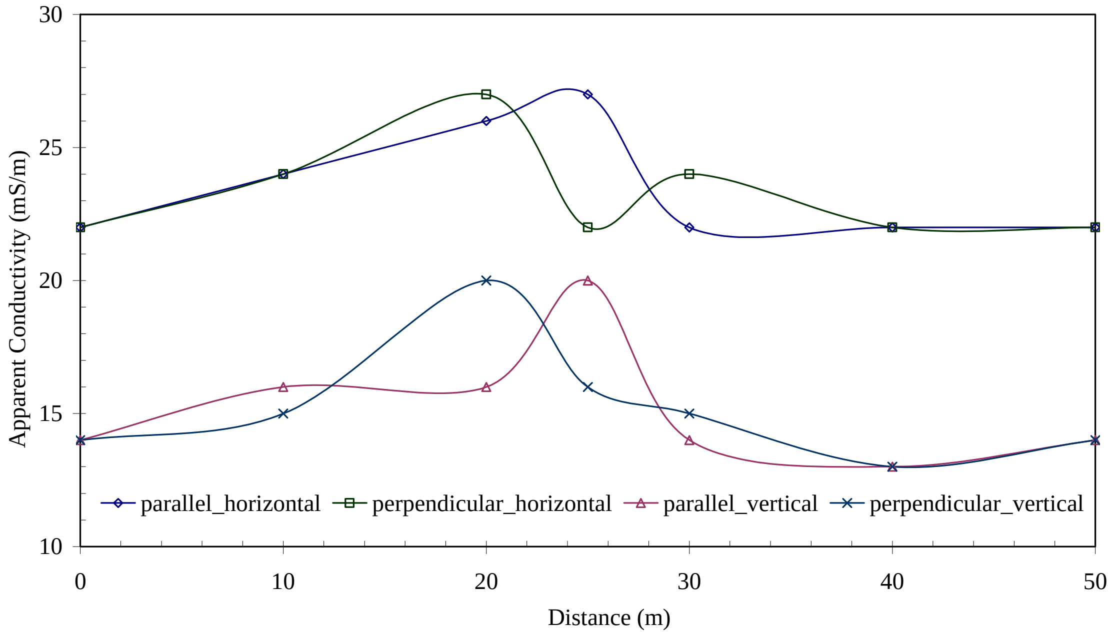

Figure 3.1: EM31 chart showing conductivity peaks for Grid 1, Line 1.

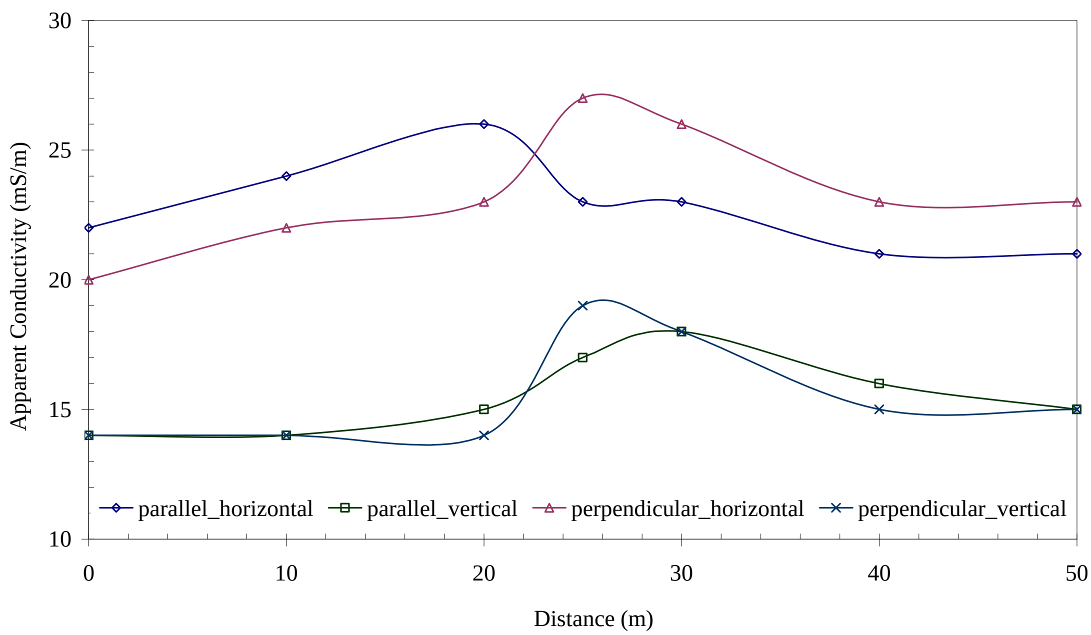

Figure 3.2: EM31 chart showing conductivity peaks for Grid 1, Line 3.

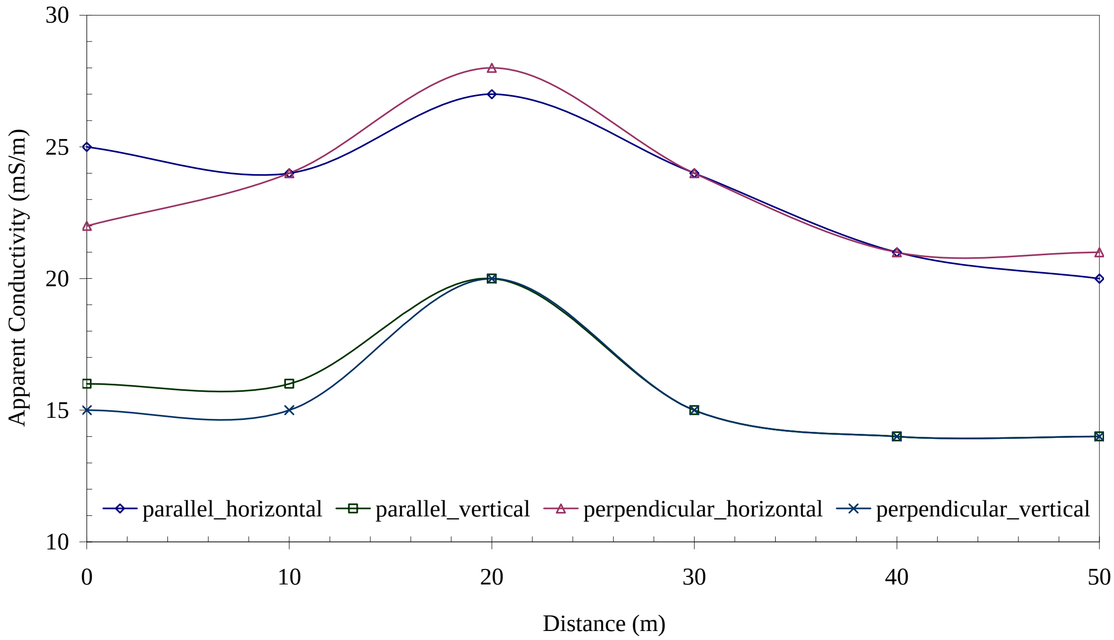

Figure 3.3: EM31 chart showing conductivity peaks for Grid 1, Line 5.

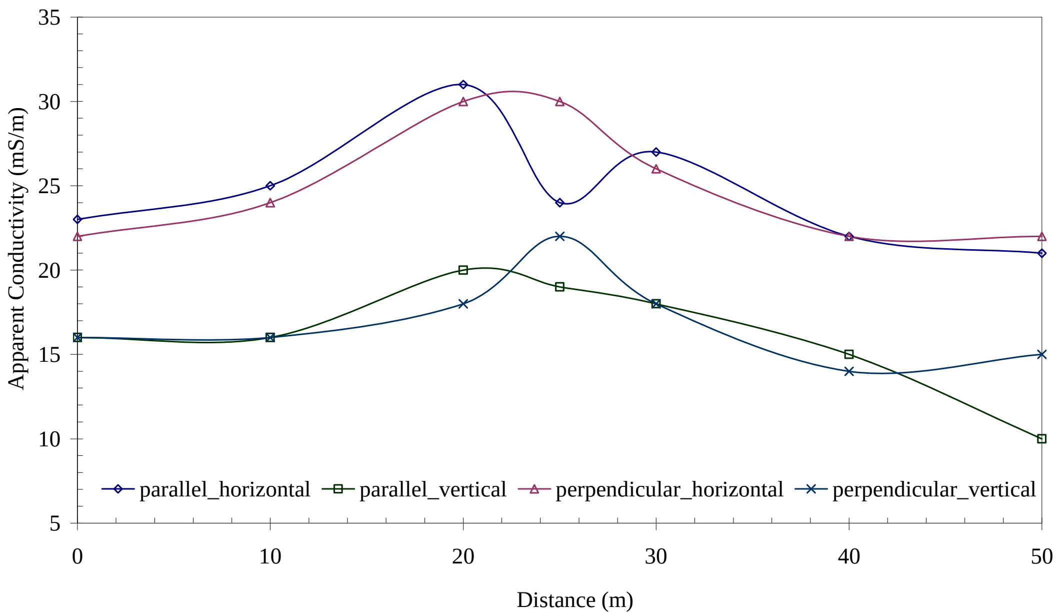

Figure 3.4: EM31 chart showing conductivity peaks for Grid 1, Line 7.

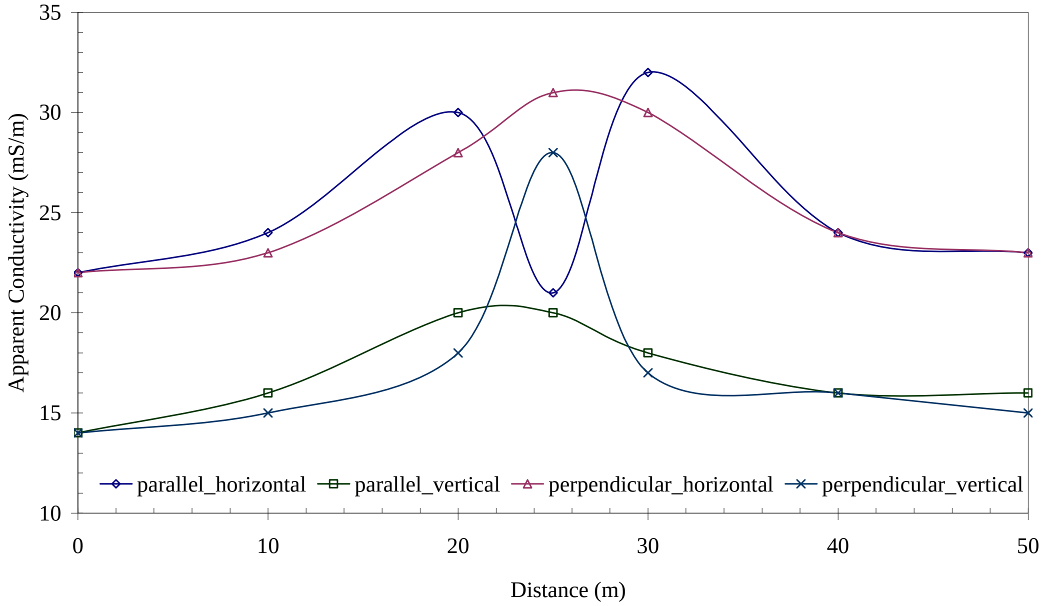

Figure 3.5: EM31 chart showing conductivity peaks for Grid 1, Line 9.

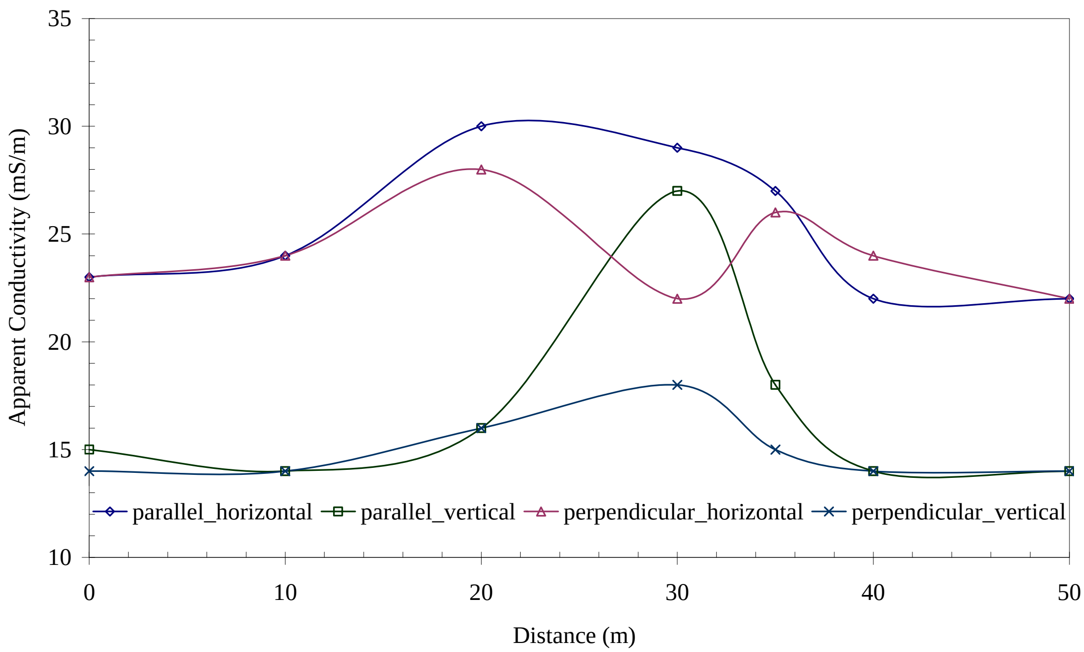

Figure 3.6: EM31 chart showing conductivity peaks for Grid 1, Line 11.

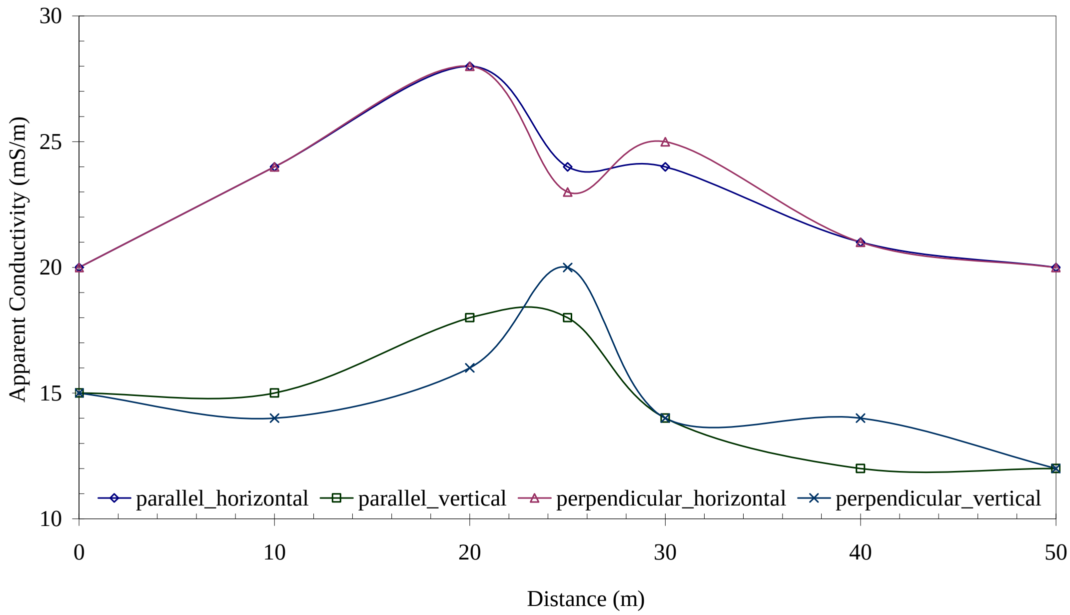

Figure 3.7: EM31 chart showing conductivity peaks for Grid 1, Line 13.

3/28/08:

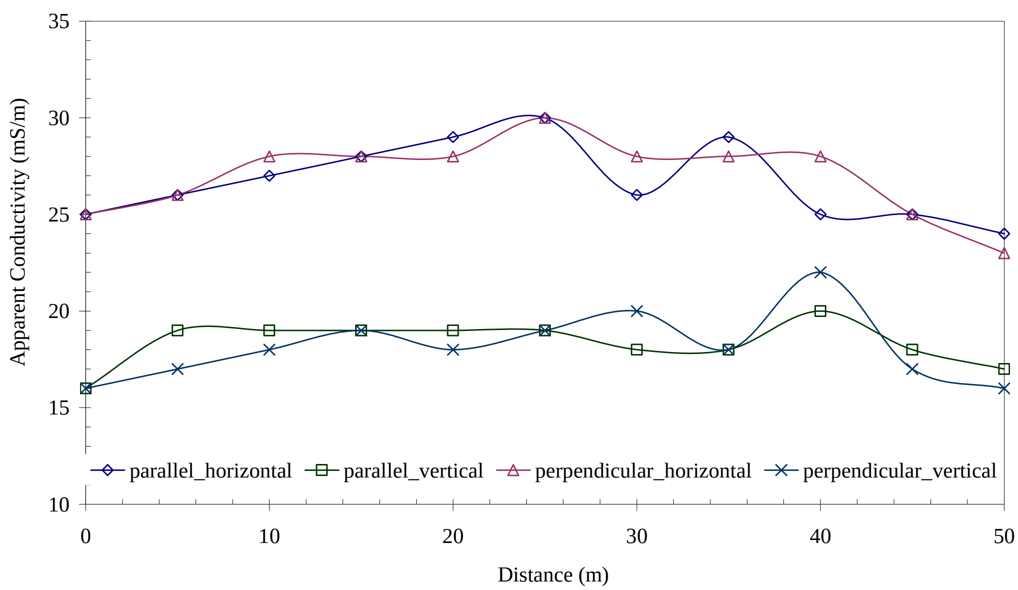

Figure 3.8: EM31 chart showing conductivity peaks for Grid 2, Line 1.

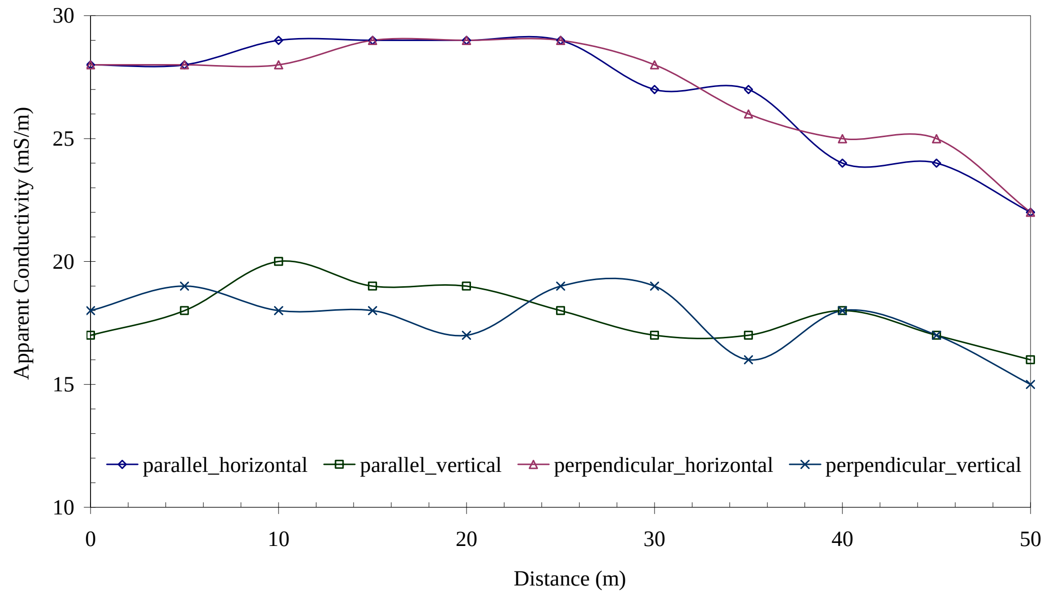

Figure 3.9: EM31 chart showing conductivity peaks for Grid 2, Line 2.

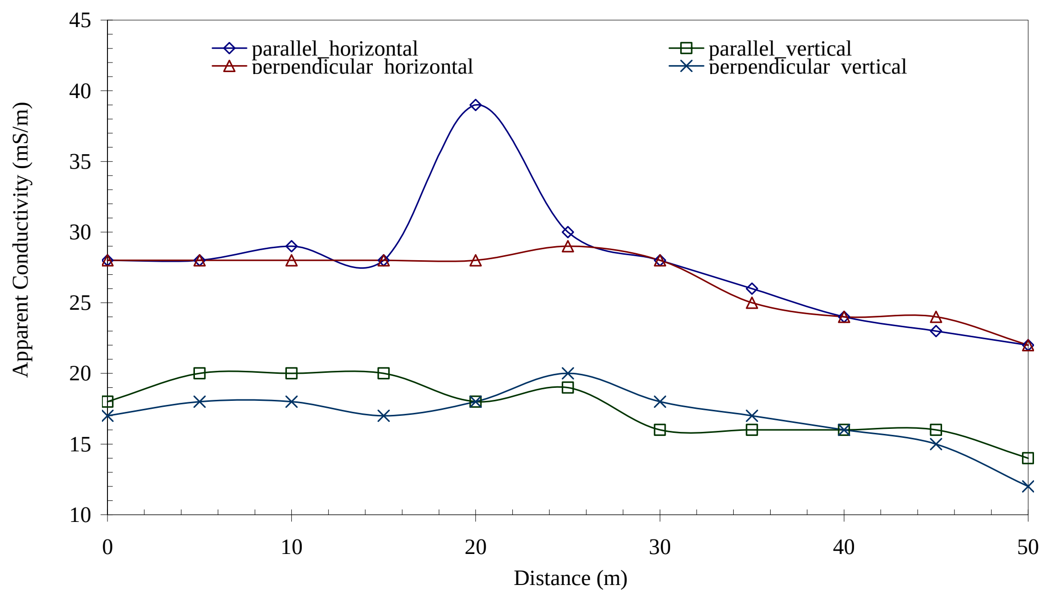

Figure 3.10: EM31 chart showing conductivity peaks for Grid 2, Line 3.

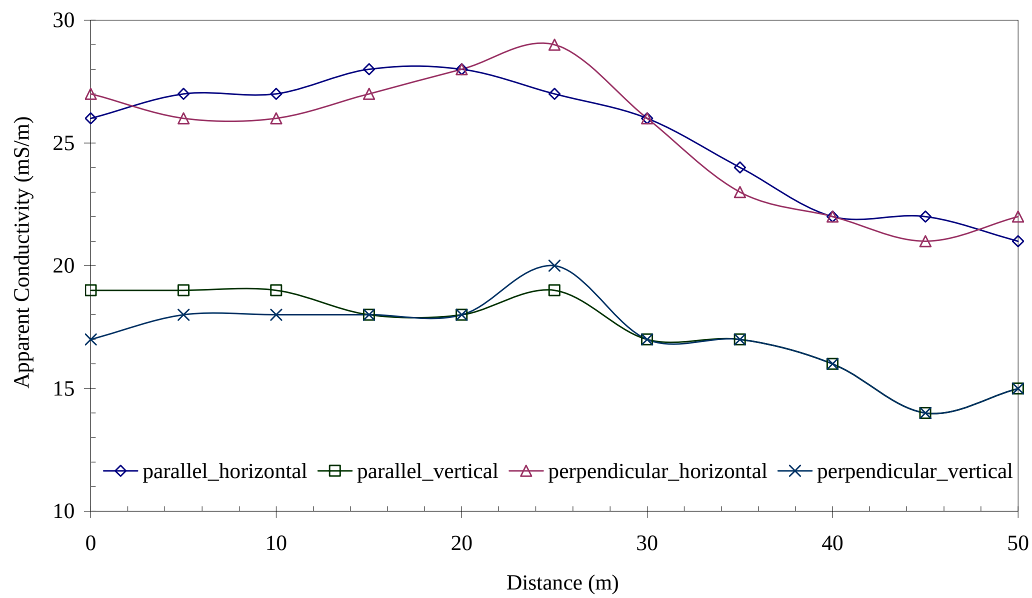

Figure 3.11: EM31 chart showing conductivity peaks for Grid 2, Line 4.

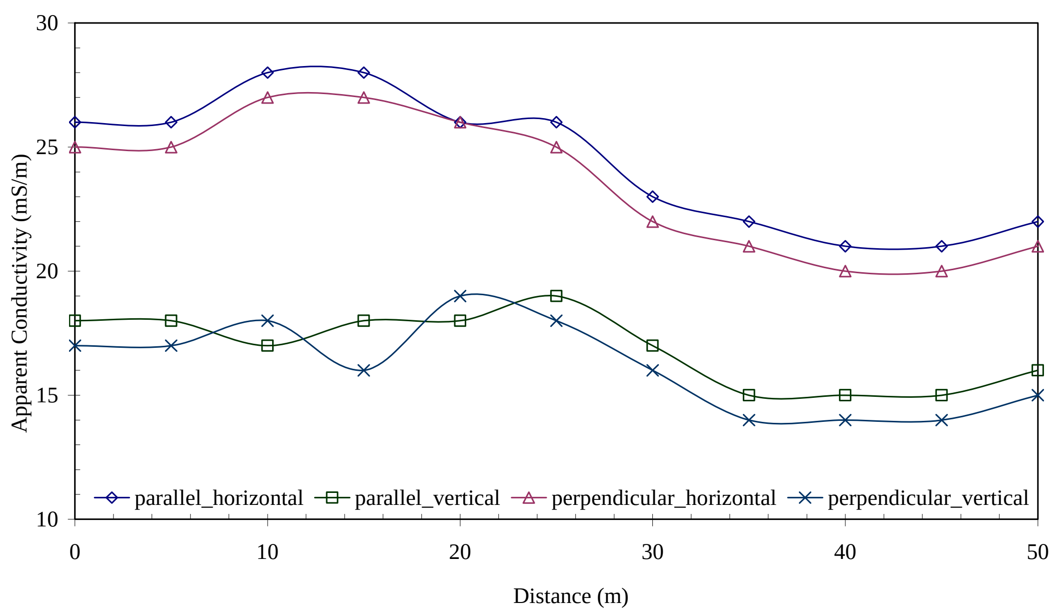

Figure 3.12: EM31 chart showing conductivity peaks for Grid 2, Line 5.

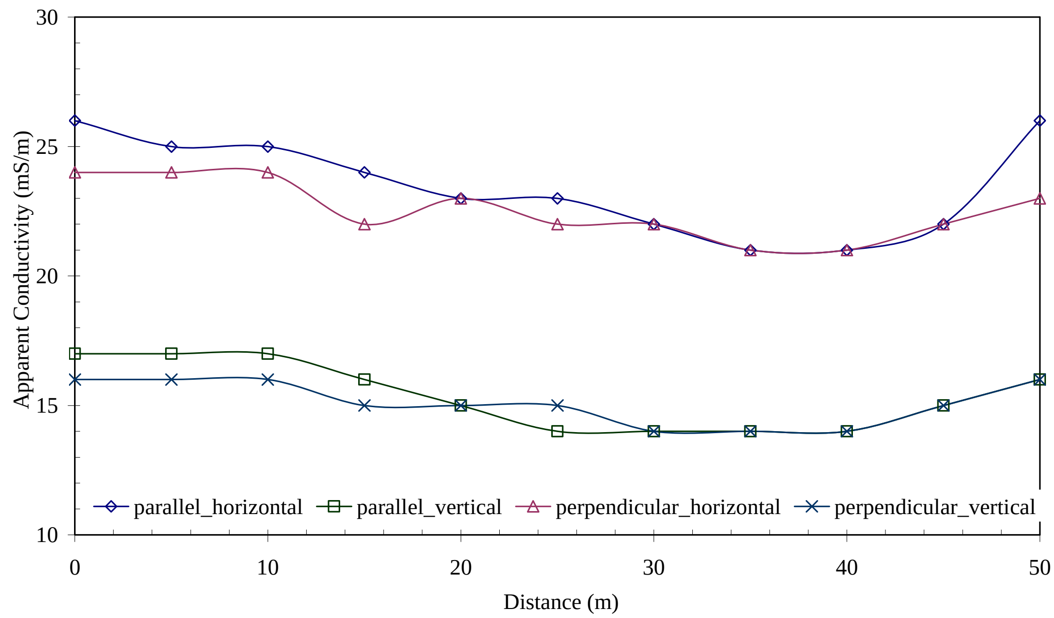

Figure 3.13: EM31 chart showing conductivity peaks for Grid 2, Line 6.

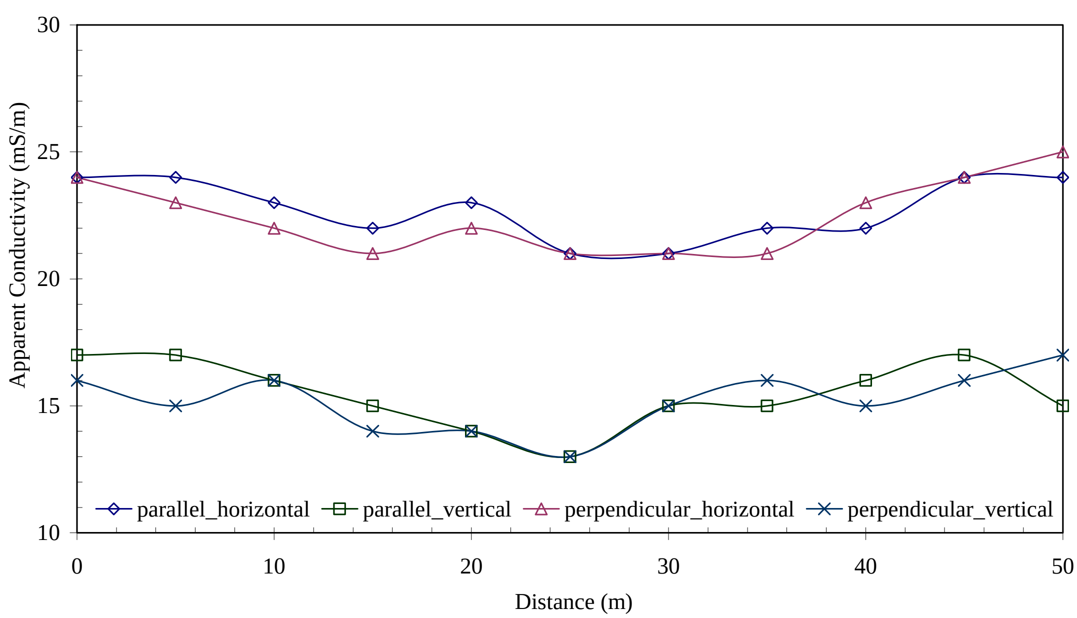

Figure 3.14: EM31 chart showing conductivity peaks for Grid 2, Line 7.

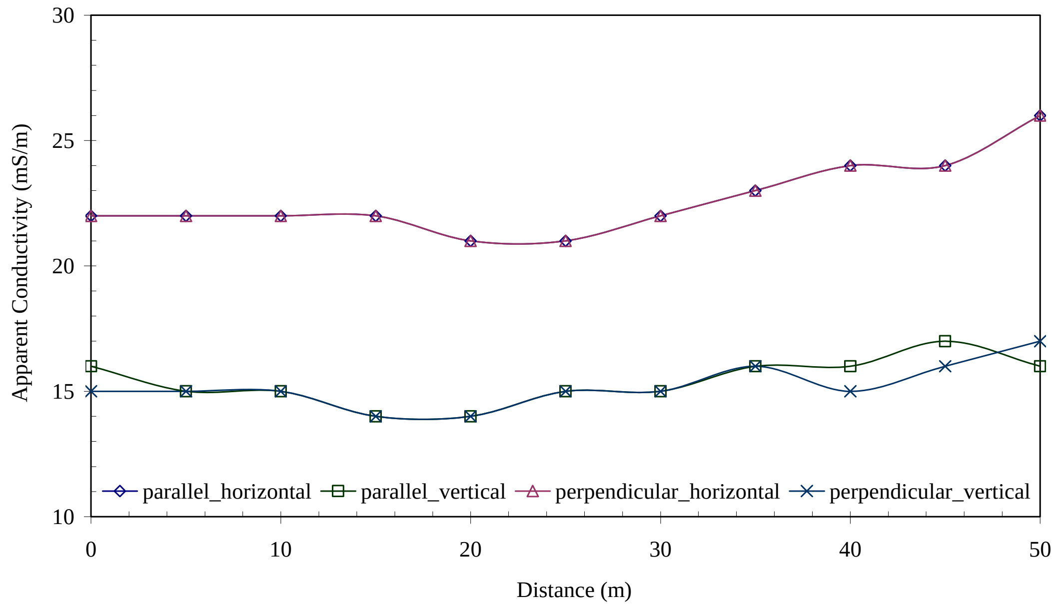

Figure 3.15: EM31 chart showing conductivity peaks for Grid 2, Line 8.

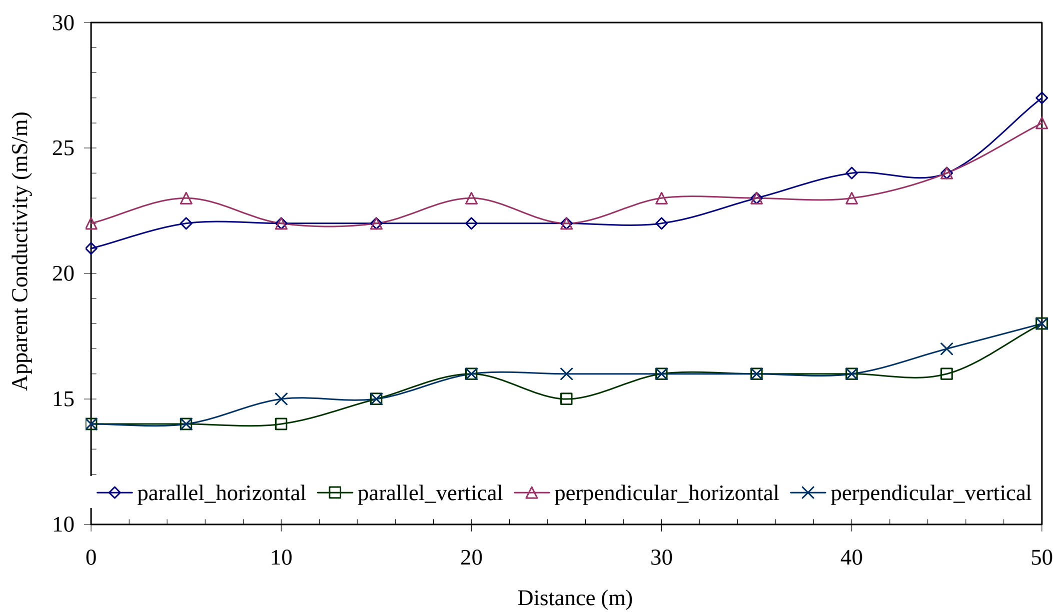

Figure 3.16: EM31 chart showing conductivity peaks for Grid 2, Line 9.

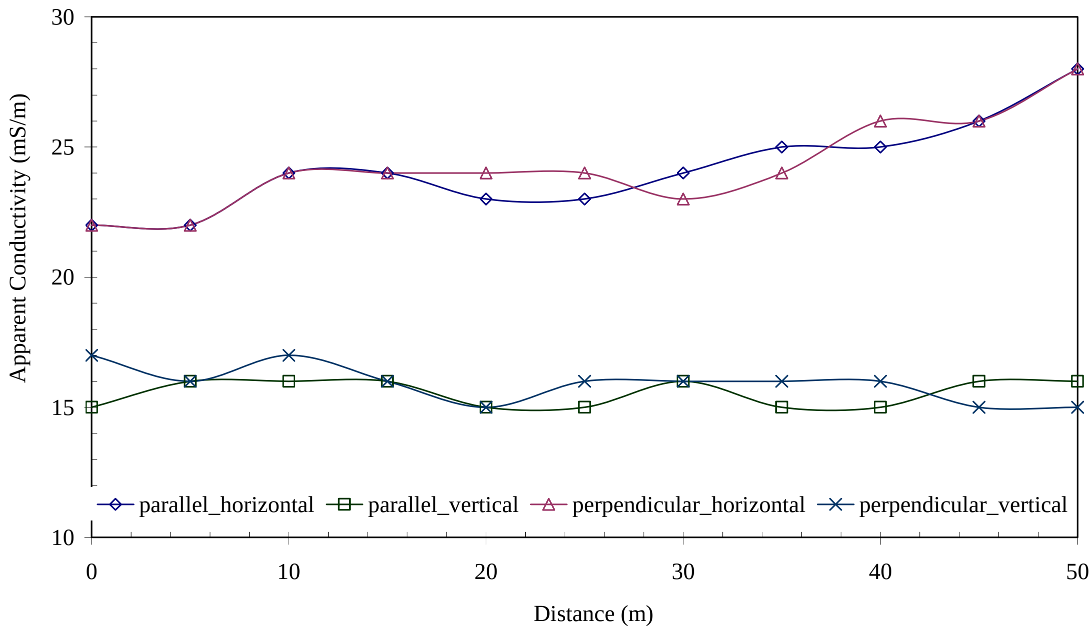

Figure 3.17: EM31 chart showing conductivity peaks for Grid 2, Line 10.

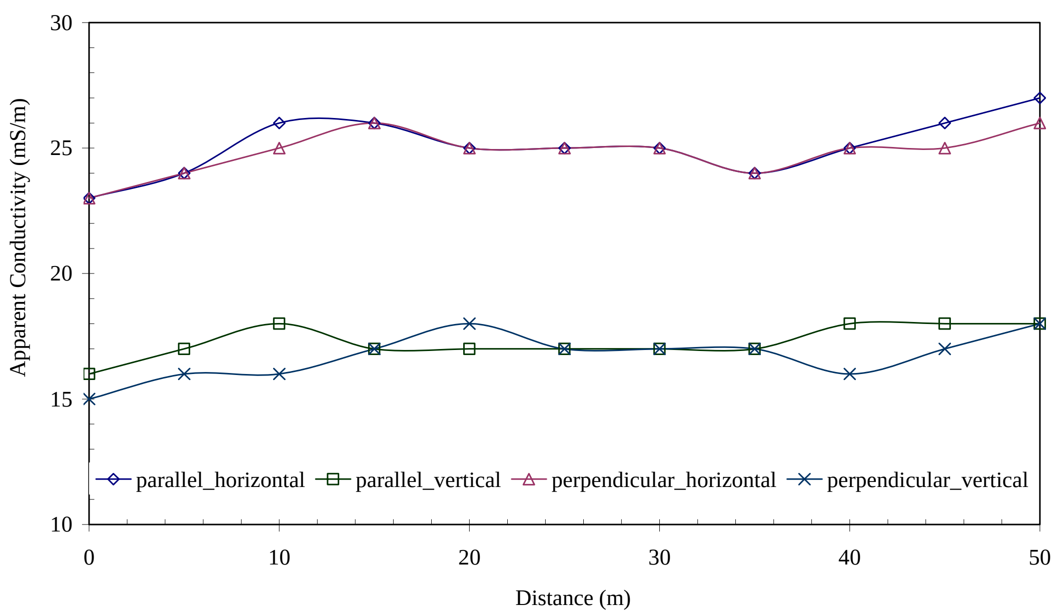

Figure 3.18: EM31 chart showing conductivity peaks for Grid 2, Line 11.

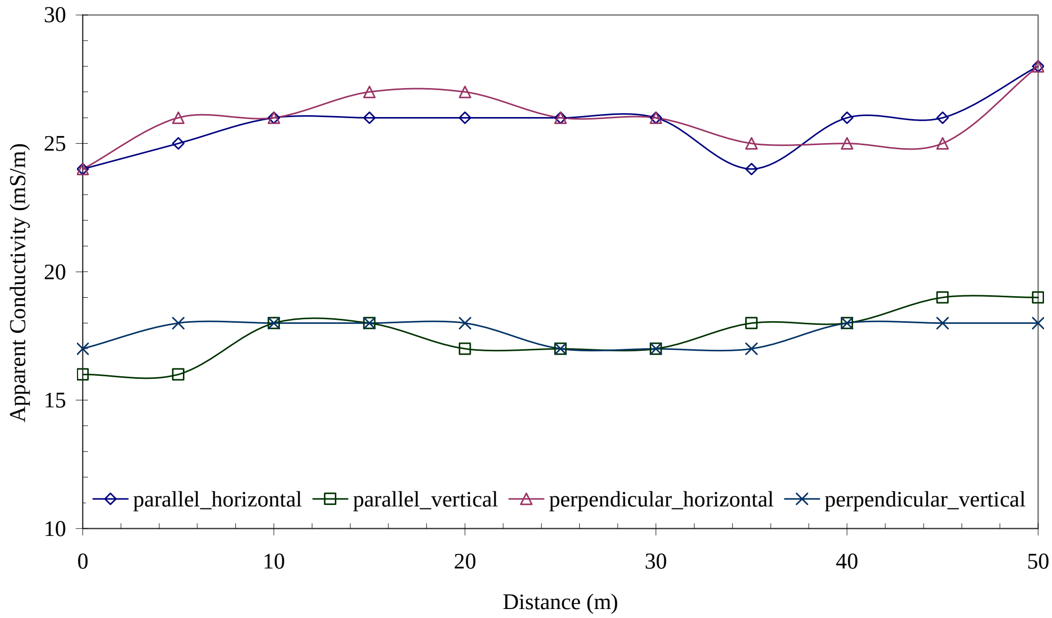

Figure 3.19: EM31 chart showing conductivity peaks for Grid 2, Line 12.

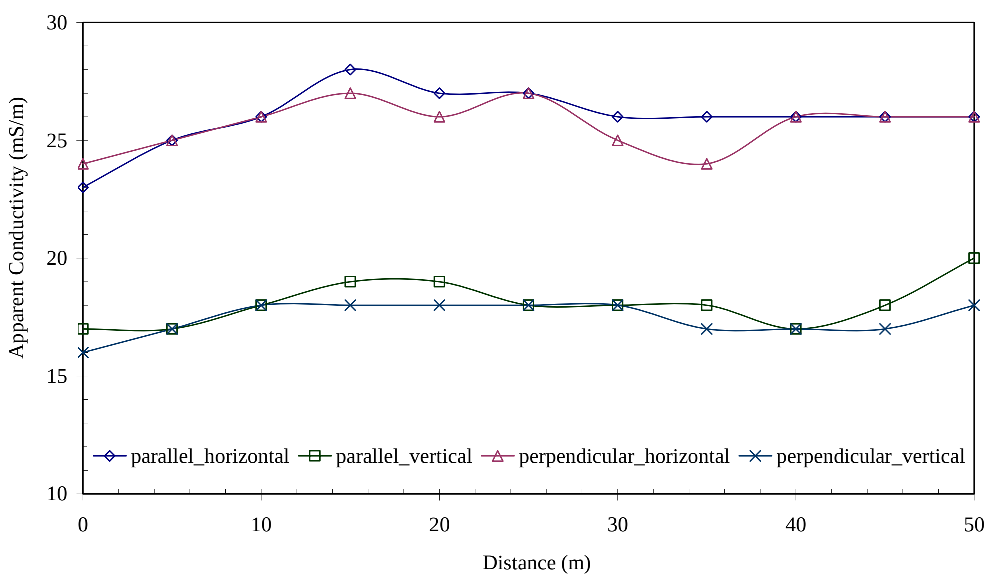

Figure 3.20: EM31 chart showing conductivity peaks for Grid 2, Line 13.

Desiccation Crack Surveys

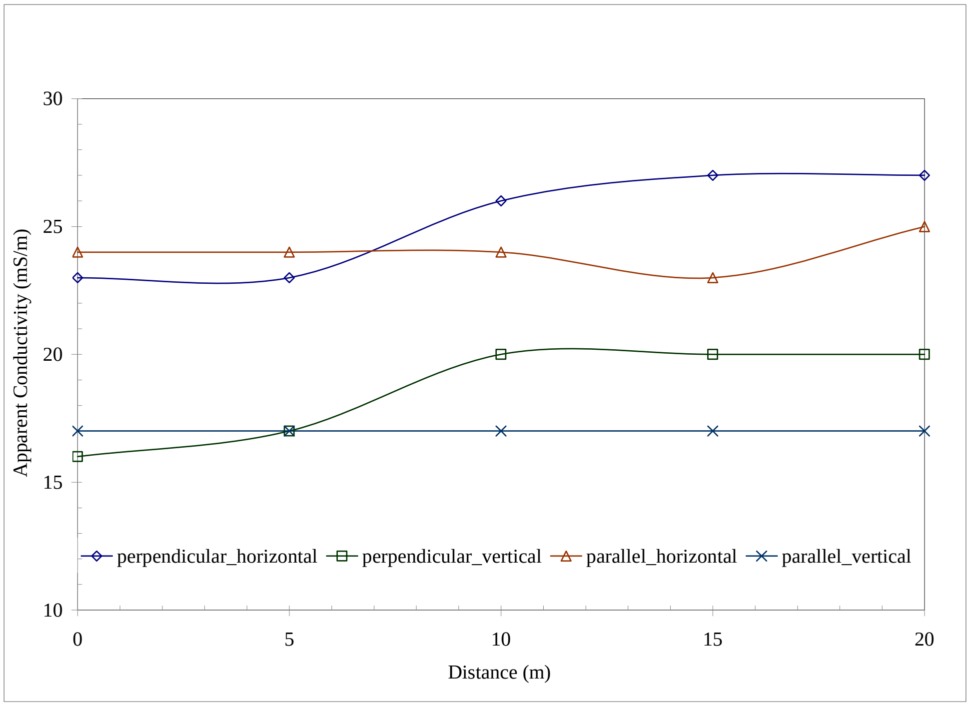

Figure 3.21: EM31 chart showing conductivity peaks for Line 1 of the desiccation crack.

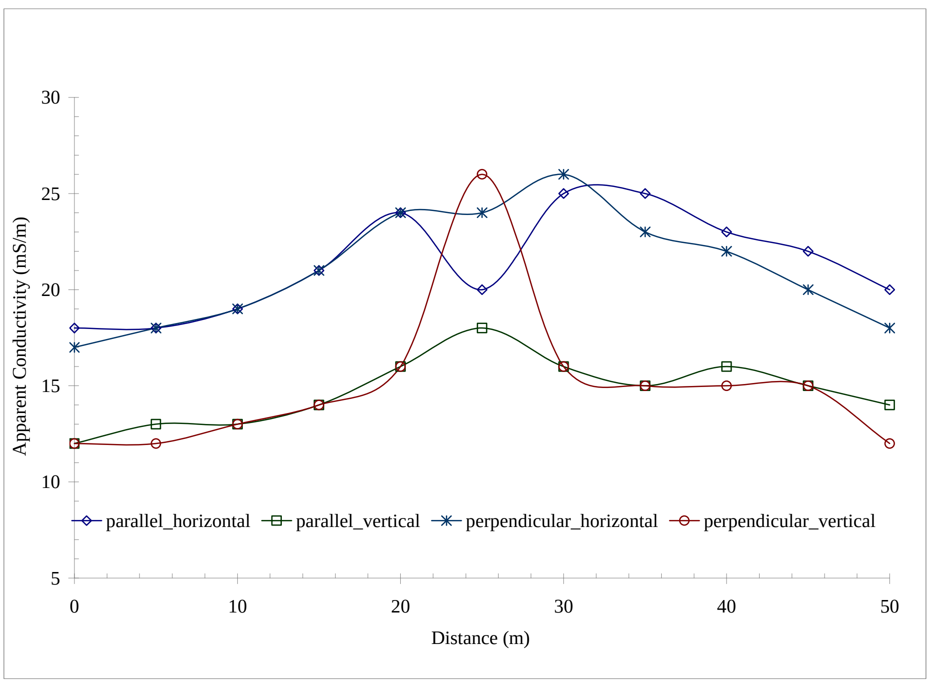

Figure 3.22: EM31 chart showing conductivity peaks for Line 2 of the desiccation crack.

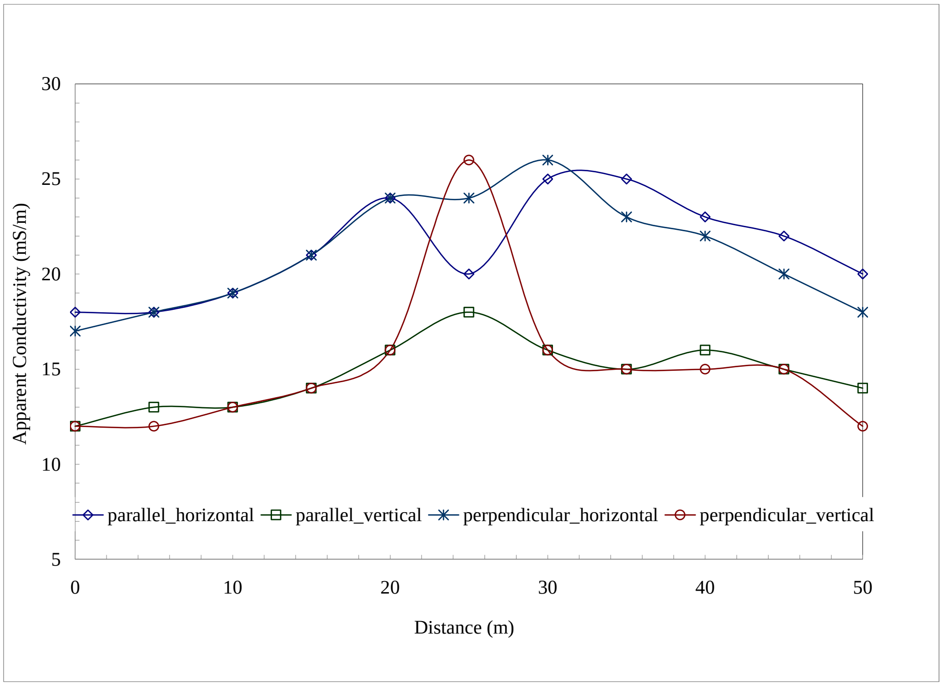

Figure 3.23: EM31 chart showing conductivity peaks for Line 3 of the desiccation crack.

Cultural Interference Tests

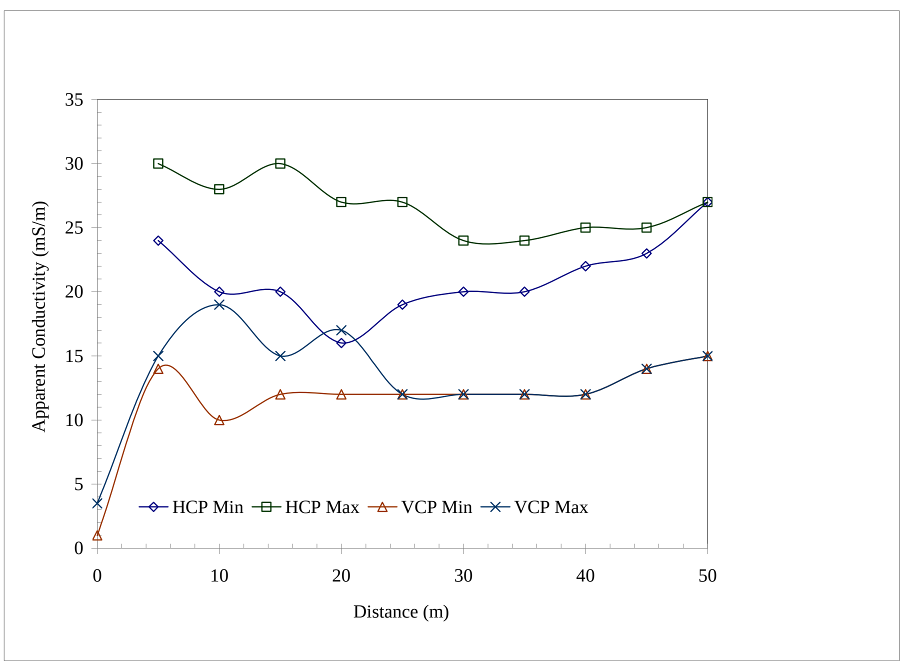

Figure 3.24: EM31 chart showing conductivity peaks for the parallel orientation during the power line test.

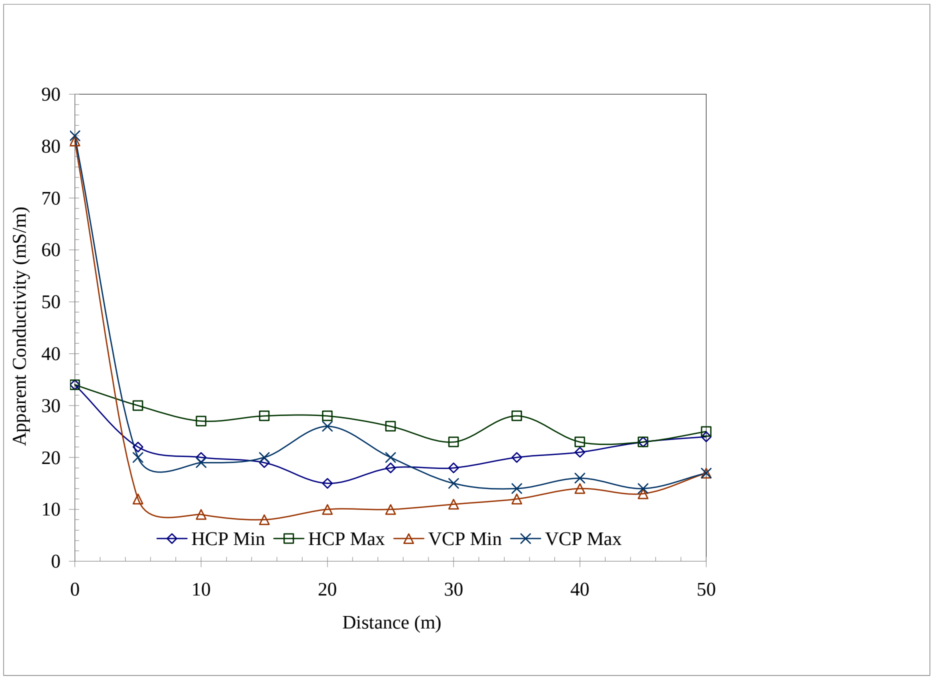

Figure 3.25: EM31 chart showing conductivity peaks for the perpendicular orientation during the power line tests

3.4 EM31 Contour Plots

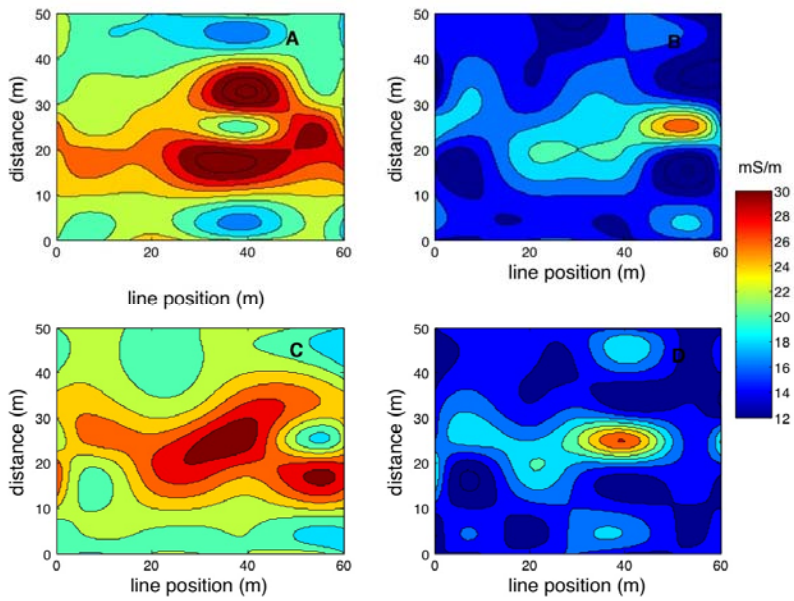

Figure 3.26: EM31 data obtained for Grid 1. Here, four different orientations are presented. Parallel and perpendicular refer to orientation of the instrument relative to the lines. HCP and VCP refer to the coplanar orientation relative to the earth. Plot A refers to the parallel oriented HCP, B refers to parallel VCP, C refers to perpendicular HCP and D refers to perpendicular VCP. The units are in milliSiemens/m. Contours were produced in MatLAB with the method 'spline' which smoothes the contour points. North is to the right in these figures.

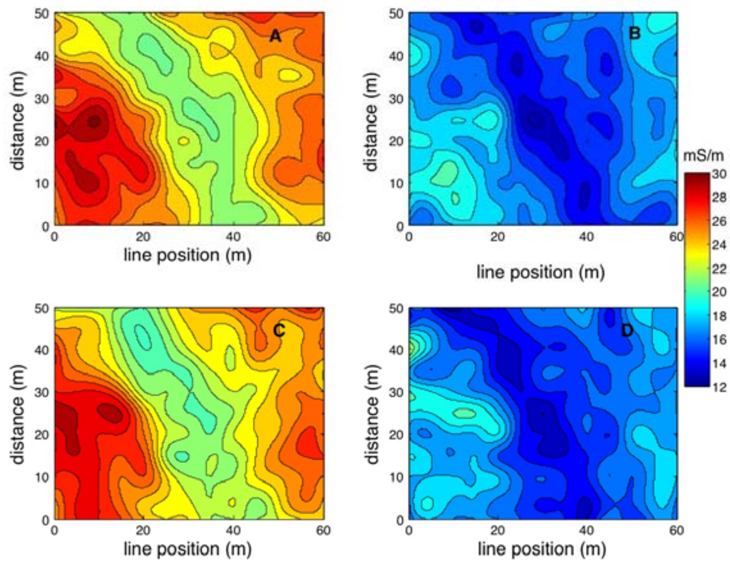

Figure 3.27: EM31 data obtained for Grid 2. Here, four different orientations are presented. HCP and VCP refer to the coplanar orientation relative to the earth. Plot A refers to the parallel oriented HCP, B refers to parallel VCP, C refers to perpendicular HCP and D refers to perpendicular VCP. The units are in milliSiemens/m. Contours are produced in MatLAB with the method 'spline' which smoothes the contour points. North is to the right.

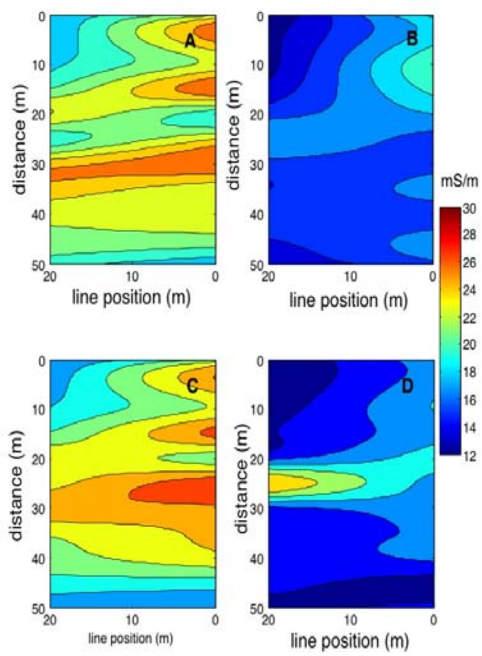

Figure 3.28: EM31 data obtained for the desiccation crack grid. Here, four different orientations are presented. HCP and VCP refer to the coplanar orientation relative to the earth. Plot A refers to the parallel oriented HCP, B refers to parallel VCP, C refers to perpendicular HCP and D refers to perpendicular VCP. Units are in milliSiemens/m. Contours were produced in MatLAB with the method 'spline' which smoothes the contour points. North is up in these figures.

4.0 EM34

4.1 Technique

The EM34 is a high-sensitivity electromagnetic method used to measure apparent electrical conductivity (Greenwood, 2004). The EM34 permits one to measure the apparent conductivity in milliSiemens per meter (mS/m). The intercoil spacing and operating frequency are: 10m at 6.4 kHz, 20 m at 1.6 kHz, 40 m at 0.4 kHz respectively. Its accuracy is +/- 0.1% of full scale, +/- 5% at 20 mS/m (www.geonics.com).

4.2 Location

A total of three grids were surveyed during two weekends near Willcox, Arizona; all of the grids were located to the NNW of the AEPCO Power Plant. The initial Line1 (S60°W; UTM 12S602112.3 - N3548731.2) for Grid1 and the initial Line1 (N76°W; UTM 12S602056.5 - N3548853.9) for Grid 2 are labeled and are shown in the Figures 1.2 and 1.3. The measurements over the lines for Grid 1 and Grid 2 were acquired every 10 meters along the Lines 1, 3, 5, 7, 9, 11 and 13. The third grid, called 'Desiccation Crack' with N-S lines is located to the East of the previous grids. The first line for the 'Desiccation Crack' was located at UTM 12S603762.6 - N3548596.2 coordinates. Finally, one test line, 50 meters in length, located between Grid 1 and Grid 2 was surveyed next to cultural interference (fence, power lines).

4.3 Data Processing

Once the data were collected, the first step was to download the data into an Excel spreadsheet. We then produced graphs corresponding to the conductivity response over each line. Finally, the compiled data for each grid was contoured (with the krigging method) using Surfer software.

4.4 Data Description

For Grid 1, we surveyed 40- and 10-meter coil separations, perpendicular to the thirteen lines. The measurements were read at 10-meter intervals along the lines for Grid 1 and Grid 2. These lines were set up perpendicular to the fissure trend where it was visible. Grid 2, located NNW of Grid 1, was configured with the same dimensions as Grid 1, but with different line directions and only 10-meter coil separation was surveyed over the lines. The third grid, called 'Desiccation Crack' was surveyed near a road where a desiccation crack was visible over part of the survey area. The line orientation was N-S for all three lines.

We measured VCP (Vertical Co-planar) and HCP (Horizontal Co-planar) orientations. In the first case, the transmitter and receiver loops are in a vertical position, while in the second case both loops are over the surface in a horizontal position. The purpose of the VCP records was to obtain detailed mapping of surface fractures, while the HCP provides a better depth of penetration.

4.5 Interpretation

From the graphs, although the conductivity values for the Grid 1 (10-meter separation loops) over the lines do not show notable changes in the conductivity values, the vertical co-planar (VCP) response next to the fissure (at 22- to 24-meter) increases at least 10 mS/m, while the horizontal co-planar (HCP) shows an irregular pattern (Fig. 4.1, 4.2, 4.3, 4.4, 4.5, 4.6, 4.7). Our interpretation is that there are probably near-surface fissures with possibly increased moisture content.

Although the responses for the Grid 1 (40-meter separation loops) show better anomaly response, the VCP and HCP values are completely opposite. The tendency next to the fissures for VCP responses is to increase, while the HCP response is going down (Fig. 4.8 to 4.14). Using 40-meter loop separation would permit a better depth of penetration, however the HCP values near the fissure decrease while the VCP are increasing, again indicating the surficial characteristic of these fissures, as suggested in the previous paragraph.

From the graphs for Grid 2 (10-meter separation loops), VCP values do no show any strong characteristics, however HCP measurements over lines 1, 5 and 13 reflect low conductivities (Fig. 4.15, 4.17, 4.21).

The graphs over the 'Desiccation Crack' lines show an interesting tendency, especially the VCP, which increases. The HCP values decrease over the same intervals (Fig.4.23, 4.24).

The contours permit an improved 2D visualization, helping effectively in the interpretation and confirming our previous observations with the graphs. Thus, based on the contour map for Grid 1 (Figures 4.28 and 4.29), 10-meter spacing loops, the VCP as well as HCP are showing anomalous conductivity near the area where there are located visible fissures. High-conductivity anomalies for VCP measurements occur for the 40-meter loop spacing. For the same separation, the HCP is completely opposite, with low conductivity in the same area.

The contours for Grid 2 (10-meter separation) show high conductivity around Line 1. This might be because of the influence of a visible fissure at 32 meters near Line 1. The HCP and VCP anomalies are almost reciprocal (Fig. 4.32, 4.33).

Contours for the 'Desiccation Crack' reflect the high conductivity anomalous HCP as well as VCP responses (Fig. 4.34, 4.35).

4.6 Cultural Interference

We surveyed test lines near cultural interference, including power lines and fences in order to estimate the magnitude of this interference. The measurement over the test line (S10W direction) was collected every 10 meters, parallel and perpendicular to the line (10- and 20-meter spacing). We noticed oscillations in our readings due to the influence of the power line (located at 17.5 meters). The measurements were taken as maximum or minimum oscillations observed in 30 seconds, labeled as VCP Max/Min or, HCP Max/Min values for each station. From Fig.4.25, we see the strong influence of the fence near the beginning of the test line. In addition, from Figure 4.25, it is possible to confirm that the readings had stabilized at 30 meters from the power line. The effect of the power line was much stronger when the instrument was oriented parallel to the power line and the effect was much weaker when the instrument was oriented perpendicular to the power line. In summary, 30 meters from power lines is recommended for the future surveys using the EM34.

4.7 Graph Plots

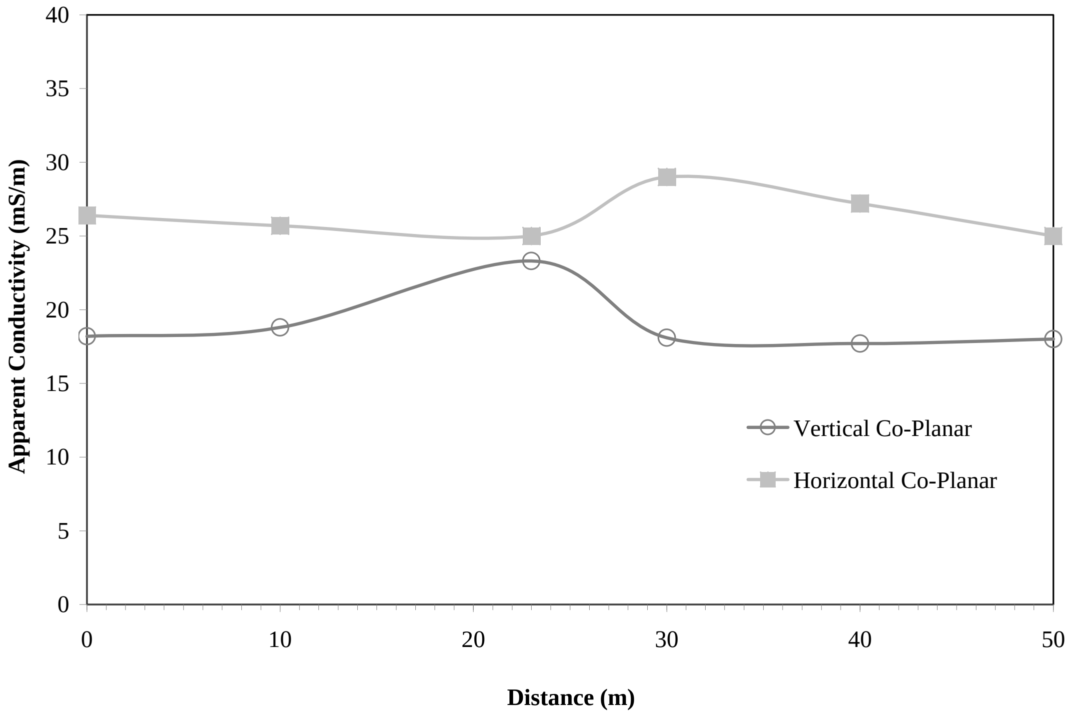

Figure 4.1: Grid 1, Line 1, with 10 m spacing, showing the disturbance in the conductivity near 23 m, location of open fracture.

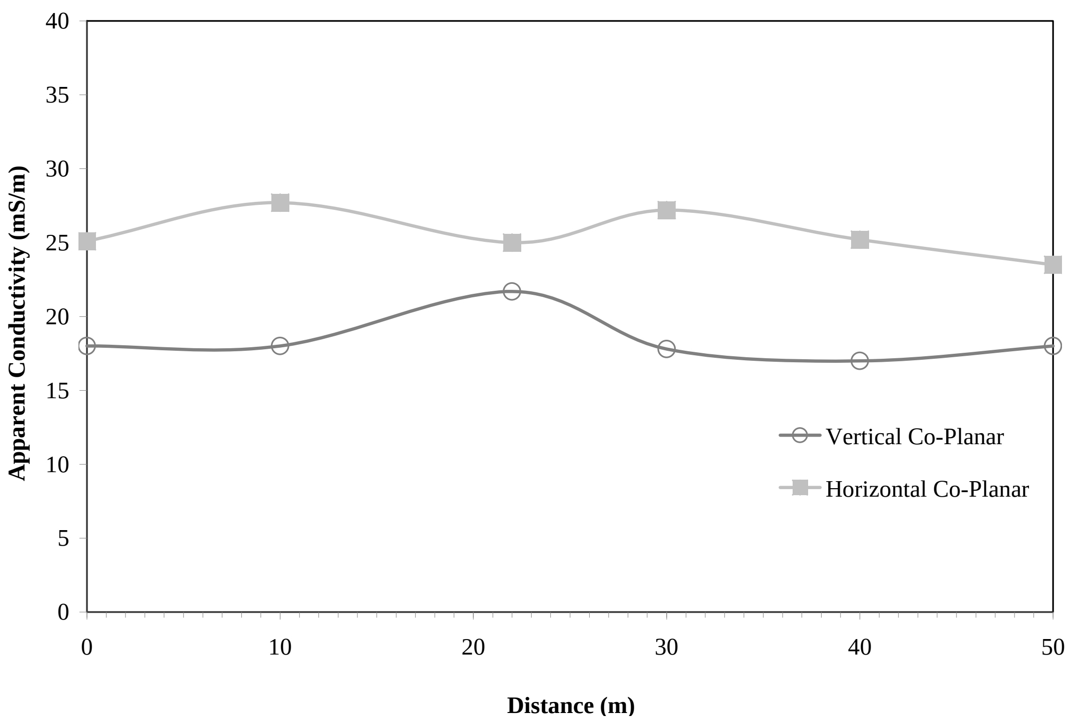

Figure 4.2: Grid 1, Line 3, with 10 m spacing, reproducing disturbance next to the fissure at 22 m.

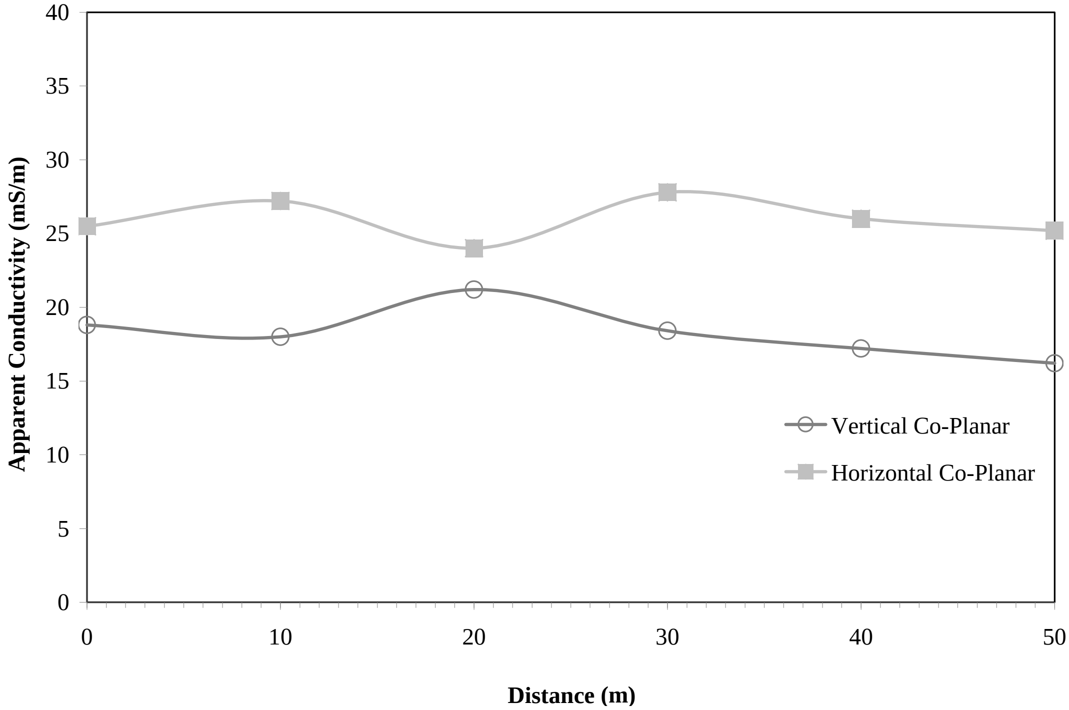

Figure 4.3: Grid 1, Line 5, with 10 m spacing; showing the disturbance in the conductivity near open fissure at 20 m.

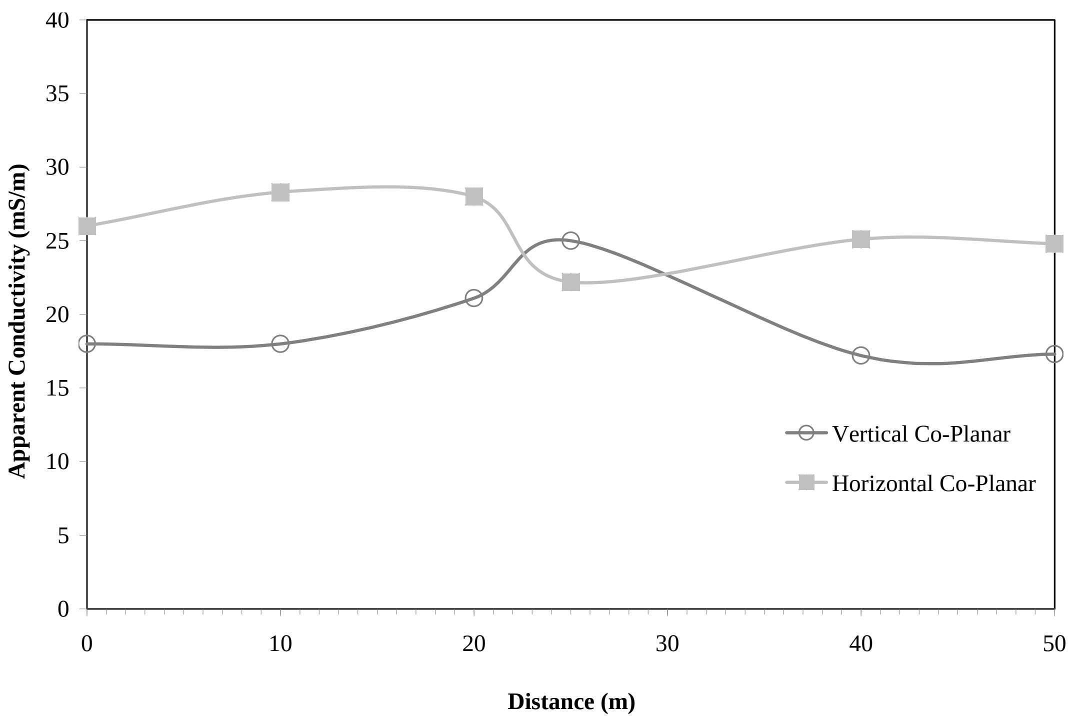

Figure 4.4: Grid 1, Line 7, with 10 m spacing, showing opposite conductivity response next to open fissure at 25 m.

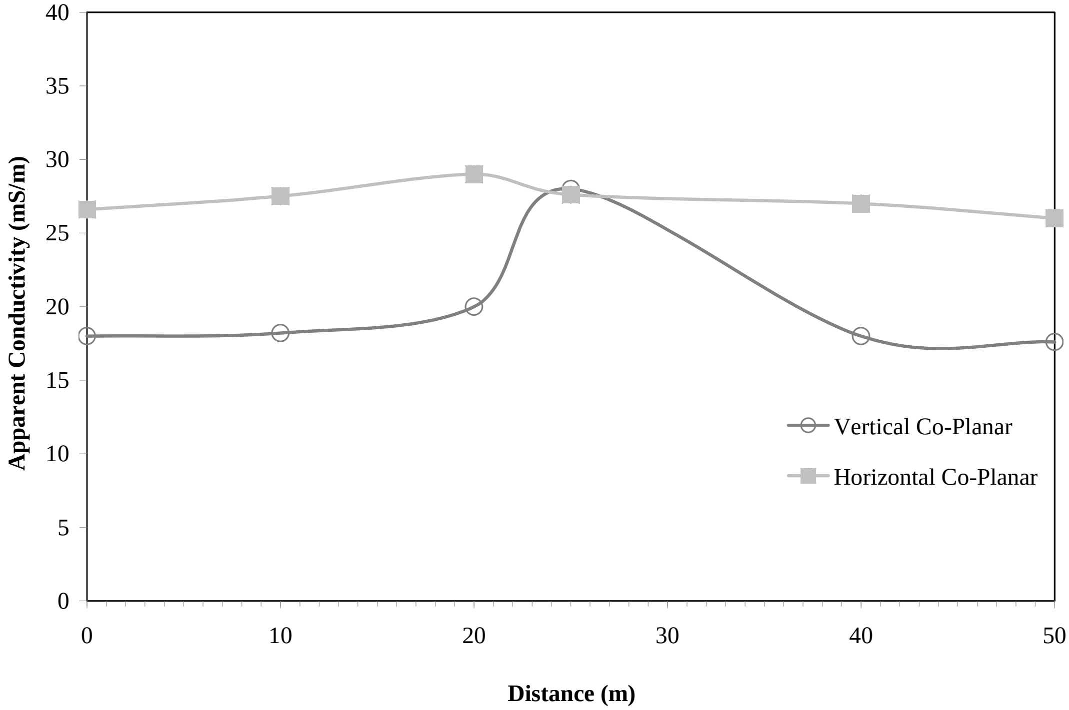

Figure 4.5: Grid 1, Line 9, with 10 m spacing, showing a peak response next to the open fissure at 25 m.

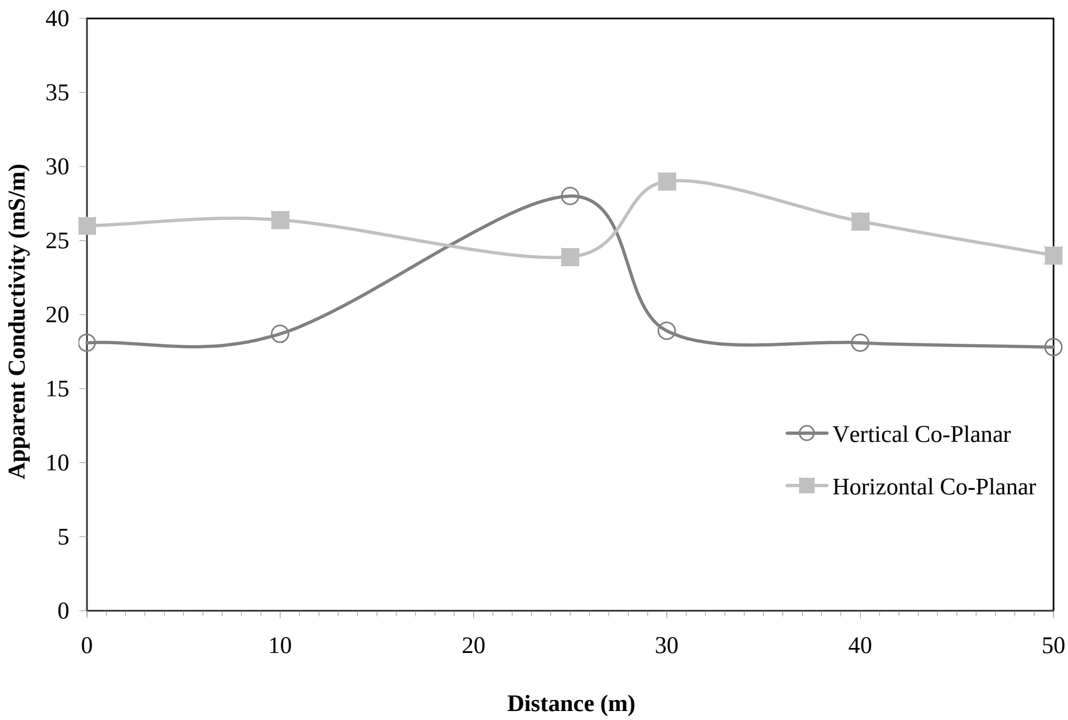

Figure 4.6: Grid1 Line11, 10 m spacing, reflecting peak anomalous next to fissure, at 25m.

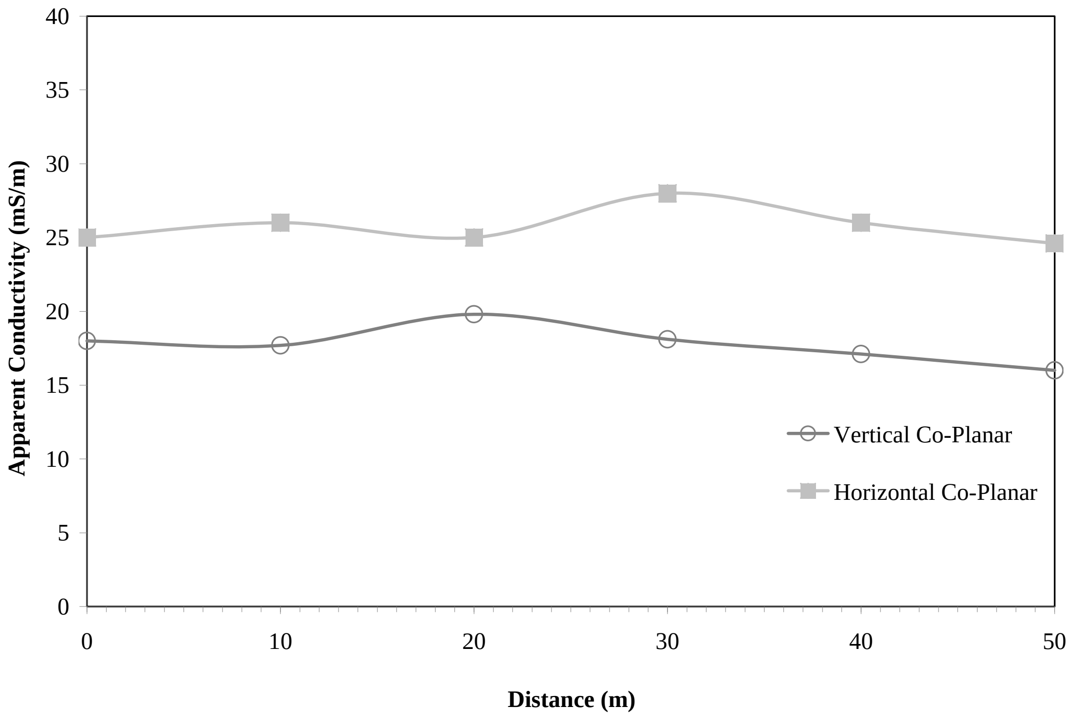

Figure 4.7: Grid 1, Line 13, 40 m spacing, do not show any notable anomaly.

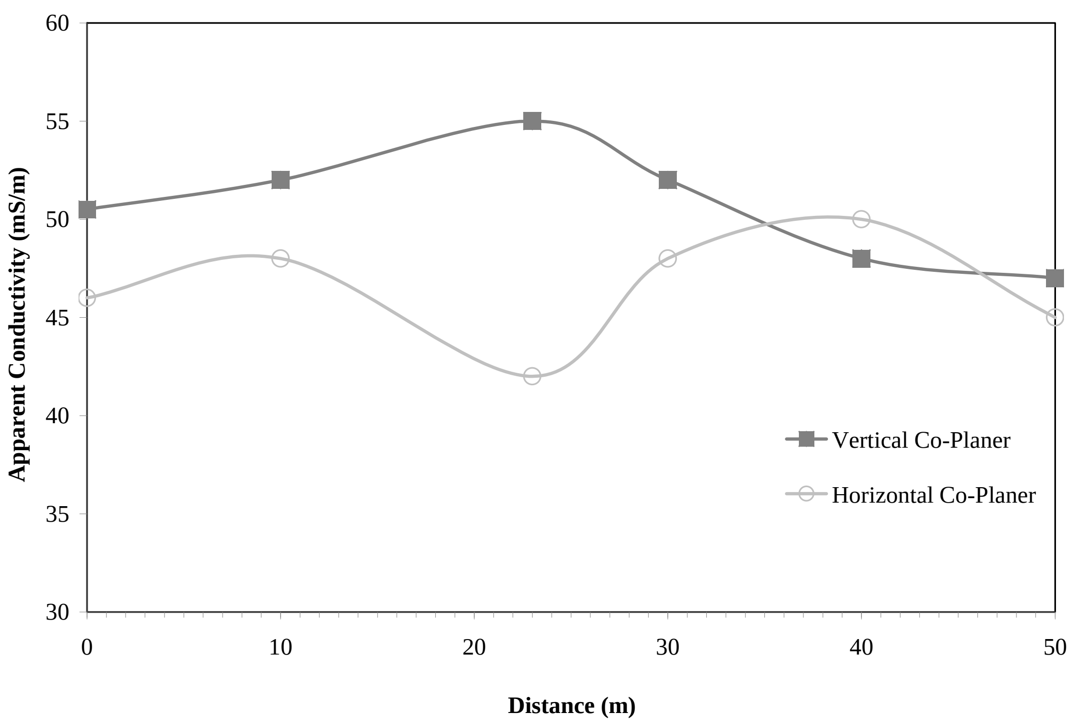

Figure 4.8: Grid 1, Line 1, 40 m spacing, showing the disturbance next to the open fissure at 23 m.

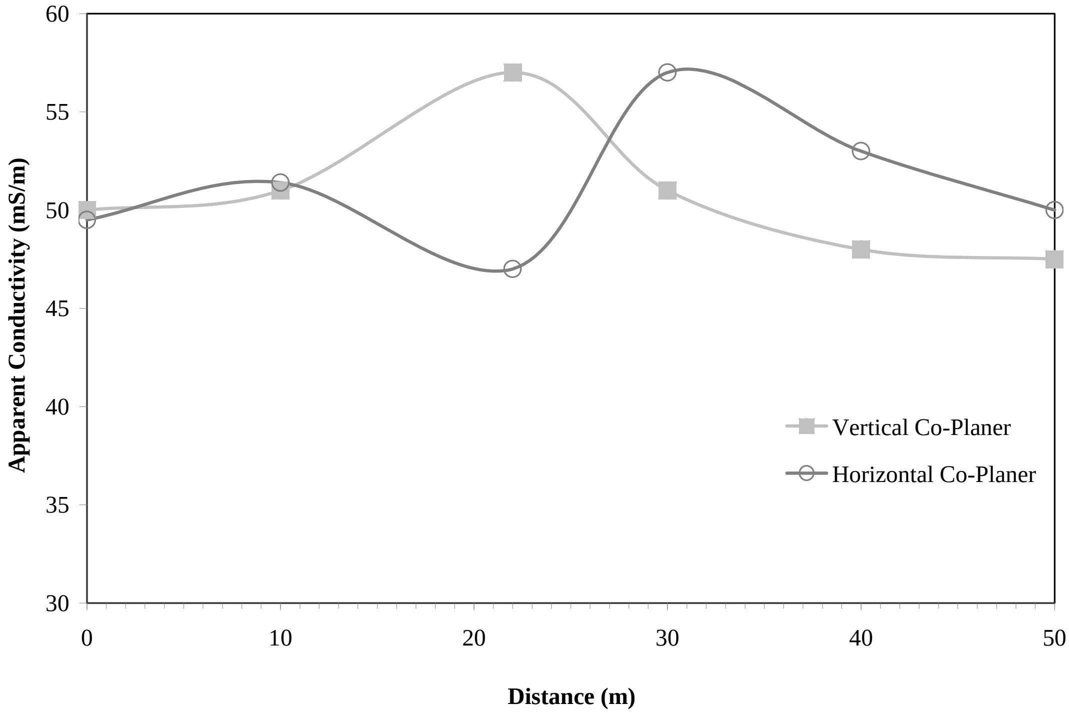

Figure 4.9: Grid 1, Line 3, 40 m spacing, showing a consistent anomaly next to fissure at 22 m

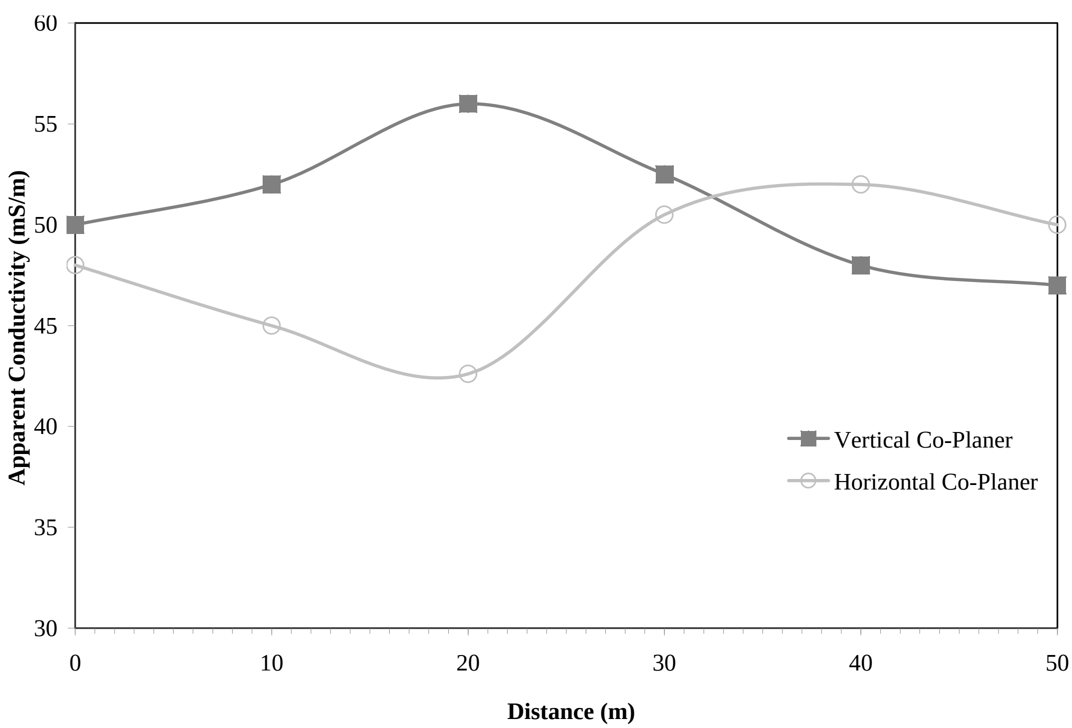

Figure 4.10: Grid 1, Line 5, 40 m spacing, again reproducing almost the same anomaly as Figure 4.9.

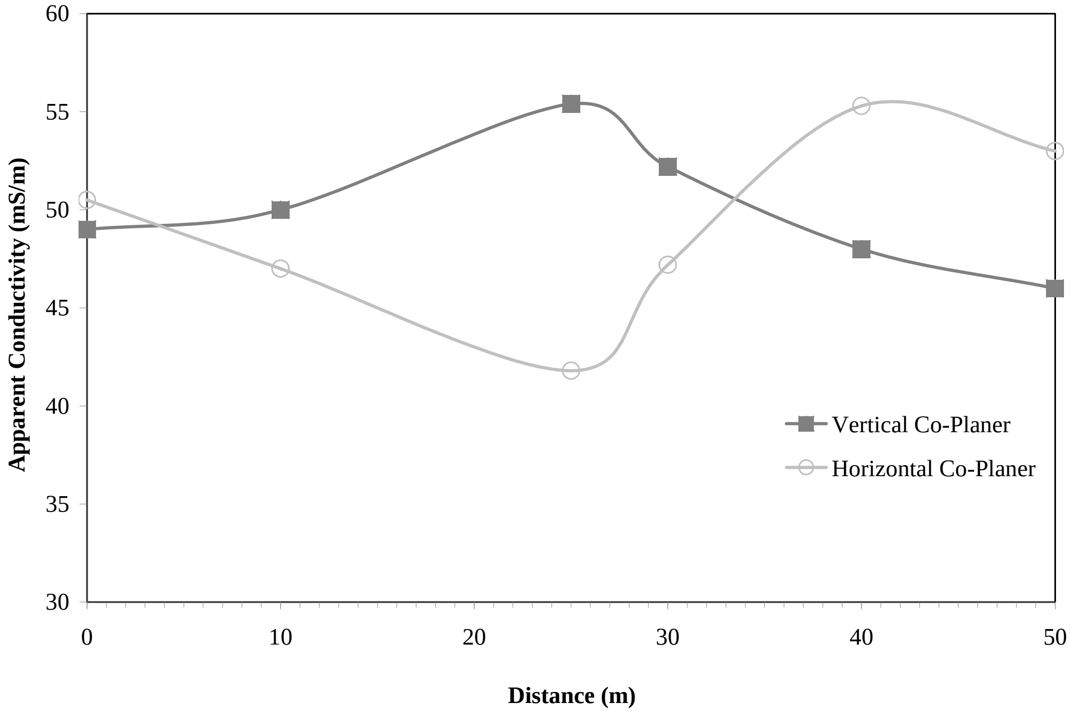

Figure 4.11: Grid 1, Line 7, with 40 m spacing, showing again the conductivity anomaly next to the fissure at 25 m.

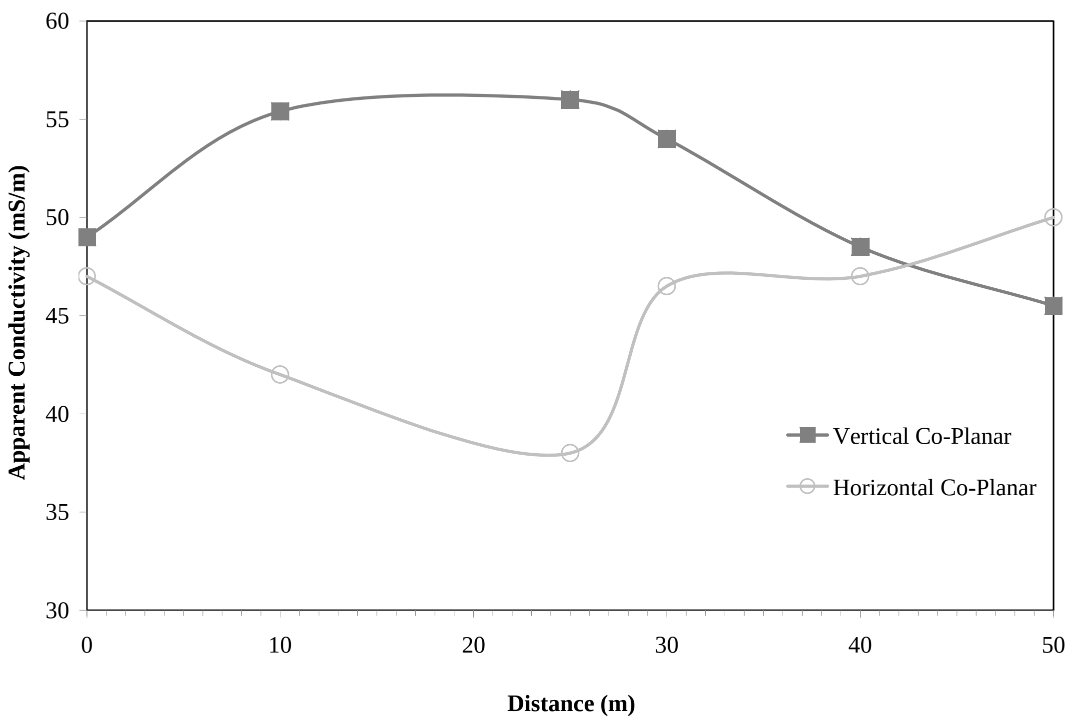

Figure 4.12: Grid 1, Line 9, 40 m spacing, showing some irregular anomaly next to the fissure at 25 m.

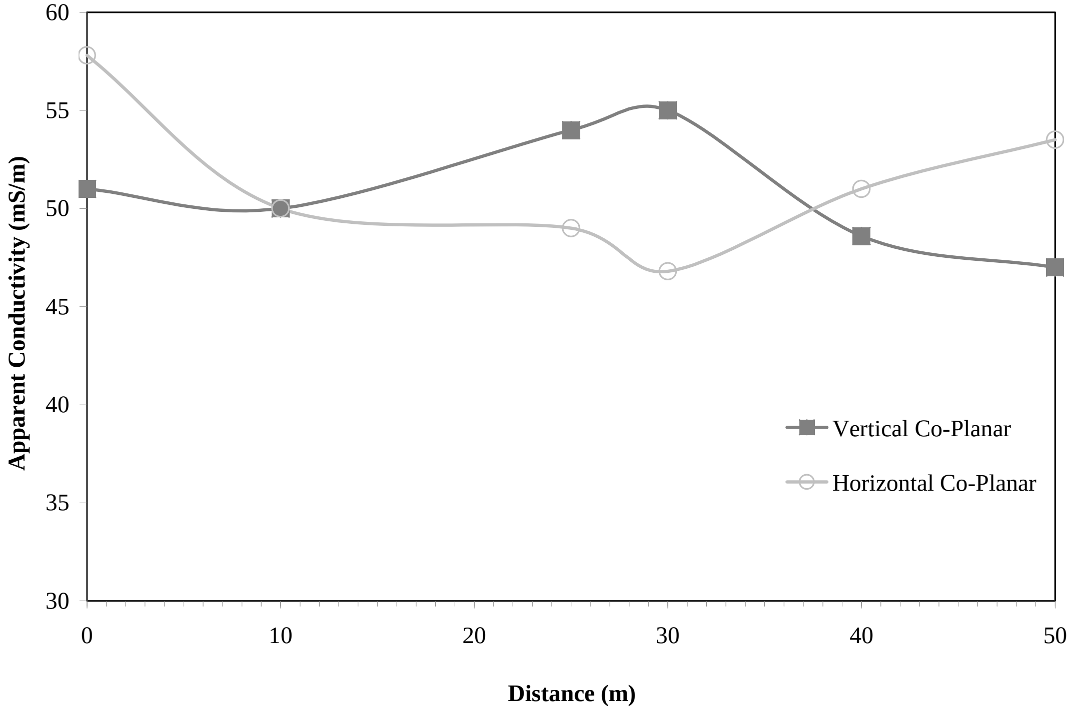

Figure 4.13: Grid 1, Line 11, 40 m spacing, showing again disturbance at 25 m, near open fissure.

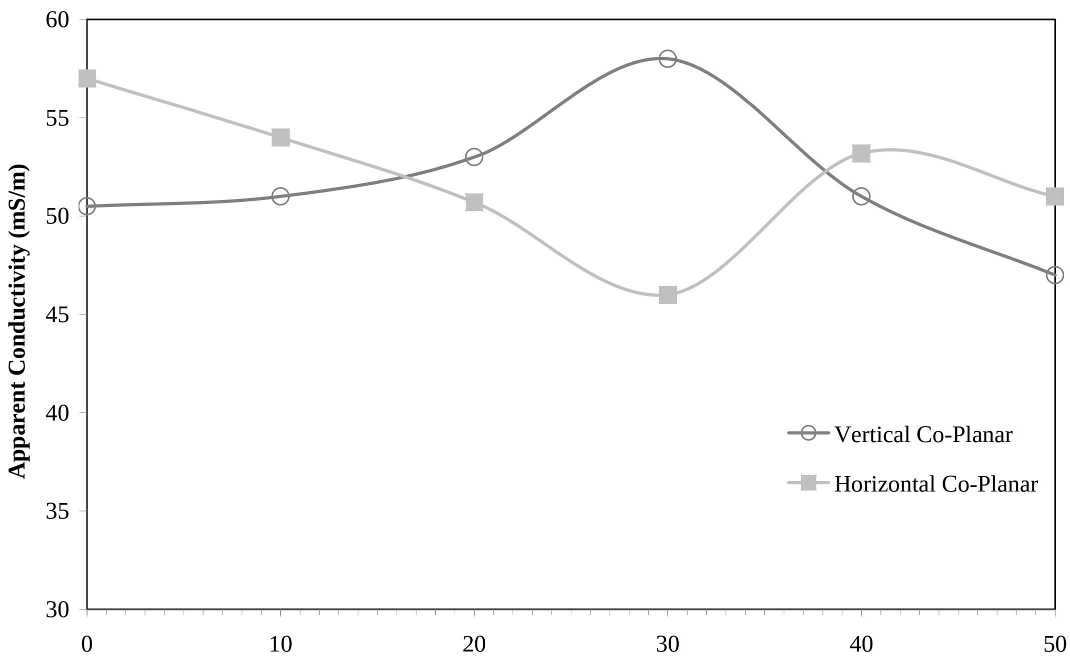

Figure 4.14: Grid 1, Line 13, 40 m spacing, showing high conductivity anomaly (up and down) next to probable fissure at 28 m.

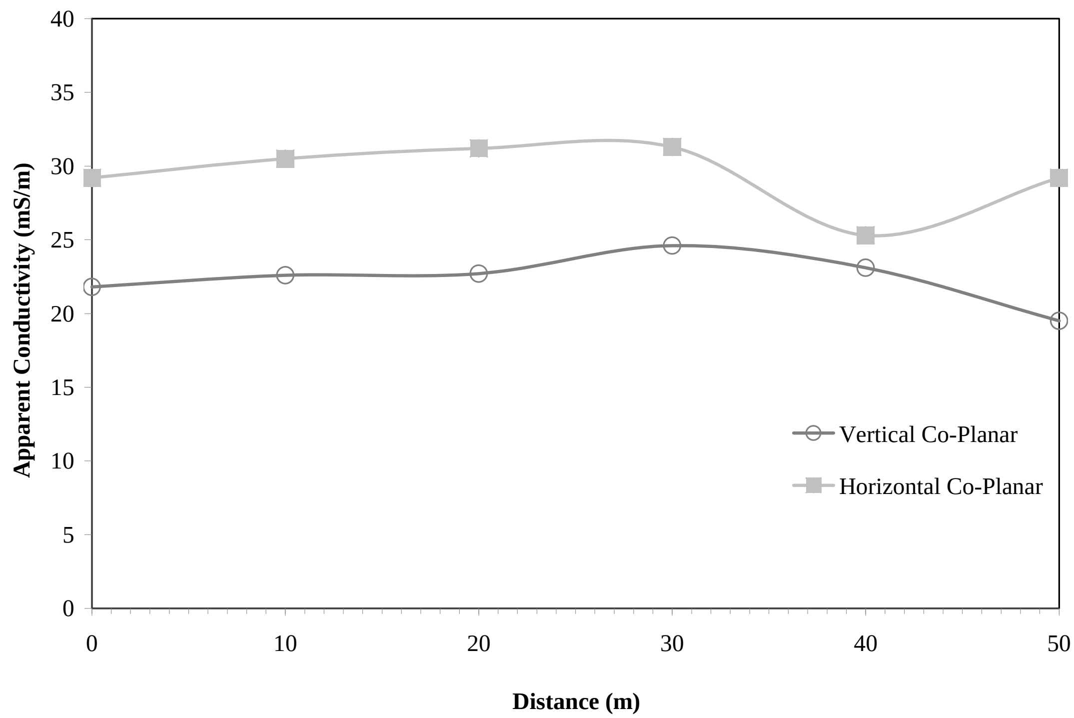

Figure 4.15: Grid 2, Line 1, 10 m spacing, showing some low conductive irregularity at 30 m, next to visible fissures.

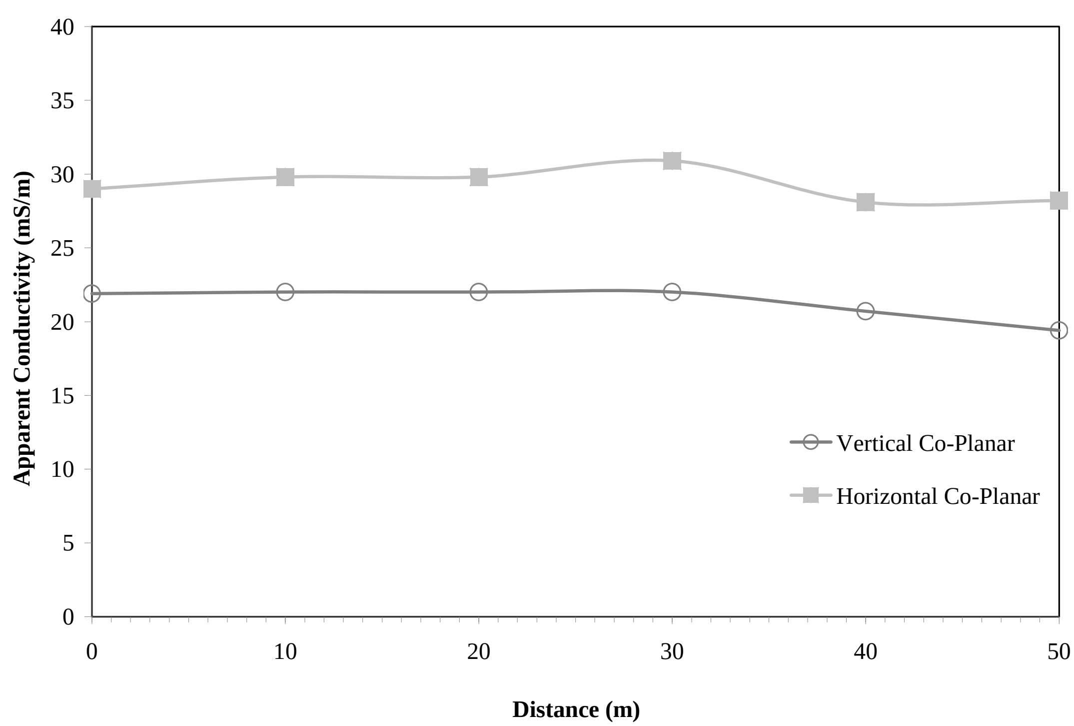

Figure 4.16: Grid 2, Line 3, 10 m spacing, without any irregularity.

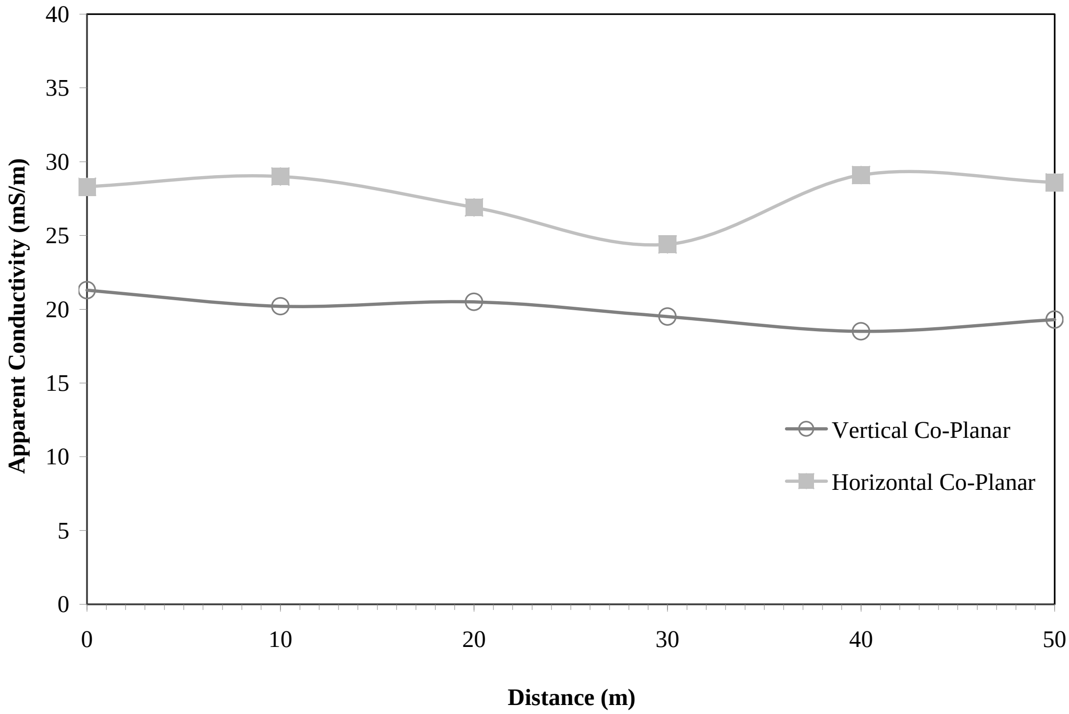

Figure 4.17: Grid 2, Line 5, 10 m spacing, with some low response next to 30 m

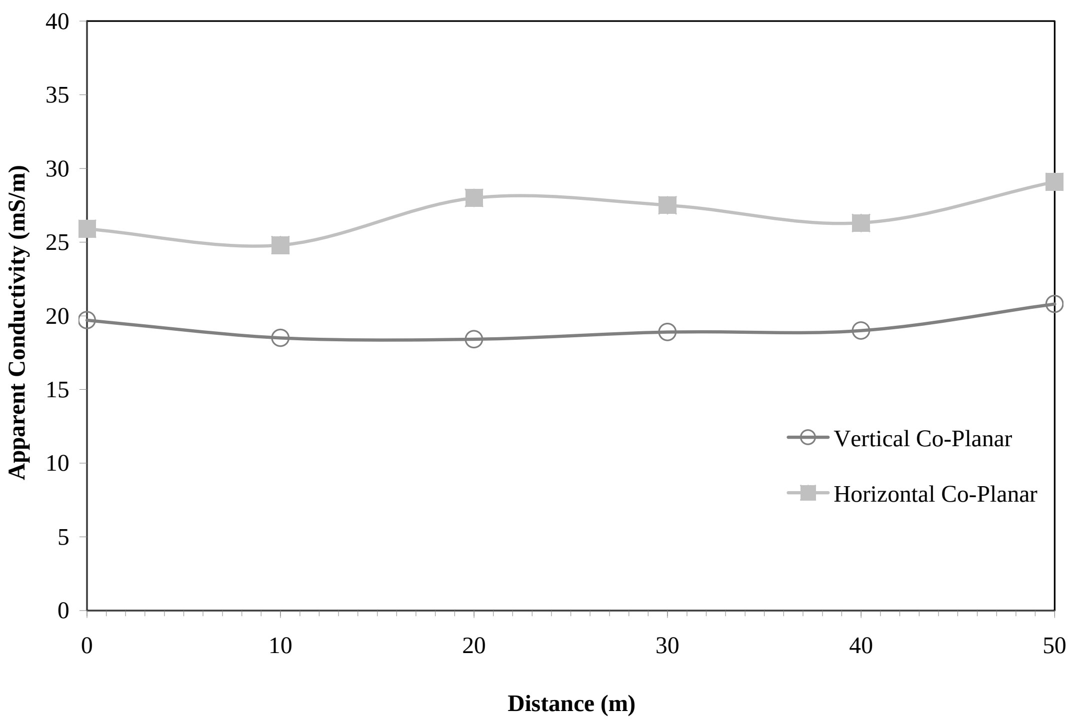

Figure 4.18: Grid2 Line7, 10m spacing, not clear irregularity.

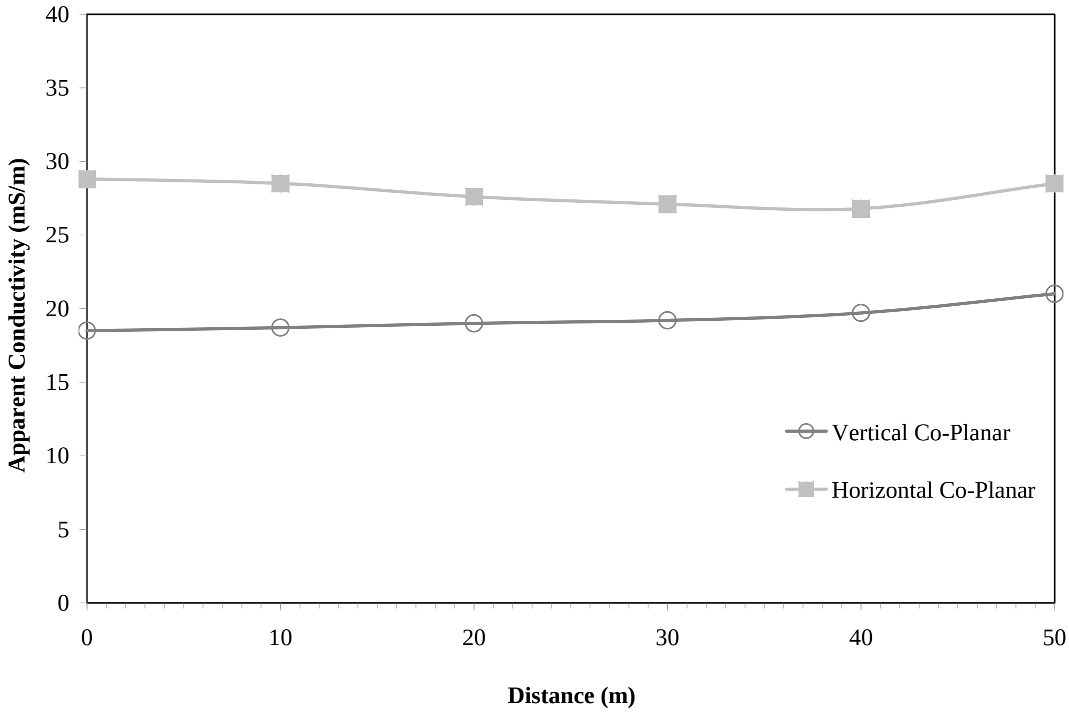

Figure 4.19: Grid 2, Line 9, 10 m spacing, without any disturbance on the conductivity.

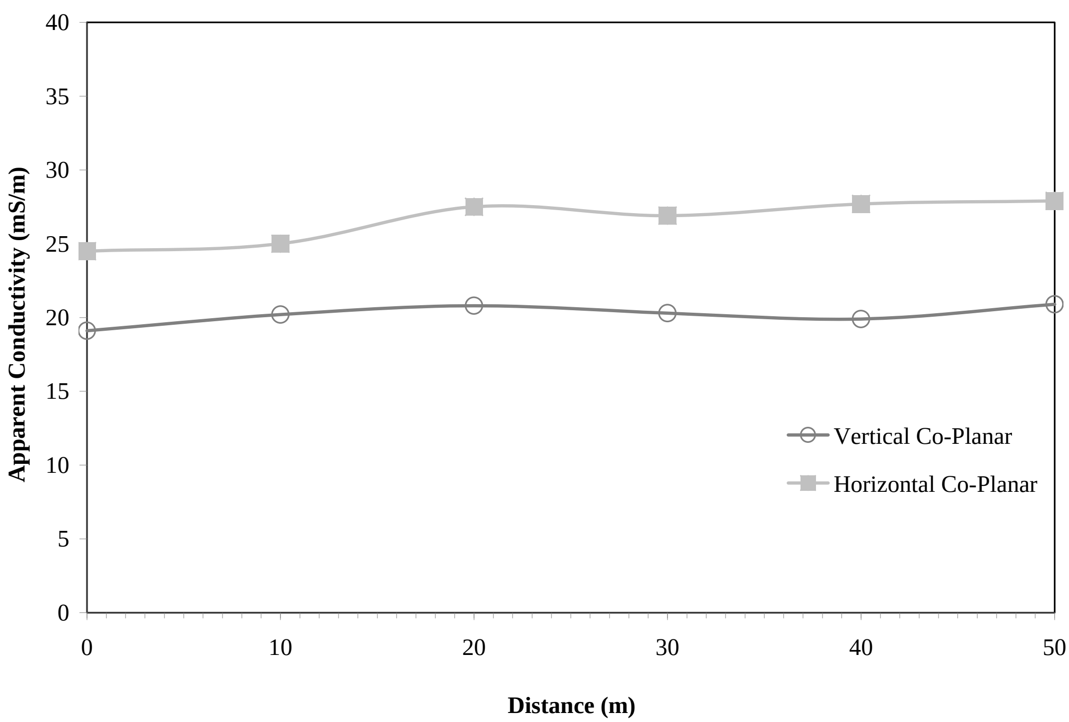

Figure 4.20: Grid 2, Line 11, 10 m spacing, without any disturbance on the conductivity.

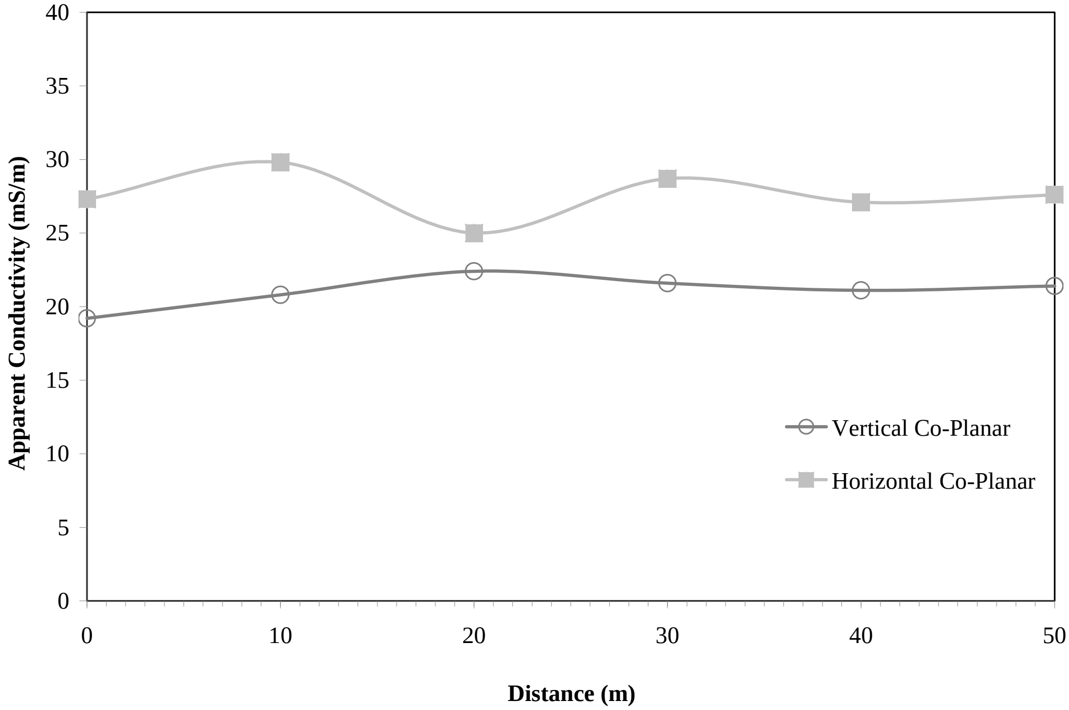

Figure 4.21: Grid 2, Line 13, 10 m spacing, with two insignificant peaks approximately over 10 m and 30 m.

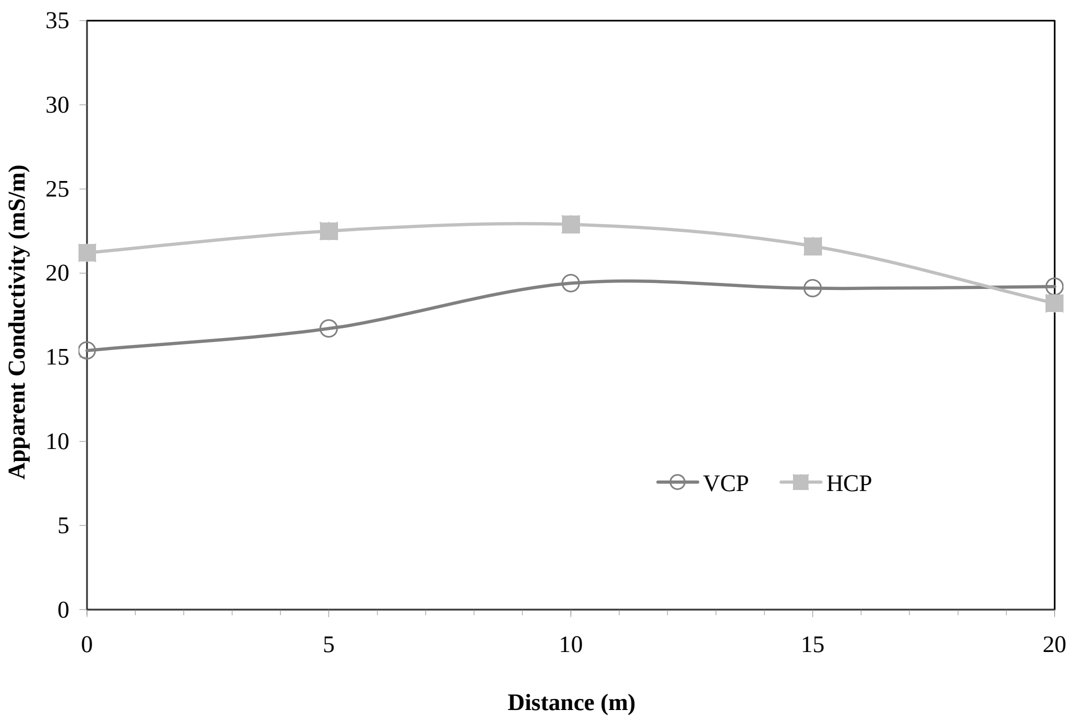

Figure 4.22: Desiccation crack Line 1, 10m spacing, do not any disturbance in conductivity anomaly.

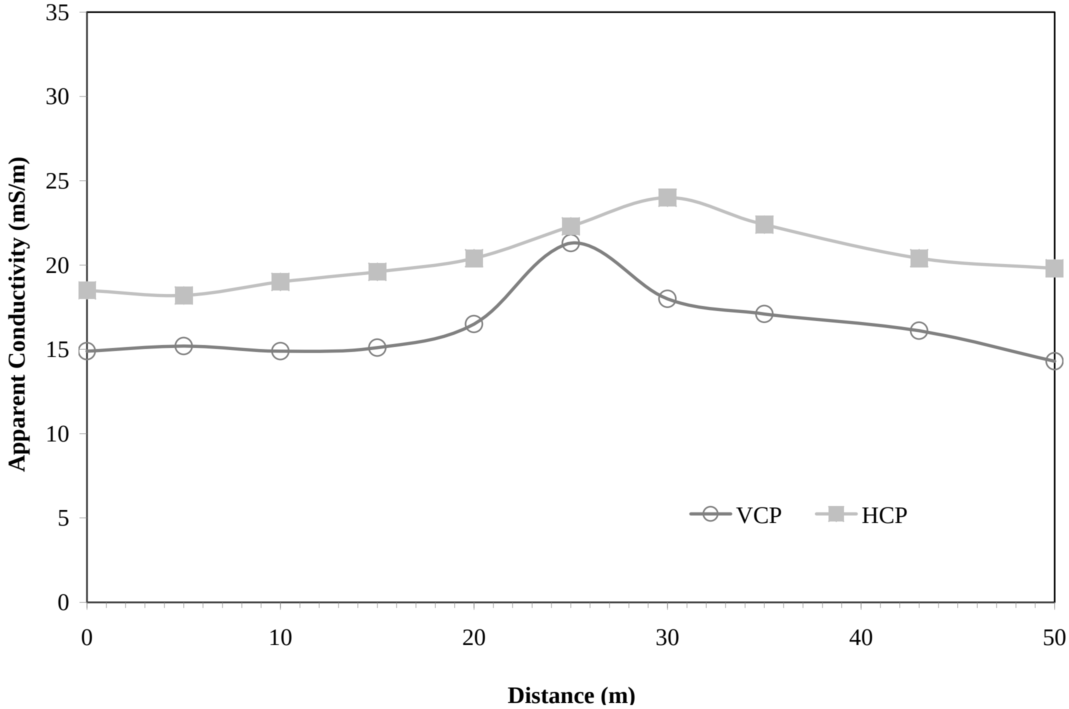

Figure 4.23: Desiccation crack Line 2, 10 m spacing, showing high conductivity near 22 m, the probable location for the desiccation crack.

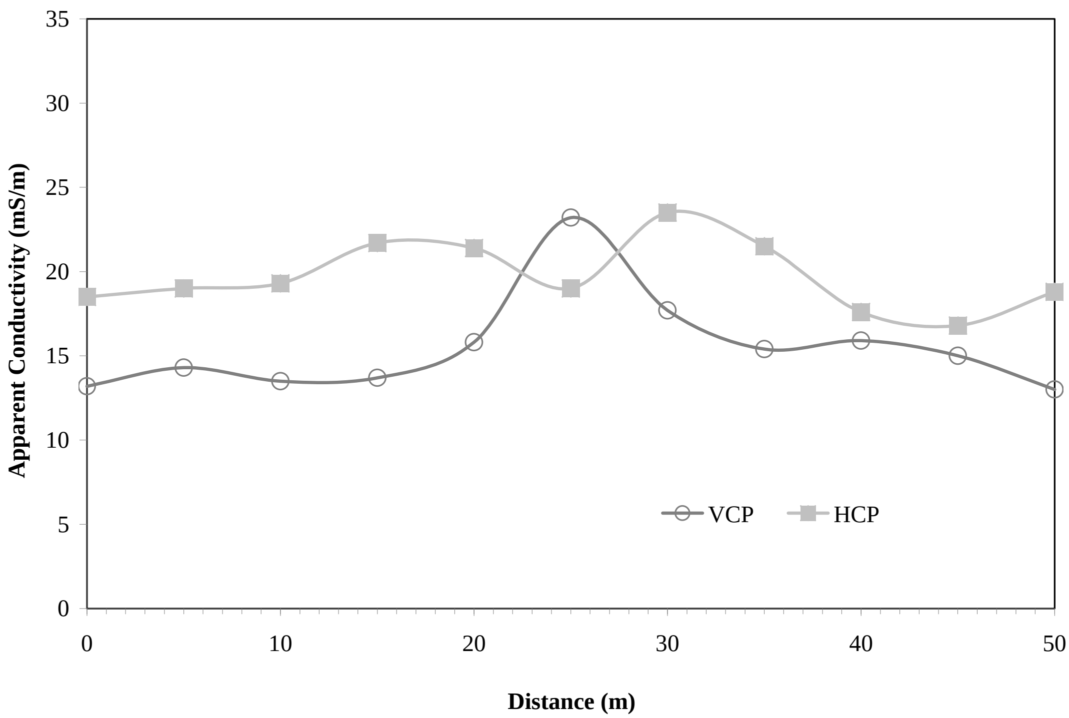

Figure 4.24: Desiccation crack Line 3, 10 m spacing, at 24 m is showing some interesting correspondence conductivity anomaly, mapping the probable desiccation crack location.

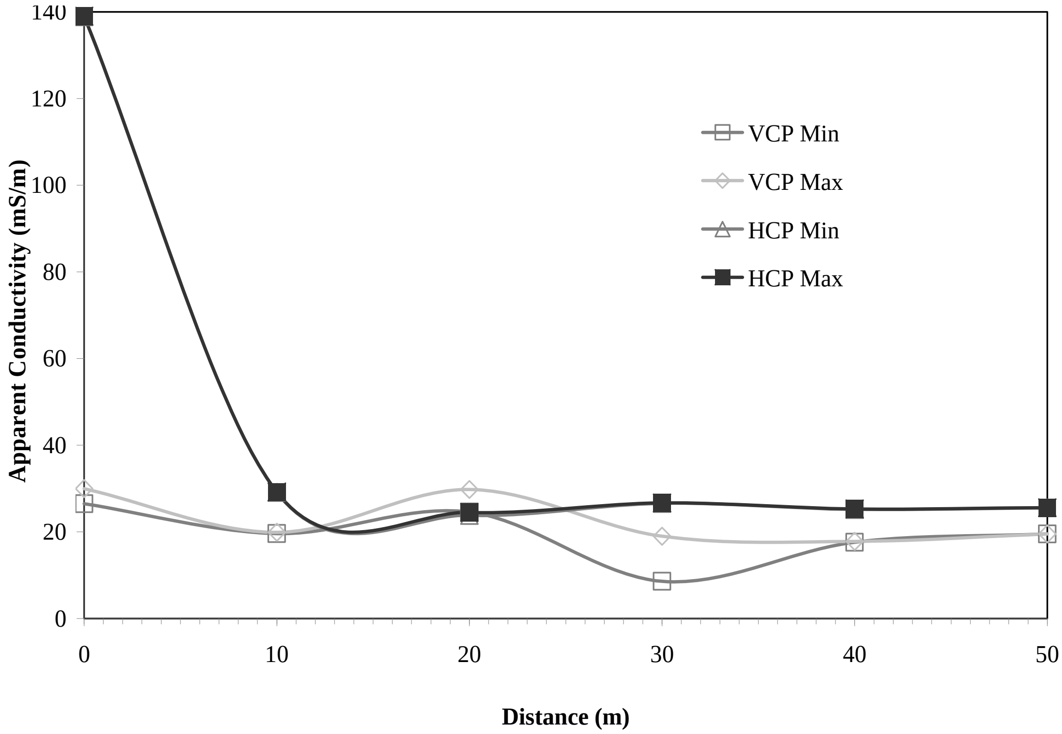

Figure 4.25: Cultural Interference test line, perpendicular to line, with 10 m spacing. Large anomaly at 0 meters is due to the interference of the fence. The power line causes a big difference for maximum and minimum values of each dipole over each point, up to 10 mS/m at 30 m. A lot more variation than values going over the fracture

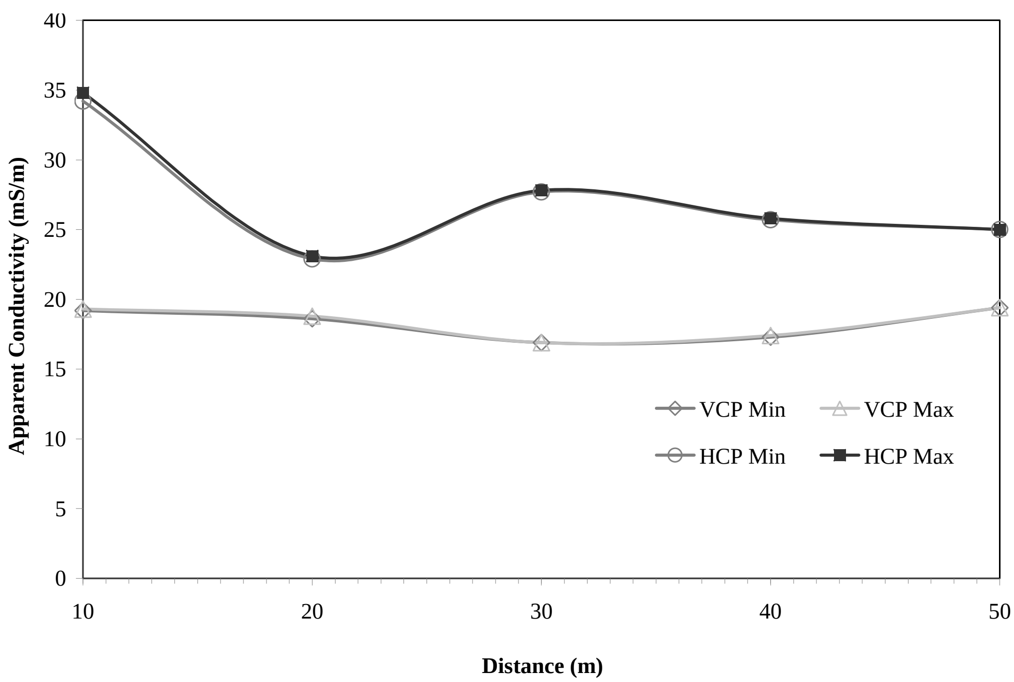

Figure 4.26: Cultural interference test line, parallel to line with 10 m spacing, the sag at 17.5 m might be due to the presence of power lines.

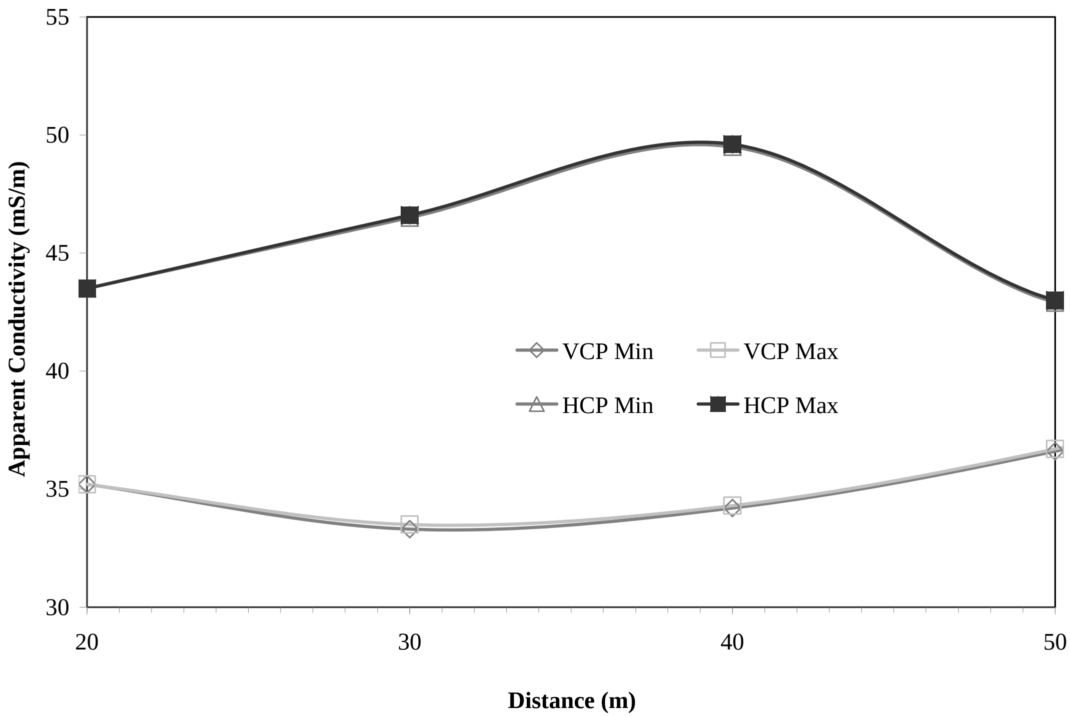

Figure 4.27: Cultural Interference test line, parallel to line with 20 m spacing.

4.8 Contour Plots

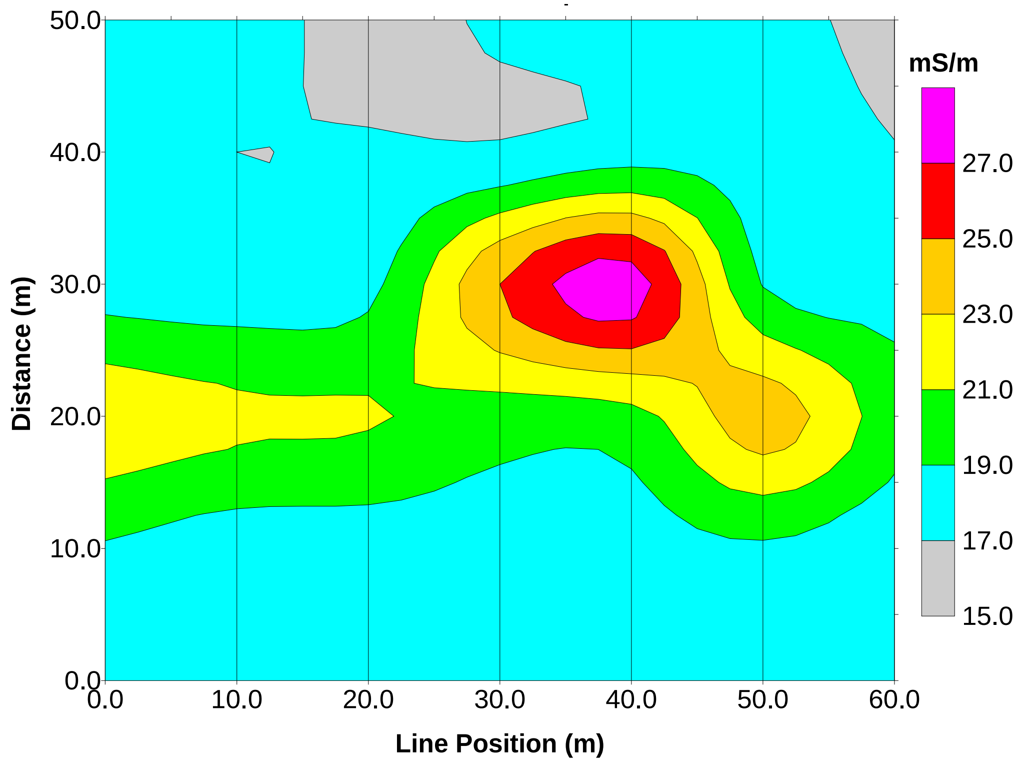

Figure 4.28: Grid 1- 10 m separation, contour for total vertical co-planar results. The high anomalies are coincident with the location of the fissure across the grid.

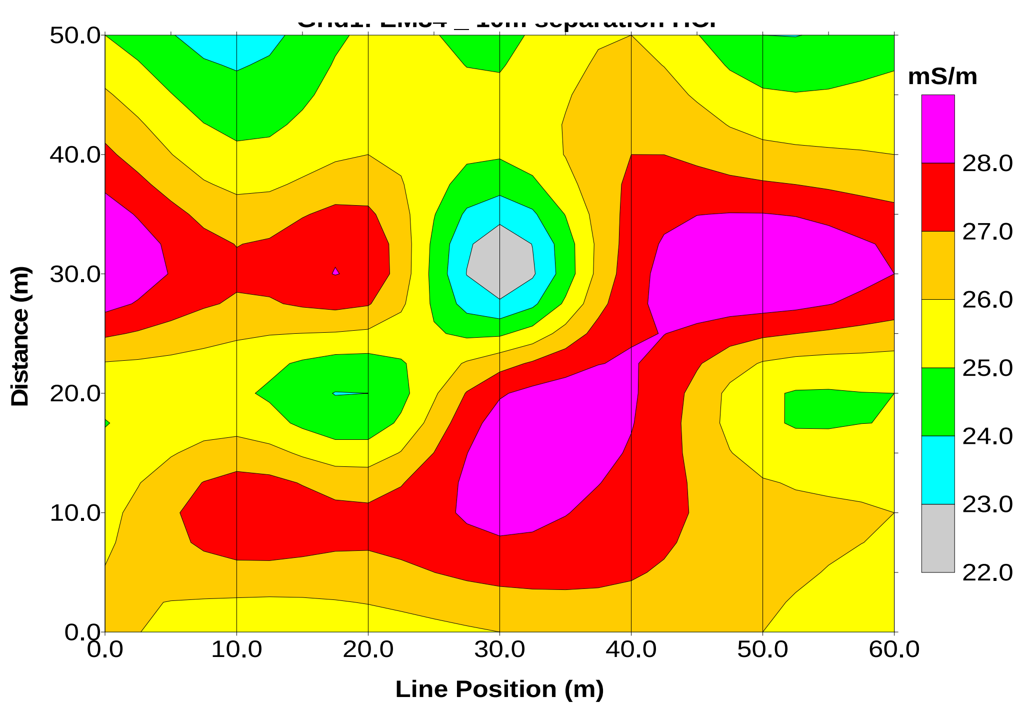

Figure 4.29: Grid 1-10 m spacing, contour for total horizontal co-planar results. The high conductivity is coincident with fissure location, probably with some ramification underneath.

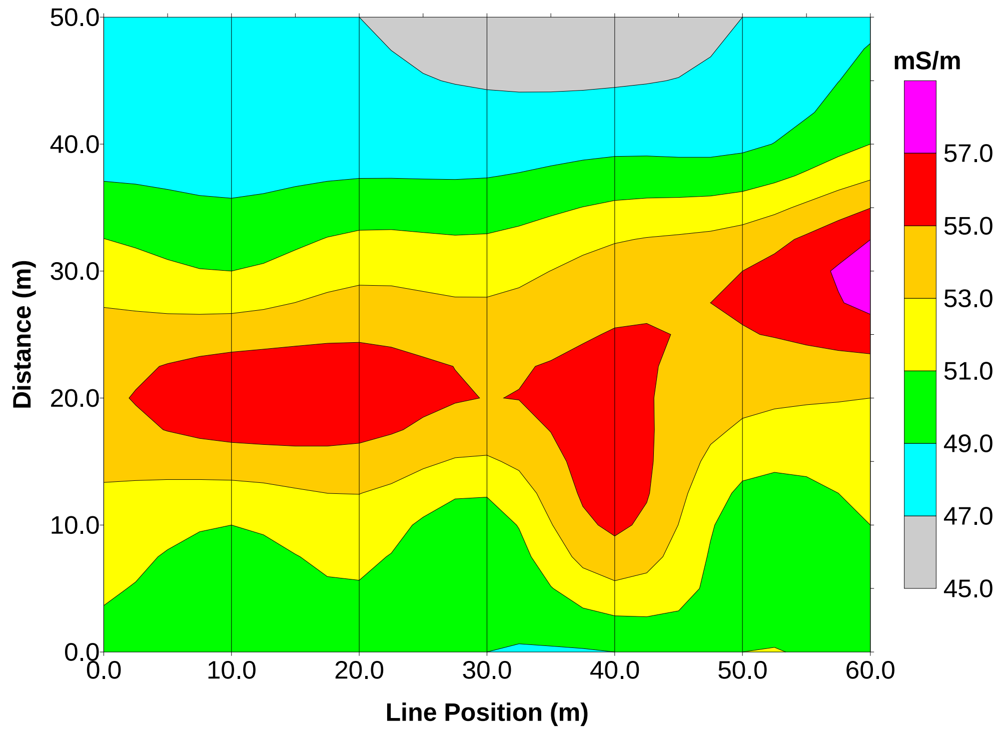

Figure 4.30: Grid 1- 40 m spacing, contour for total vertical co-planar results. The high conductivity region is coincident with the 3 fissures in the field.

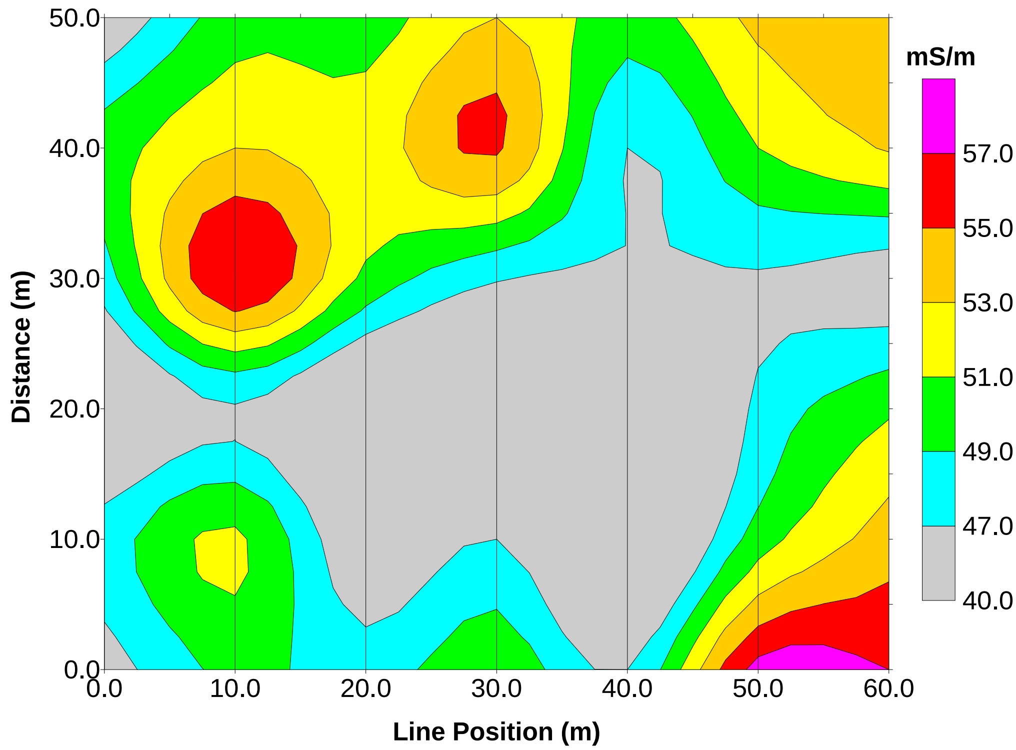

Figure 4.31: Grid 1- 40 m spacing, contour for horizontal co-planar results, showing opposite anomaly to the previous.

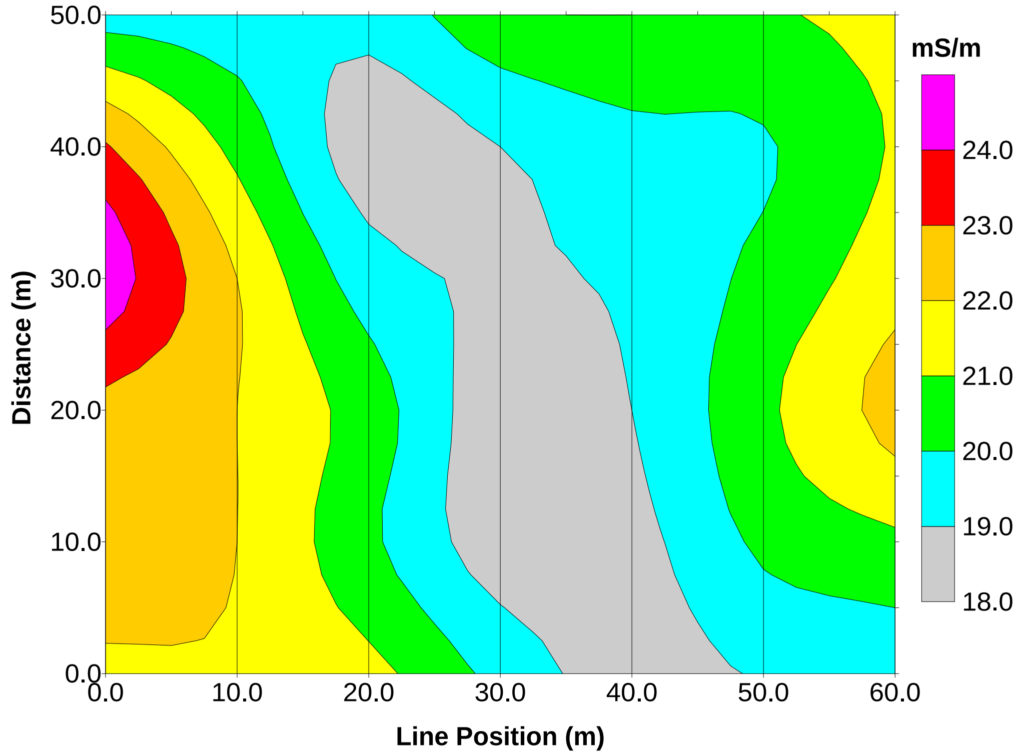

Figure 4.32: Grid 2-10 m spacing, contour for total vertical co-planar results, showing a clear high conductivity next to Line1 coincident with fissures existing in the field.

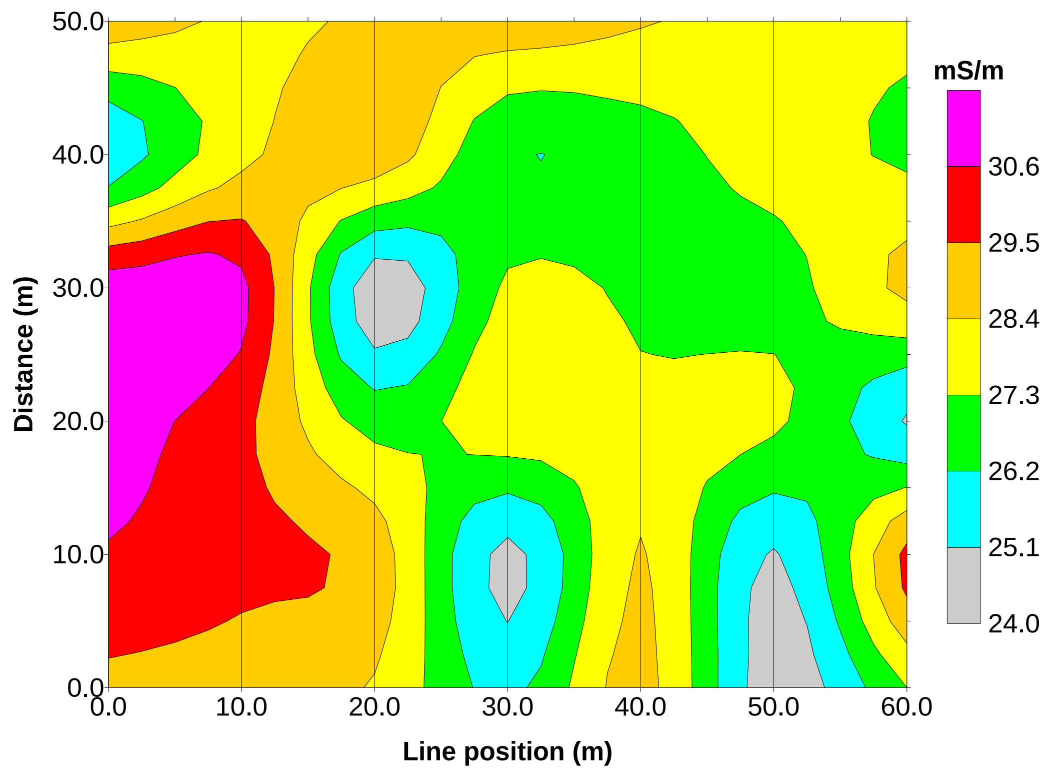

Figure 4.33: Grid 2-10 m spacing, contour for total horizontal co-planar results, showing high conductivity reproducing again as the Figure 4.25 the location of visible fissure on the field.

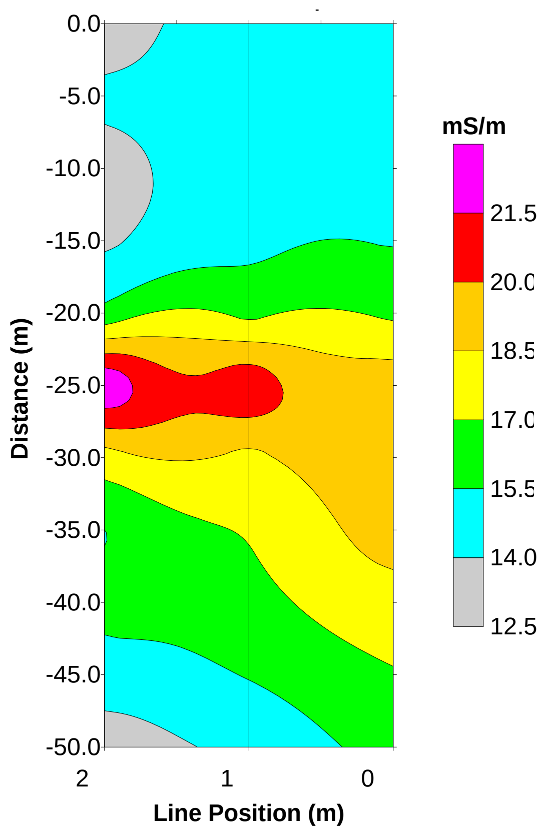

Figure 4.34: Desiccation crack-10 m spacing, contour for total vertical co-planar results, showing high conductivity, which might have the same tendency with the location of desiccation crack beneath the road.

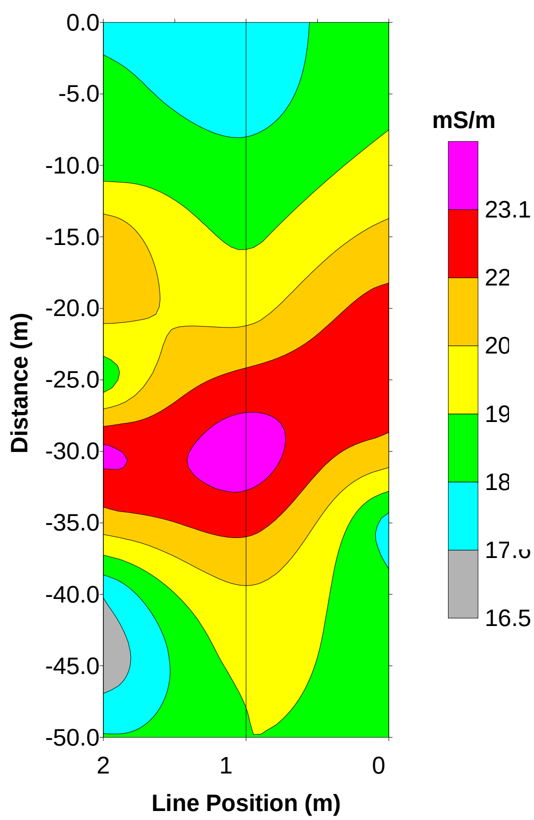

Figure 4.35: Desiccation crack 10 m spacing, contour for total horizontal co-planar results showing again the high conductivity the probable tendency and depth of the desiccation crack.

5.0 EM38

5.1 Technique

The EM38 measures ground conductivity (quadrature-phase) and magnetic susceptibility (in-phase) and is best suited for near-surface studies. It can provide a depth of investigation of up to 1.5 m in the vertical dipole mode and 0.75 m in the horizontal dipole mode. The device measures conductivity in milliSiemens per meter (mS/m) and magnetic susceptibility in parts per thousand (ppt). The EM38 operates at a frequency of 14.6 KHz, and has an accuracy of ± 5 % at 30 mS/m. (www.geonics.com)

5.2 Location

The EM38 was run over both of the study grids at 5-meter intervals. For Grid 1, measurements were collected every ten meters along lines 1, 3, 5, 7, 9, 11, and 13. For Grid 2, data were collected along lines 1, 2, 3, 4, 12 and 13. Due to suspected calibration and drift problems with the instrument, it was not possible to measure the equivalent lines in Grid 2. Measurements were repeated in Grid 1 for lines 9 and 11 to test accuracy.

Measurements were also collected along three lines over desiccation cracks at a nearby location. In addition, measurements were taken near a power line and a barbed wire fence to determine cultural noise levels.

5.3 Data Processing

The data were input to Excel in order to display XY plots and also input into MatLAB for contour processing and interpretation.

5.4 Data Description

At the outset of the first excursion to the study location, initial measurements were taken along a test line using the EM38 at ground level, at waist level, and at head level. Afterwards, it was clear that the best data acquired were from measurements with the EM38 on the ground. The instrument was positioned perpendicular and parallel to the test lines with both the horizontal and vertical dipoles measured at each point. The EM38 measured ground conductivity (Quad-phase) and magnetic susceptibility (In-phase) at each point. We measured both of these values at 5-meter intervals with the two orientations (perpendicular and parallel) at both dipoles (vertical co-planar VCP and horizontal co-planar HCP). This provided eight different readings at every point along the line. As mentioned previously, measurements were also collected along three lines extending over desiccation cracks.

The graphs for Grid 1 show a conductivity increase over the suspected earth fissure for both horizontal and vertical orientations in all plots. The magnetic susceptibility graphs, however, show no change over the fissure in most graphs. Several graphs show slightly decreased values over the fissure, as noted, for example in the plots for line 11 - vertical dipole. The contour lines for Grid 1 show a distinct anomaly for ground conductivity in line with the known fissure at around the 25-meter mark. The In-phase contours show no sign of the suspected fissure, however they do show a slight increase in magnetic susceptibility over the whole area, from line 1 to line 13.

The conductivity graphs for Grid 2 show some spikes that may correlate to fissures, as depicted in the plot for line one. Other graphs, such as line 12 and 13 show no recognizable signs of fissures. Any spikes that are seen on a graph are not repeated for the same point at different orientations and dipoles, unlike the known fissure for Grid 1. It is important to note that the operators were having difficulty with the instrument during data collection in Grid 2. Possible causes of this could be heat drift outlined in the paper Minimizing Drift in Electrical Conductivity Measurements in High Temperature Environments using the EM38 by Robertson et al., 2004. The same type of pattern is evident in the magnetic susceptibility graphs. The graphs for conductivity and susceptibility do not correlate with each other. The contour lines for Grid 2 show no significant anomalies that could be linked to a fissure. There are a few local anomalies at the 25-meter mark, perpendicular, in-phase, vertical being an example of this. The In-phase contours show a slight increase in magnetic susceptibility over the whole area, from line 1 to line 4, similar to Grid one.

The desiccation crack graphs show strong anomalies around the 25-meter point. For the conductivity graphs, the anomalies increased steeply over the fissures, and for the magnetic susceptibility they decreased when the instrument was in horizontal mode, and increased when the instrument was in vertical dipole mode. The contour plots show a strong anomaly across where it is believed the desiccation cracks are located. This anomaly was observed for both the conductivity and magnetic susceptibility graphs. The conductivity contours increase over the 25-meter mark, while the magnetic susceptibility increases in the vertical dipole orientation and decreases in the horizontal dipole over the same location.

5.5 Interpretation

Fissures and desiccation cracks may collect water when it rains. This water may then precipitate minerals, which have higher conductivity compared to the surrounding soil. This may explain the observed positive anomalies in the conductivity graphs and some negative anomalies in the magnetic susceptibility graphs for Grid 1. The fissure is visible at the surface in several places within the grid, therefore it is possible to correlate its position to the observed anomalies.

Along the desiccation cracks, we can see a strong anomaly where we believe the crack exists. However, the crack is also on a road, and consideration must be given to the possibility that the instrument may be detecting channeled water runoff along the road.

In Grid 2, the fissure is not visible, and there are no repeatable anomalies on the graph. This could be an indication that the relatively wide subsurface fissure has already stopped before this point. Very small fractures may not be detectable by the EM38.

5.6 Cultural Interference

Due to the EM38's primary use as a close-range instrument, it did not show significant change in signal by being in close proximity to the power lines. There is an extremely large increase in the vertical dipole measurements at 0 meters, which is due to the nearby fence. Only when the instrument was brought within 1.5 meters of the fence could the operators of the EM38 notice any effect, again due to the instrument's small field and space-limited range of operation. Tests across the seismic line show higher measured values than other lines, probably due to the interference of the fence. There is no sign of a fissure across this section. The fissure was underground across the seismic line, same as Grid 2.

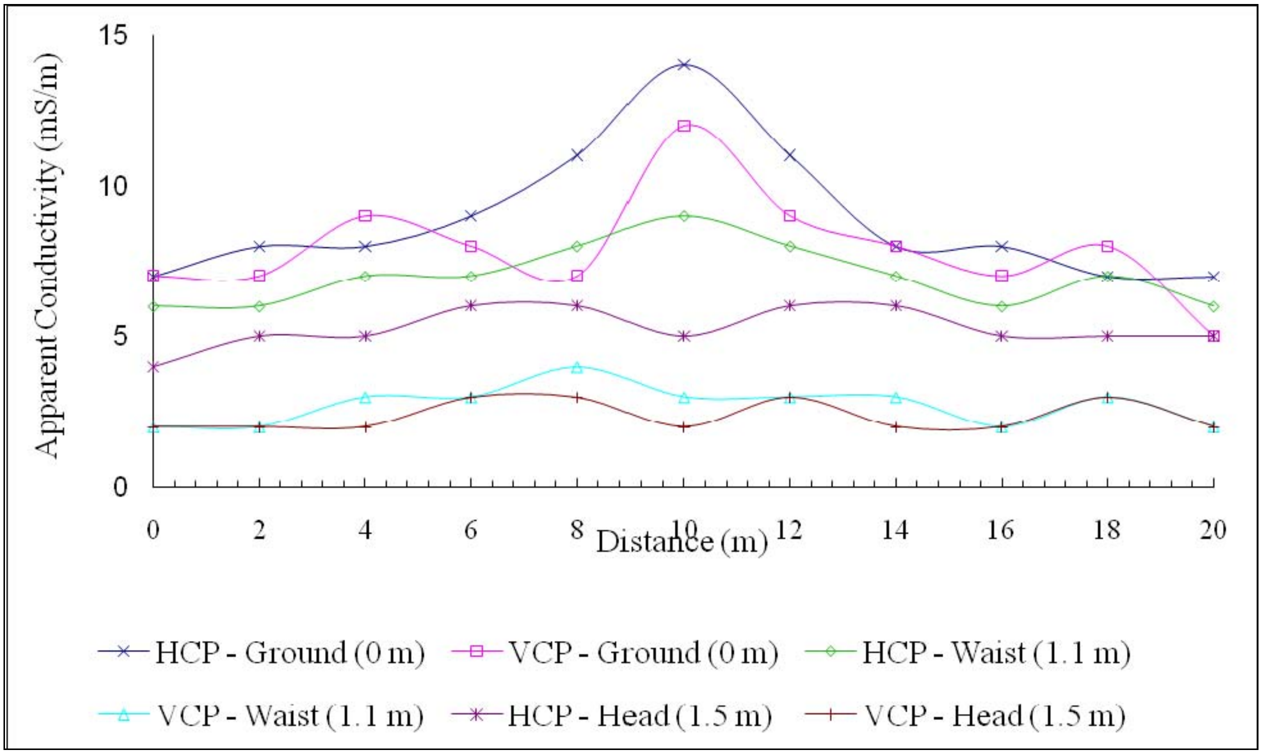

Figure 5.1 – Initial test lines, Ground Conductivity (Quad-phase), Parallel to Line

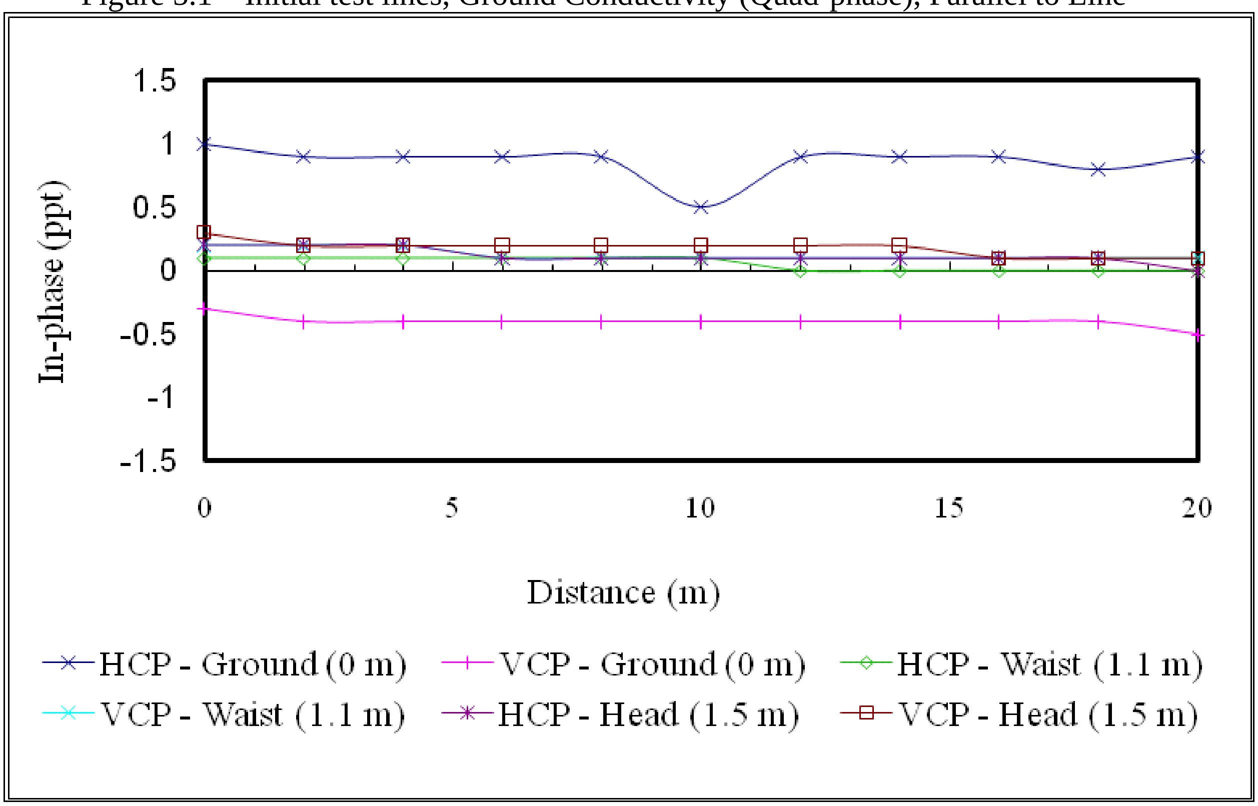

Figure 5.2 – Initial test Lines, Magnetic Susceptibility (In-phase), Parallel to Line

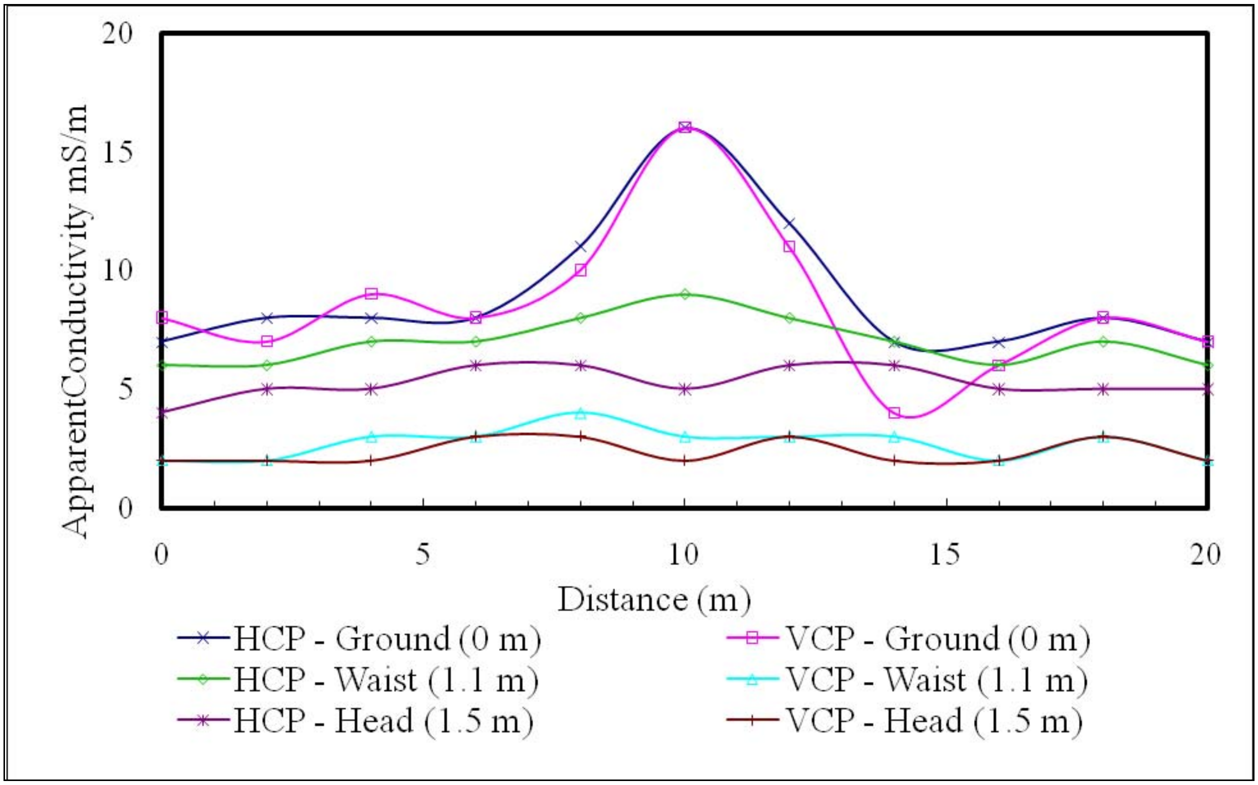

Figure 5.3 – Initial test lines, Ground Conductivity (Quad-phase), Perpendicular to Line

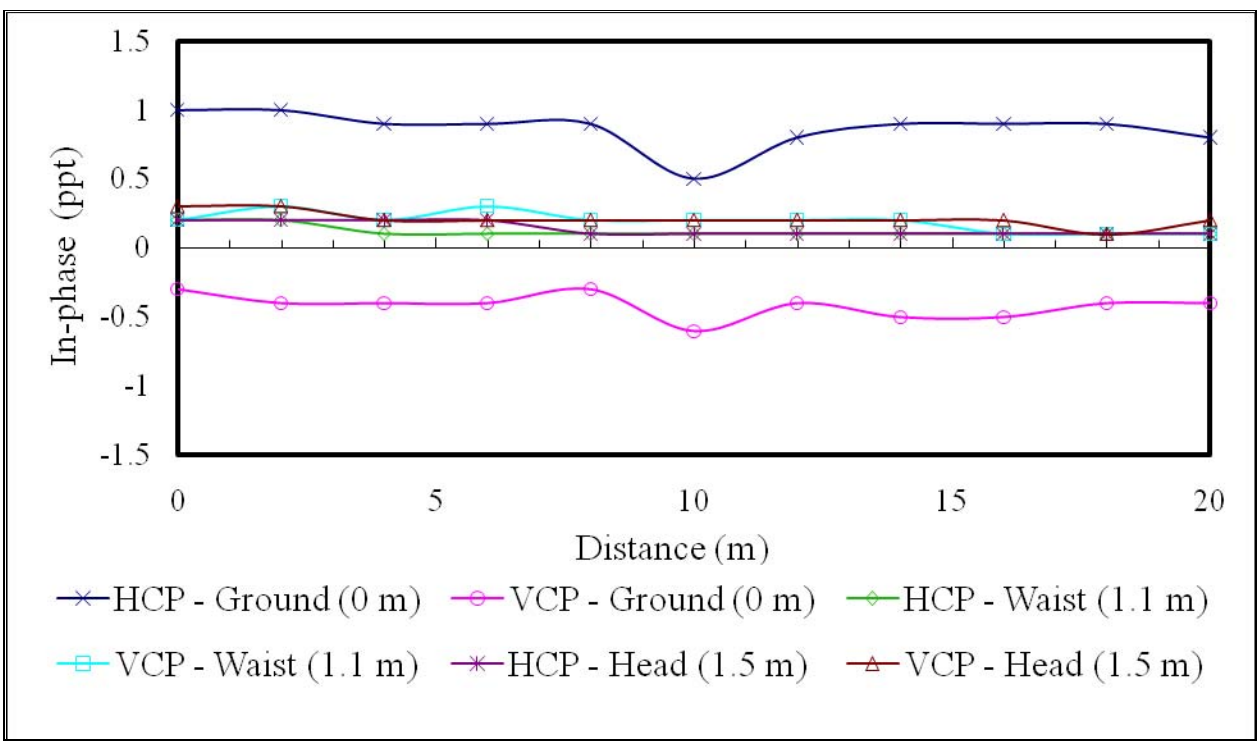

Figure 5.4 – Initial test lines, Magnetic Susceptibility (In-phase), Perpendicular to Line

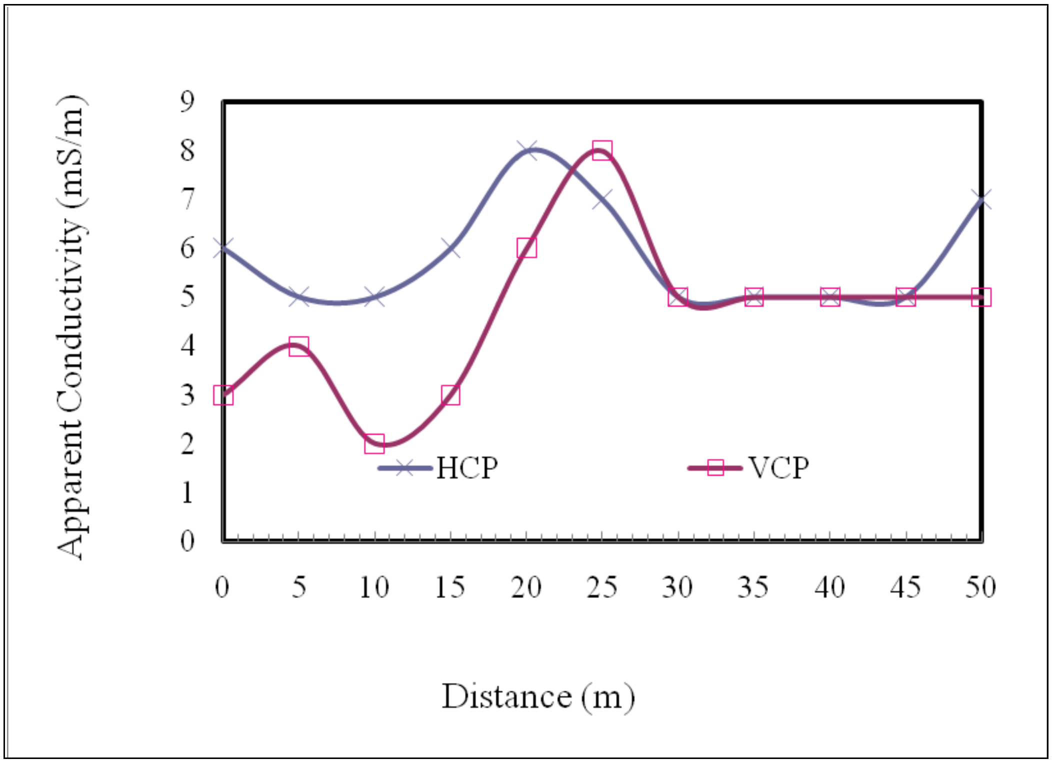

Figure 5.5 - Grid 1 Line 1 (0m), Ground Conductivity (Quad-phase), Perpendicular to Line

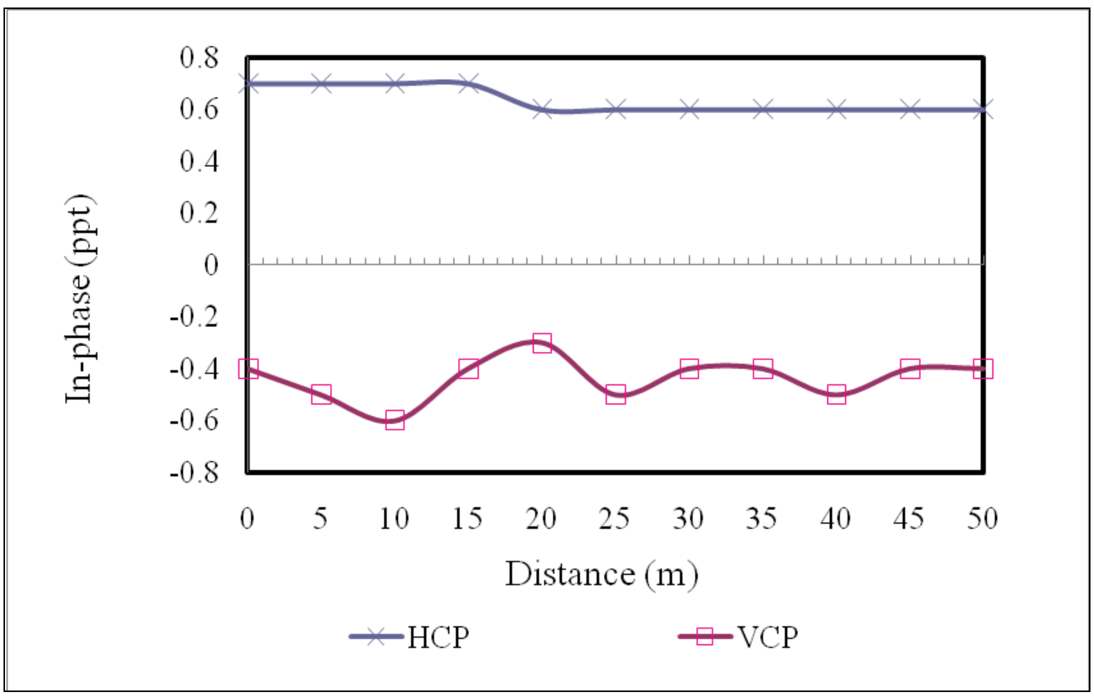

Figure 5.6 - Grid 1 Line 1 (0m), Magnetic Susceptibility (In-phase), Perpendicular to L

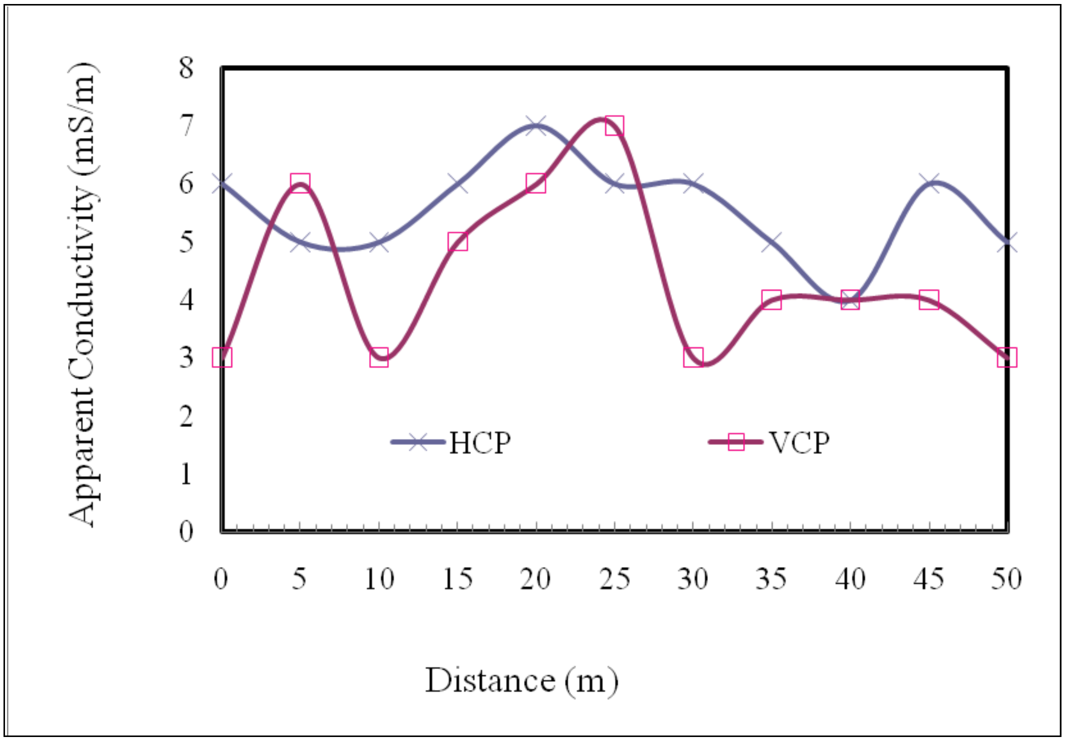

Figure 5.7 - Grid 1 Line 1 (0m), Ground Conductivity (Quad-phase), Parallel to Line

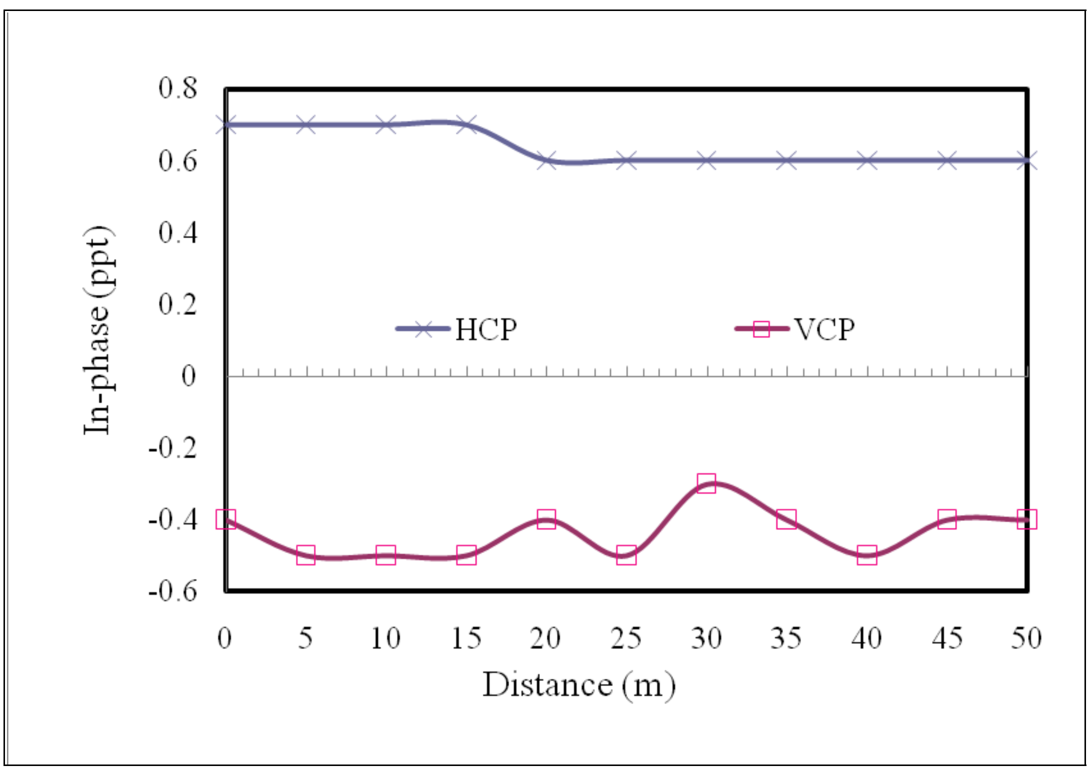

Figure 5.8 - Grid 1 Line 1 (0m), Magnetic Susceptibility (In-phase), Parallel to Line

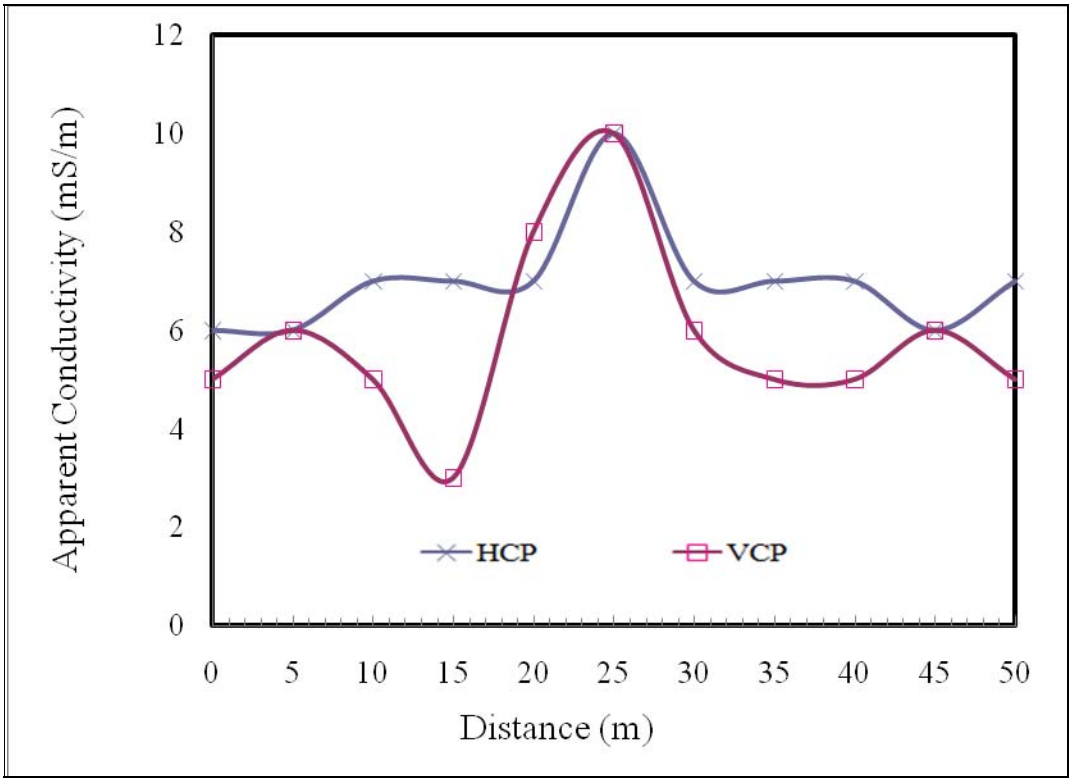

Figure 5.9 - Grid 1 Line 3 (10m), Ground Conductivity (Quad-phase), Perpendicular to Line

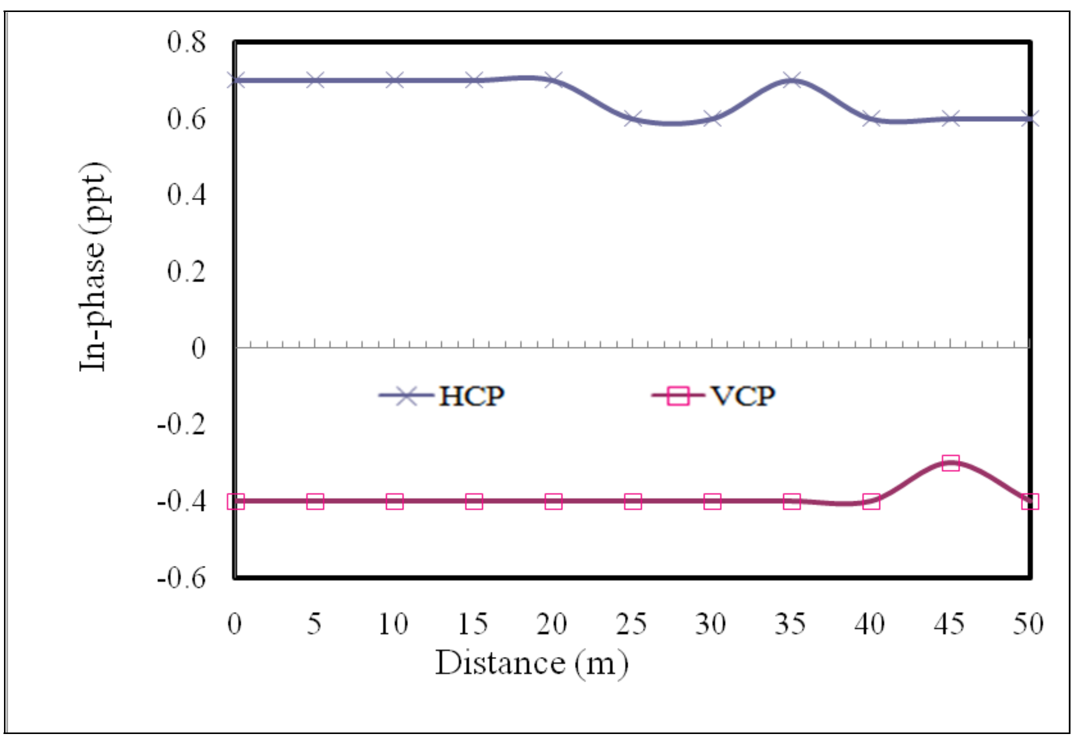

Figure 5.10 - Grid 1 Line 3 (10m), Magnetic Susceptibility (In-phase), Perpendicular to Line

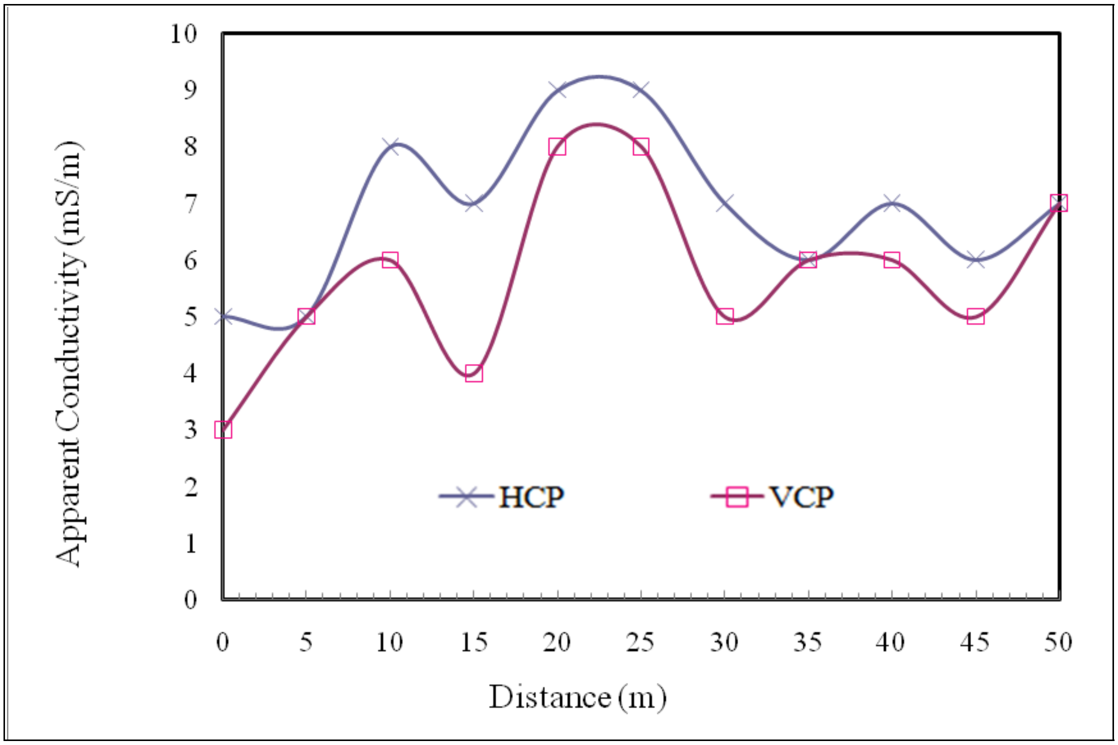

Figure 5.11 - Grid 1 Line 3 (10m), Ground Conductivity (Quad-phase), Parallel to Line

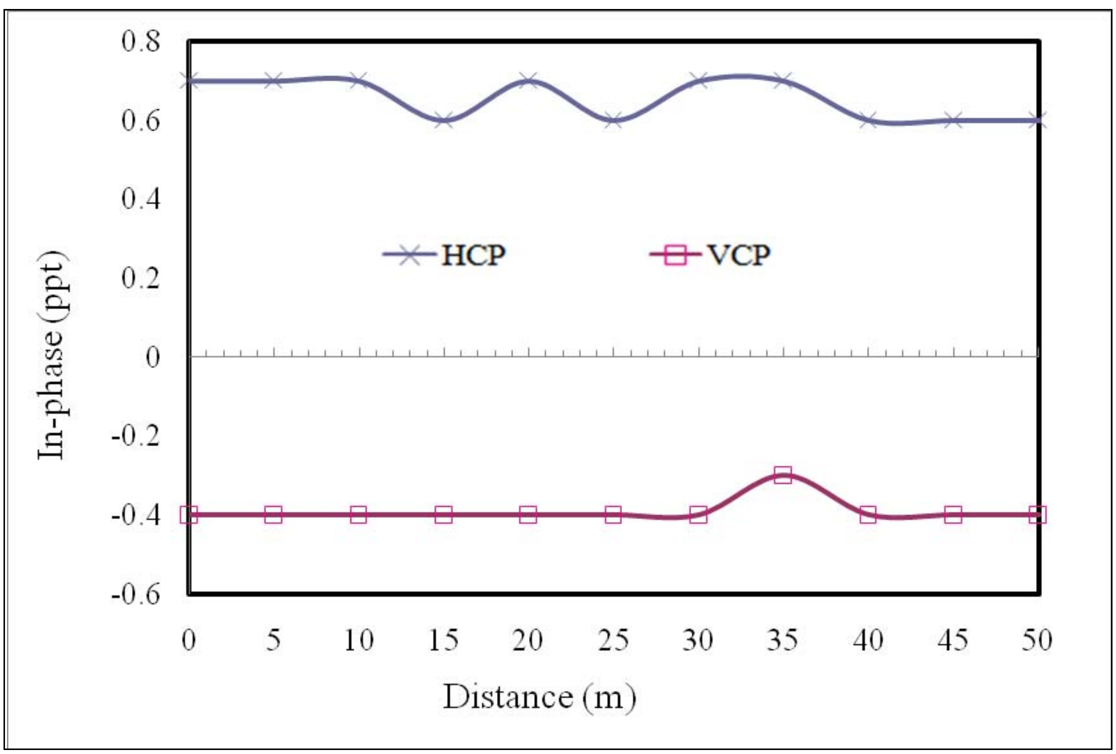

Figure 5.12 - Grid 1 Line 3 (10m), Magnetic Susceptibility (In-phase), Parallel to Line

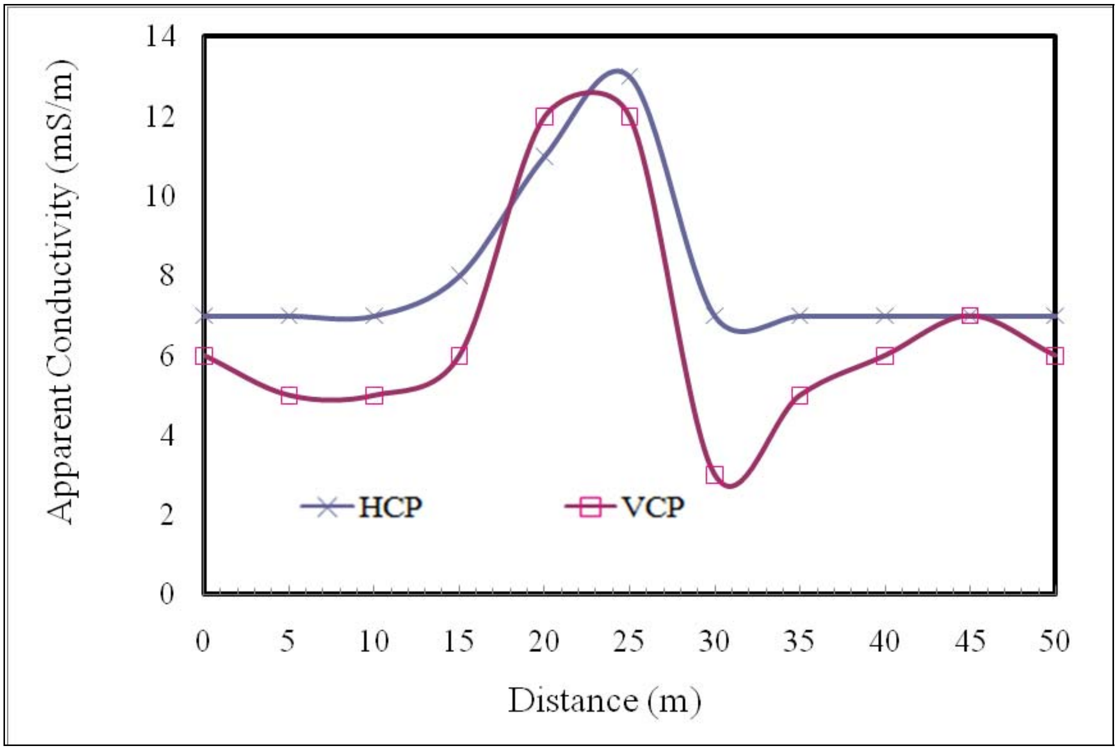

Figure 5.13 - Grid 1 Line 5 (20m), Ground Conductivity (Quad-phase), Perpendicular to Line

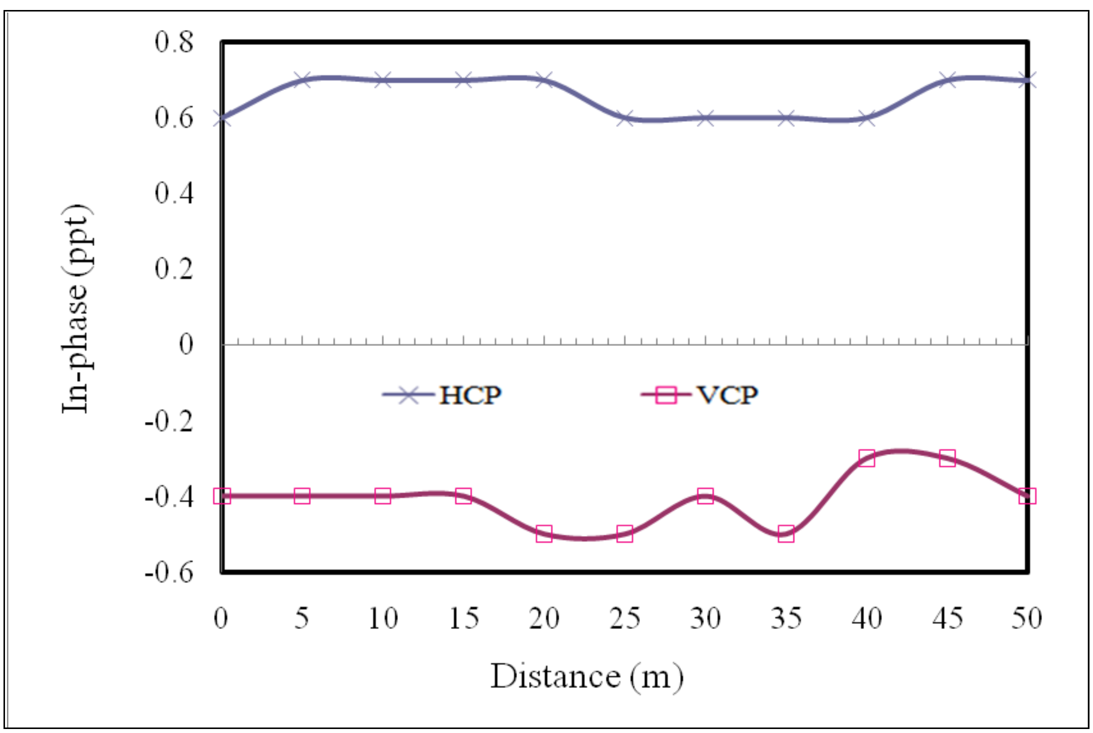

Figure 5.14 - Grid 1 Line 5 (20m), Magnetic Susceptibility (In-phase), Perpendicular to Line

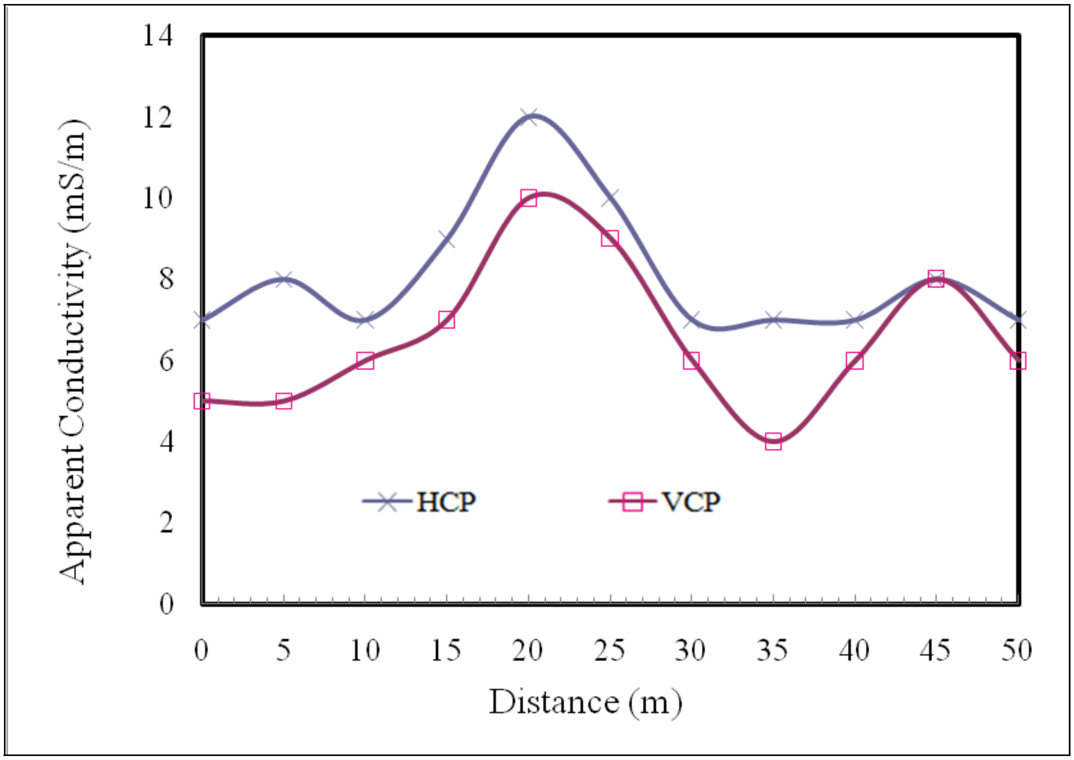

Figure 5.15 - Grid 1 Line 5 (20m), Ground Conductivity (Quad-phase), Parallel to Line

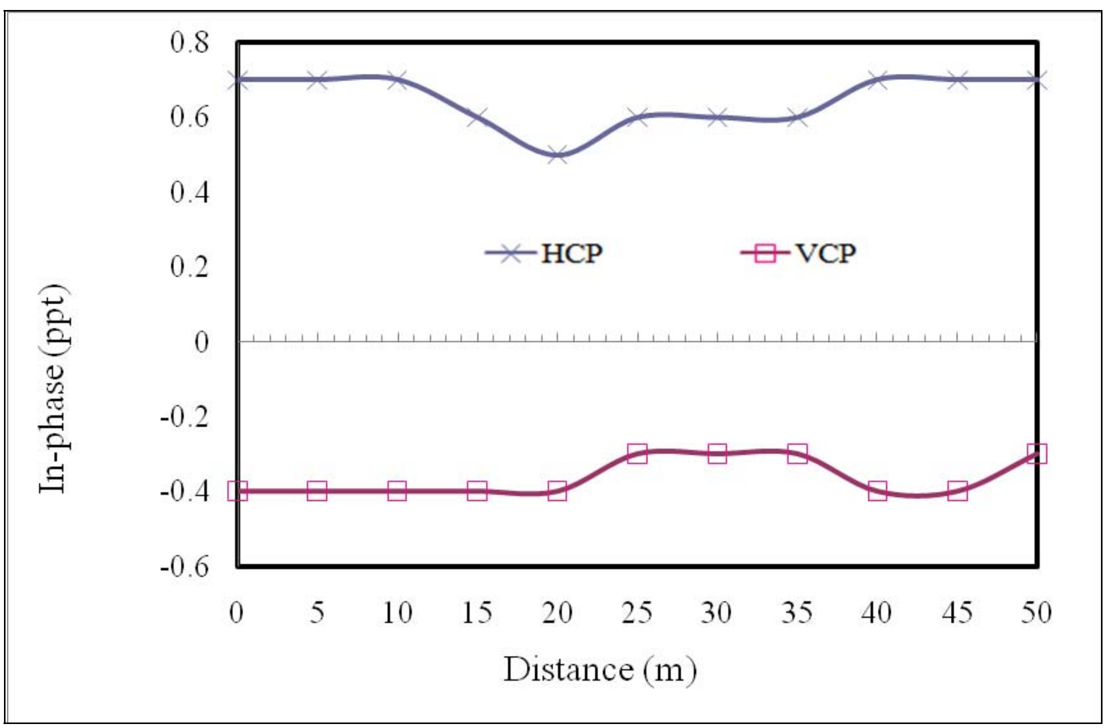

Figure 5.16 - Grid 1 Line 5 (20m), Magnetic Susceptibility (In-phase), Parallel to Line

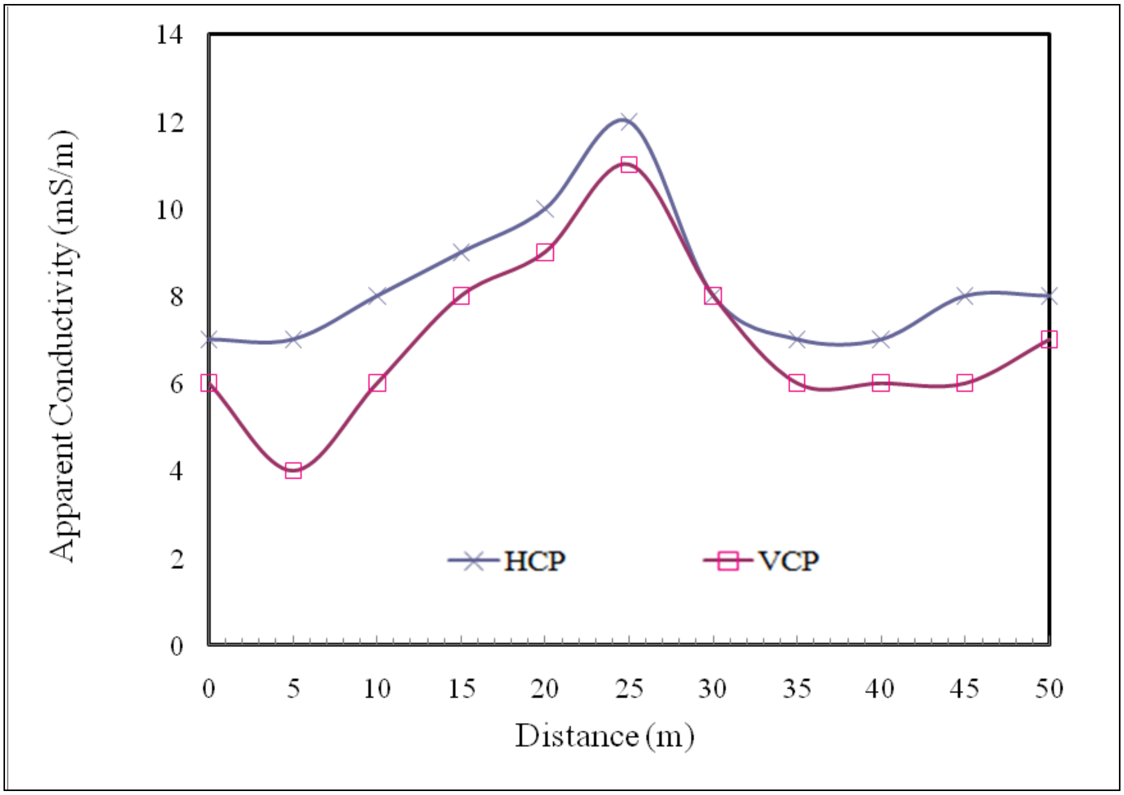

Figure 5.17 - Grid 1 Line 7 (30m), Ground Conductivity (Quad-phase), Perpendicular to Line

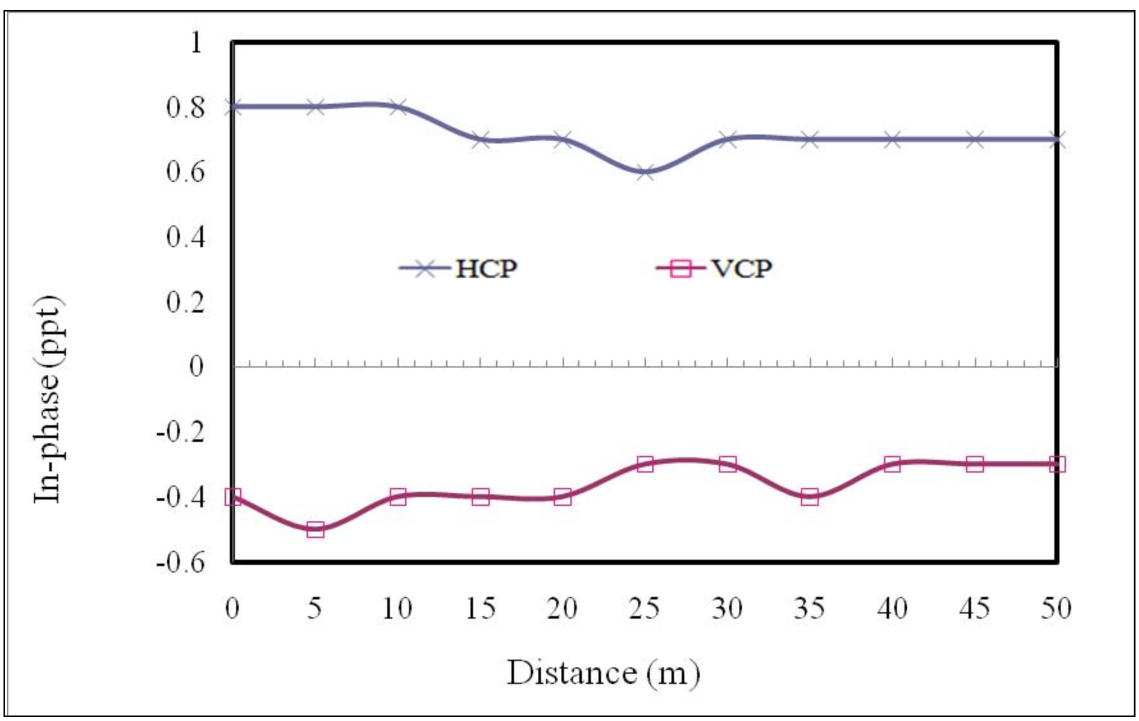

Figure 5.18 - Grid 1 Line 7 (30m), Magnetic Susceptibility (In-phase), Perpendicular to Line

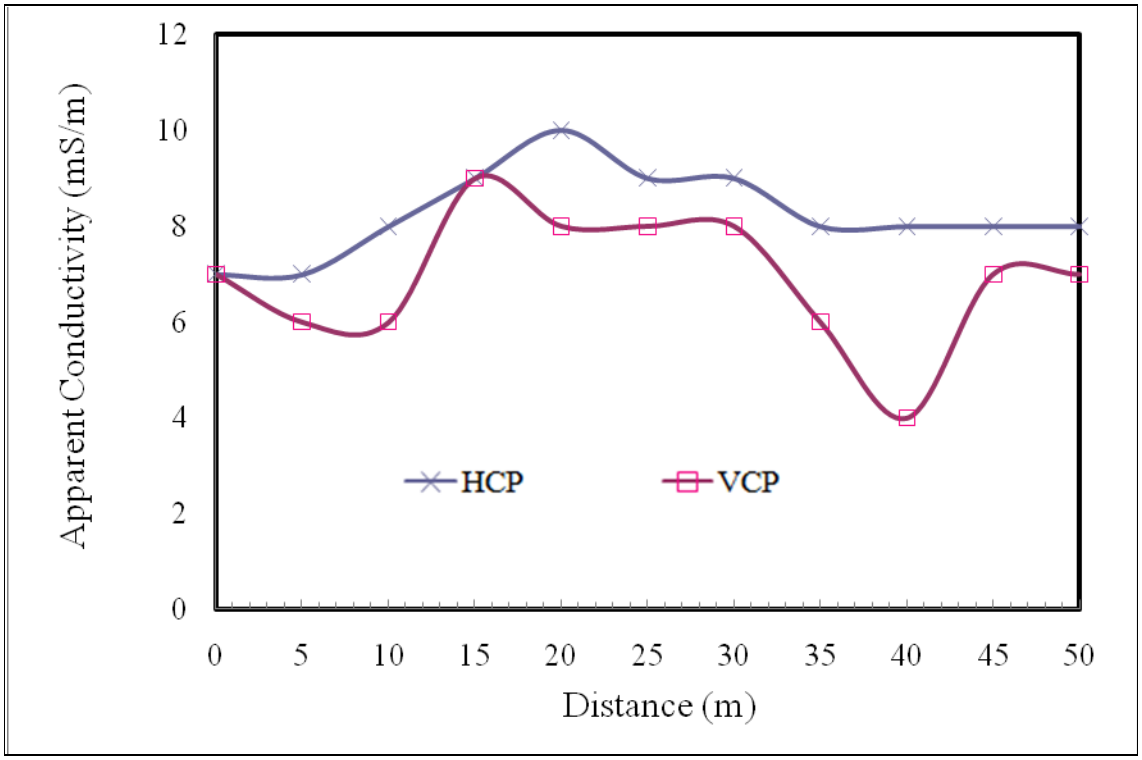

Figure 5.19 - Grid 1 Line 7 (30m), Ground Conductivity (Quad-phase), Parallel to Line

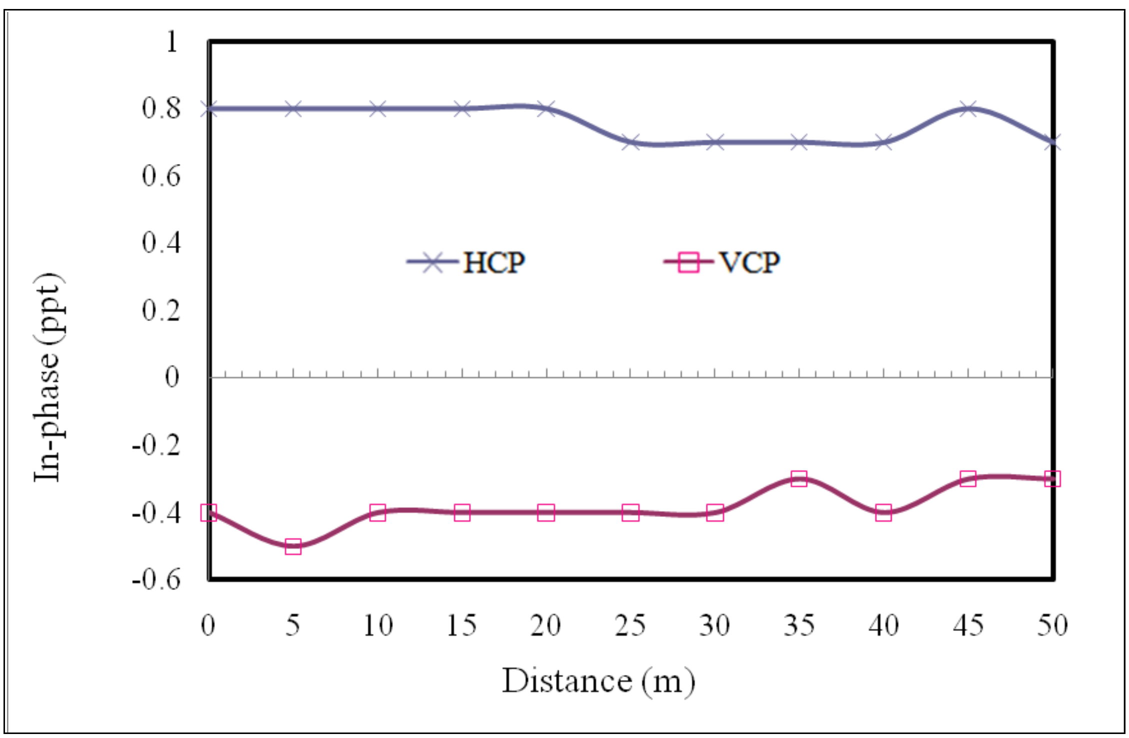

Figure 5.20 - Grid 1 Line 7 (30m), Magnetic Susceptibility (In-phase), Parallel to Line

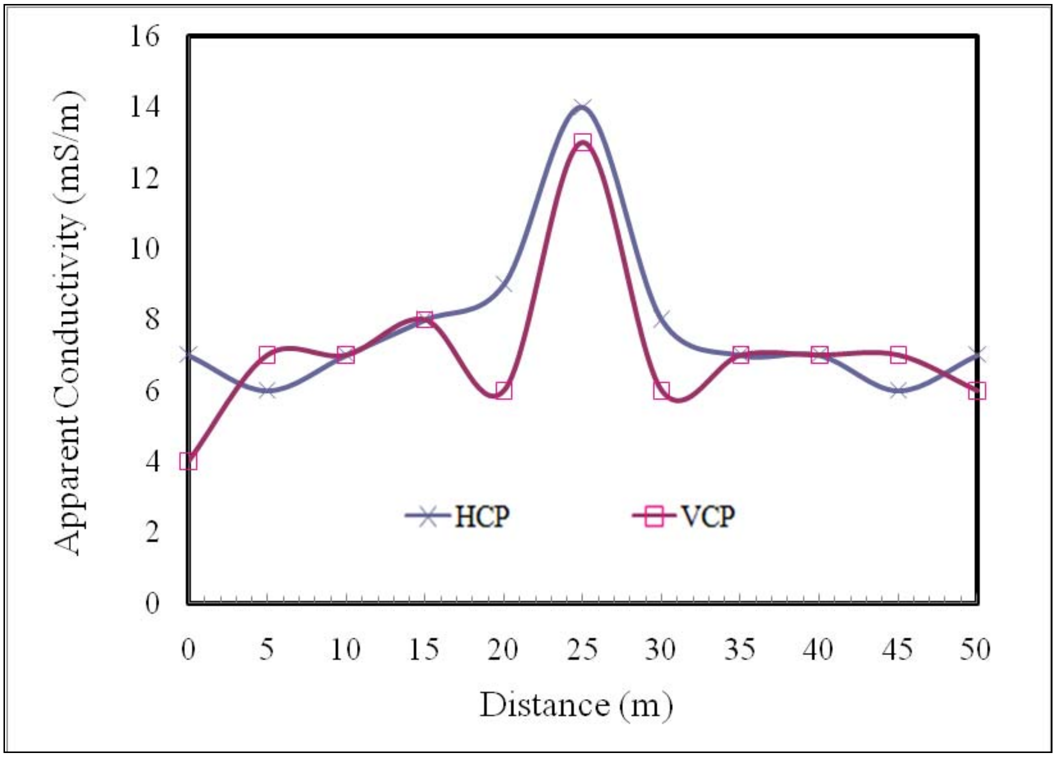

Figure 5.21 - Grid 1 Line 9 (40m), Ground Conductivity (Quad-phase), Perpendicular to Line

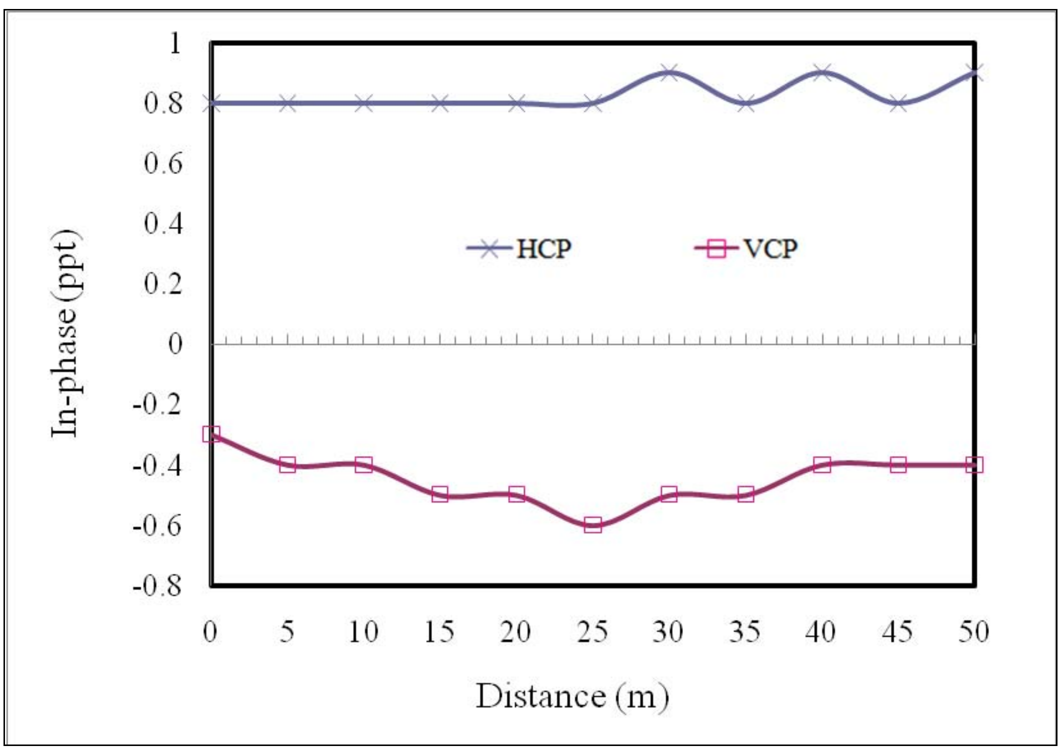

Figure 5.22 - Grid 1 Line 9 (40m), Magnetic Susceptibility (In-phase), Perpendicular to Line

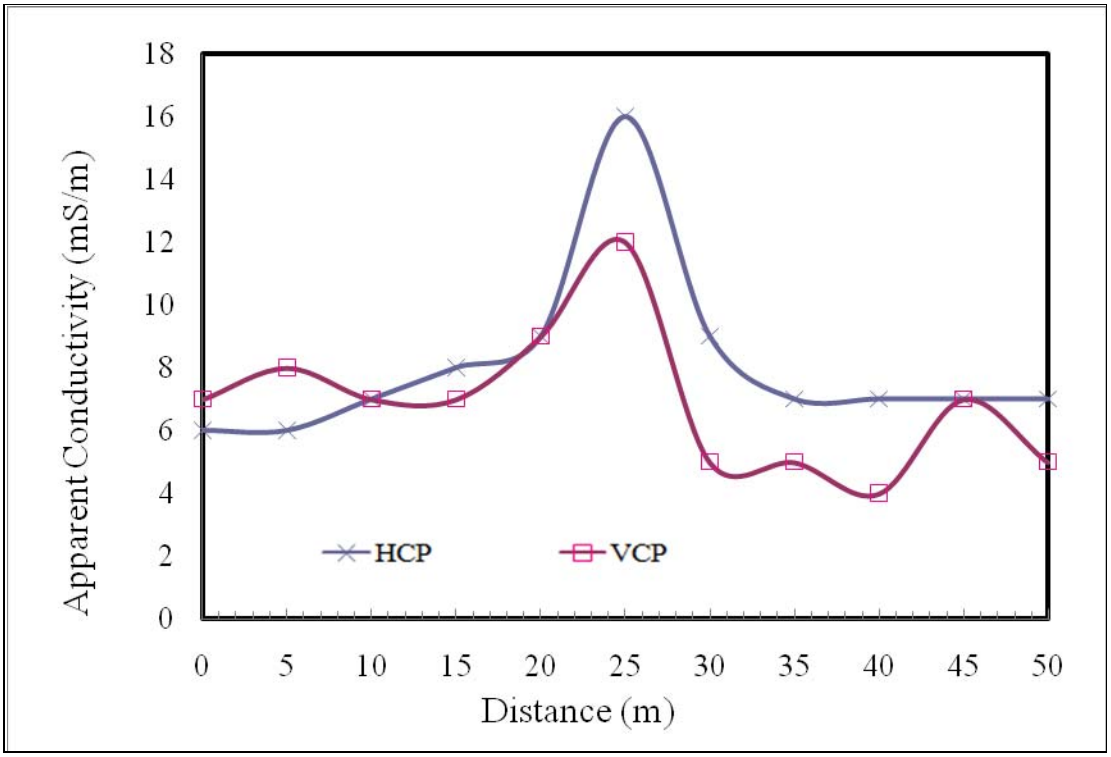

Figure 5.23 - Grid 1 Line 9 (40m), Ground Conductivity (Quad-phase), Parallel to Line

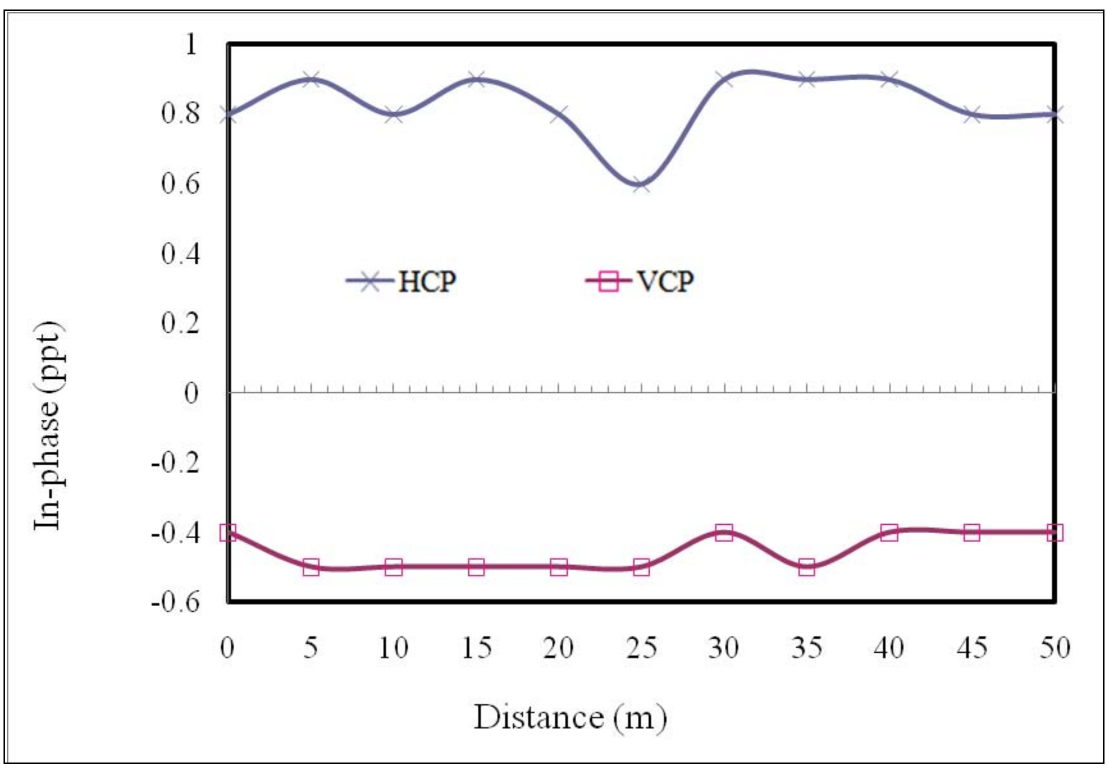

Figure 5.24 - Grid 1 Line 9 (40m), Magnetic Susceptibility (In-phase), Parallel to Line

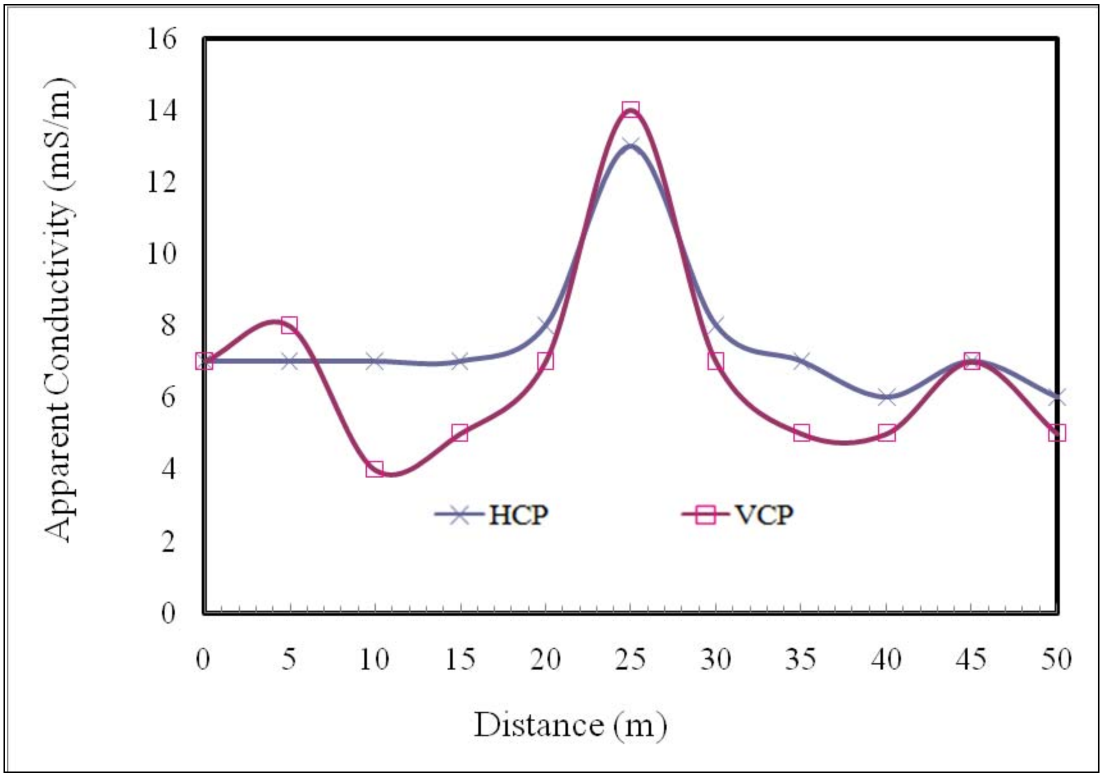

Figure 5.25 - Grid 1 Line 11 (50m), Ground Conductivity (Quad-phase), Perpendicular to Line

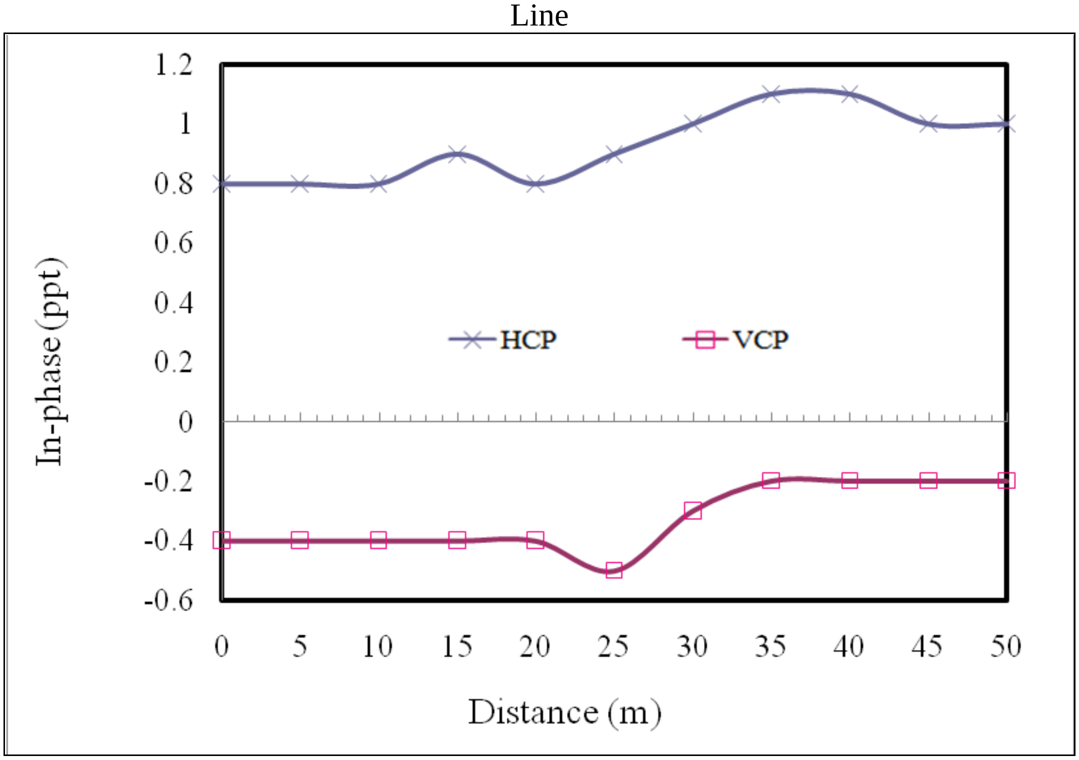

Figure 5.26 - Grid 1 Line 11 (50m), Magnetic Susceptibility (In-phase), Perpendicular to Line

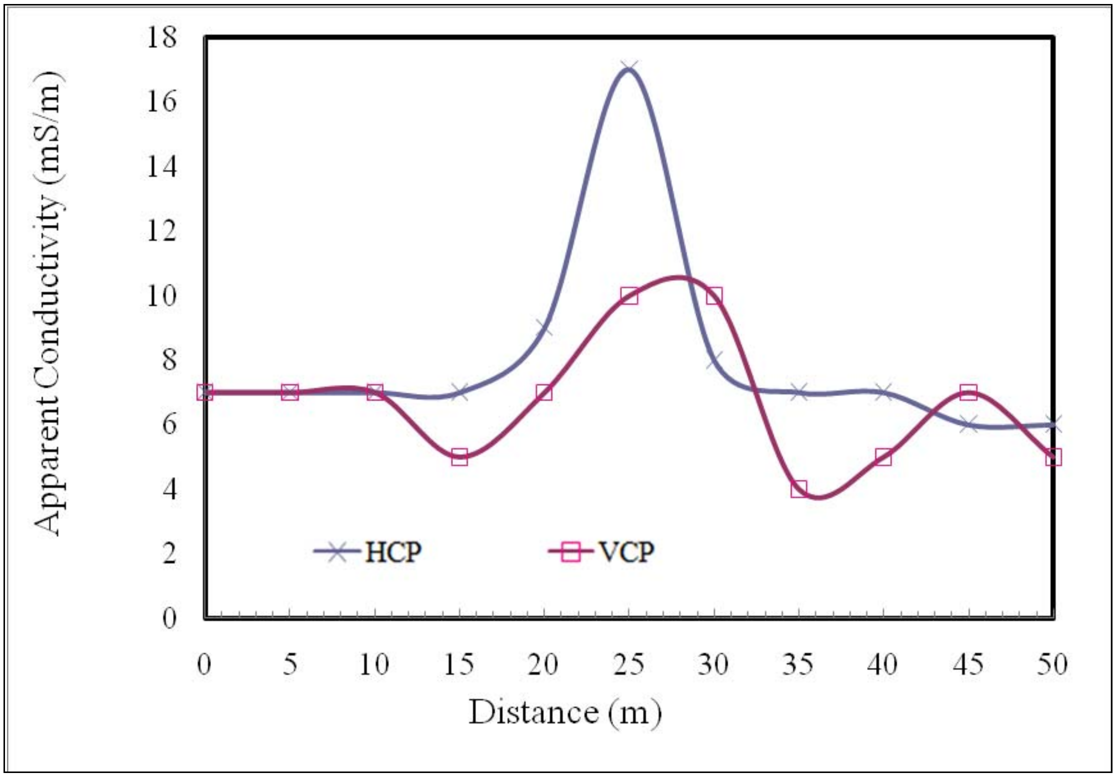

Figure 5.27 - Grid 1 Line 11 (50m), Ground Conductivity (Quad-phase), Parallel to Line

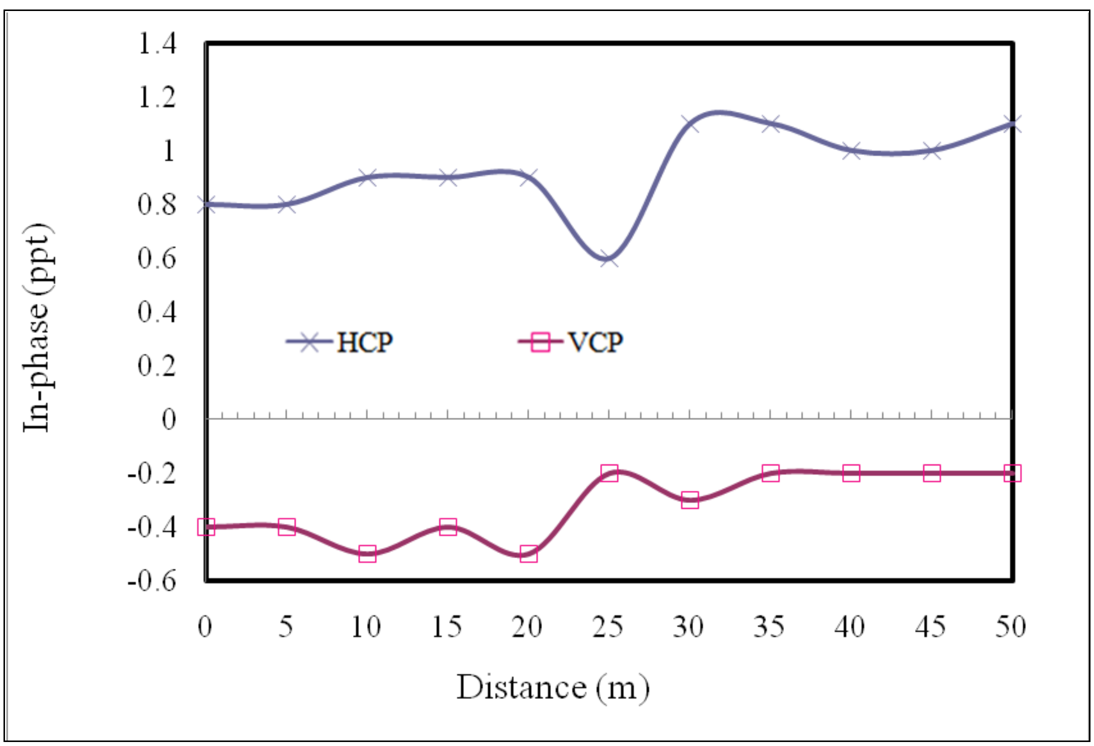

Figure 5.28 - Grid 1 Line 11 (50m), Magnetic Susceptibility (In-phase), Parallel to Line

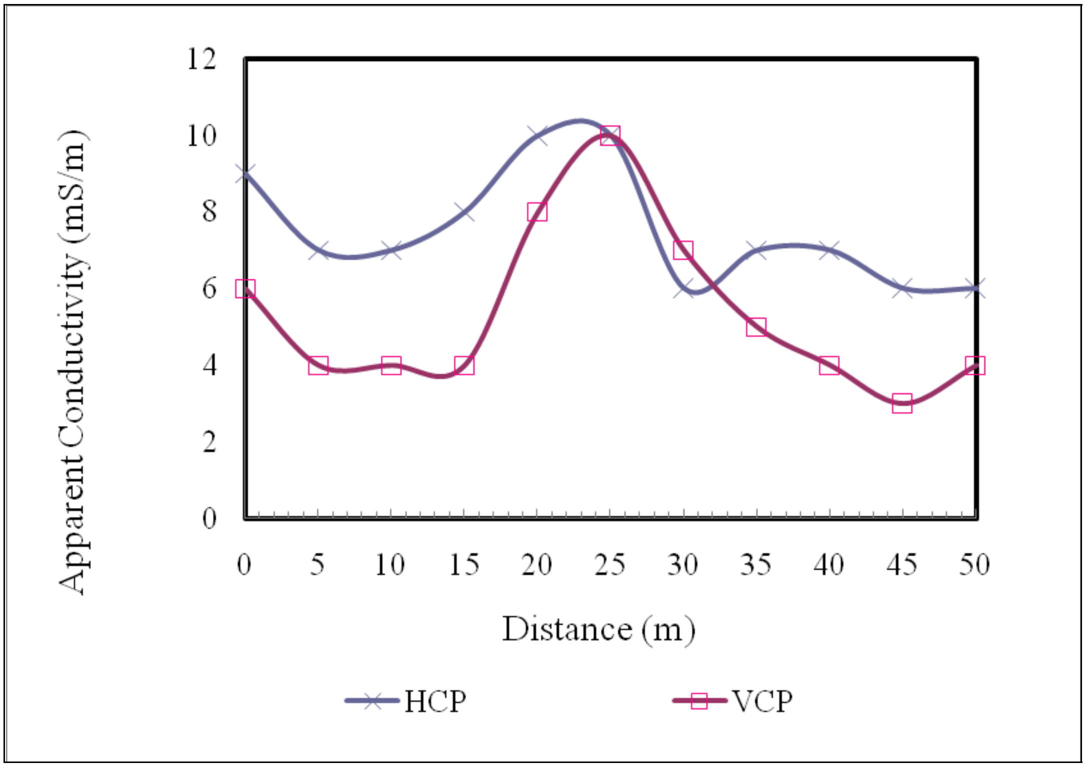

Figure 5.29 - Grid 1 Line 13 (60m), Ground Conductivity (Quad-phase), Perpendicular to Line

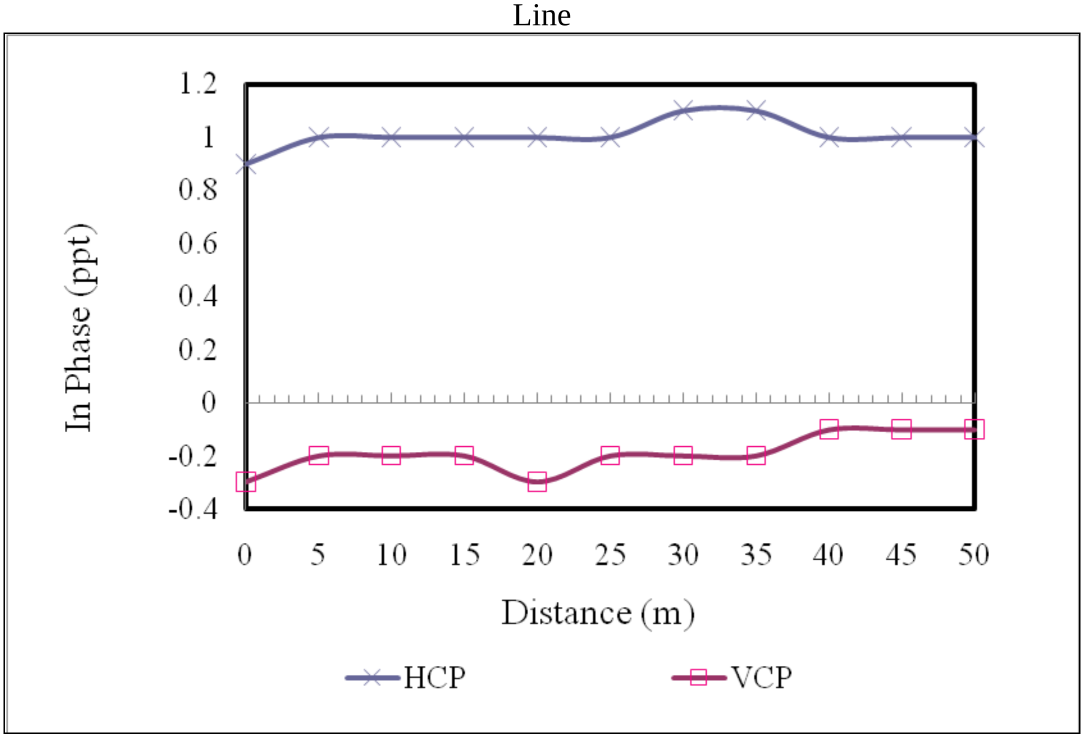

Figure 5.30 - Grid 1 Line 13 (60m), Magnetic Susceptibility (In-phase), Perpendicular to Line

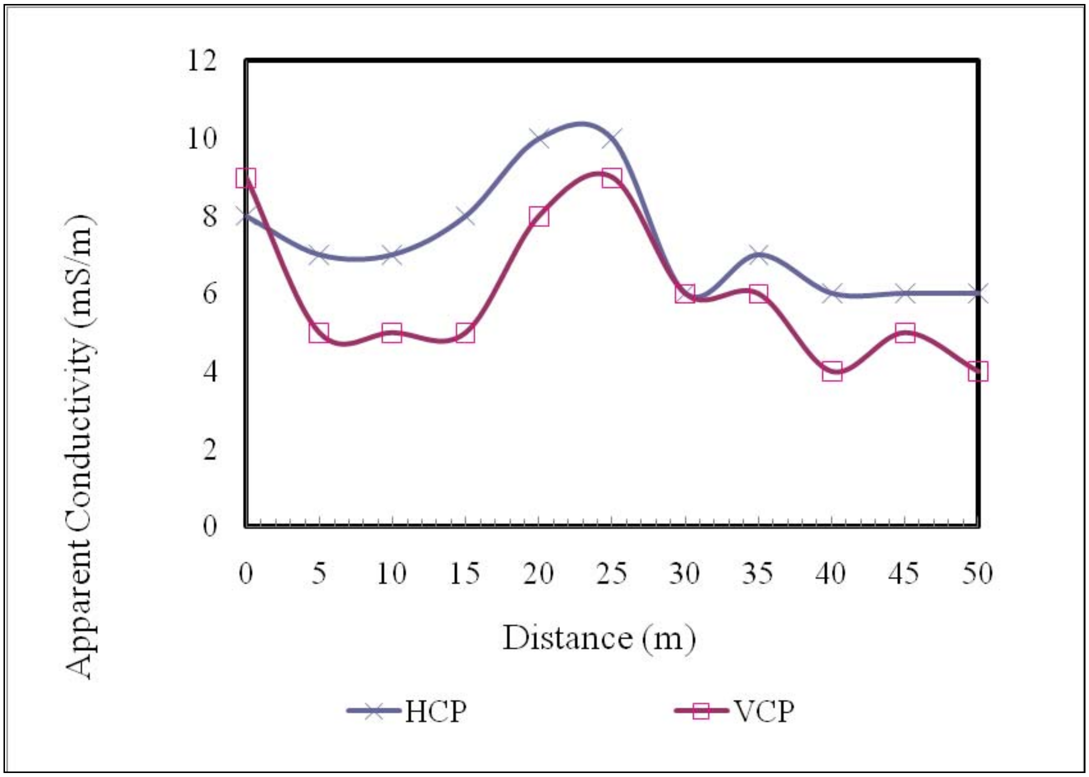

Figure 5.31 - Grid 1 Line 13 (60m), Ground Conductivity (Quad-phase), Parallel to Line

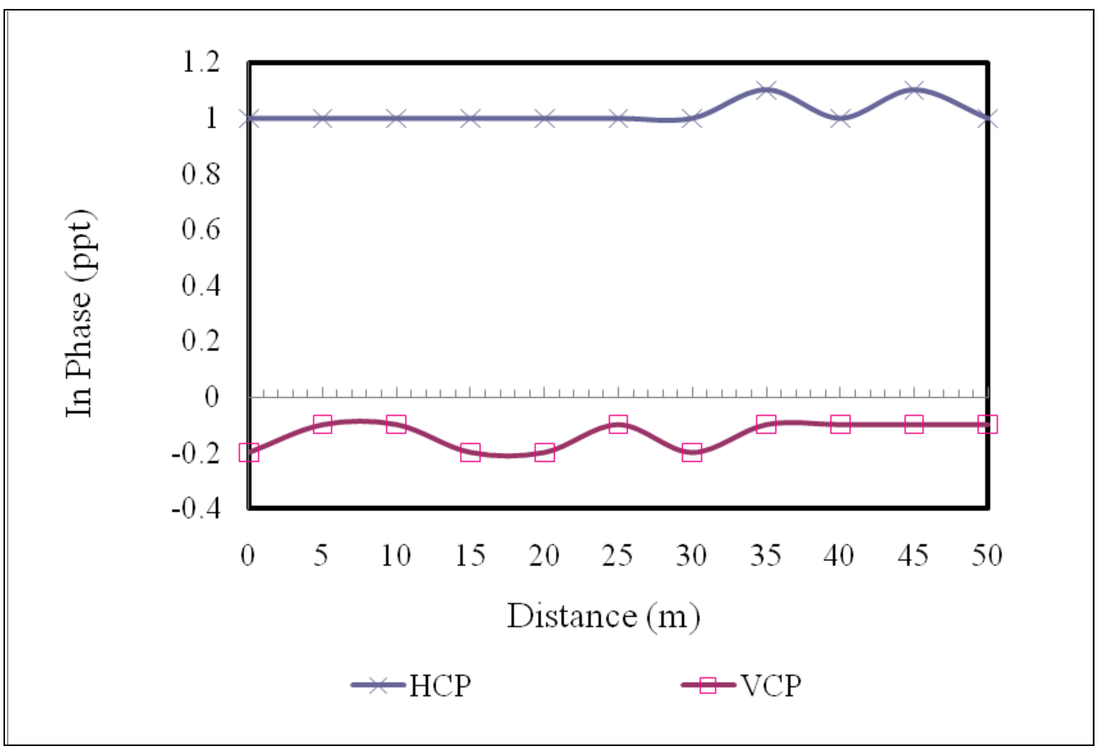

Figure 5.32 - Grid 1 Line 13 (60m), Magnetic Susceptibility (In-phase), Parallel to Line

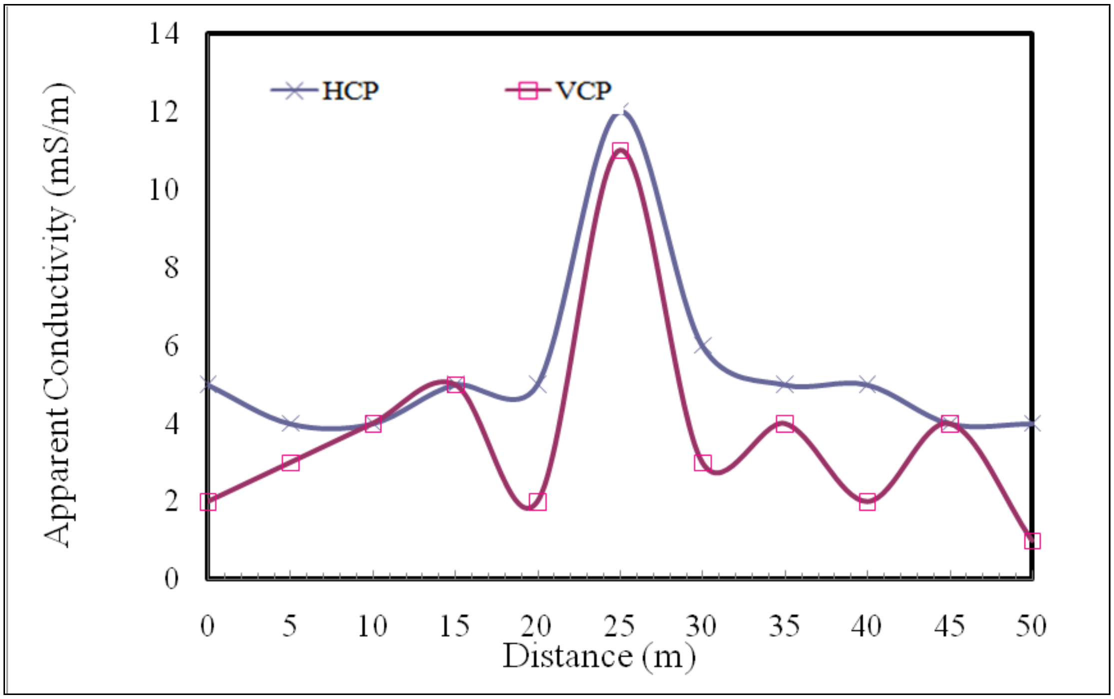

Figure 5.33 - Grid 1 Line 9 Repeat (40m), Ground Conductivity (Quad-phase), Perpendicular to Line

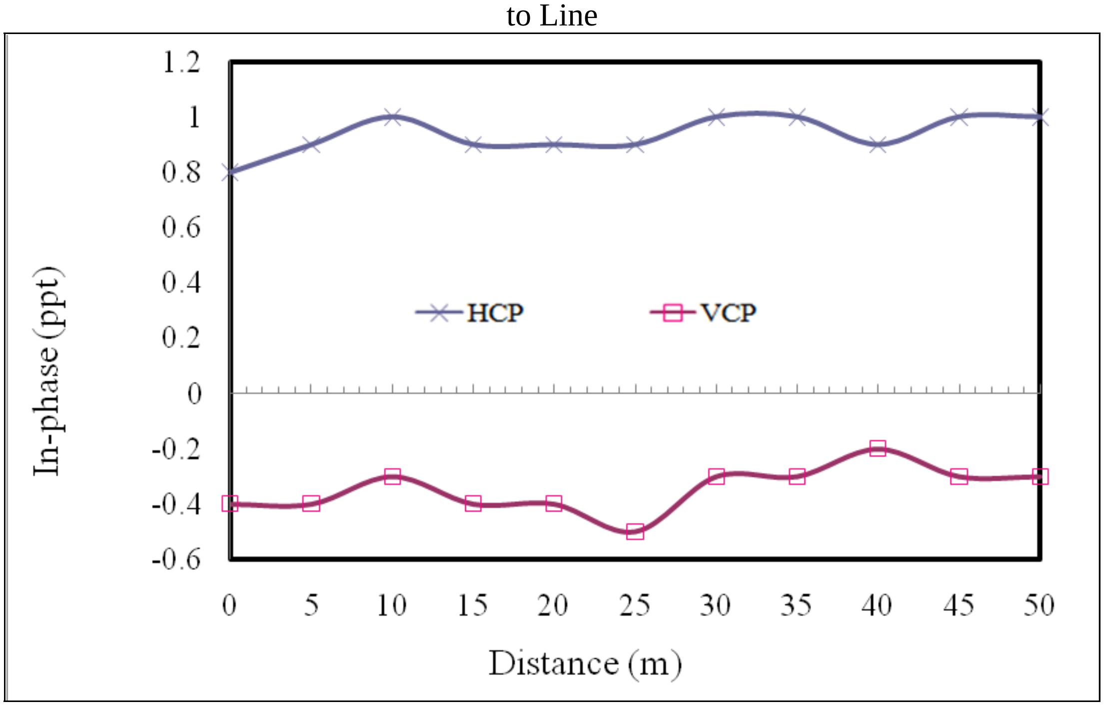

Figure 5.34 - Grid 1 Line 9 Repeat (40m), Magnetic Susceptibility (In-phase), Perpendicular to Line

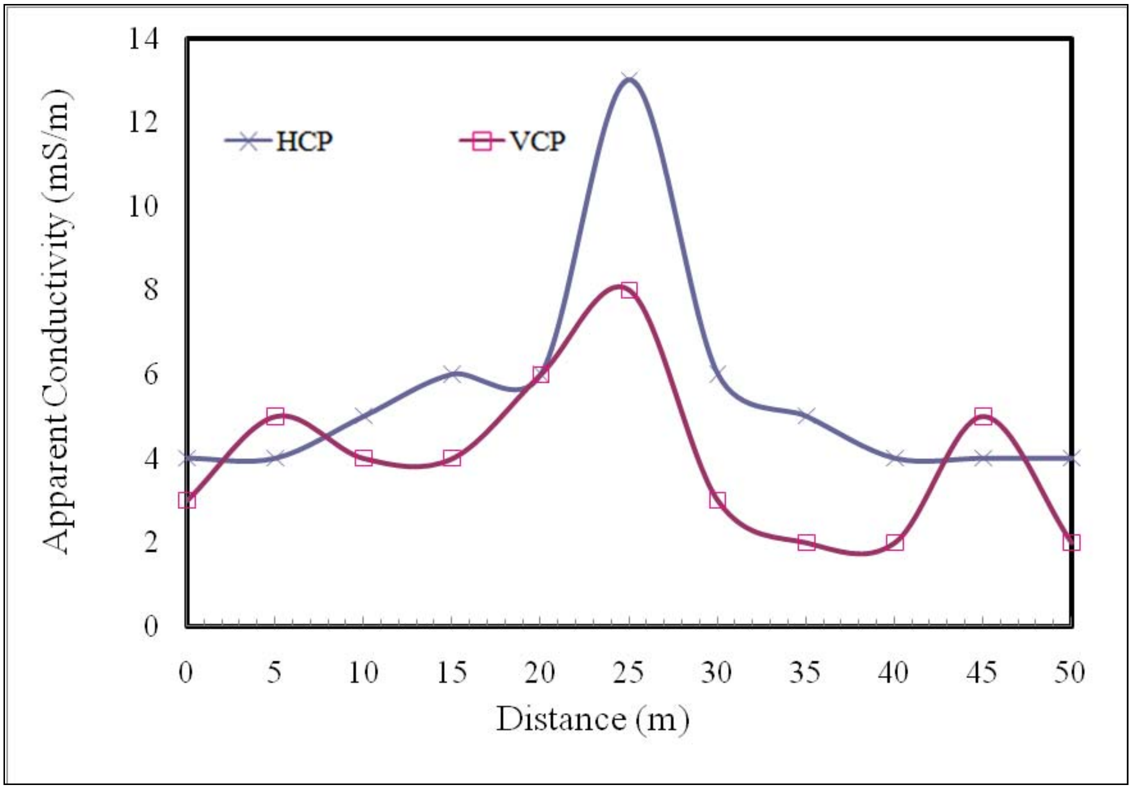

Figure 5.35 - Grid 1 Line 9 Repeat (40m), Ground Conductivity (Quad-phase), Parallel to Line

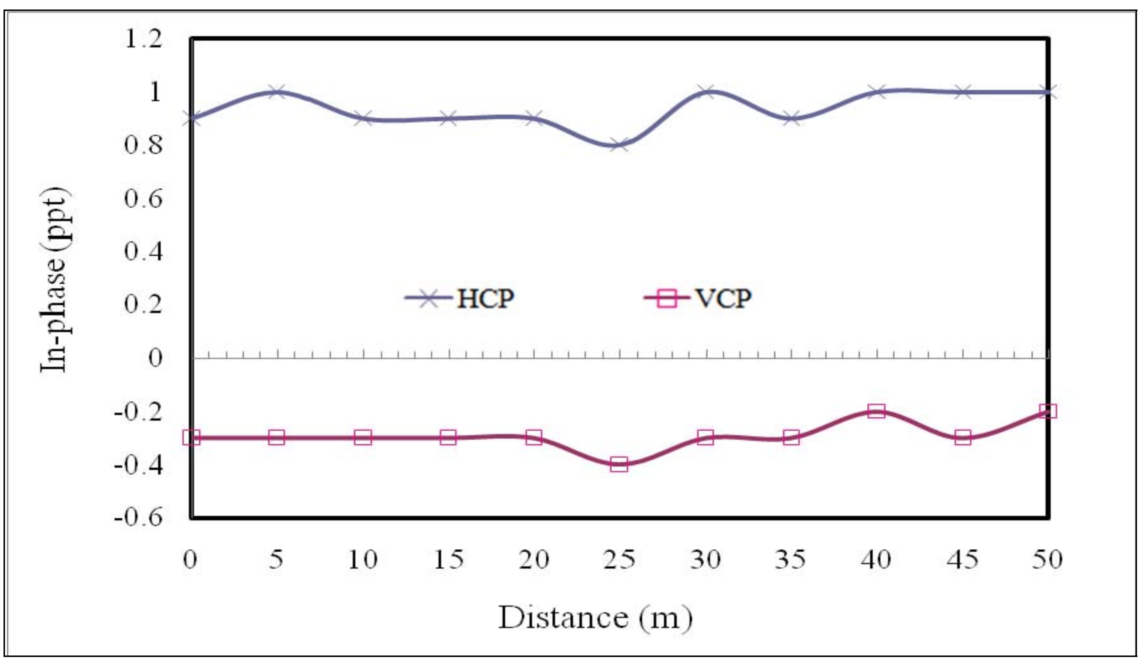

Figure 5.36 - Grid 1 Line 9 (40m), Magnetic Susceptibility (In-phase), Parallel to Line

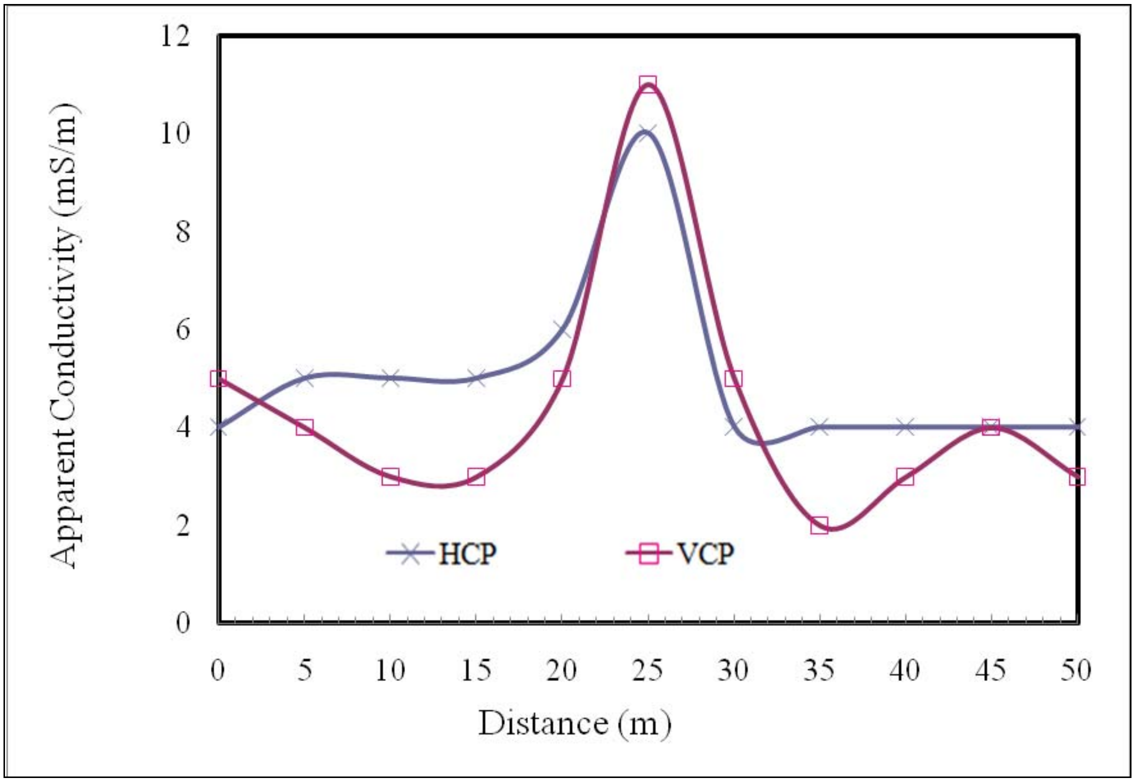

Figure 5.37 - Grid 1 Line11 Repeat (50m), Ground Conductivity (Quad-phase), Perpendicular to Line

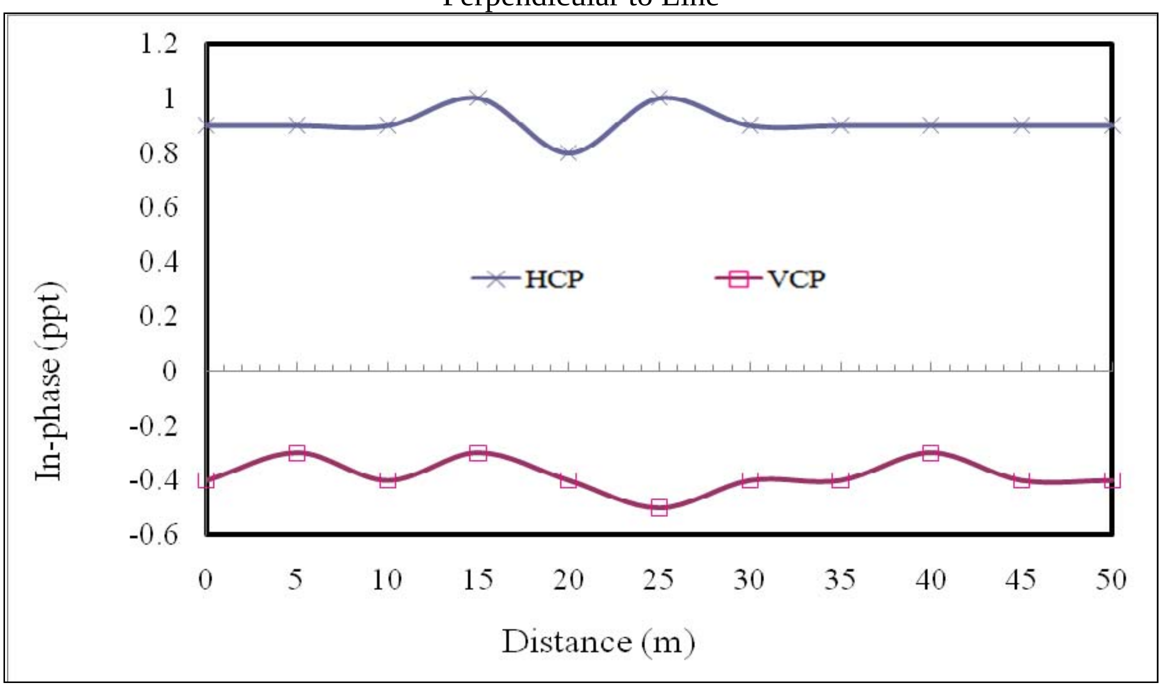

Figure 5.38 - Grid 1 Line11 Repeat (50m), Magnetic Susceptibility (In-phase), Perpendicular to Line

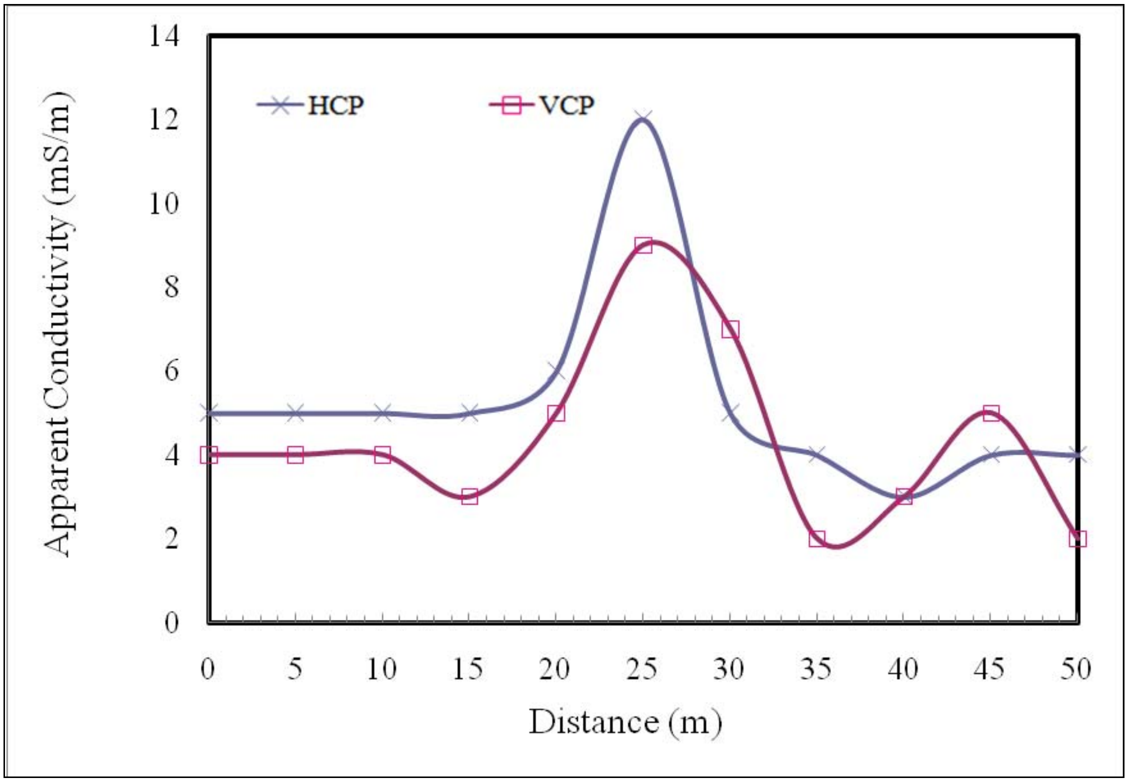

Figure 5.39 - Grid 1 Line 11 Repeat (50m), Ground Conductivity (Quad-phase), Parallel to Line

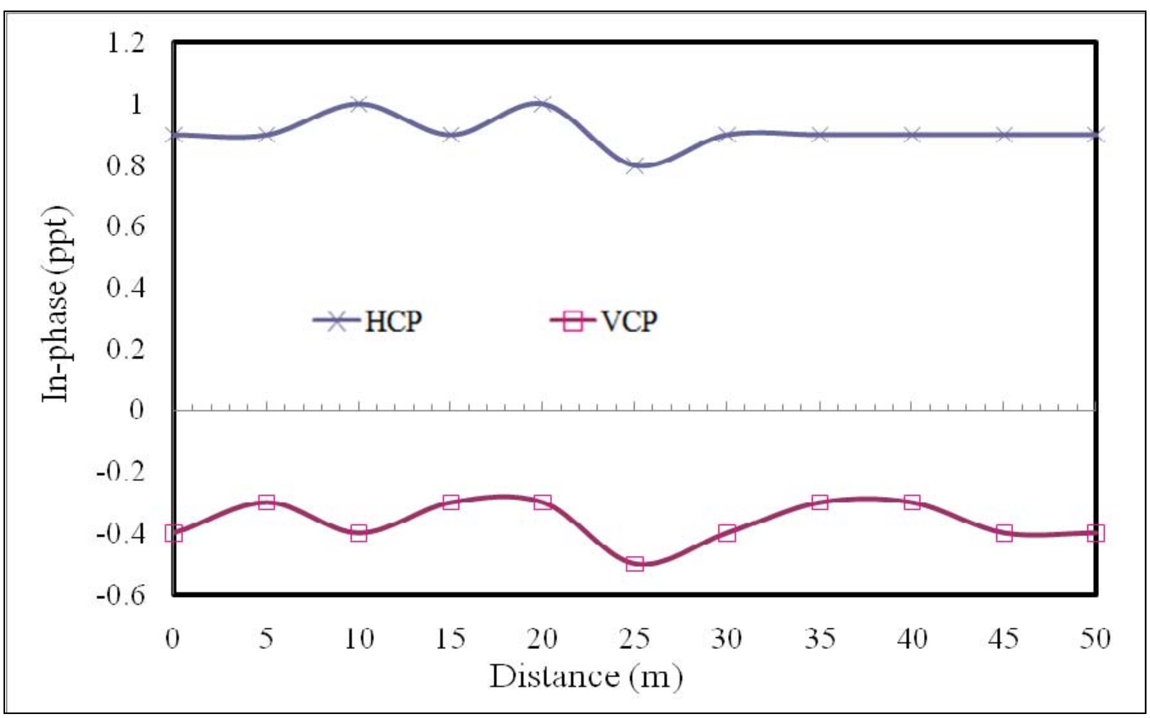

Figure 5.40 - Grid 1 Line 11 (50m), Magnetic Susceptibility (In-phase), Parallel to Line

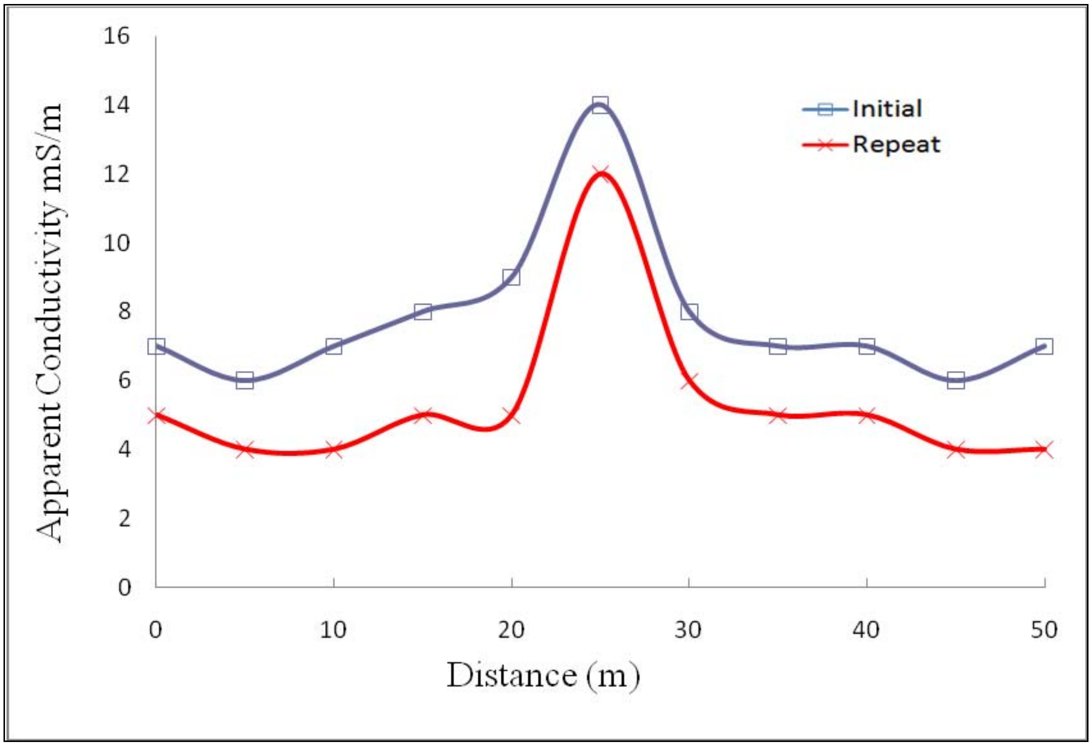

Figure 5.41 - Grid 1 Line 9 Repeats (40m), Ground Conductivity (Quad-phase), Perpendicular to Line, HCP

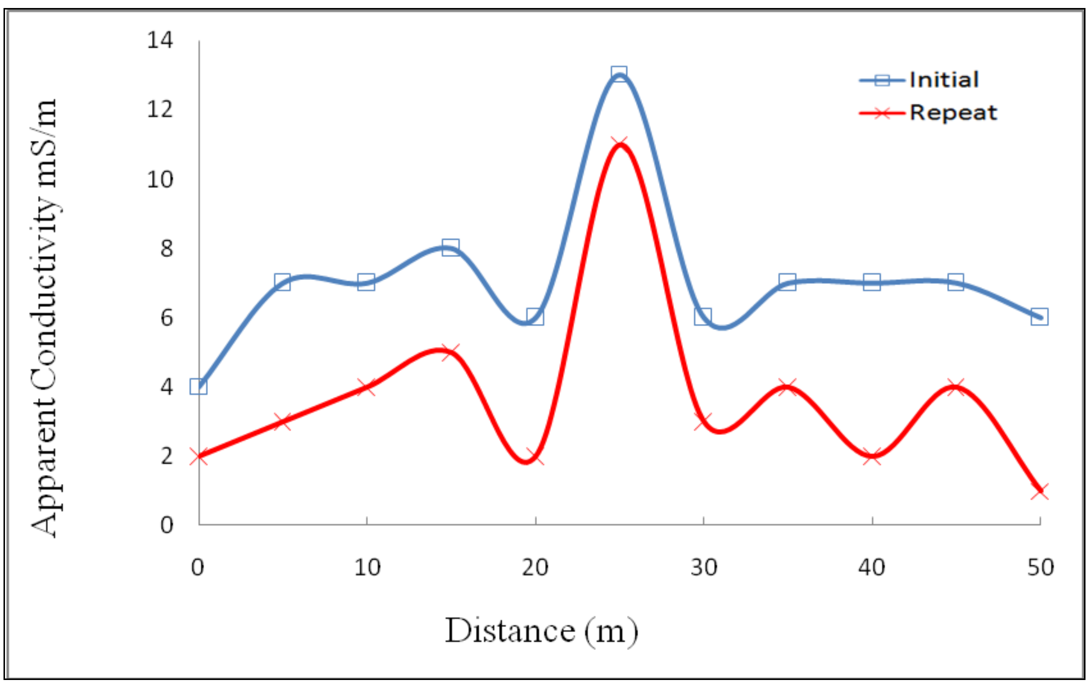

Figure 5.42 - Grid 1 Line 9 Repeats (40m), Ground Conductivity (Quad-phase), Perpendicular to Line, VCP

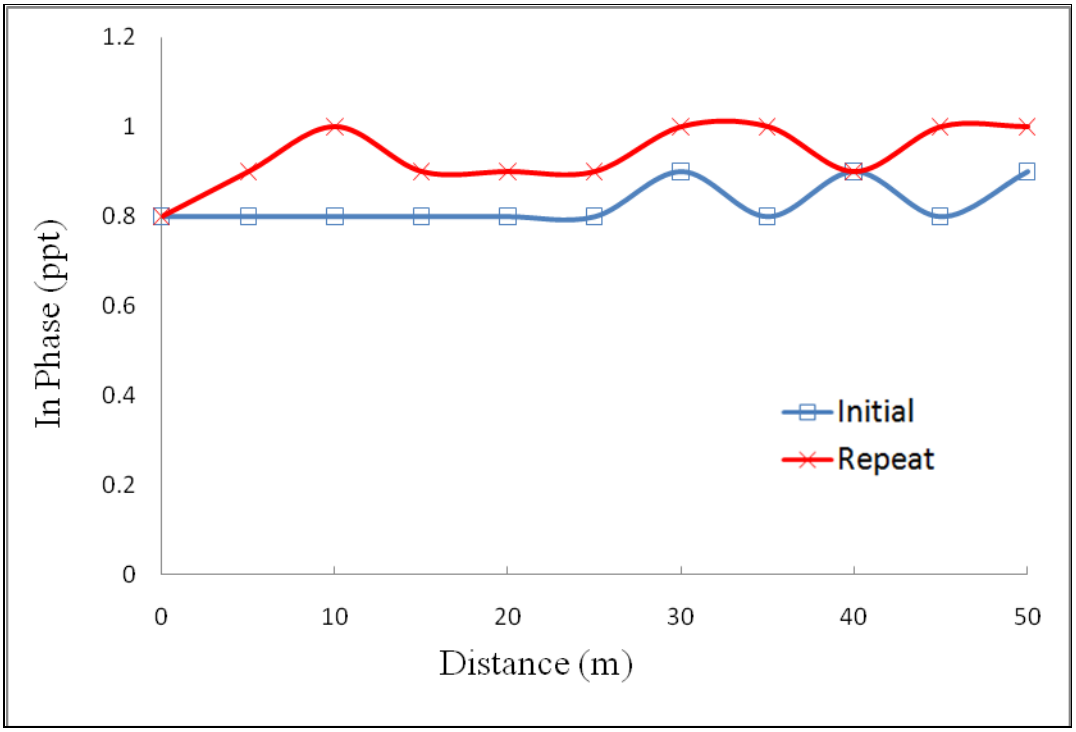

Figure 5.43 - Grid 1 Line 9 Repeats (40m), Magnetic Susceptibility (In-phase), Perpendicular to Line, HCP

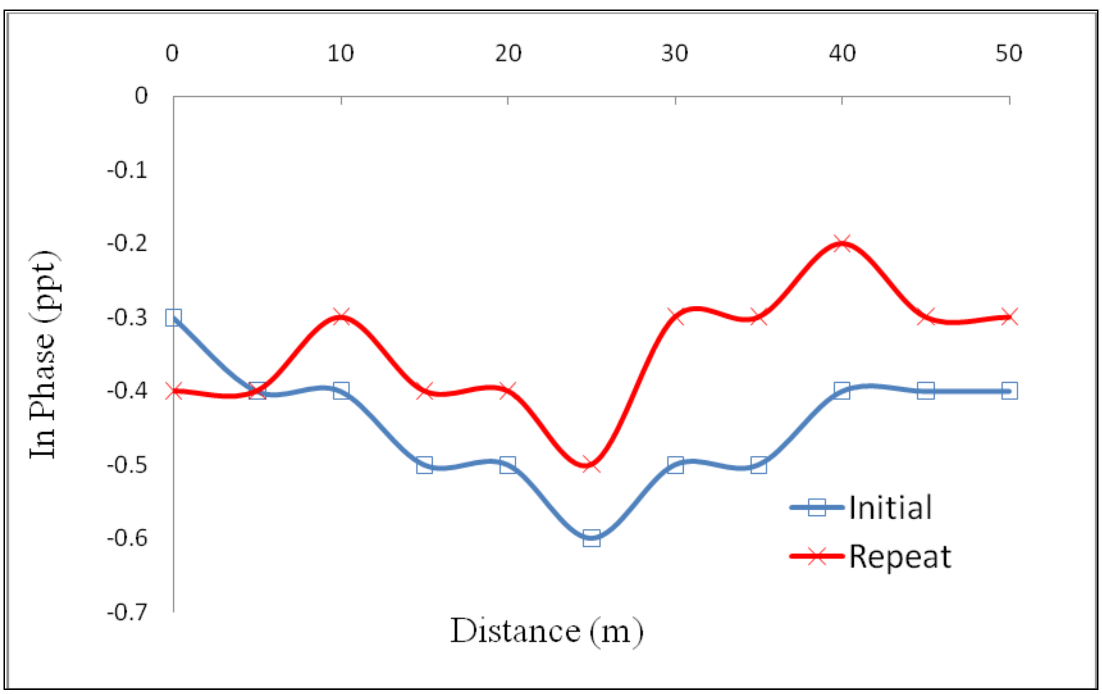

Figure 5.44 - Grid 1 Line 9 Repeats (40m), Magnetic Susceptibility (In-phase), Perpendicular to Line, VCP

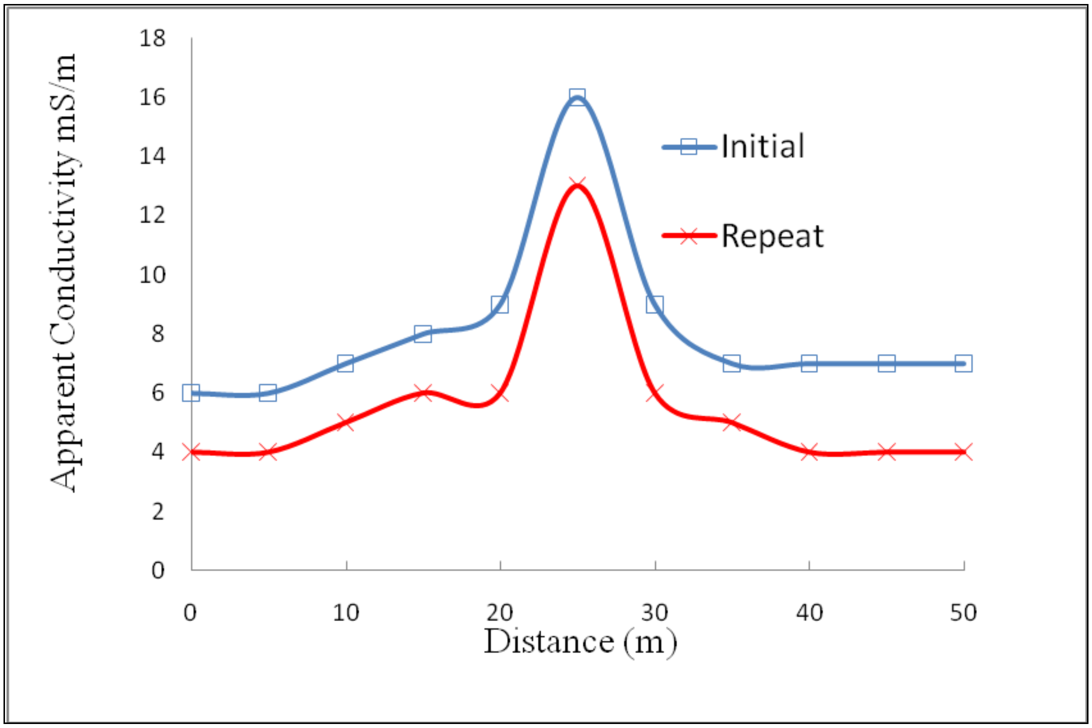

Figure 5.45 - Grid 1 Line 9 Repeats (40m), Ground Conductivity (Quad-phase), Parallel to Line, HCP

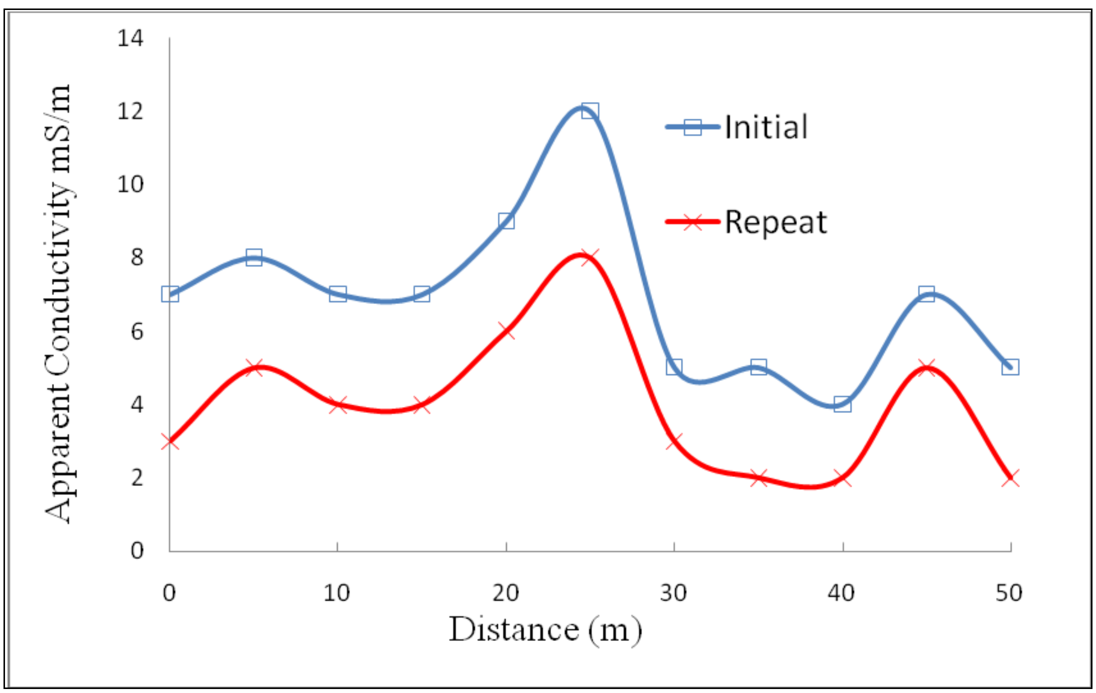

Figure 5.46 - Grid 1 Line 9 Repeats (40m), Ground Conductivity (Quad-phase), Parallel to Line, VCP

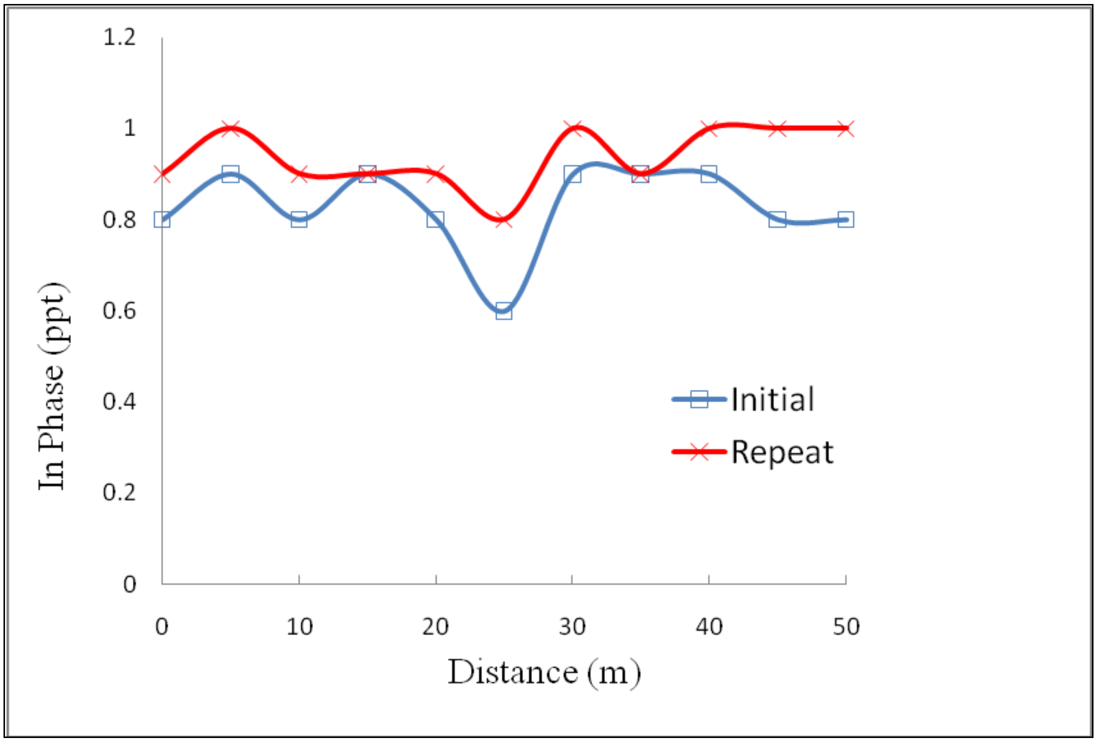

Figure 5.47 - Grid 1 Line 9 Repeats (40m), Magnetic Susceptibility (In-phase), Parallel to Line, HCP

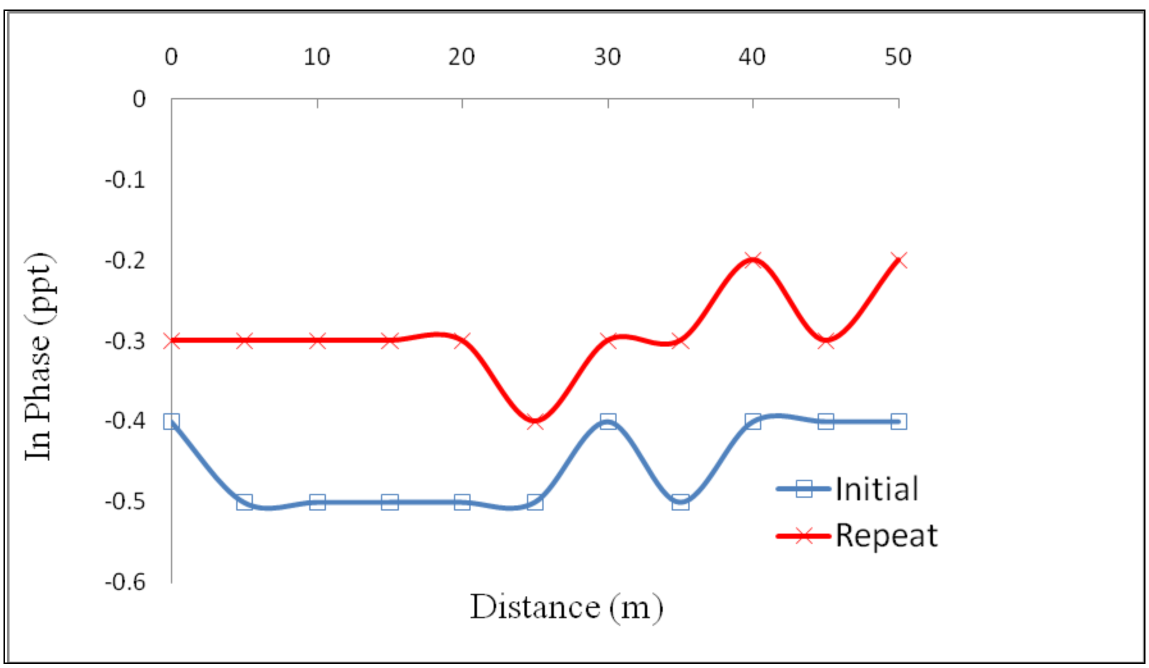

Figure 5.48 - Grid 1 Line 9 Repeats (40m), Magnetic Susceptibility (In-phase), Parallel to Line, VCP

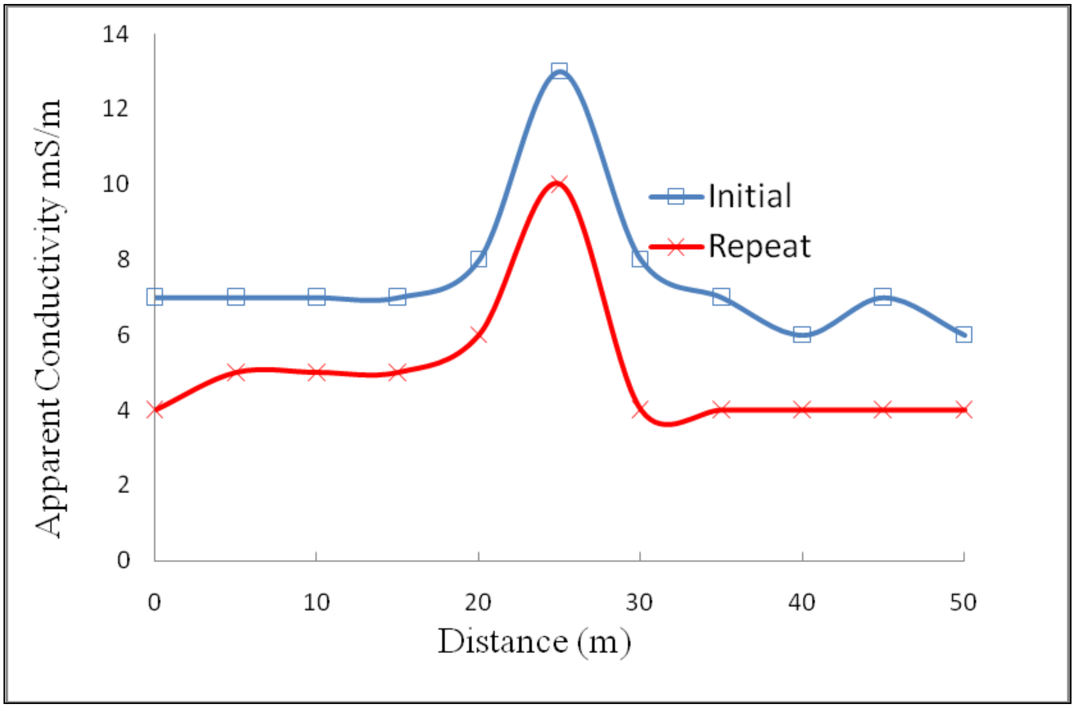

Figure 5.49 - Grid 1 Line 11 Repeats (40m), Ground Conductivity (Quad-phase), Perpendicular to Line, HCP

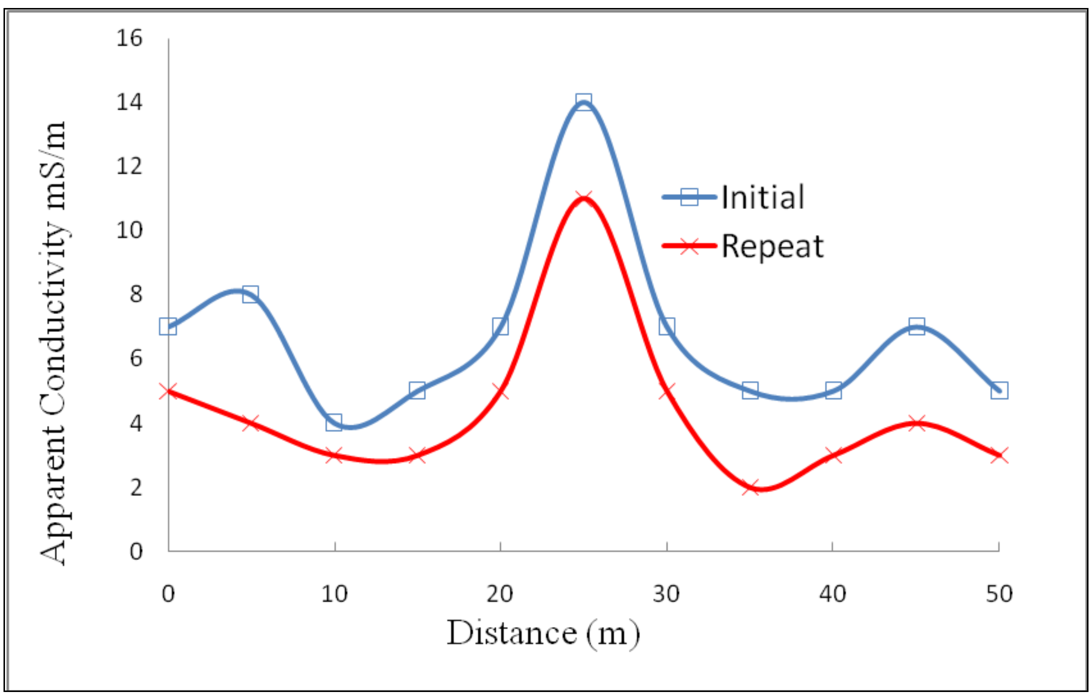

Figure 5.50 - Grid 1 Line 11 Repeats (50m), Ground Conductivity (Quad-phase), Perpendicular to Line, VCP

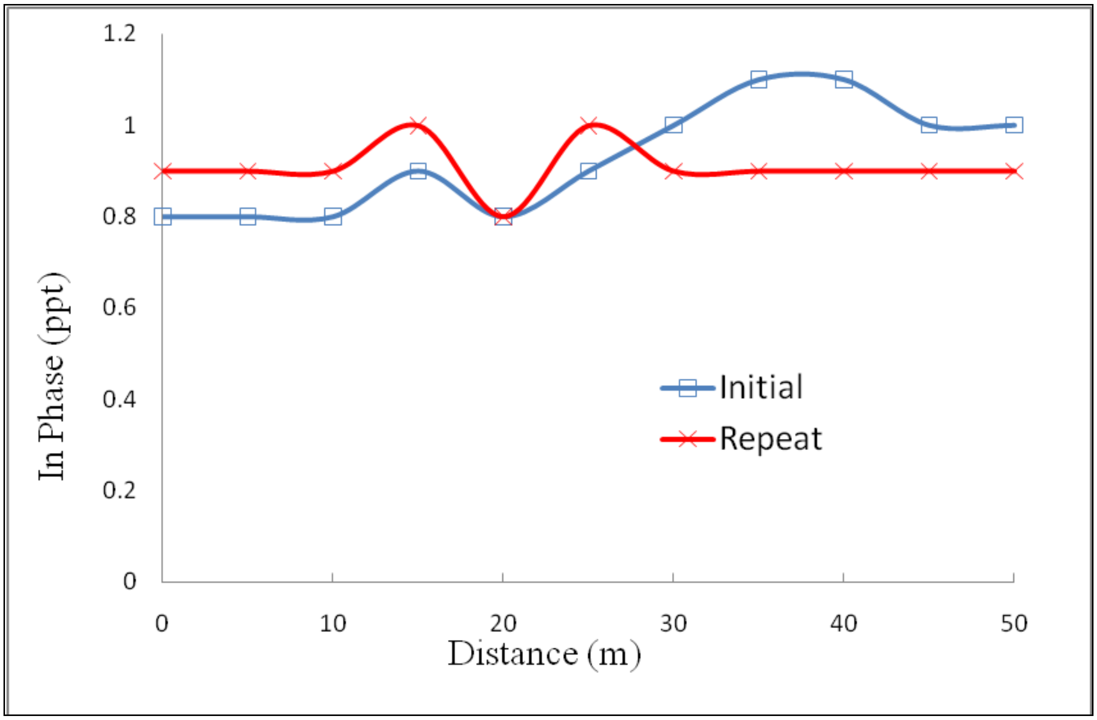

Figure 5.51 - Grid 1 Line 11 Repeats (50m), Magnetic Susceptibility (In-phase), Perpendicular to Line, HCP

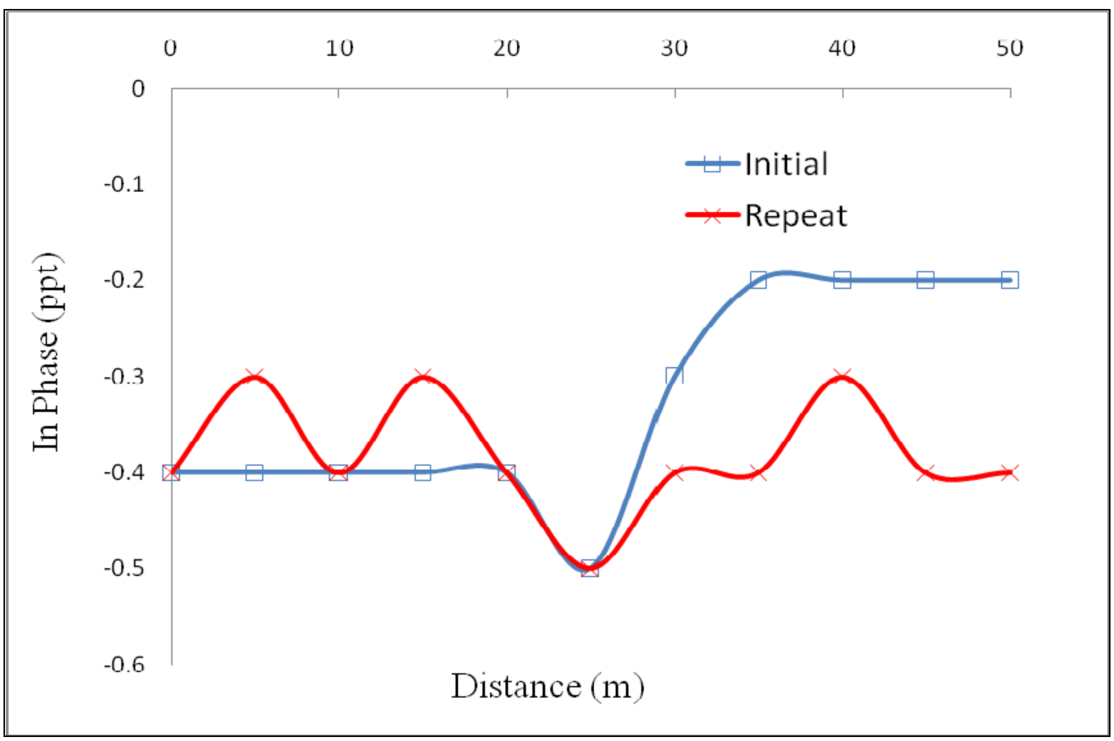

Figure 5.52 - Grid 1 Line 11 Repeats (50m), Magnetic Susceptibility (In-phase), Perpendicular to Line, VCP

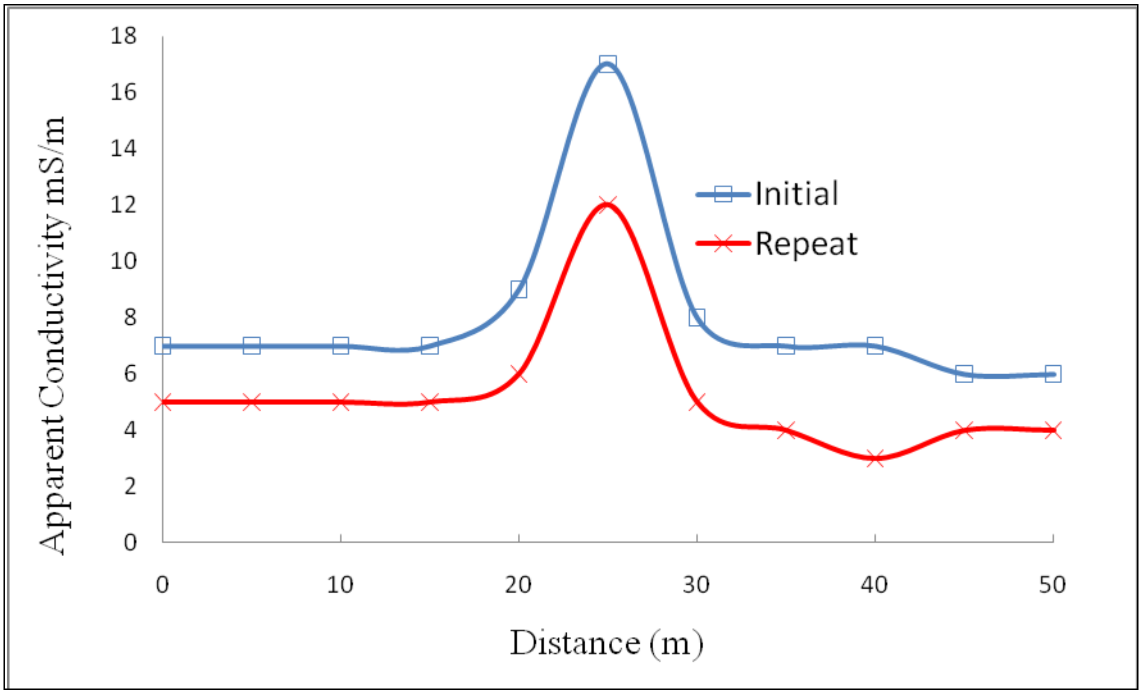

Figure 5.53 - Grid 1 Line 11 Repeats (50m), Ground Conductivity (Quad-phase), Parallel to Line, HCP

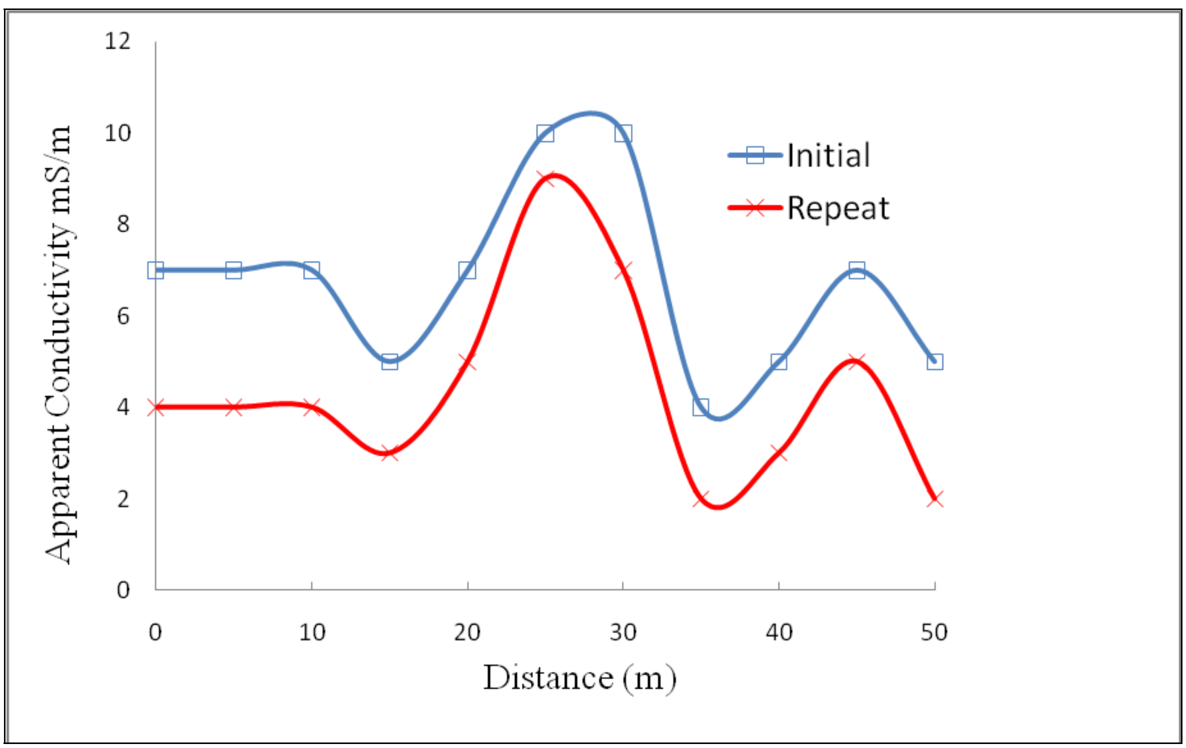

Figure 5.54 - Grid 1 Line 11 Repeats (50m), Ground Conductivity (Quad-phase), Parallel to Line, VCP

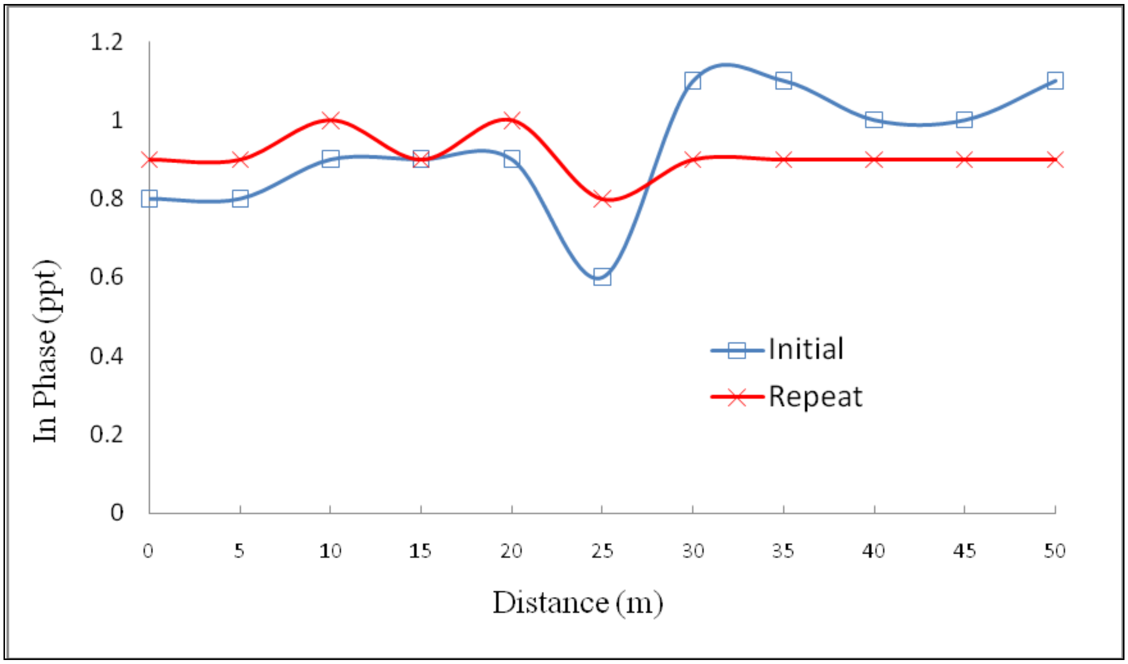

Figure 5.55 - Grid 1 Line 11 Repeats (50m), Magnetic Susceptibility (In-phase), Parallel to Line, HCP

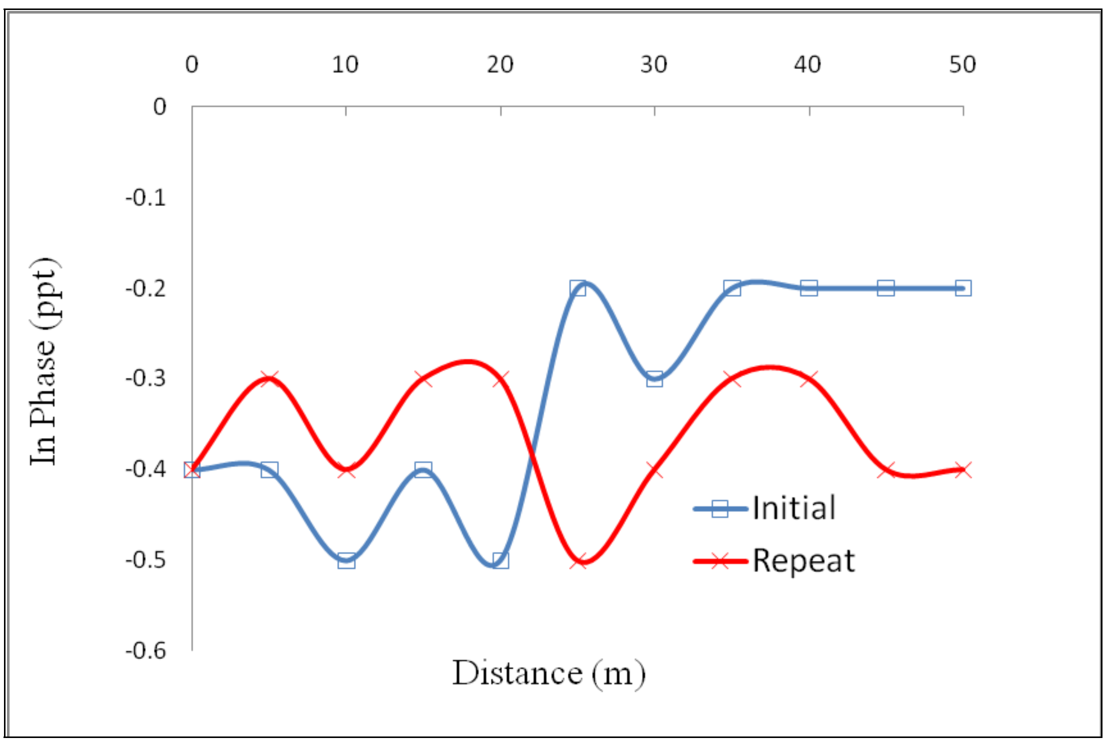

Figure 5.56 - Grid 1 Line 11 Repeats (50m), Magnetic Susceptibility (In-phase), Parallel to Line, VCP

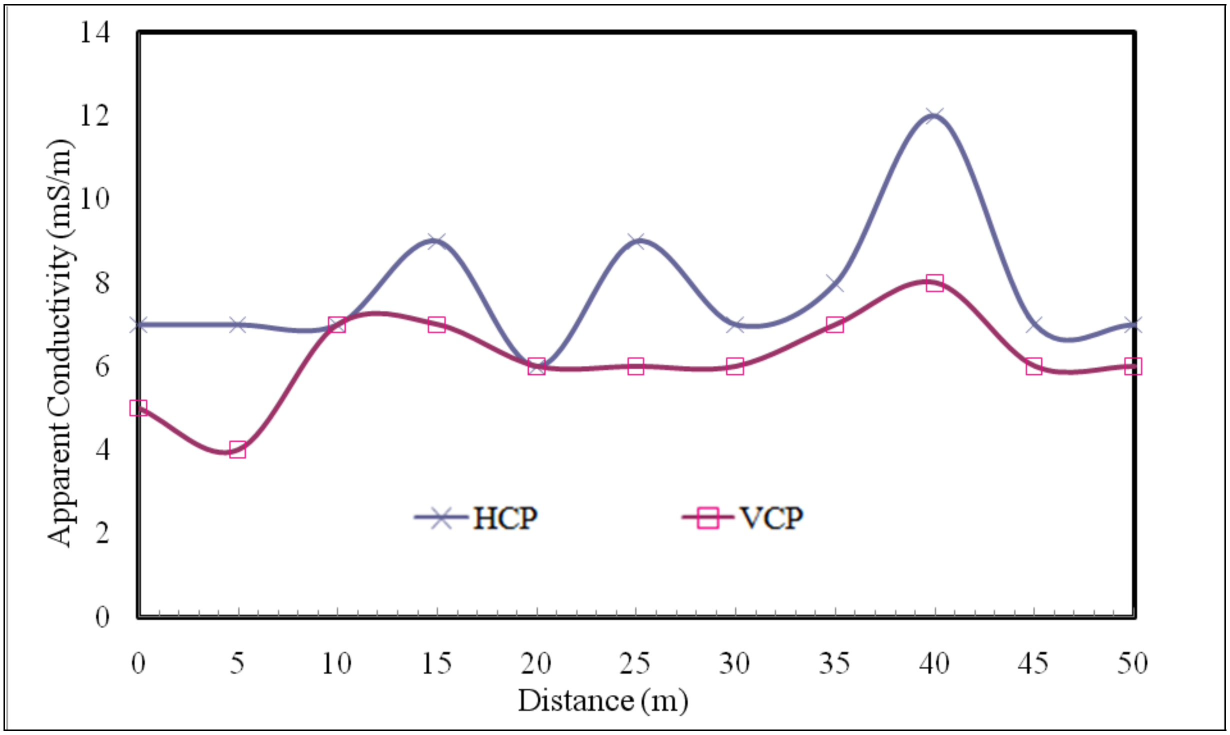

Figure 5.57 - Grid 2 Line 1 (0m), Ground Conductivity (Quad-phase), Perpendicular to Line

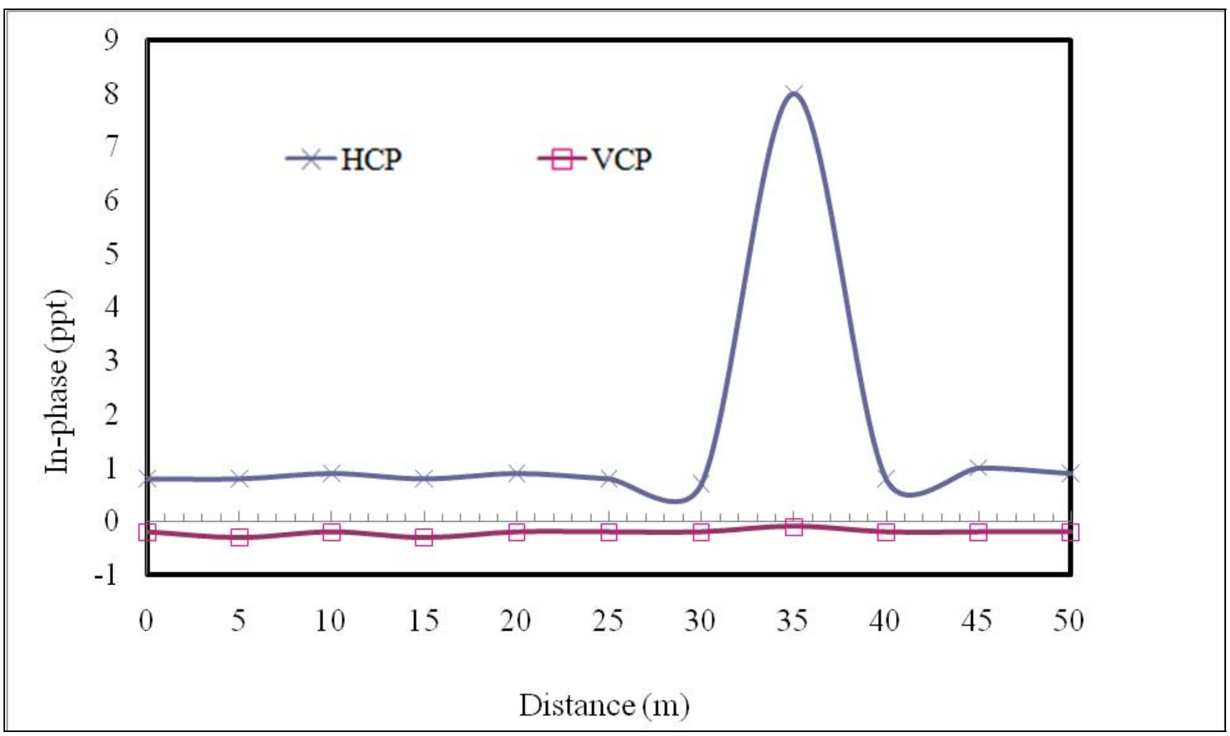

Figure 5.58 - Grid 2 Line 1 (0m), Magnetic Susceptibility (In-phase), Perpendicular to Line

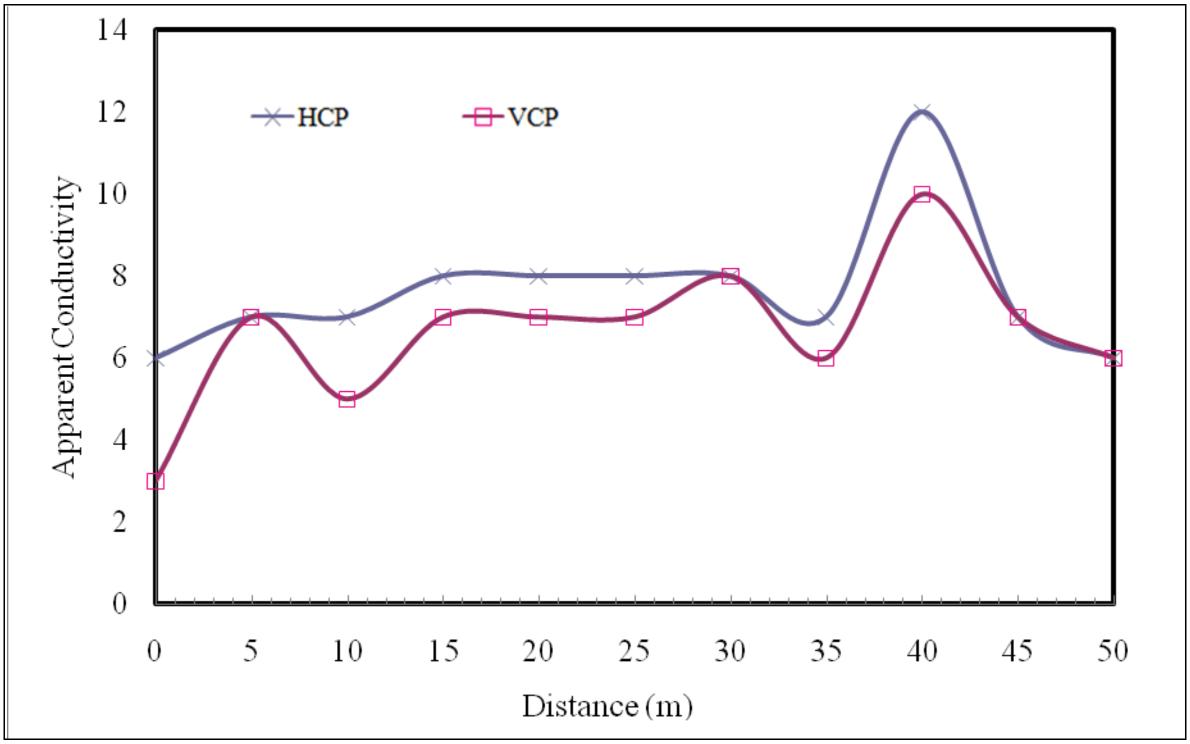

Figure 5.59 - Grid 2 Line 1 (0m), Ground Conductivity (Quad-phase), Parallel to Line

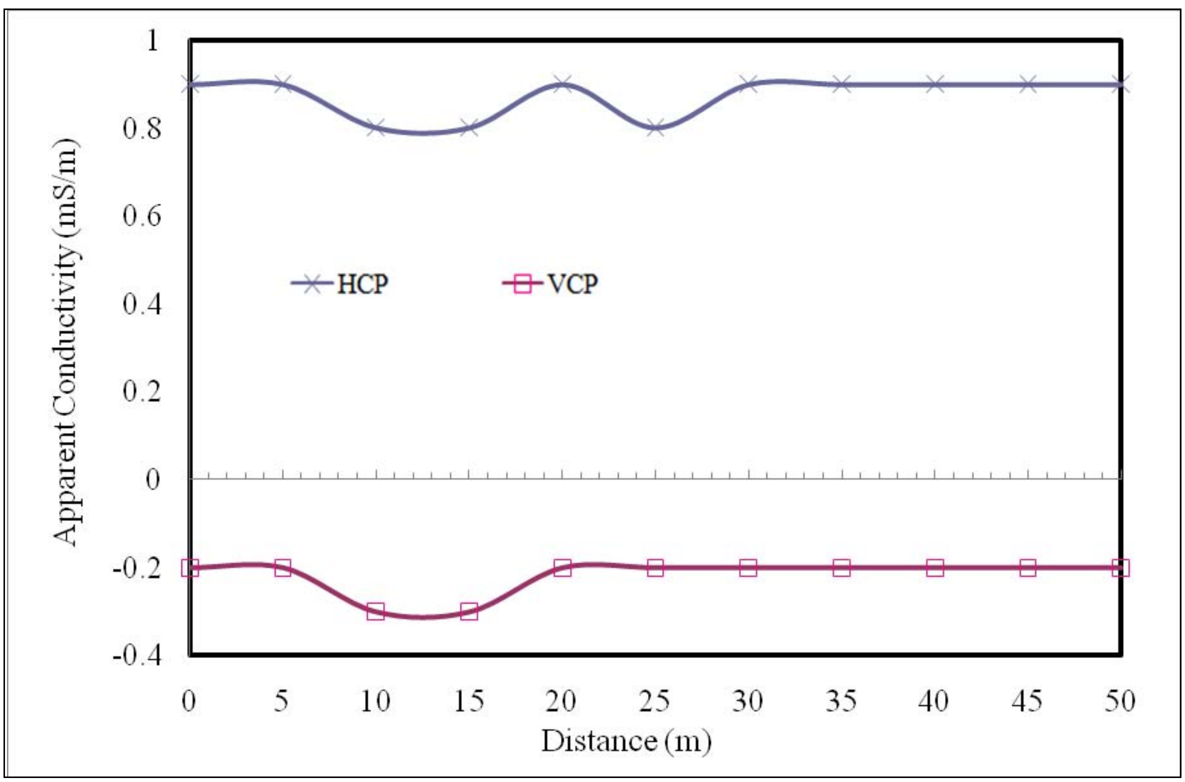

Figure 5.60 - Grid 2 Line 1 (0m), Magnetic Susceptibility (In-phase), Parallel to Line

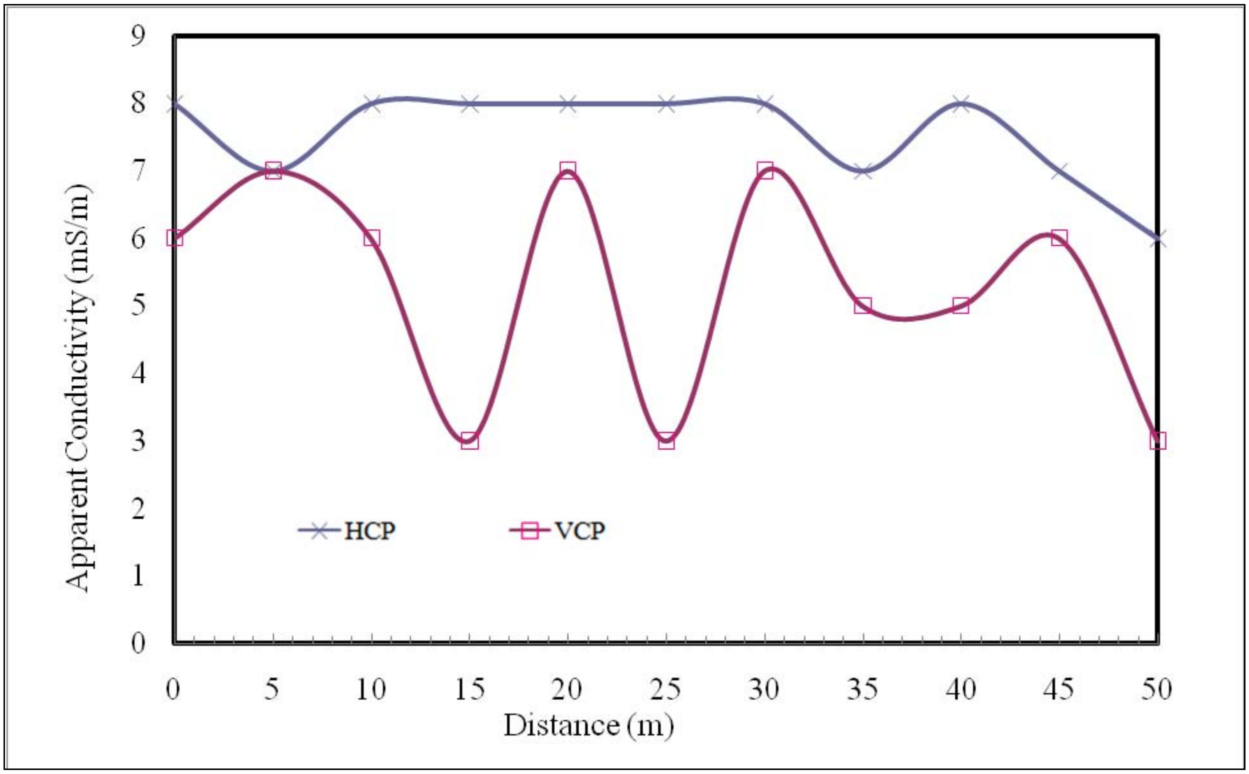

Figure 5.61 - Grid 2 Line 2 (5m), Ground Conductivity (Quad-phase), Perpendicular to Line

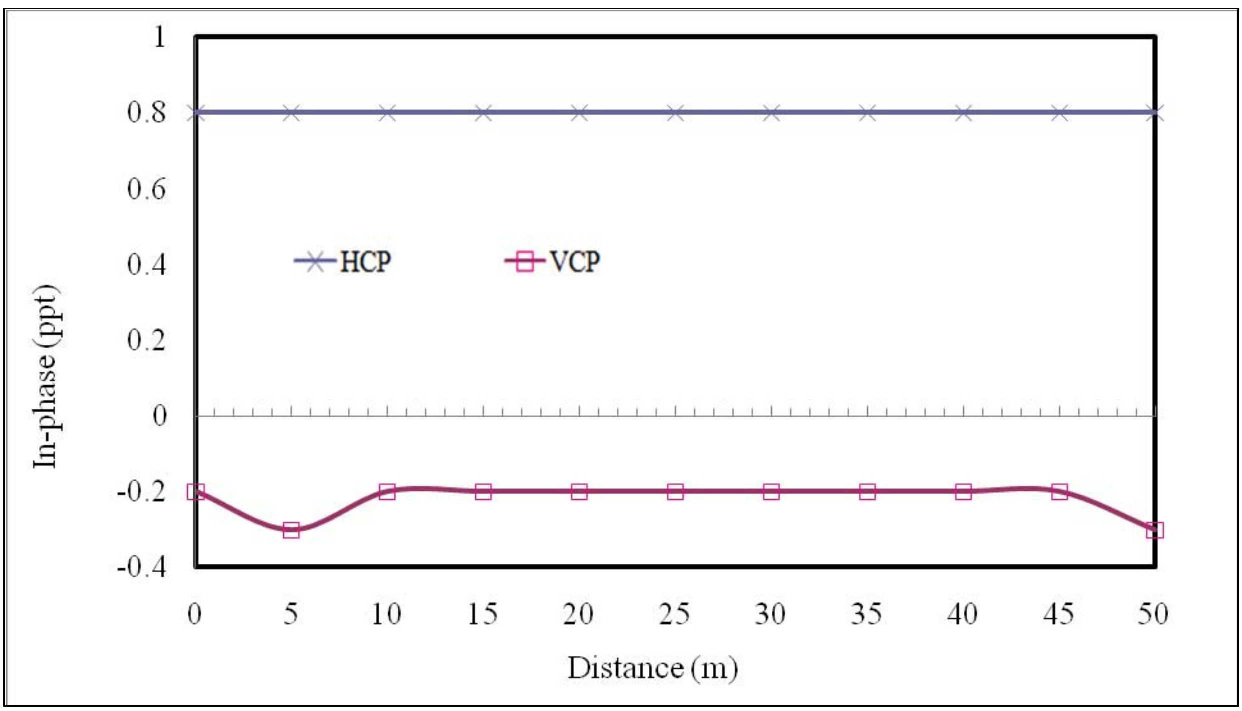

Figure 5.62 - Grid 2 Line 2 (5m), Magnetic Susceptibility (In-phase), Perpendicular to Line

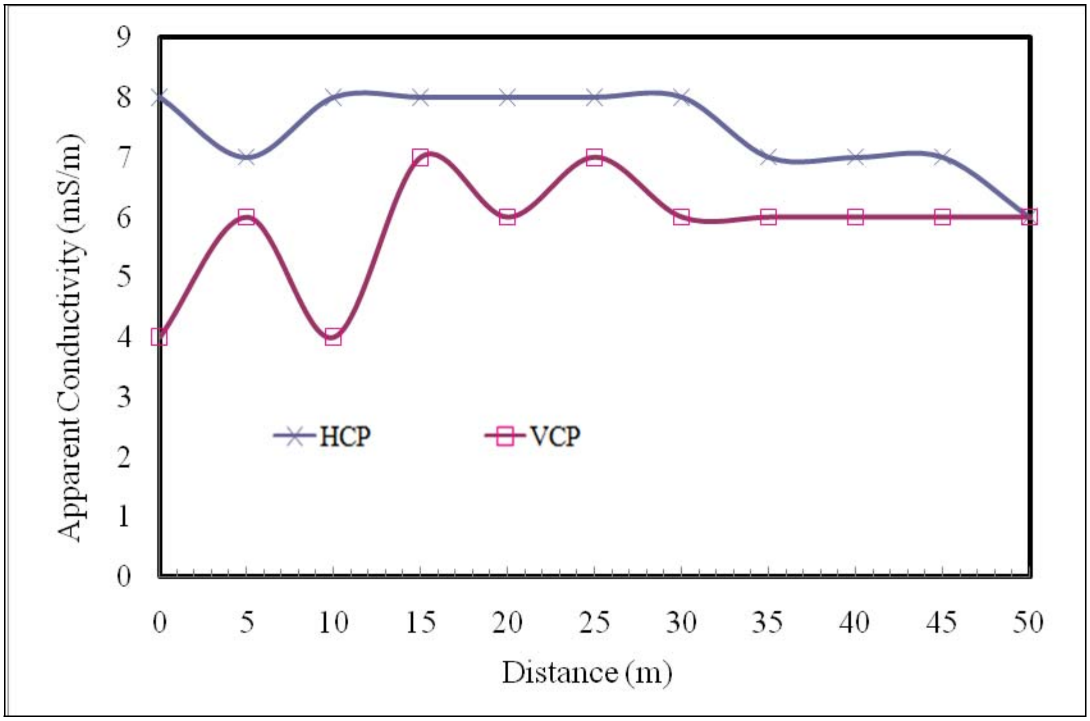

Figure 5.63 - Grid 2 Line 2 (5m), Ground Conductivity (Quad-phase), Parallel to Line

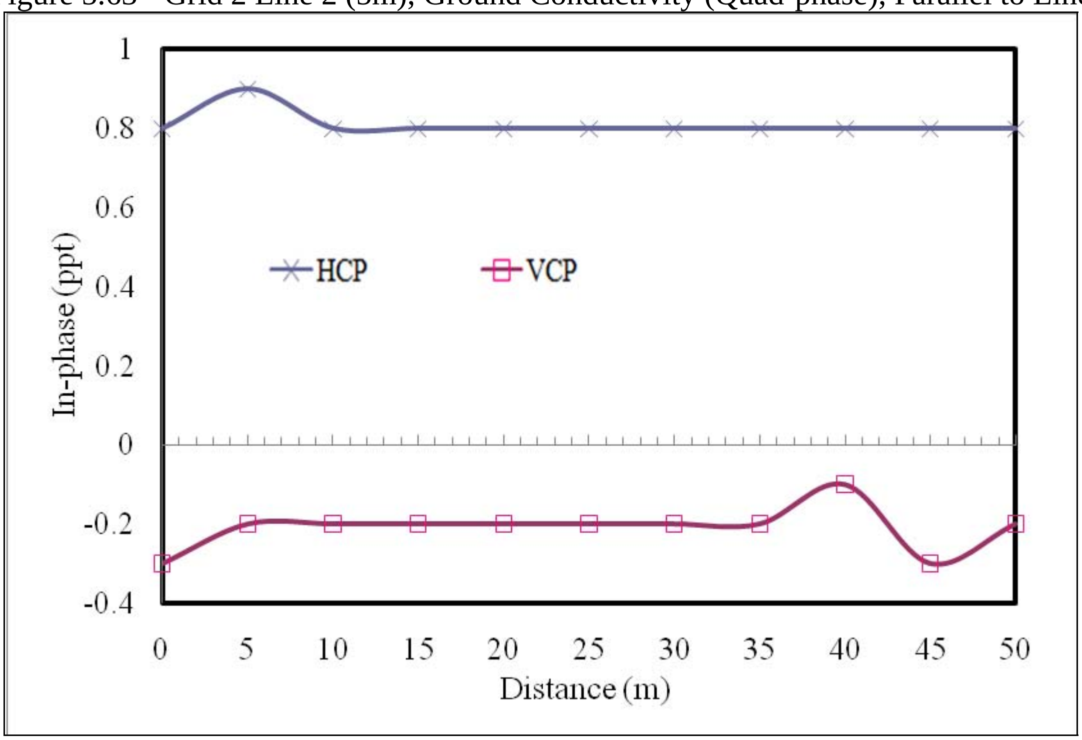

Figure 5.64 - Grid 2 Line 2 (5m), Magnetic Susceptibility (In-phase), Parallel to Line

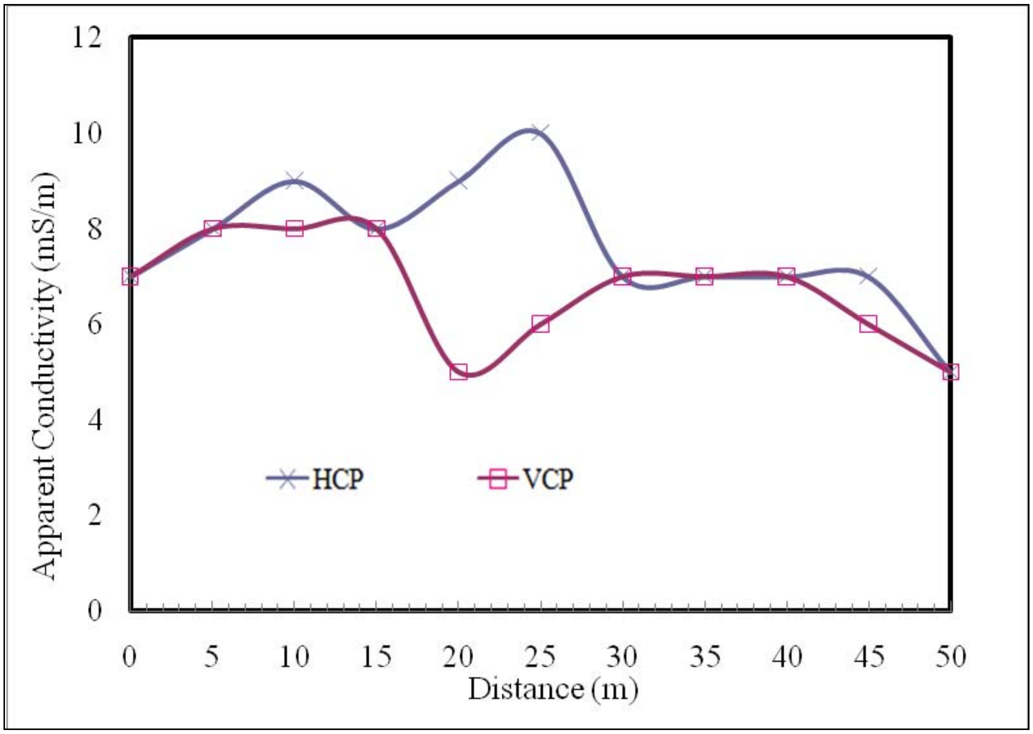

Figure 5.65 - Grid 2 Line 3 (10m), Ground Conductivity (Quad-phase), Perpendicular to Line

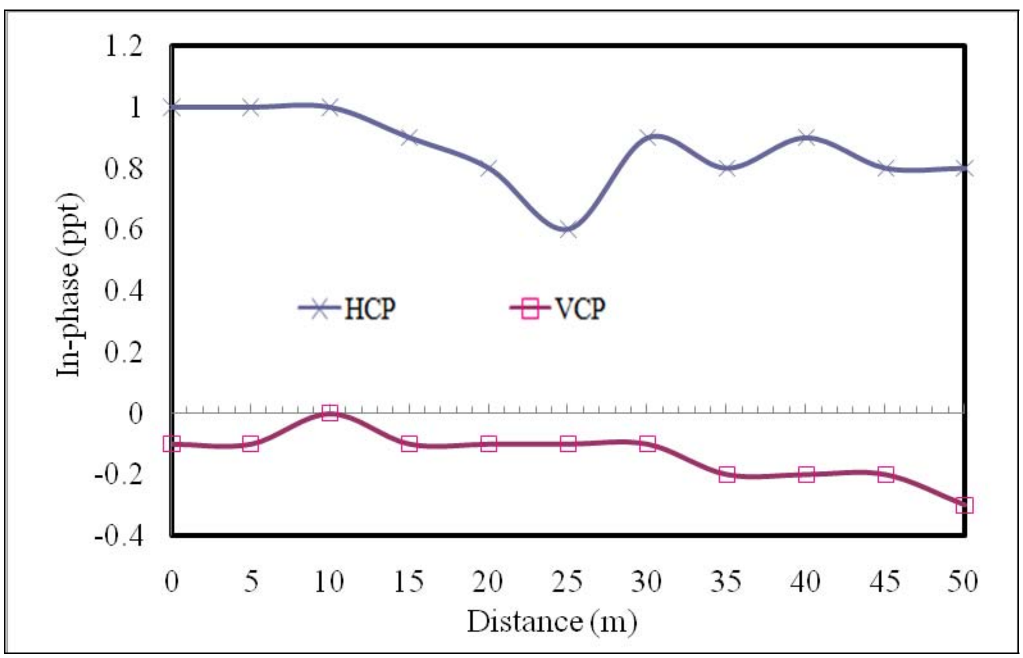

Figure 5.66 - Grid 2 Line 3 (10m), Magnetic Susceptibility (In-phase), Perpendicular to Line

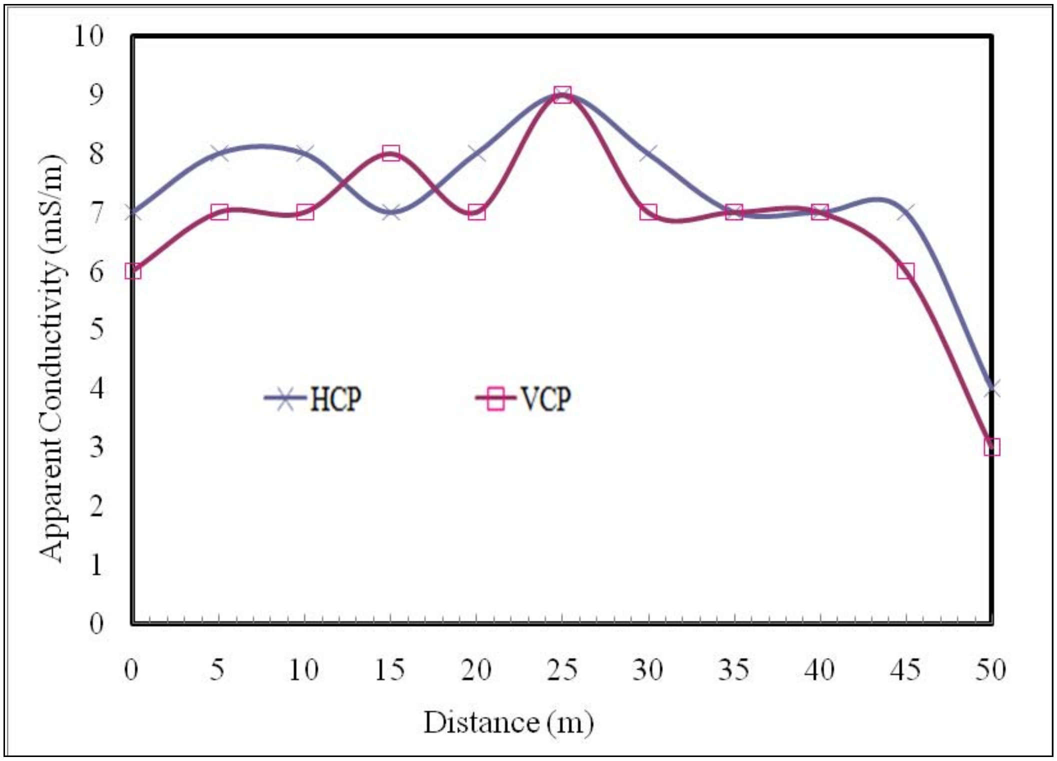

Figure 5.67 - Grid 2 Line 3 (10m), Ground Conductivity (Quad-phase), Parallel to Line

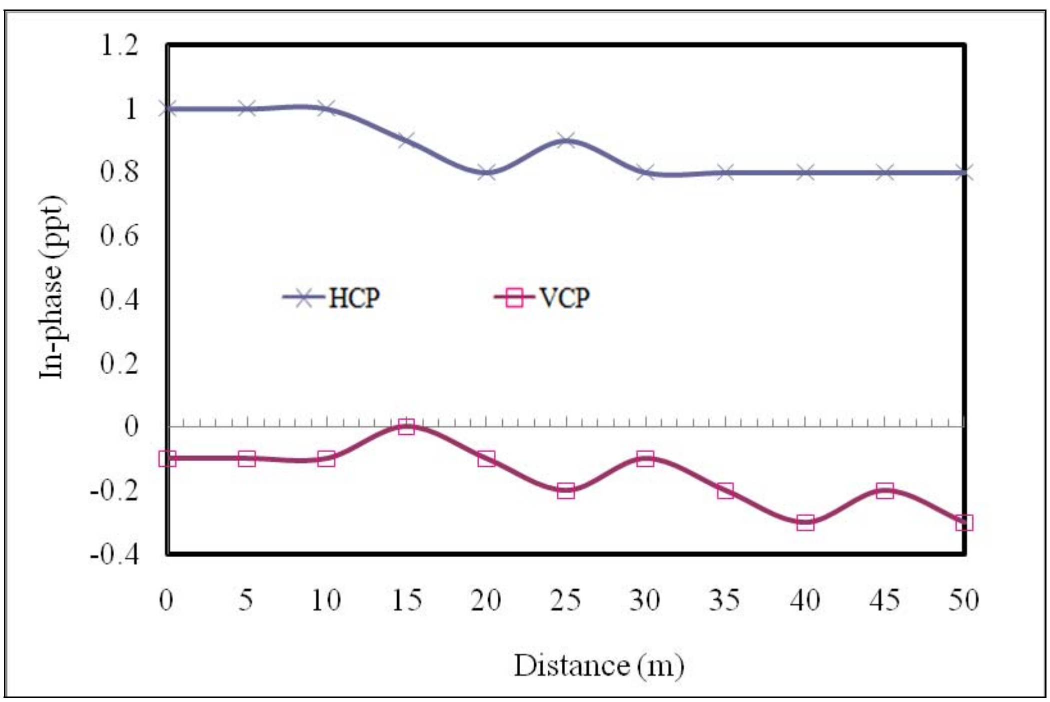

Figure 5.68 - Grid 2 Line 3 (10m), Magnetic Susceptibility (In-phase), Parallel to Line

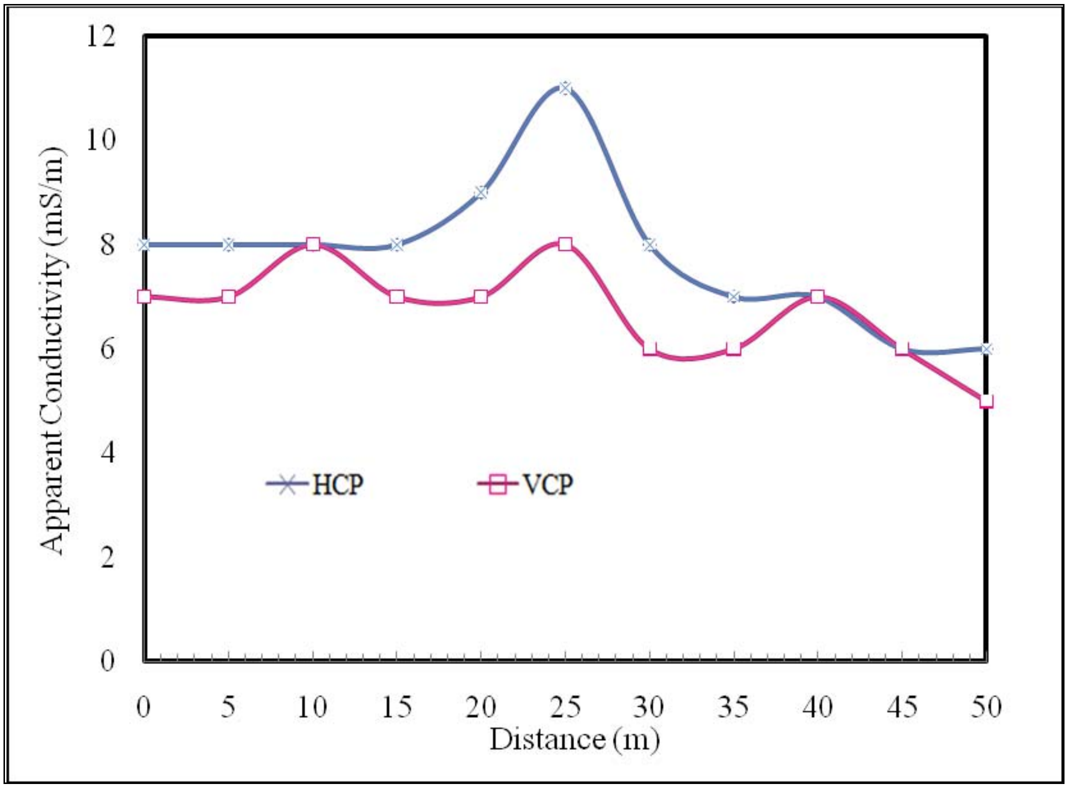

Figure 5.69 - Grid 2 Line 4 (15m), Ground Conductivity (Quad-phase), Perpendicular to Line

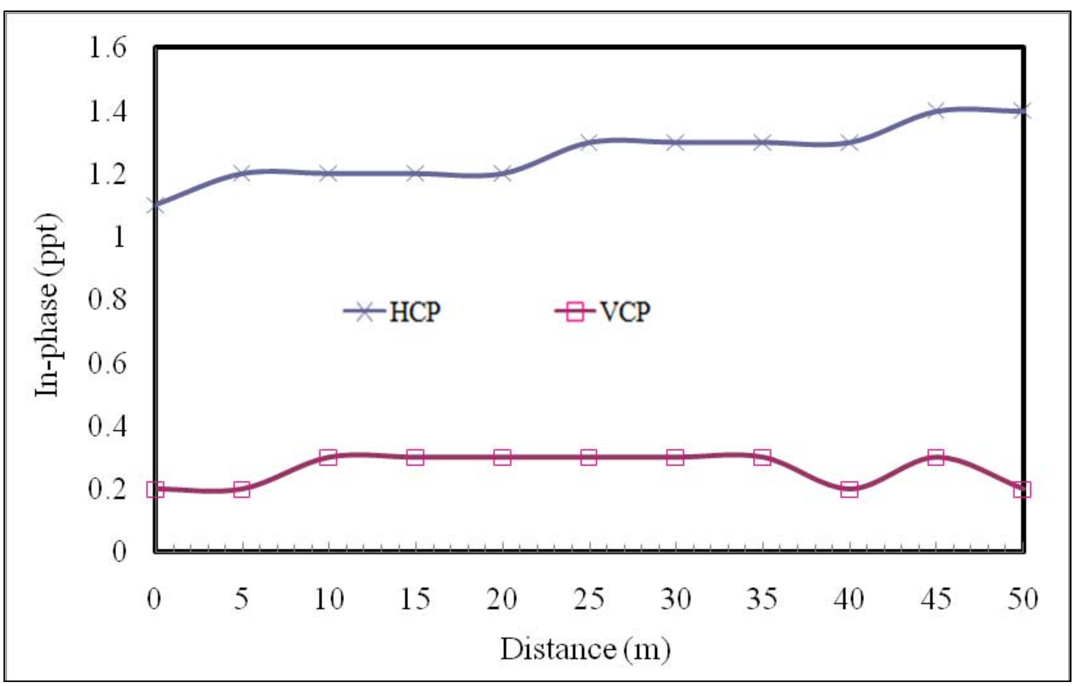

Figure 5.70 - Grid 2 Line 4 (15m), Magnetic Susceptibility (In-phase), Perpendicular to Line

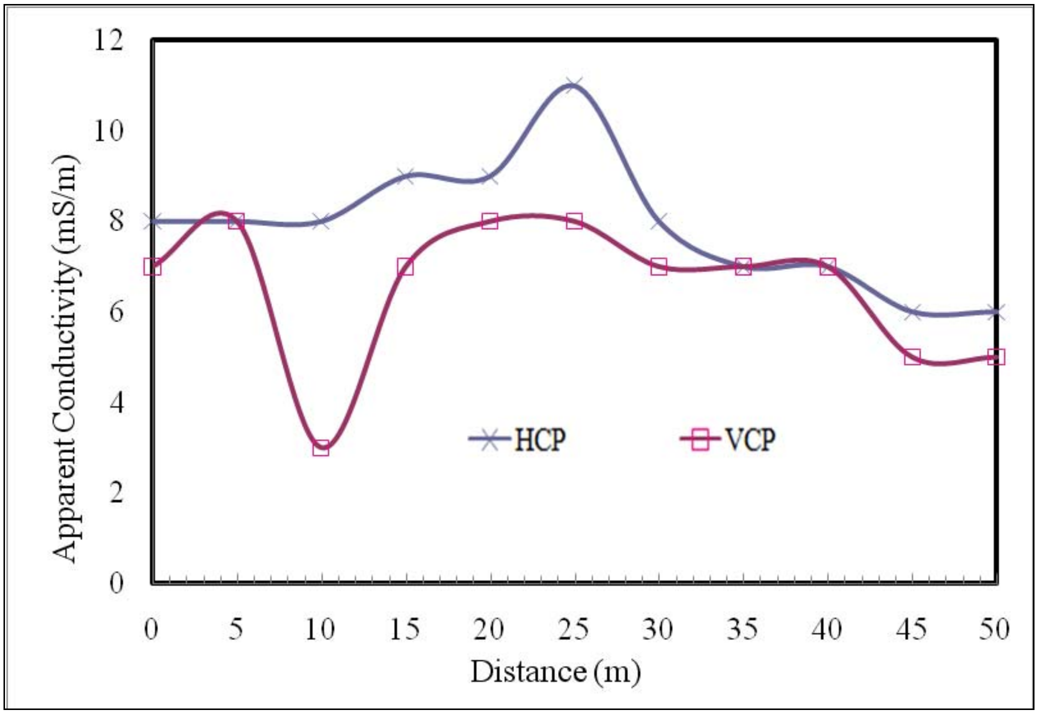

Figure 5.71 - Grid 2 Line 4 (15m), Ground Conductivity (Quad-phase), Parallel to Line

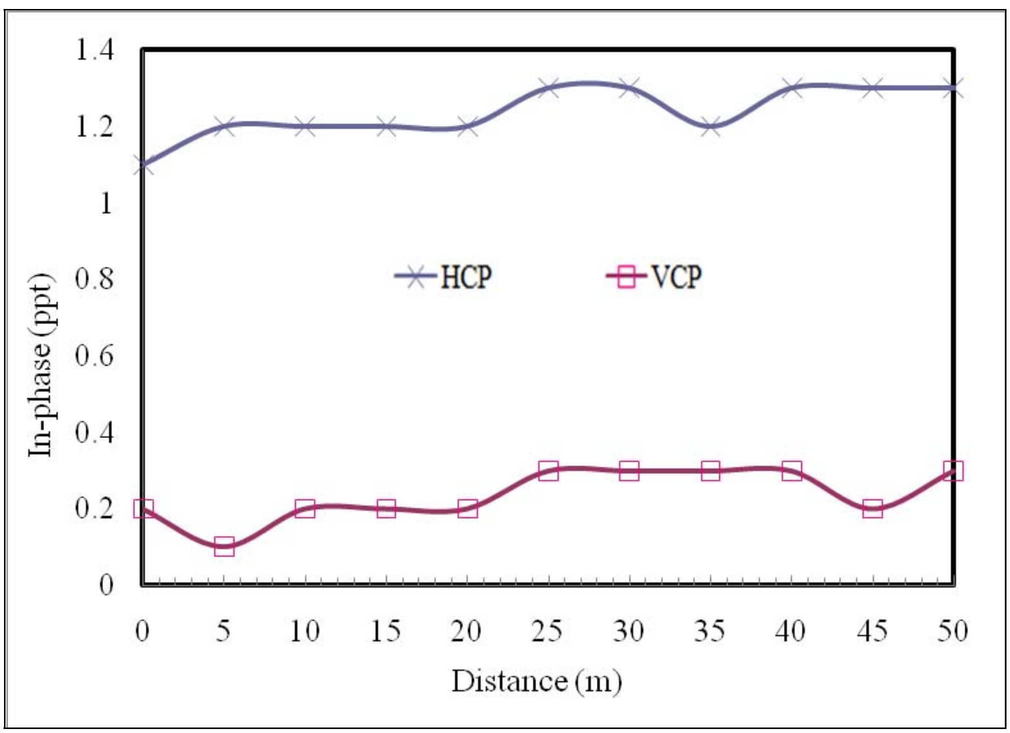

Figure 5.72 - Grid 2 Line 4 (15m), Magnetic Susceptibility (In-phase), Parallel to Line

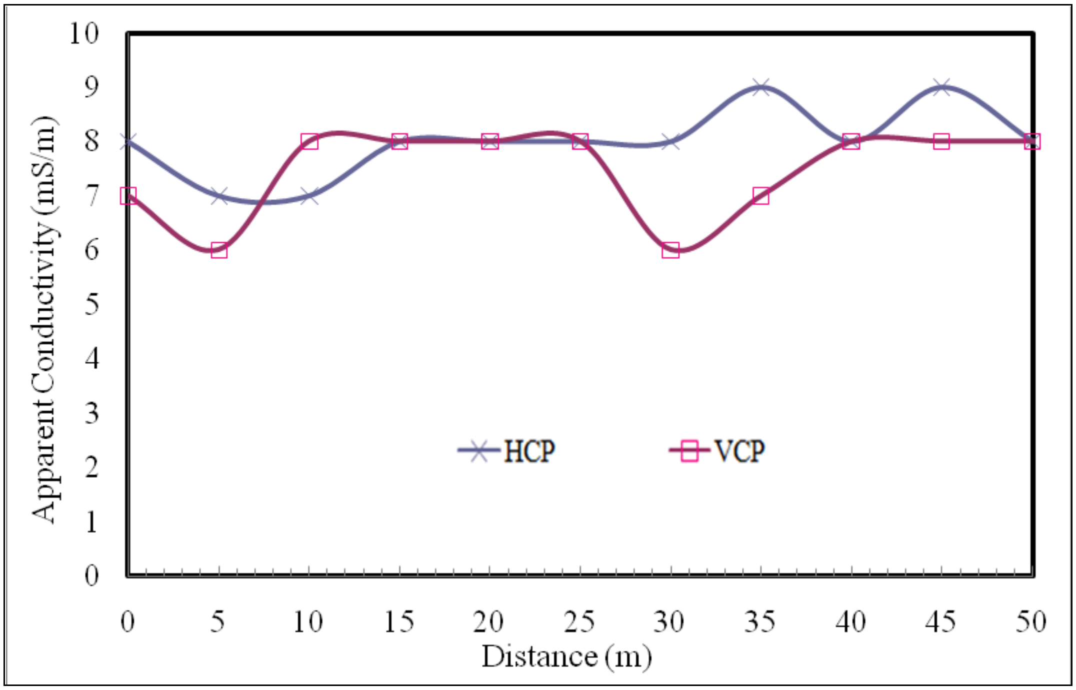

Figure 5.73 - Grid 2 Line 12 (55m), Ground Conductivity (Quad-phase), Perpendicular to Line

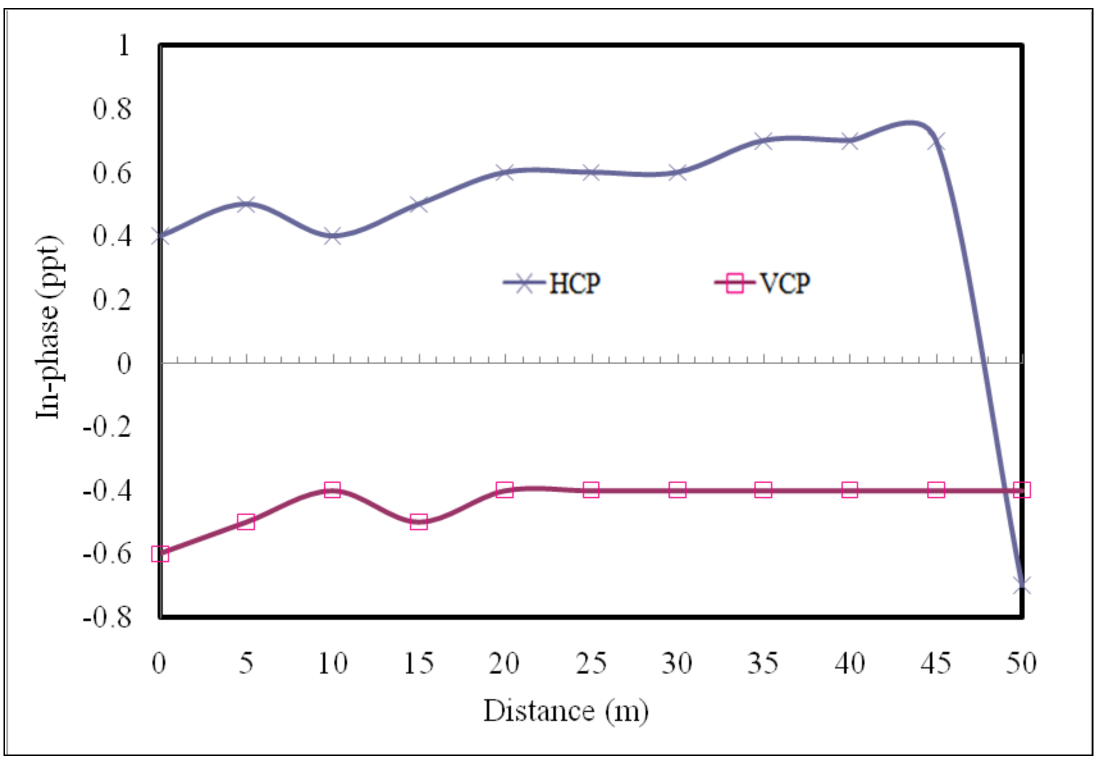

Figure 5.74 - Grid 2 Line 12 (55m), Magnetic Susceptibility (In-phase), Perpendicular to Line

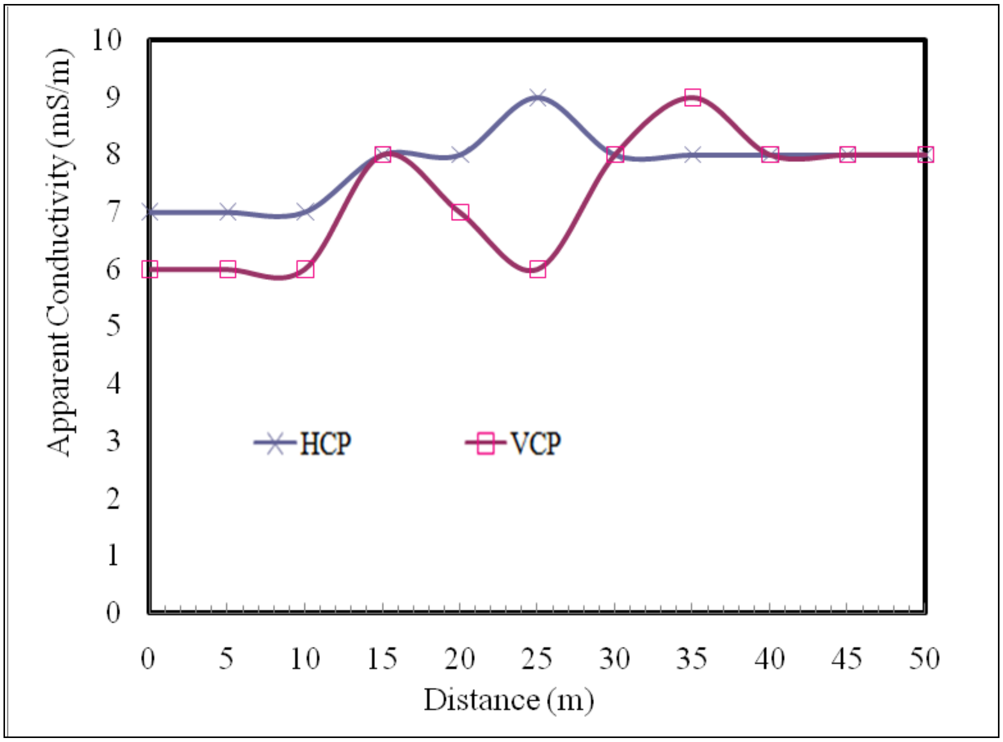

Figure 5.75 - Grid 2 Line 12 (55m), Ground Conductivity (Quad-phase), Parallel to Line

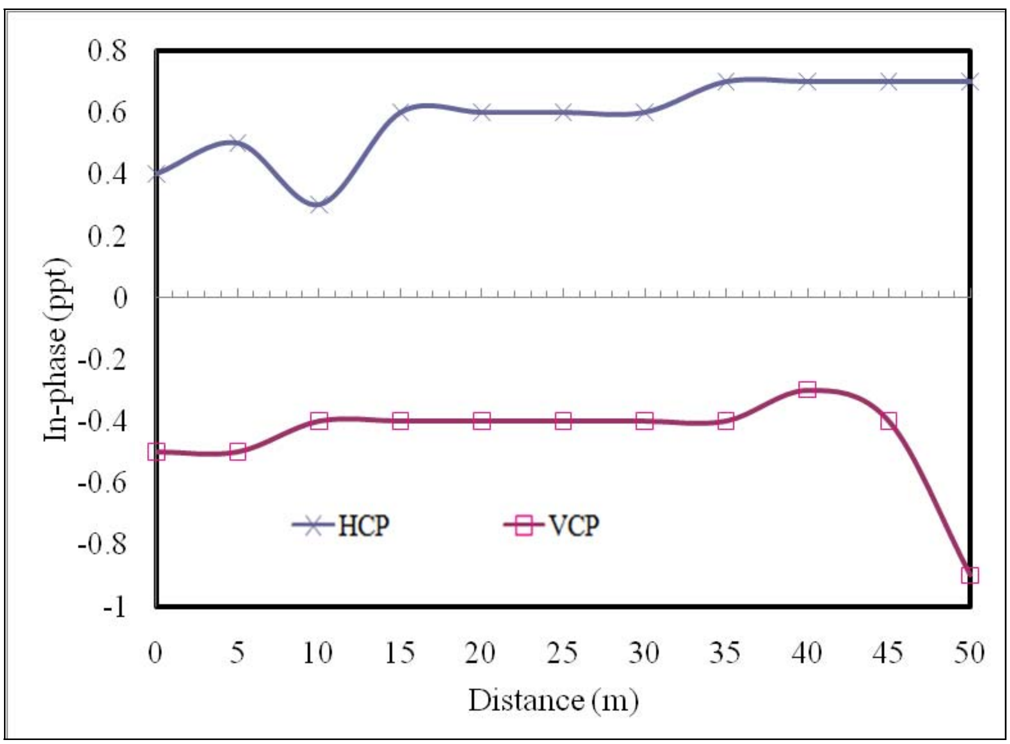

Figure 5.76 - Grid 2 Line 12 (55m), Magnetic Susceptibility (In-phase), Parallel to Line

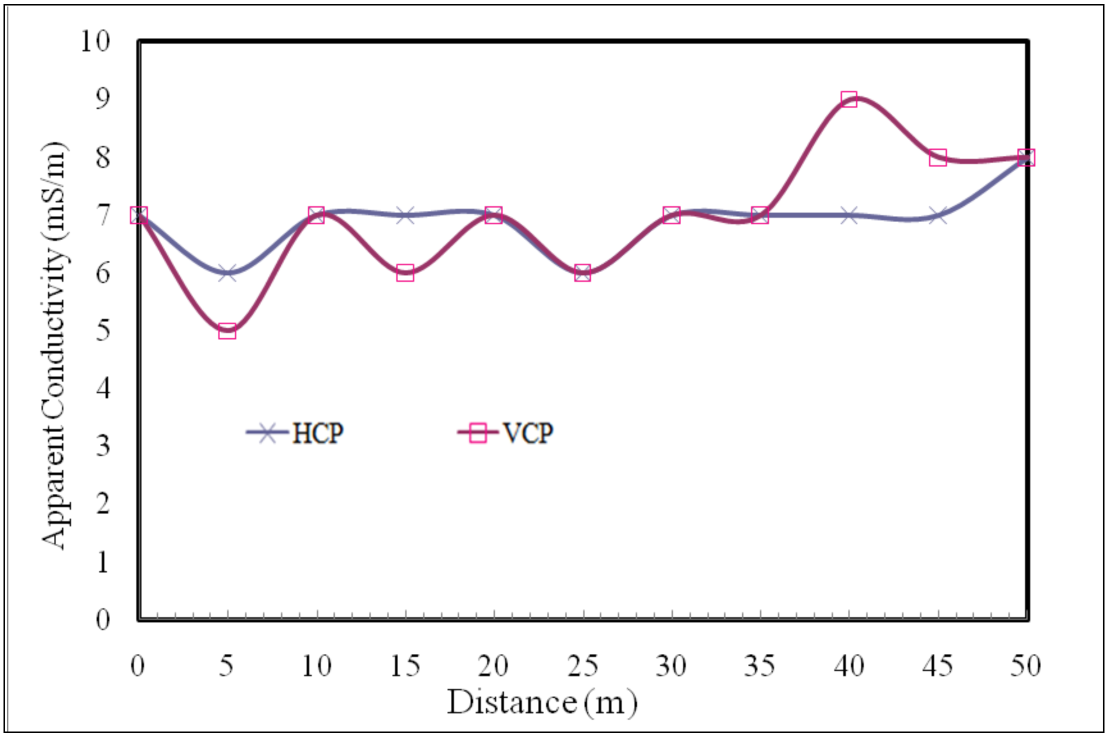

Figure 5.77 - Grid 2 Line 13 (60m), Ground Conductivity (Quad-phase), Perpendicular to Line

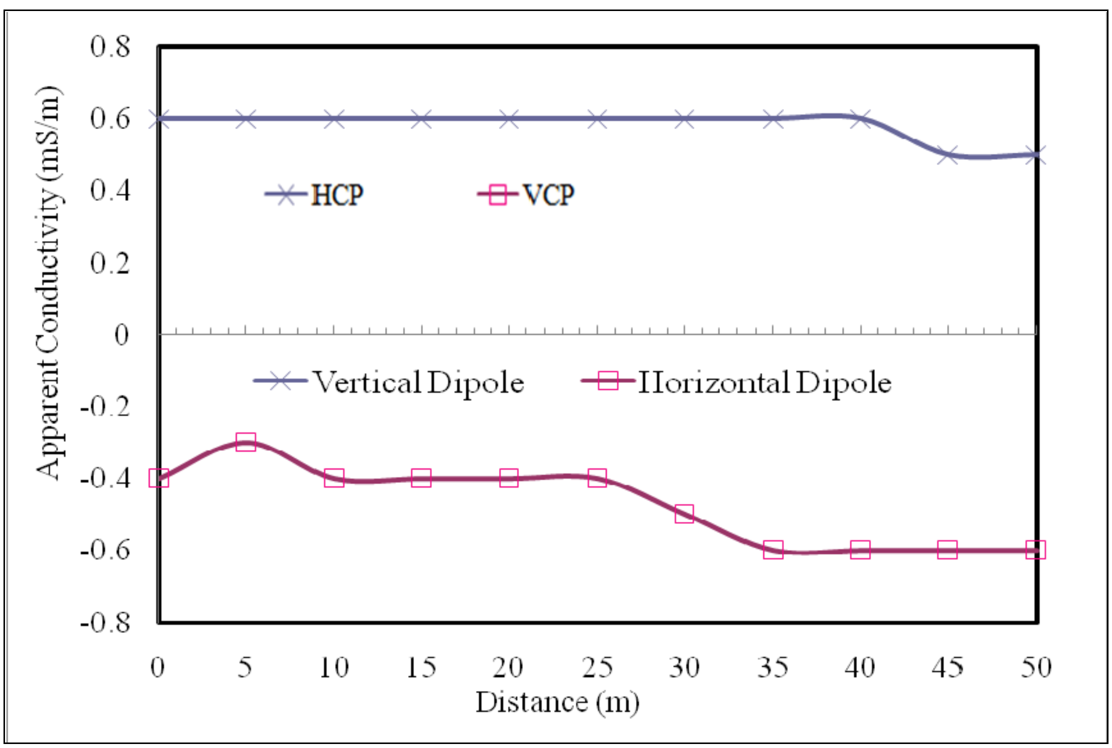

Figure 5.78 - Grid 2 Line 13 (60m), Magnetic Susceptibility (In-phase), Perpendicular to Line

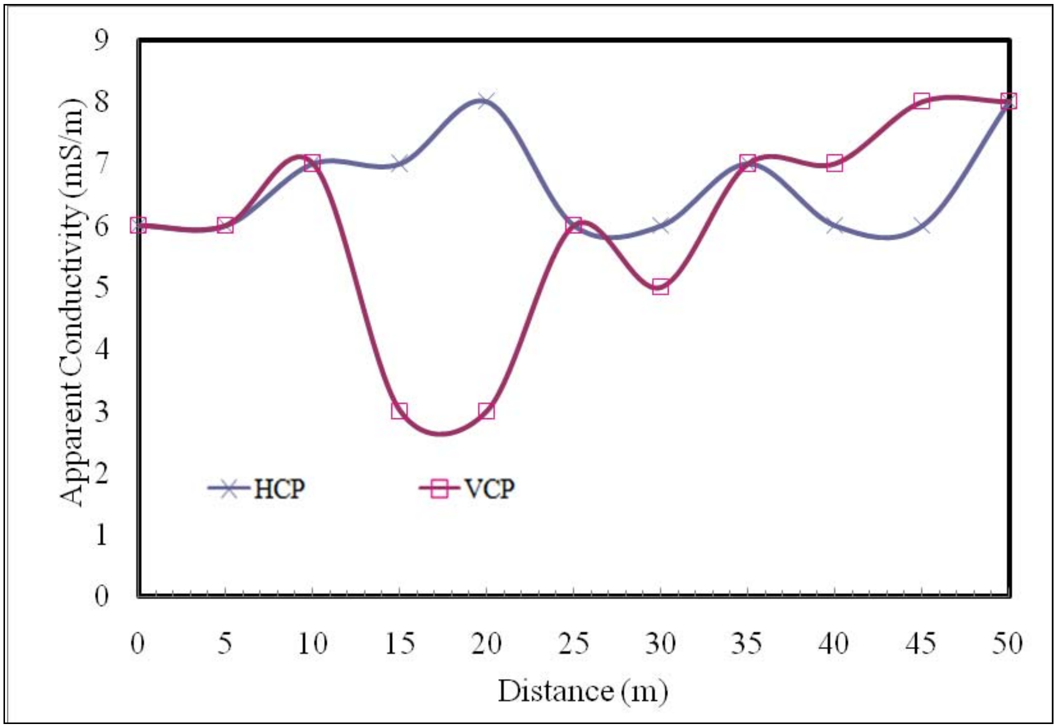

Figure 5.79 - Grid 2 Line 13 (60m), Ground Conductivity (Quad-phase), Parallel to Line

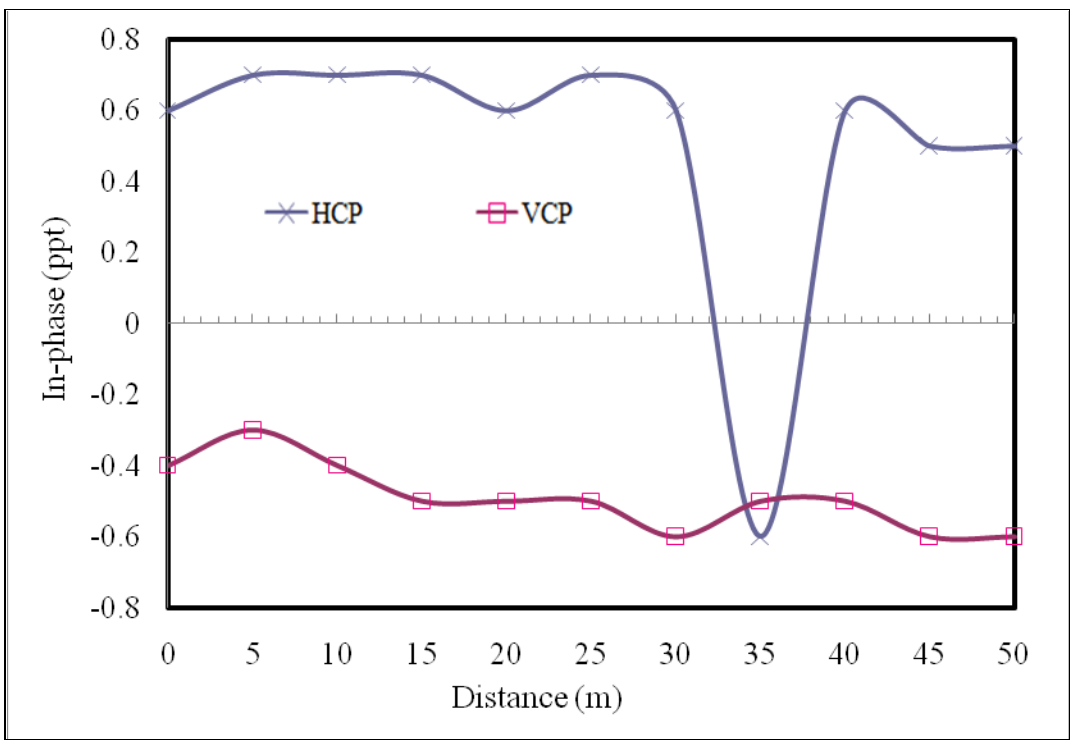

Figure 5.80 - Grid 2 Line 13 (60m), Magnetic Susceptibility (In-phase), Parallel to Line

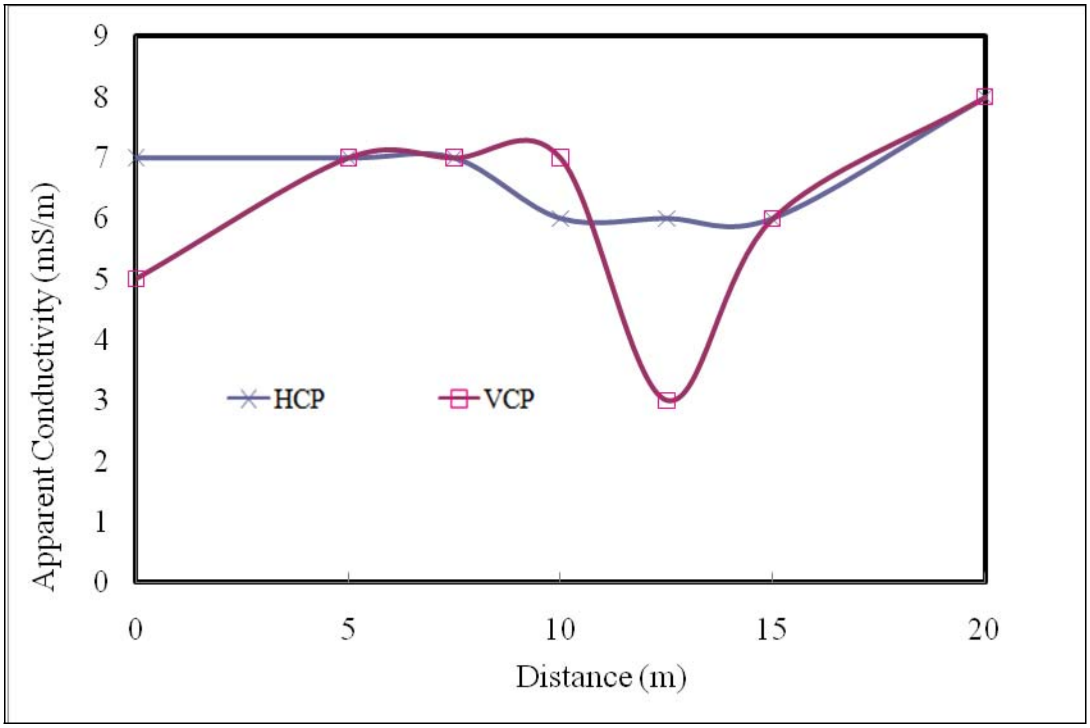

Figure 5.81 – Desiccation Cracks Line 1 (0m), Ground Conductivity (Quad-phase), Perpendicular to Line

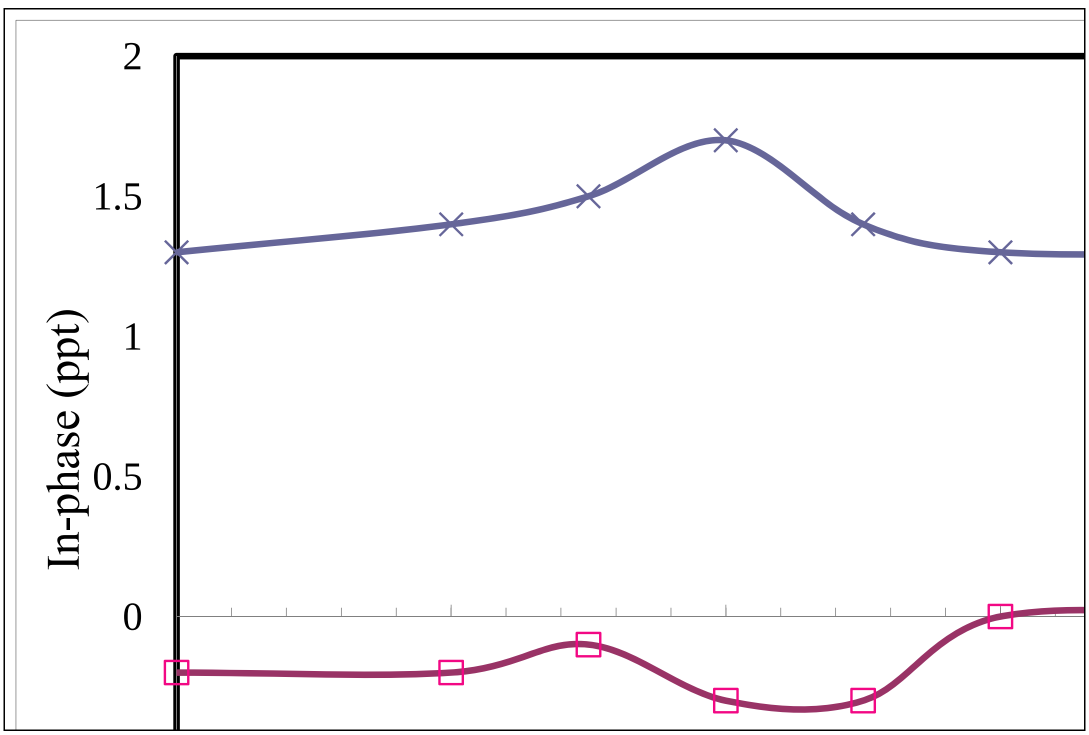

Figure 5.82 – Desiccation Cracks Line 1 (0m), Magnetic Susceptibility (In-phase), Perpendicular to Line

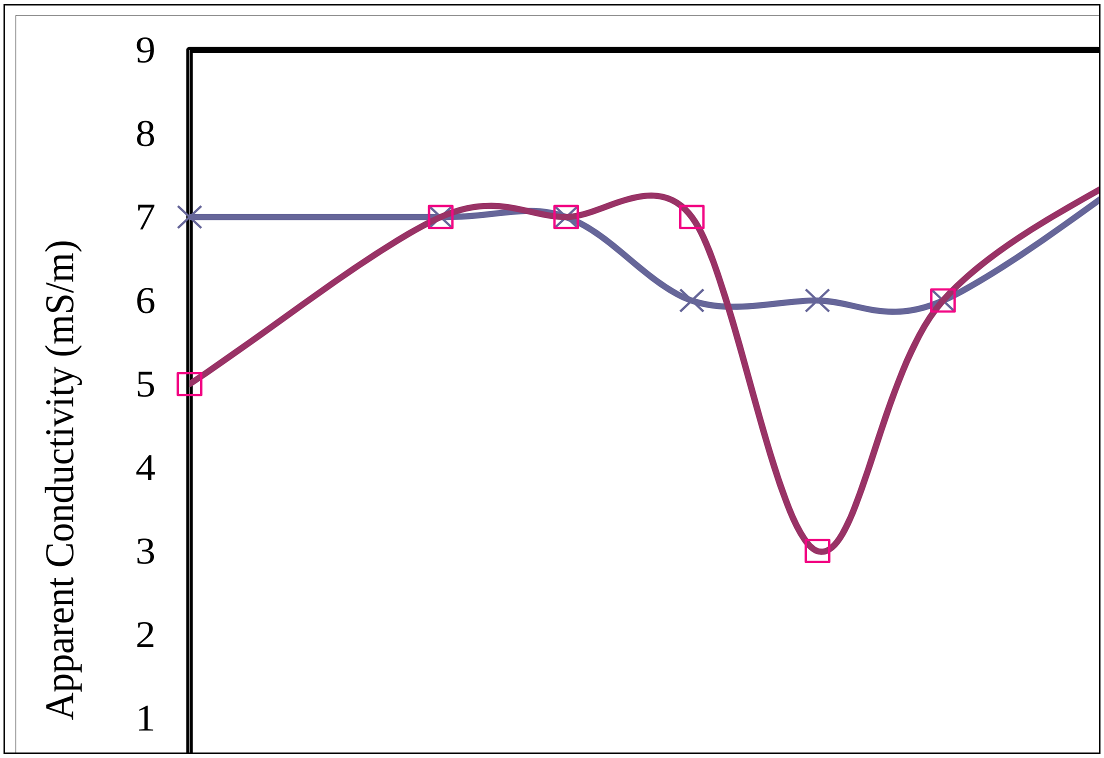

Figure 5.83 – Desiccation Cracks Line 1 (0m), Ground Conductivity (Quad-phase), Parallel to Line

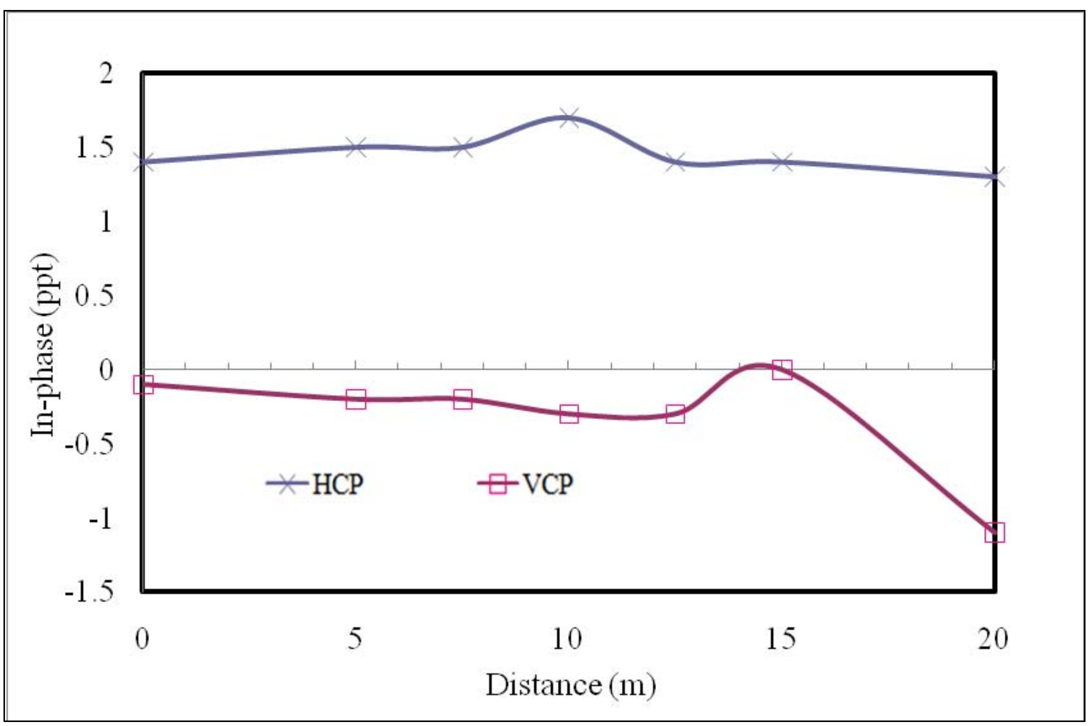

Figure 5.84 – Desiccation Cracks Line 1 (0m), Magnetic Susceptibility (In-phase), Parallel to Line

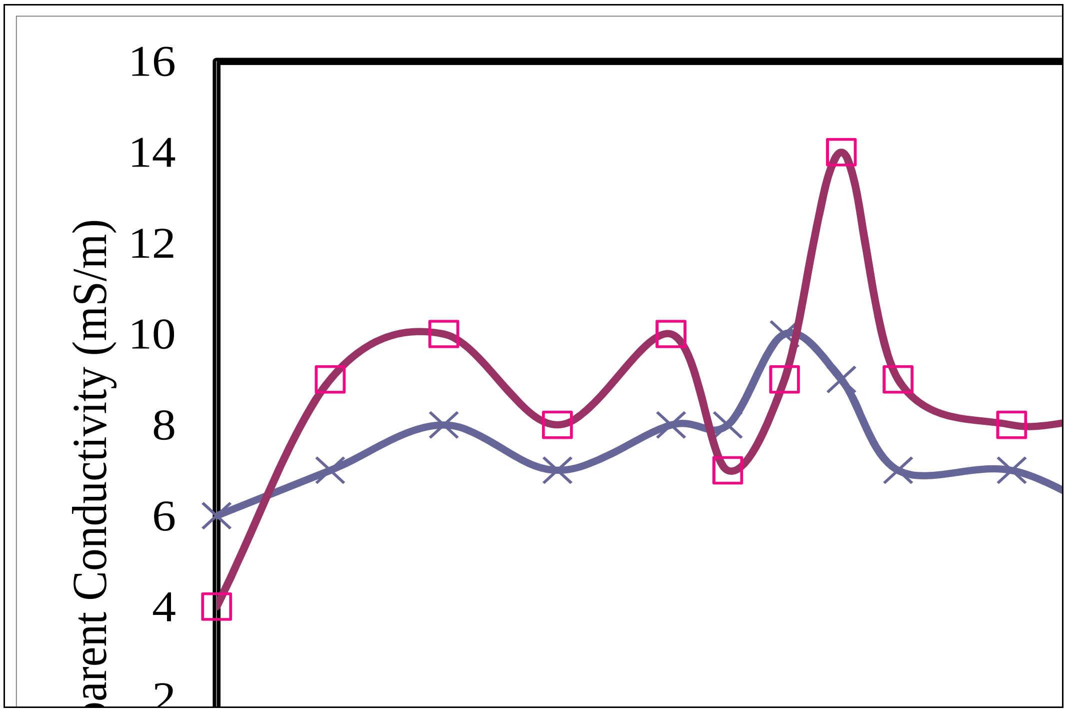

Figure 5.85 – Desiccation Cracks Line 2 (10m), Ground Conductivity (Quad-phase), Perpendicular to Line

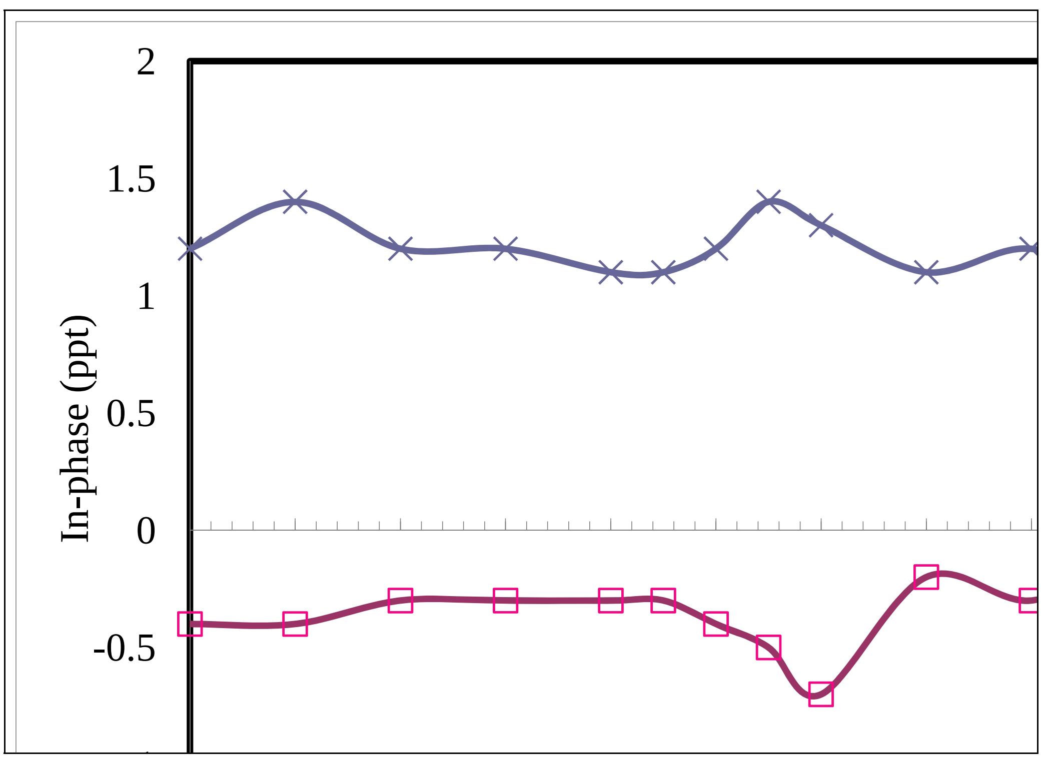

Figure 5.86 – Desiccation Cracks Line 2 (10m), Magnetic Susceptibility (In-phase), Perpendicular to Line

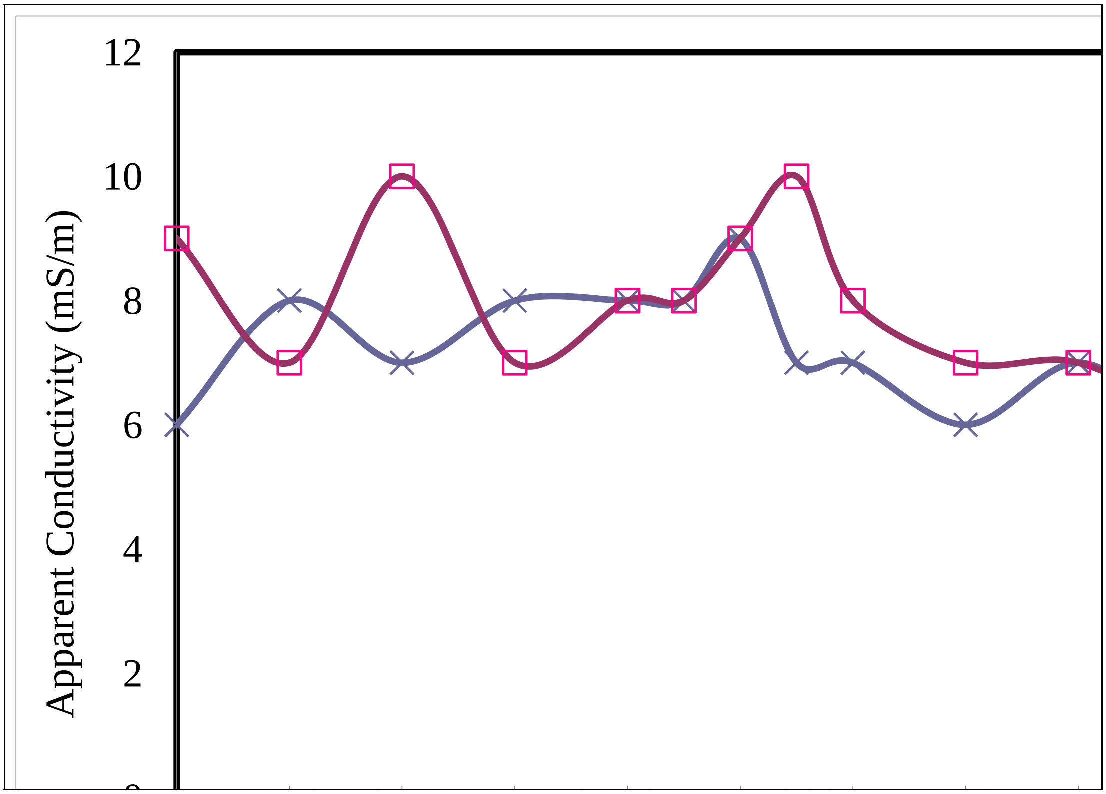

Figure 5.87 – Desiccation Cracks Line 2 (10m), Ground Conductivity (Quad-phase), Parallel to Line

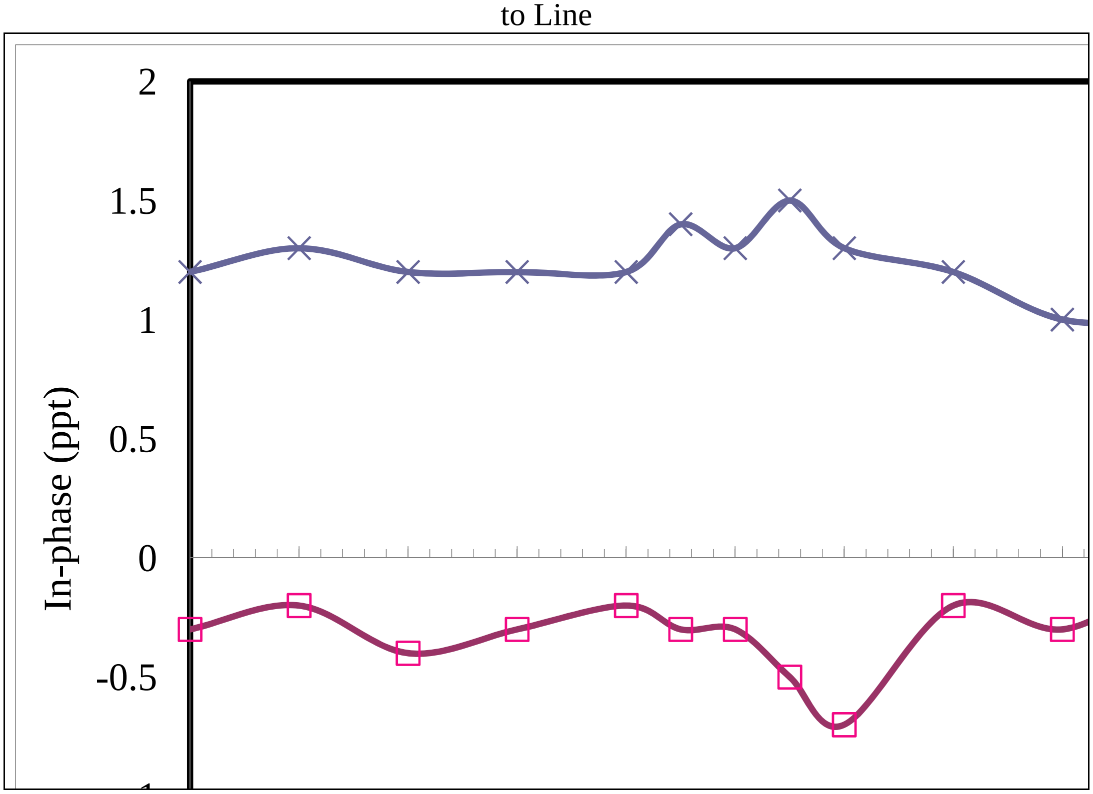

Figure 5.88 – Desiccation Cracks Line 2 (10m), Magnetic Susceptibility (In-phase), Parallel to Line

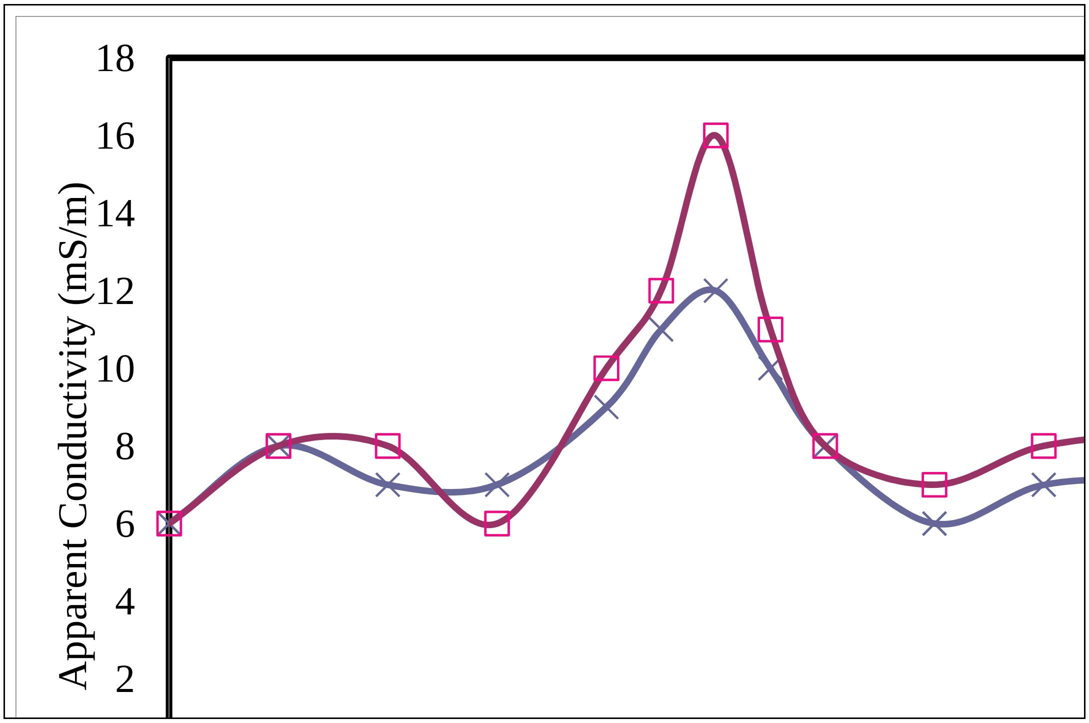

Figure 5.89 – Desiccation Cracks Line 3 (15m), Ground Conductivity (Quad-phase), Perpendicular to Line

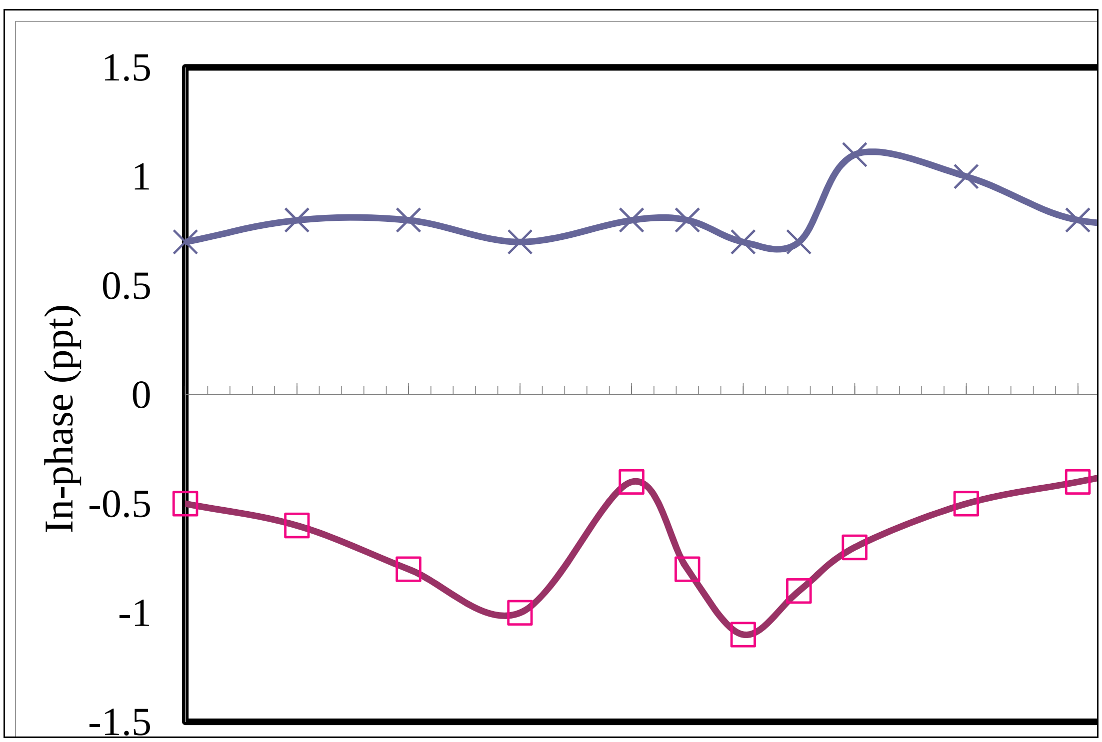

Figure 5.90 – Desiccation Cracks Line 3 (15m), Magnetic Susceptibility (In-phase), Perpendicular to Line

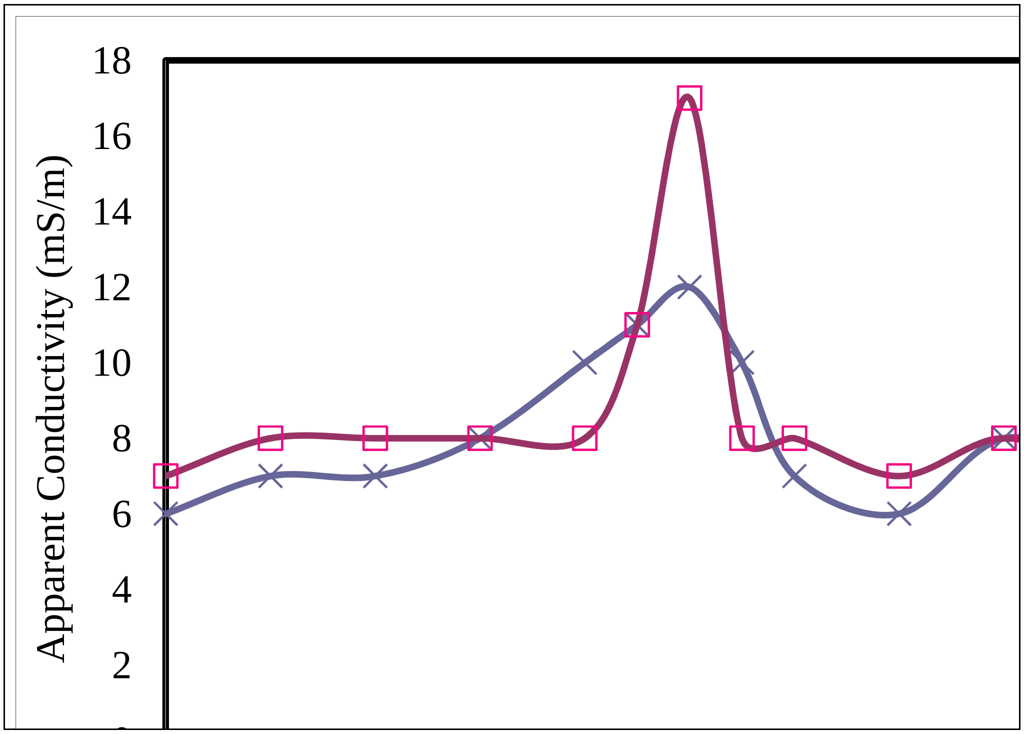

Figure 5.91 – Desiccation Cracks Line 3 (15m), Ground Conductivity (Quad-phase), Parallel to Line

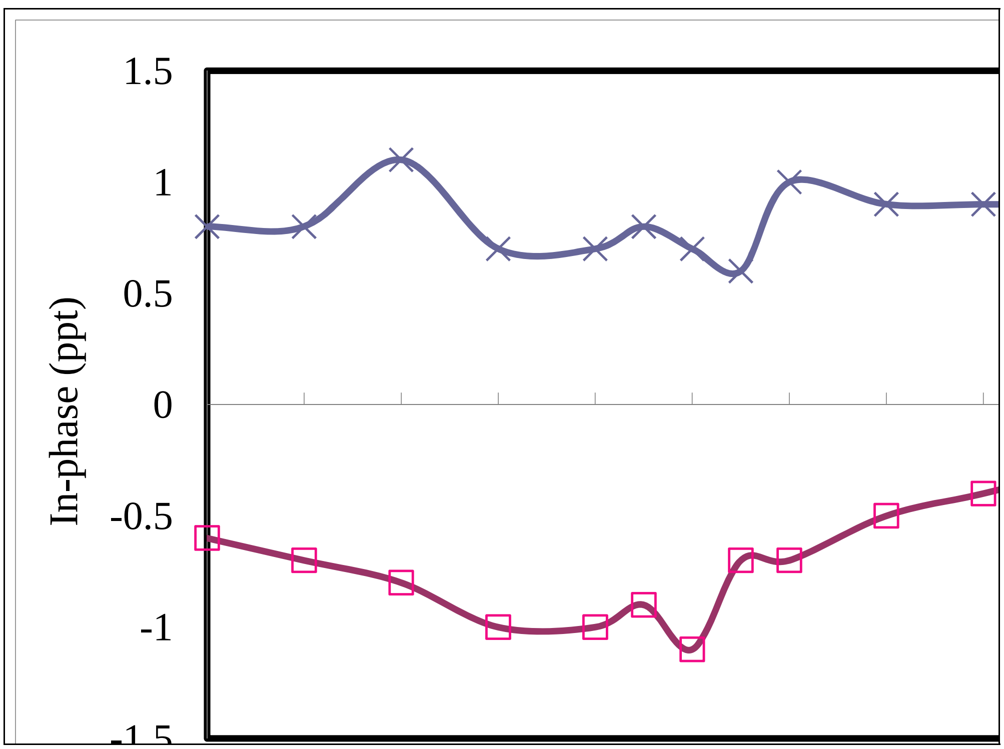

Figure 5.92 – Desiccation Cracks Line 3 (15m), Magnetic Susceptibility (In-phase), Parallel to Line

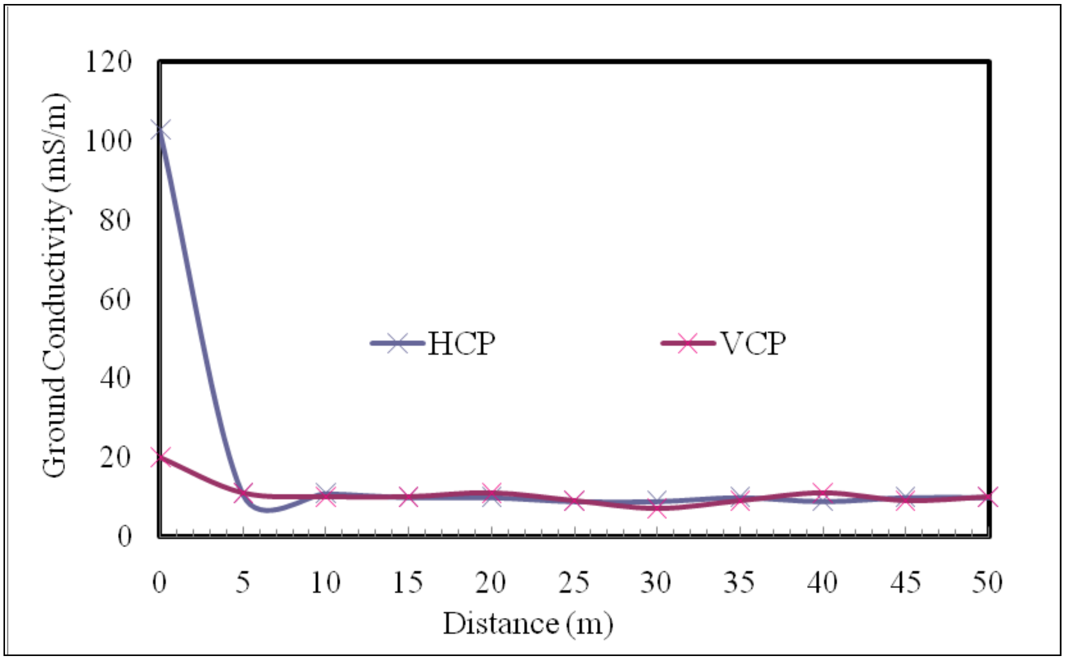

Figure 5.93 – Culture Plot Power Line, Ground Conductivity (Quad-phase), Perpendicular to Line

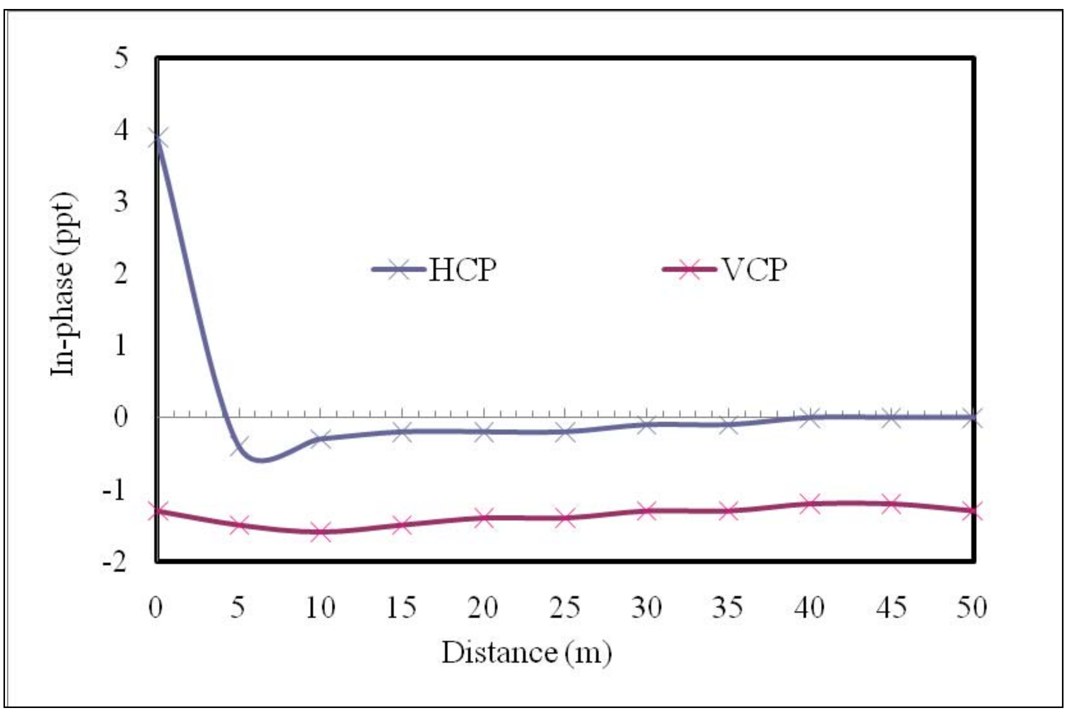

Figure 5.94 – Culture Plot Power Line, Magnetic Susceptibility (In-phase), Perpendicular to Line

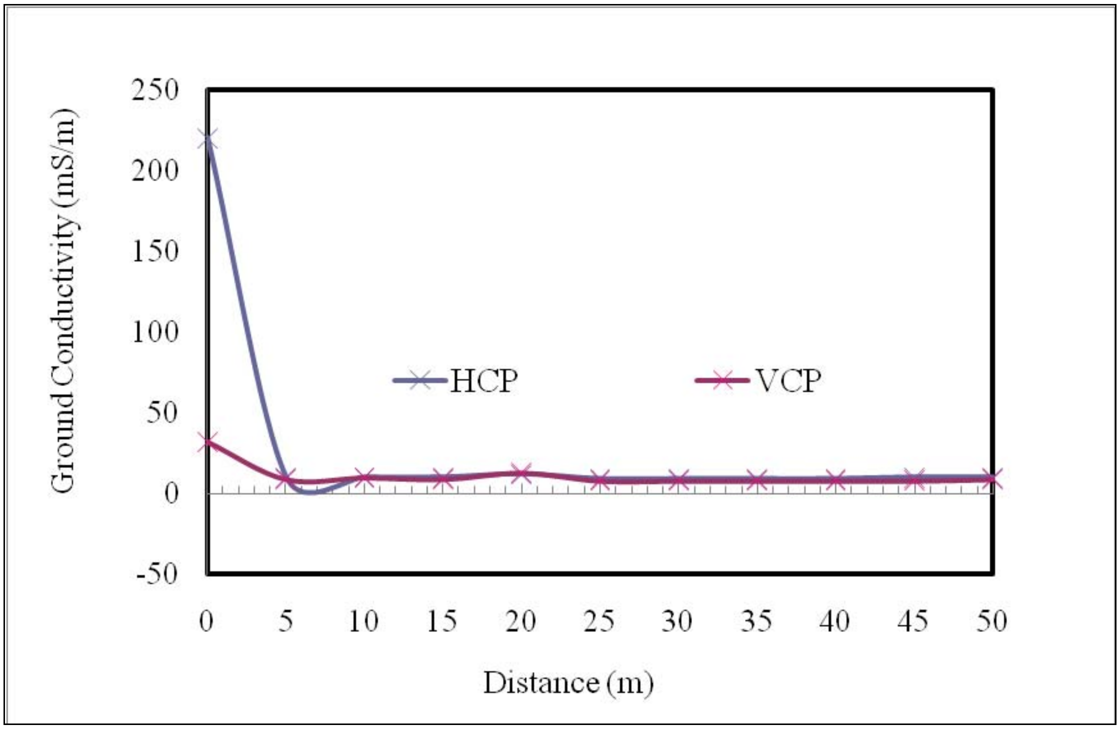

Figure 5.95 – Culture Plot Power Line, Ground Conductivity (Quad-phase), Parallel to Line

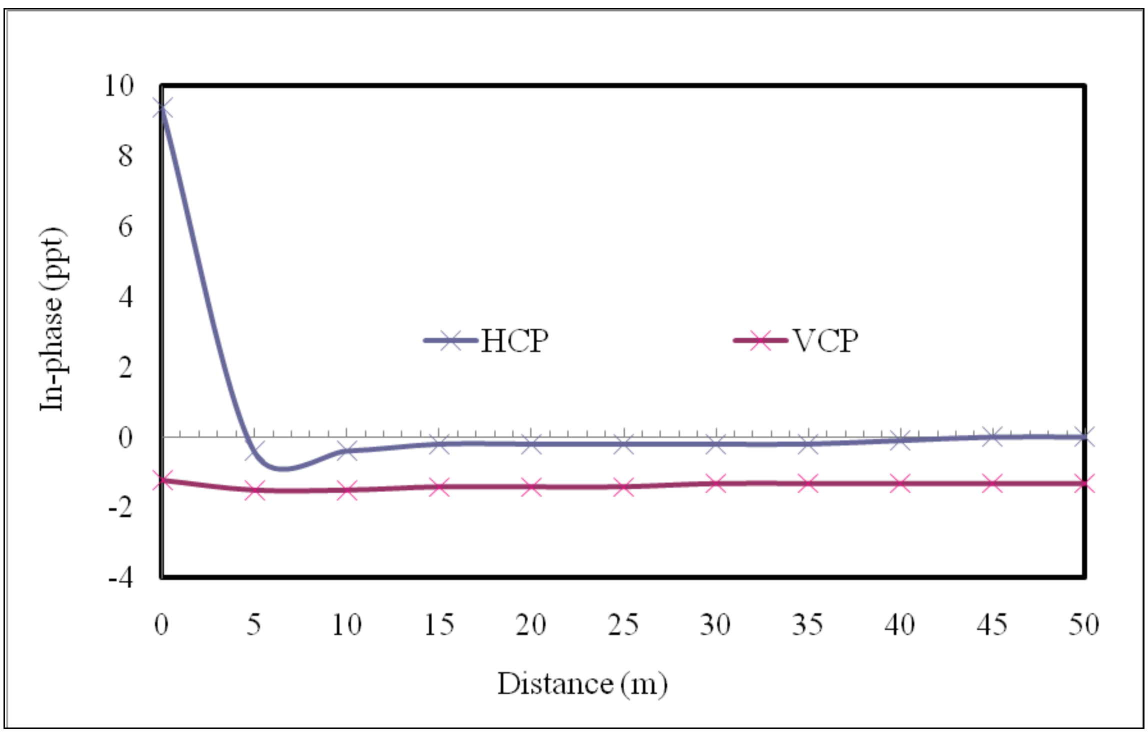

Figure 5.96 – Culture Plot Power Line, Magnetic Susceptibility (In-phase), Parallel to Line

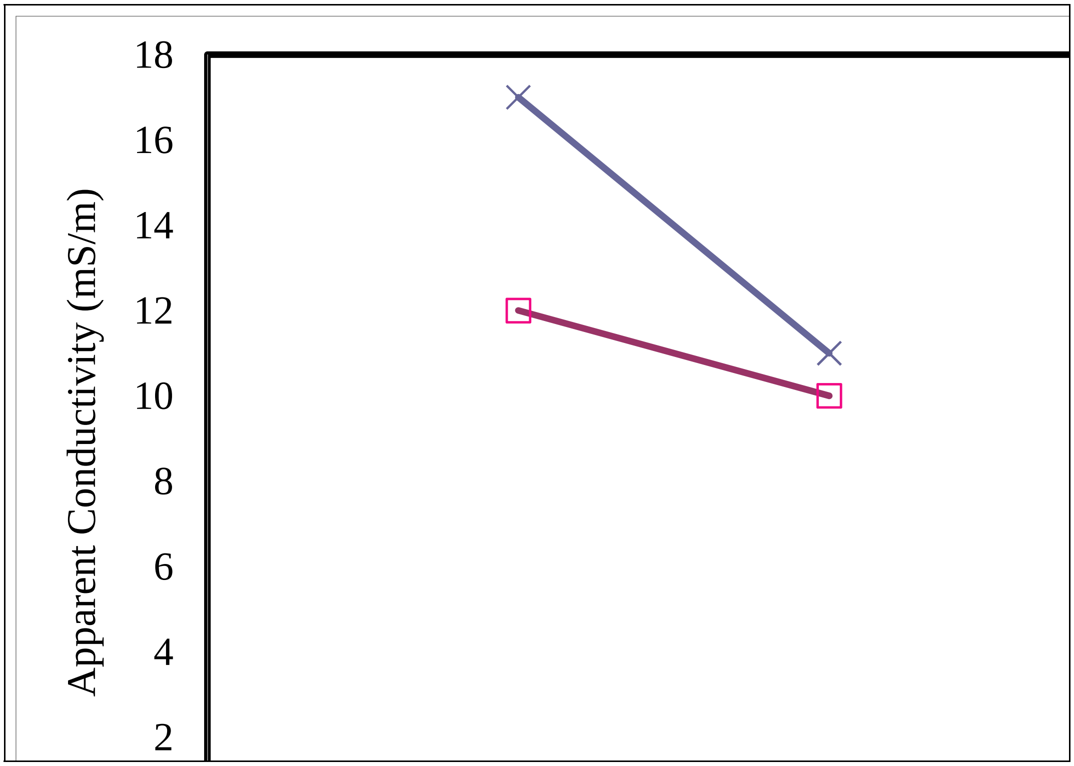

Figure 5.97 – Culture Plots Fence Line, Ground Conductivity (Quad-phase), Perpendicular to Line

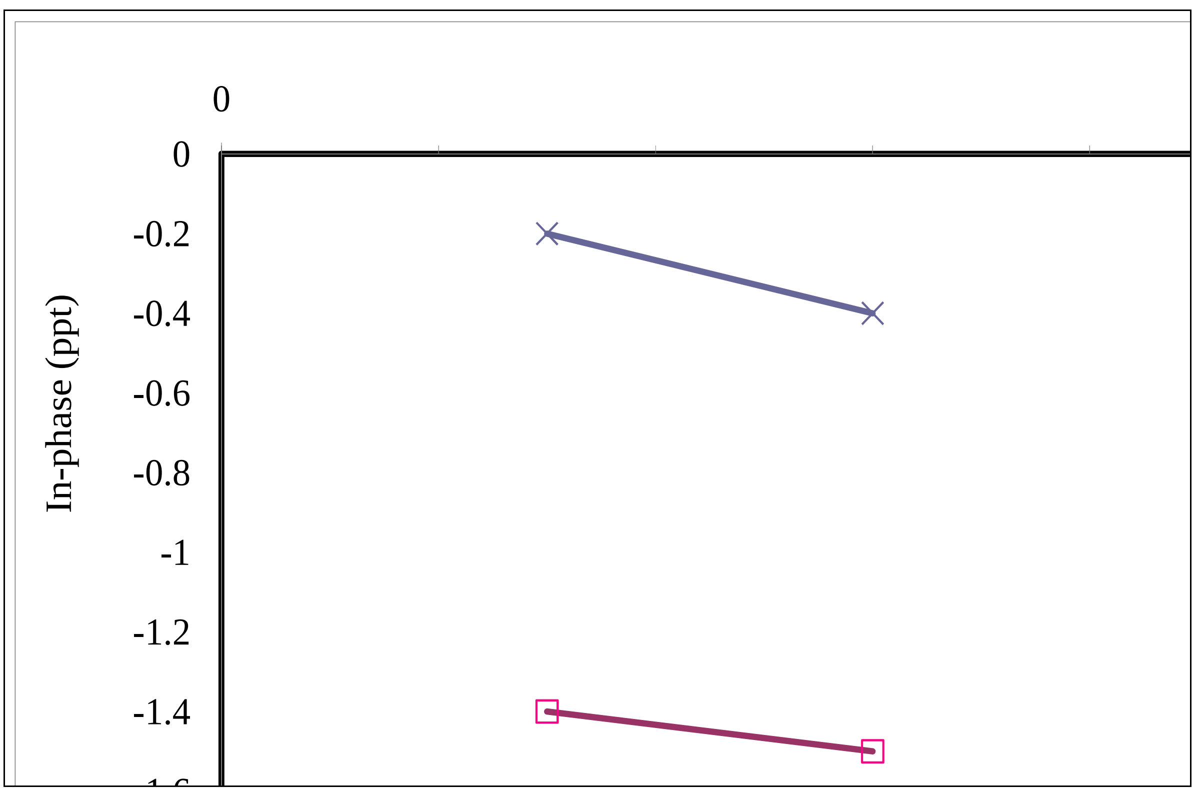

Figure 5.98 – Culture Plots Fence Line, Magnetic Susceptibility (In-phase), Perpendicular to Line

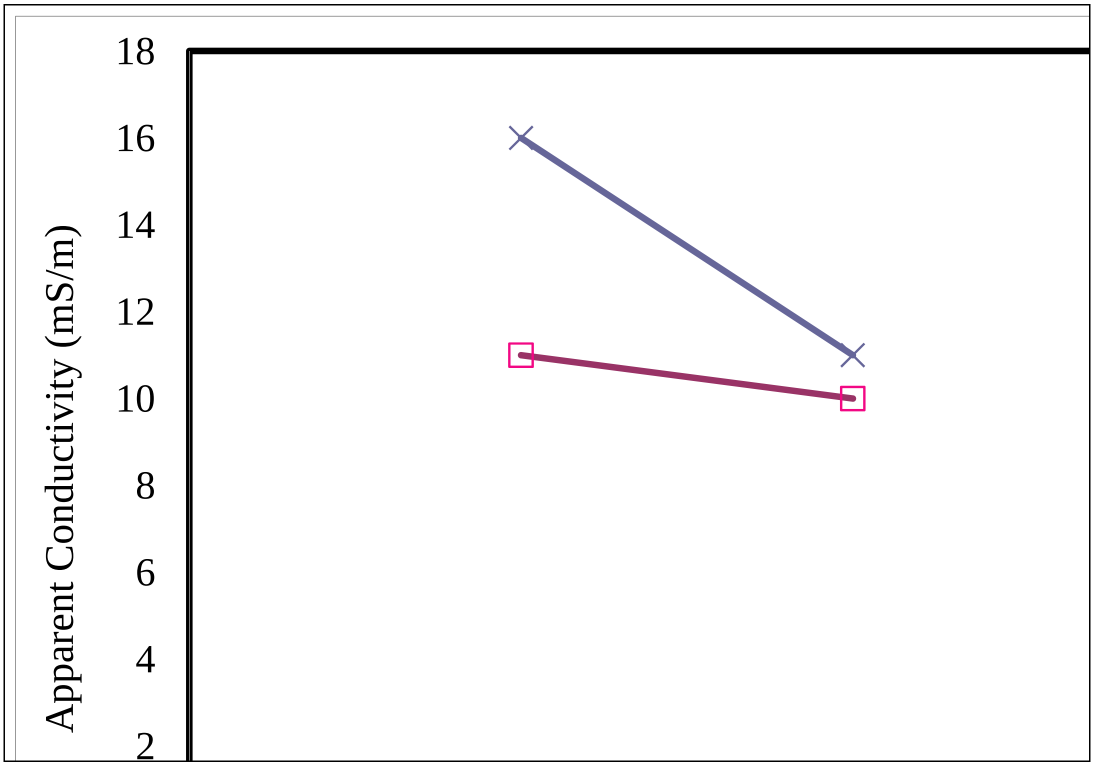

Figure 5.99 – Culture Plots Fence Line, Ground Conductivity (Quad-phase), Parallel to Line

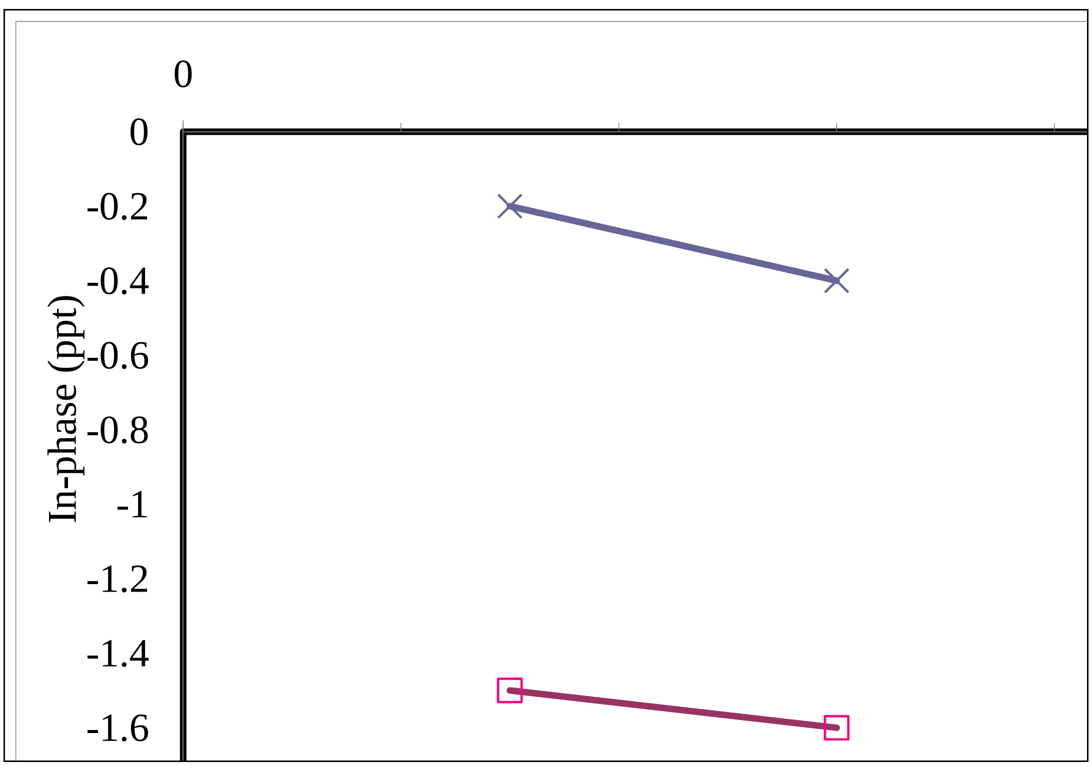

Figure 5.100 – Culture Plots Fence Line, Magnetic Susceptibility (In-phase), Parallel to Line

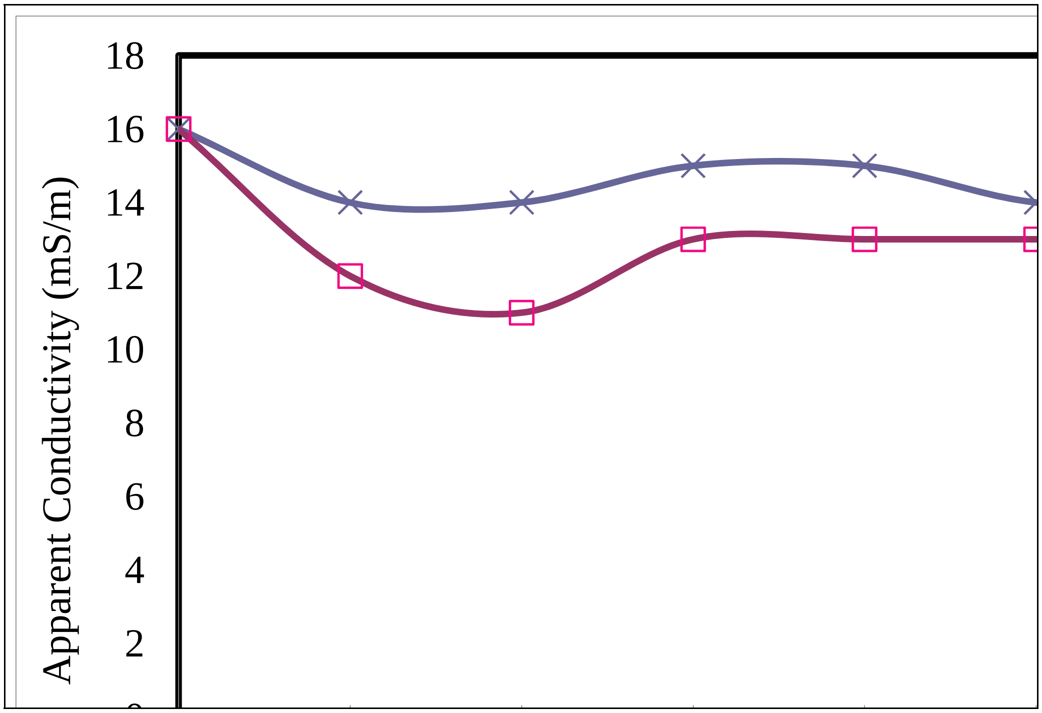

Figure 5.101 – Culture Plot Seismic Line, Ground Conductivity (Quad-phase), Perpendicular to Line

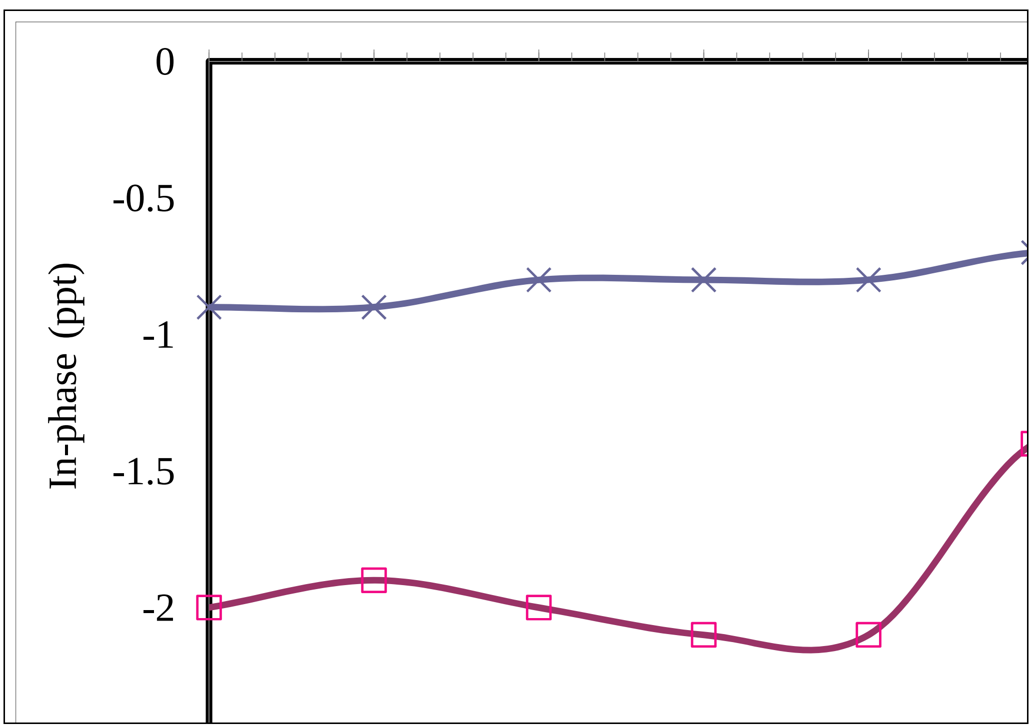

Figure 5.102 – Culture Plot Seismic Line, Magnetic Susceptibility (In-phase), Perpendicular to Line

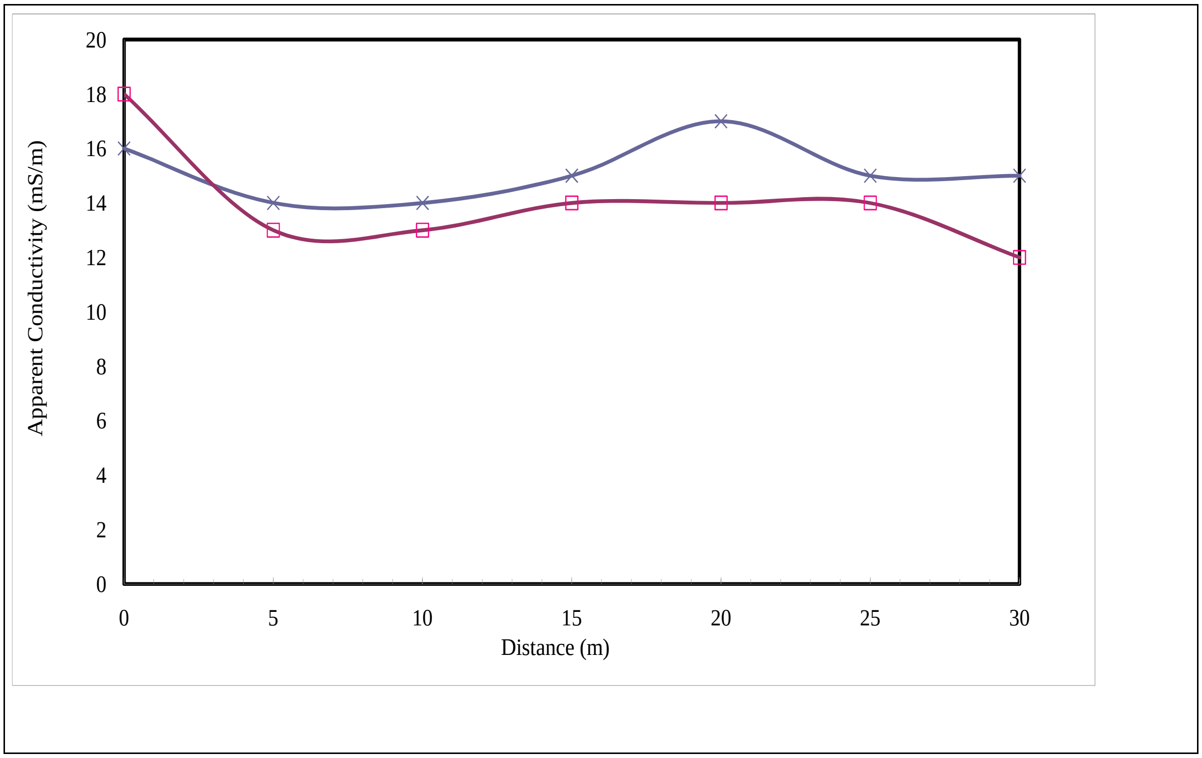

Figure 5.103 – Culture Plot Seismic Line, Ground Conductivity (Quad-phase), Parallel to Line

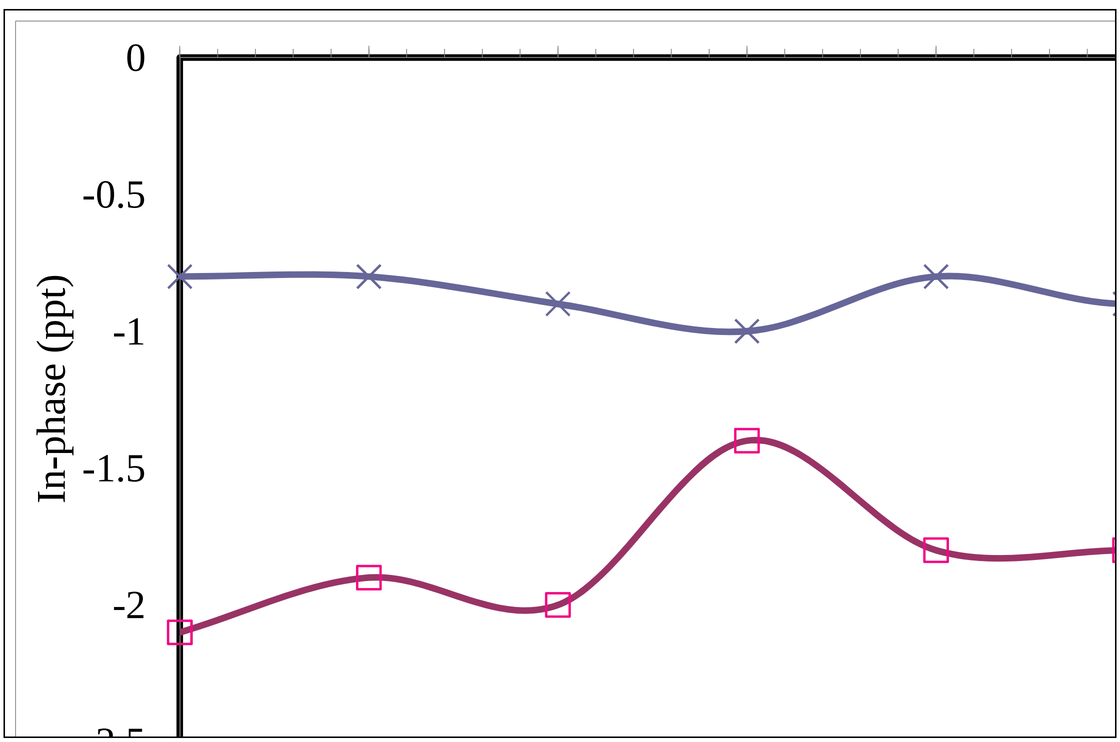

Figure 5.104 – Culture Plot Seismic Line, Magnetic Susceptibility (In-phase), Parallel to Line

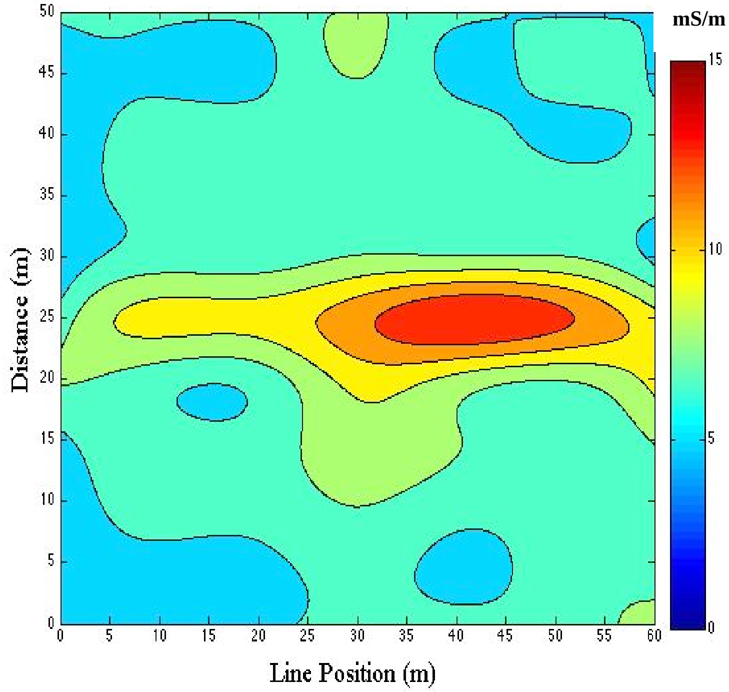

Figure 5.105 Grid 1 - Quad-phase – HCP, Perpendicular to Line

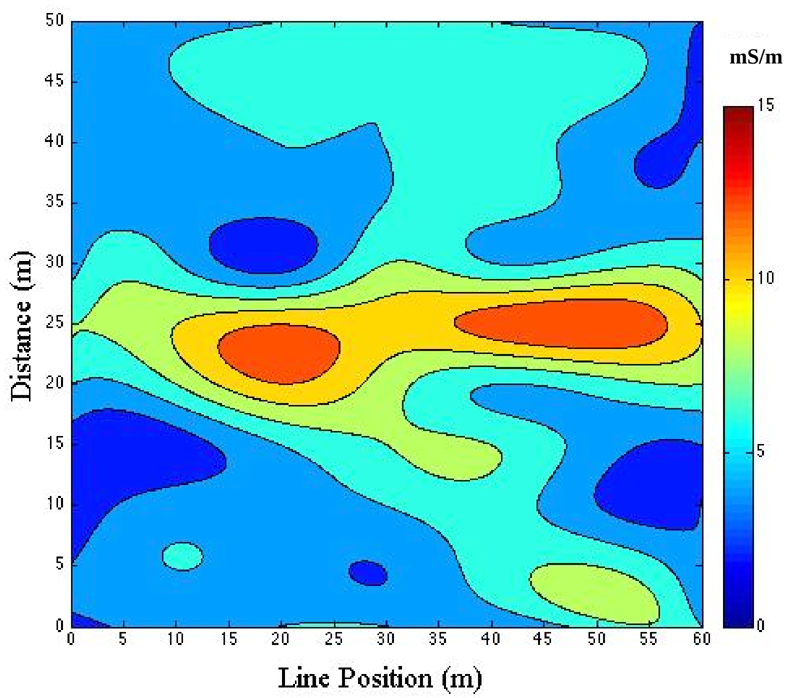

Figure 5.106 Grid 1 – Quad-phase – VCP, Perpendicular to Line

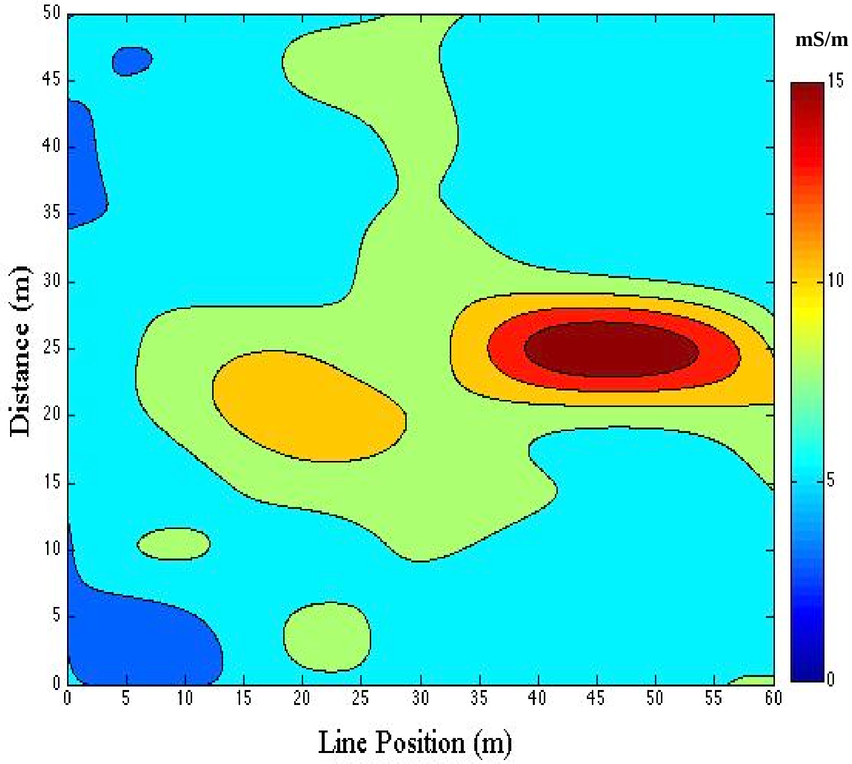

Figure 5.107 Grid - Quad-phase – HCP, Parallel to Line

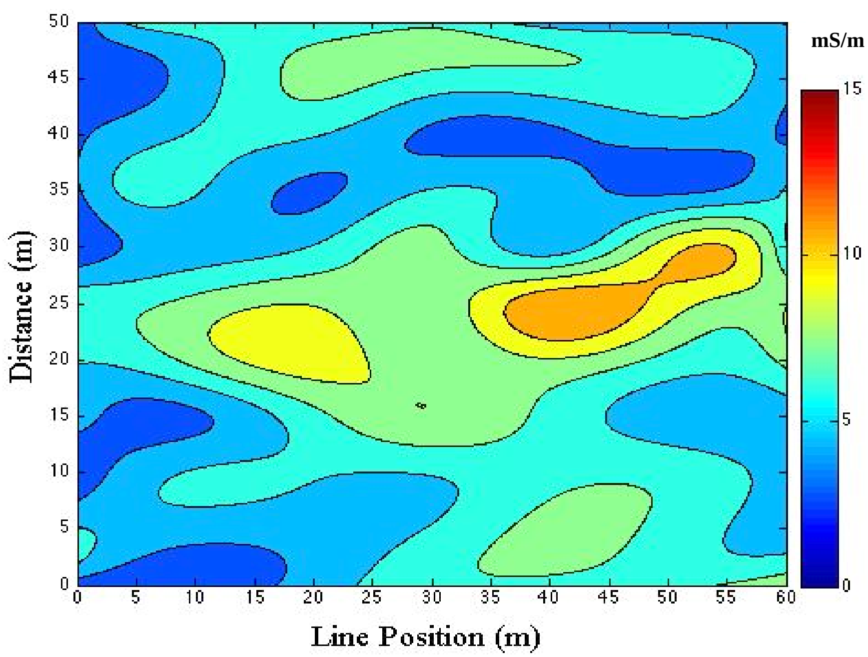

Figure 5.108 Grid 1 - Quad-phase – VCP, Parallel to Line

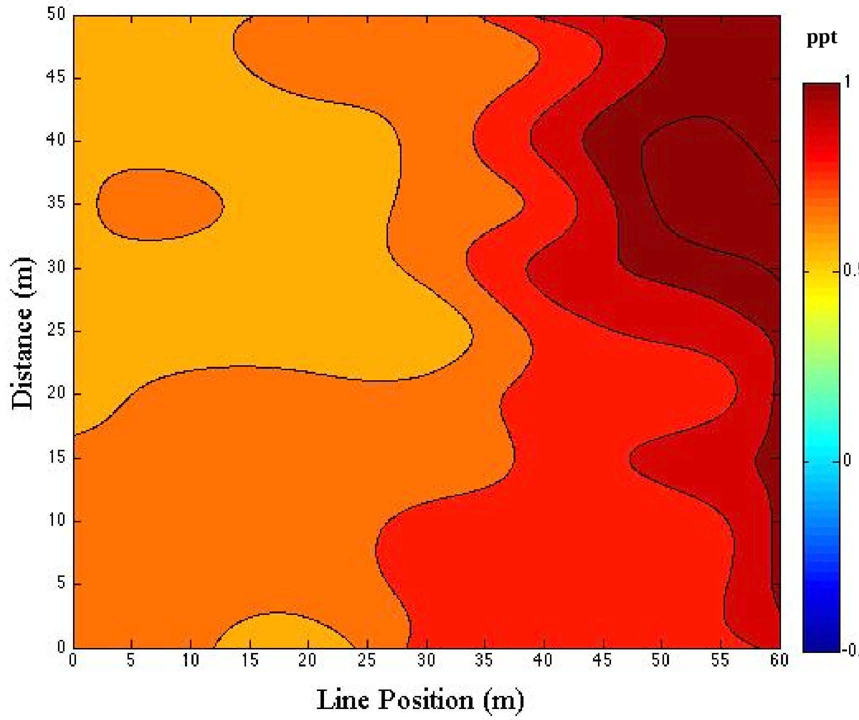

Figure 5.109 Grid 1 - In-phase – HCP, Perpendicular to Line

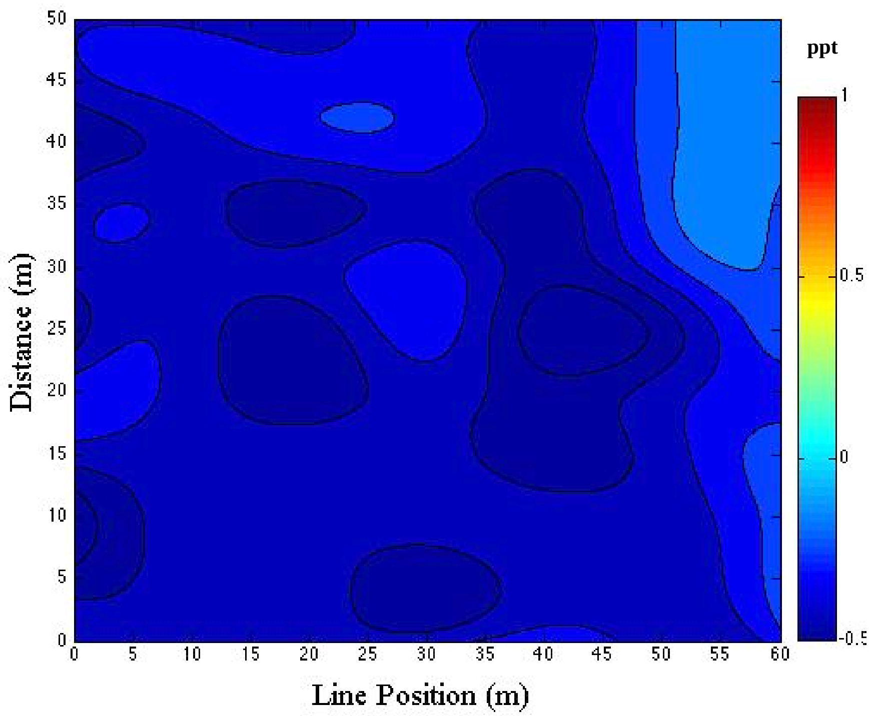

Figure 5.110 Grid 1 - In-phase – VCP, Perpendicular to Line

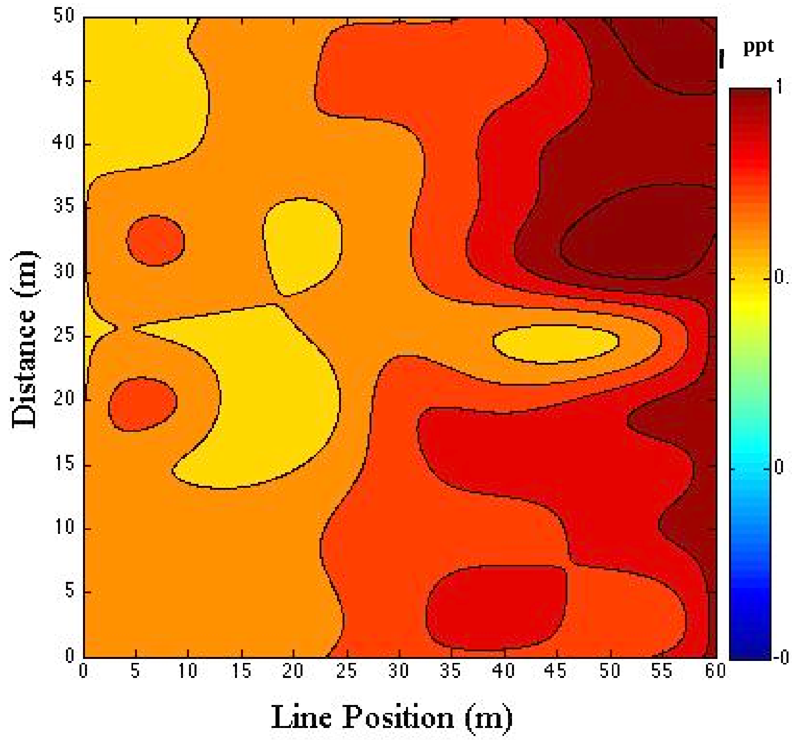

Figure 5.111 Grid 1 - In-phase – HCP, Parallel to Line

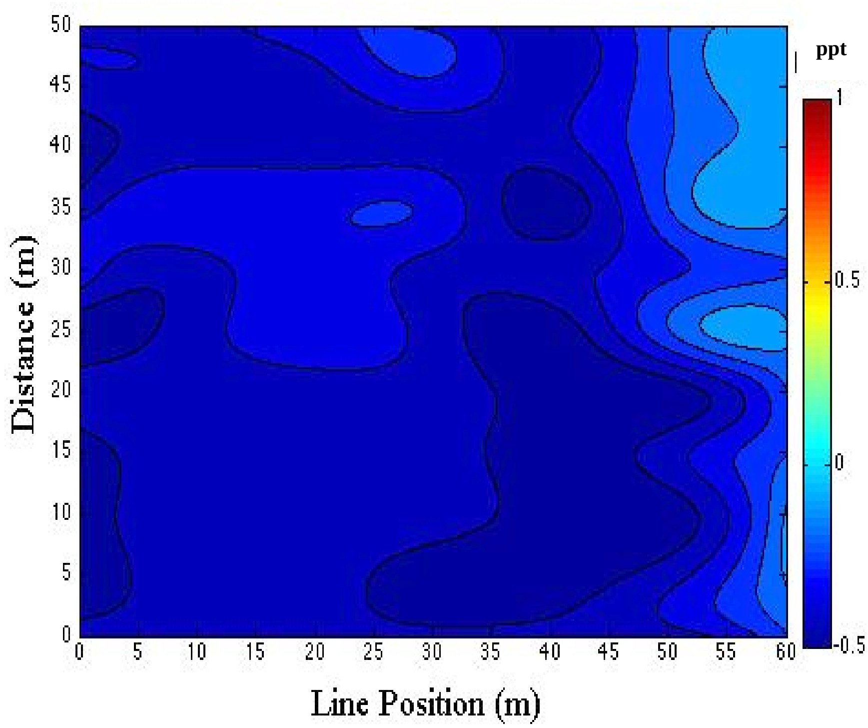

Figure 5.112 Grid 1 - In-phase – VCP, Parallel to Line

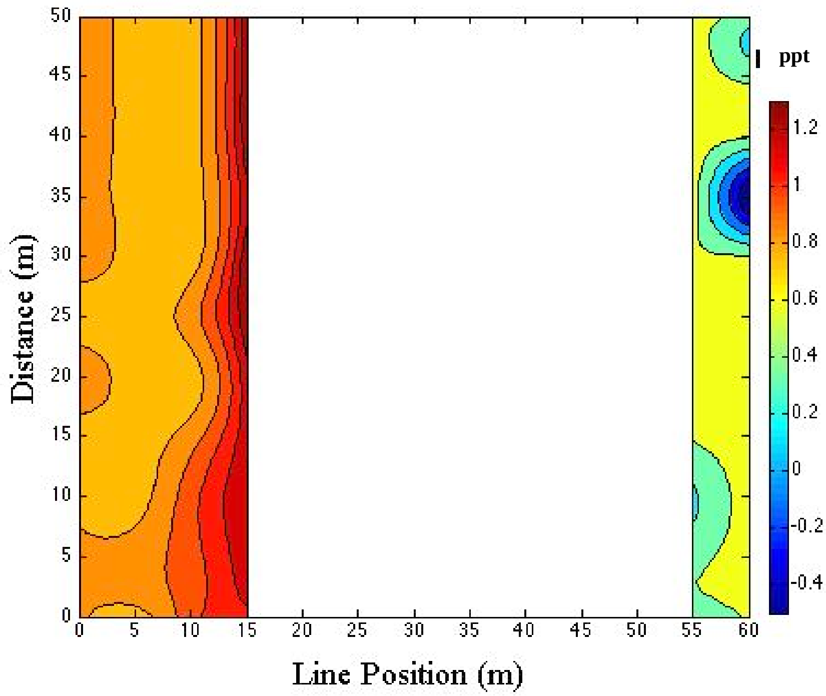

Figure 5.113 Grid 2 - In-phase – HCP, Parallel to Line

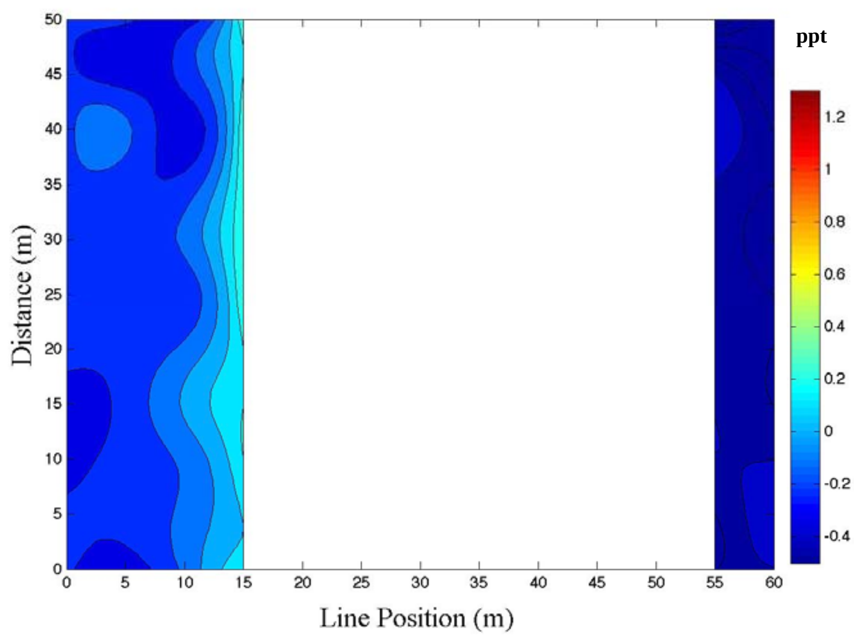

Figure 5.114 Grid 2 - In-phase – VCP, Parallel to Line

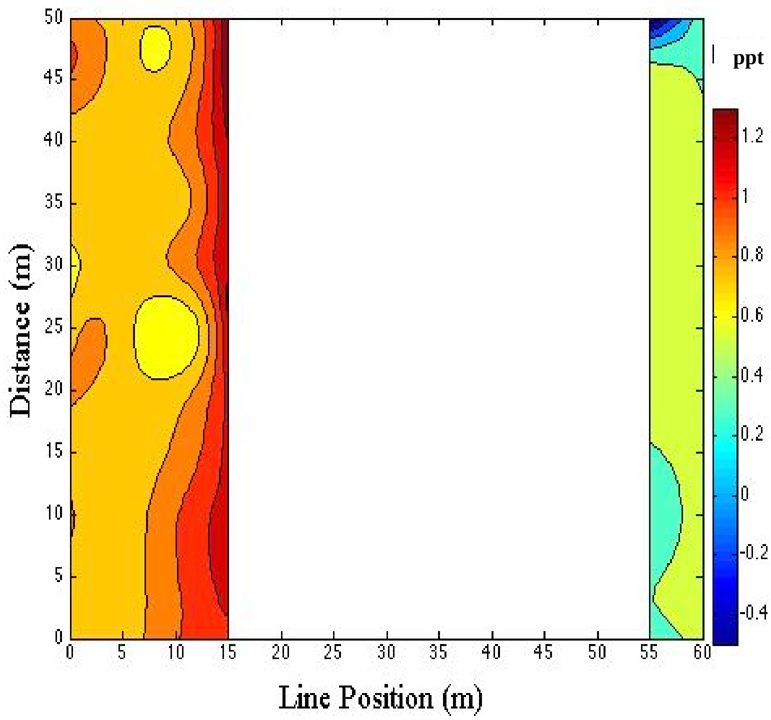

Figure 5.115 Grid 2 - In-phase – HCP, Perpendicular to Line

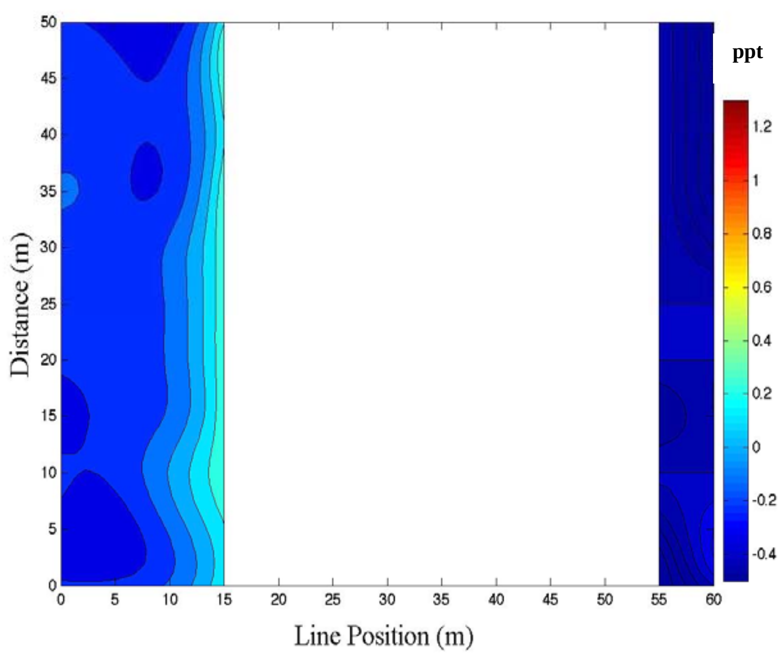

Figure 5.116 Grid 2 - In-phase – VCP, Perpendicular to Line

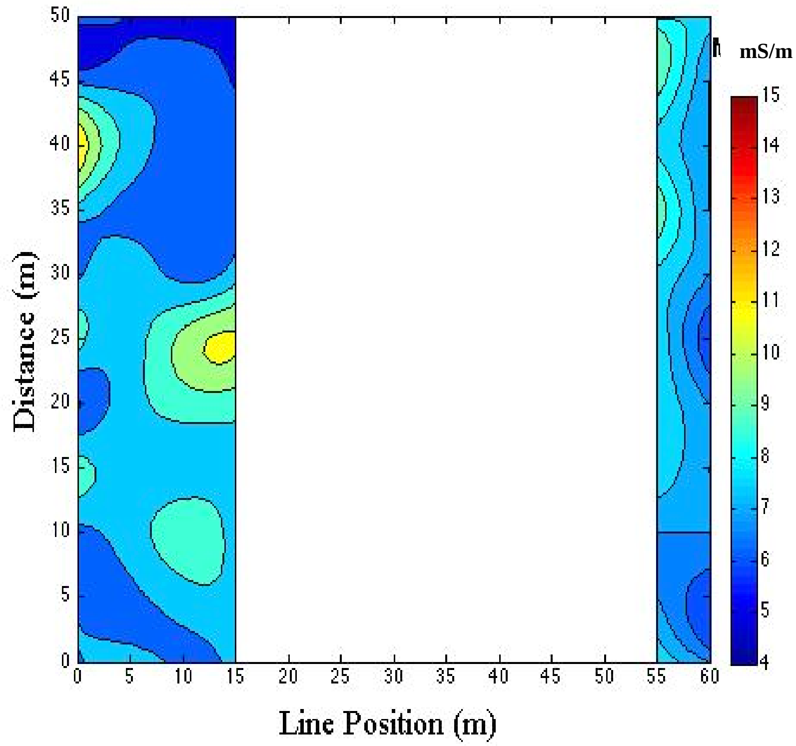

Figure 5.117 Grid 2 - Quad-phase – HCP, Perpendicular

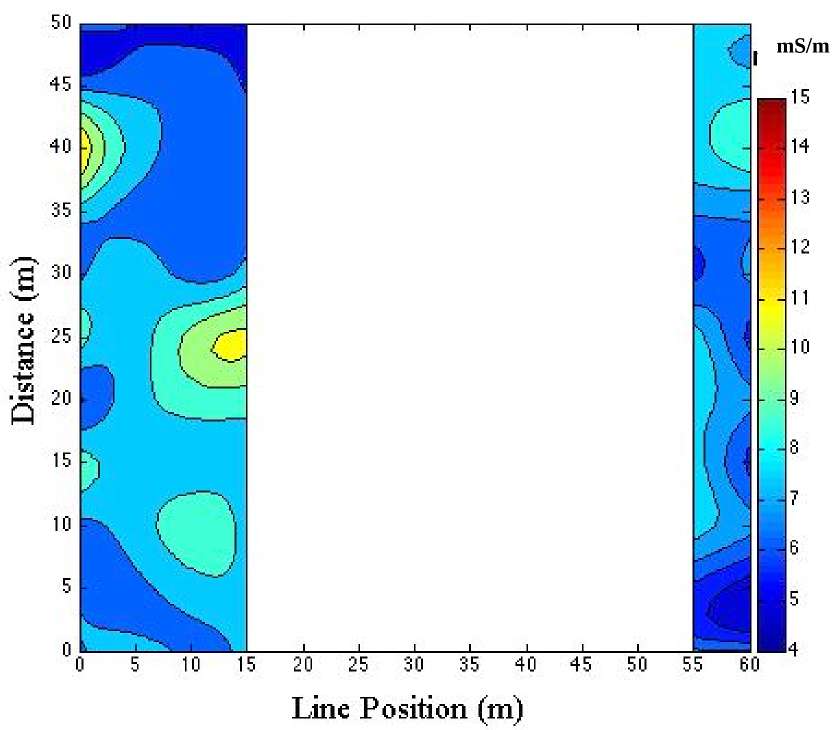

Figure 5.118 Grid 2 - Quad-phase – VCP, Perpendicular to Line

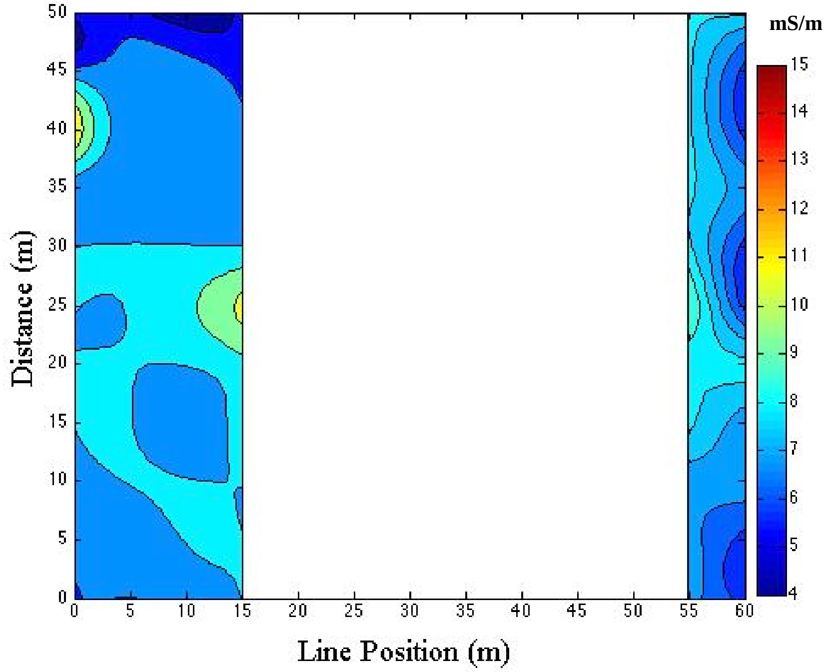

Figure 5.119 Grid 2: Quad-phase – HCP, Parallel to Line

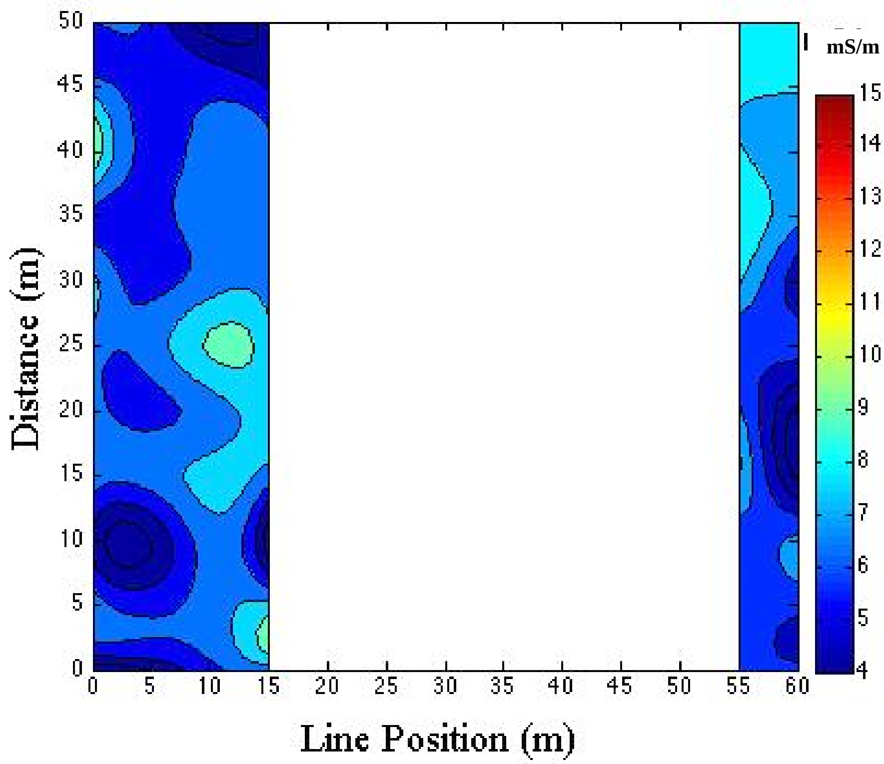

Figure 5.120 Grid 2 Quad-phase – VCP, Parallel to Line

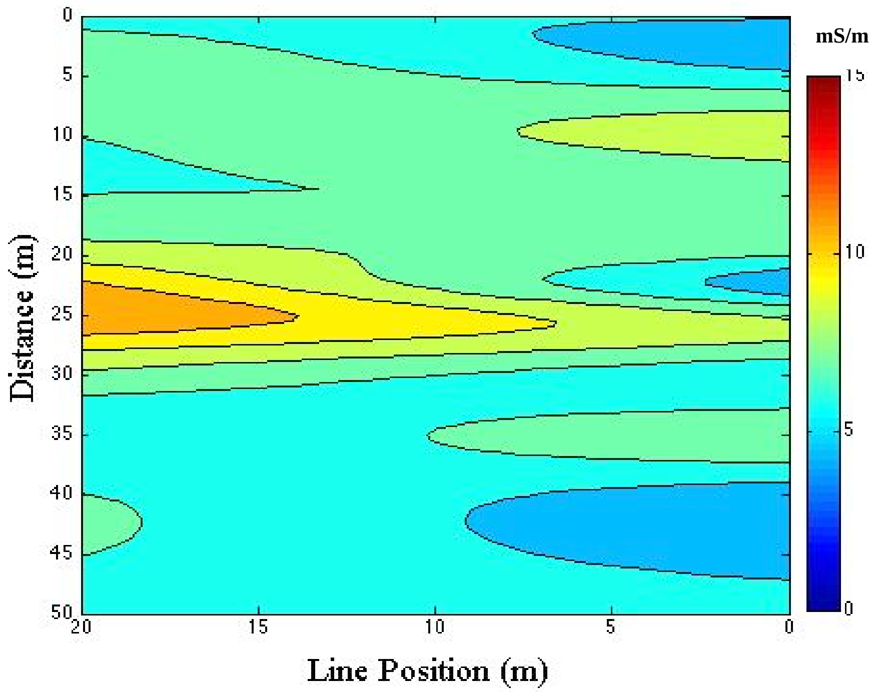

Figure 5.121 Desiccation Cracks - Quad-phase – HCP, Perpendicular to Line

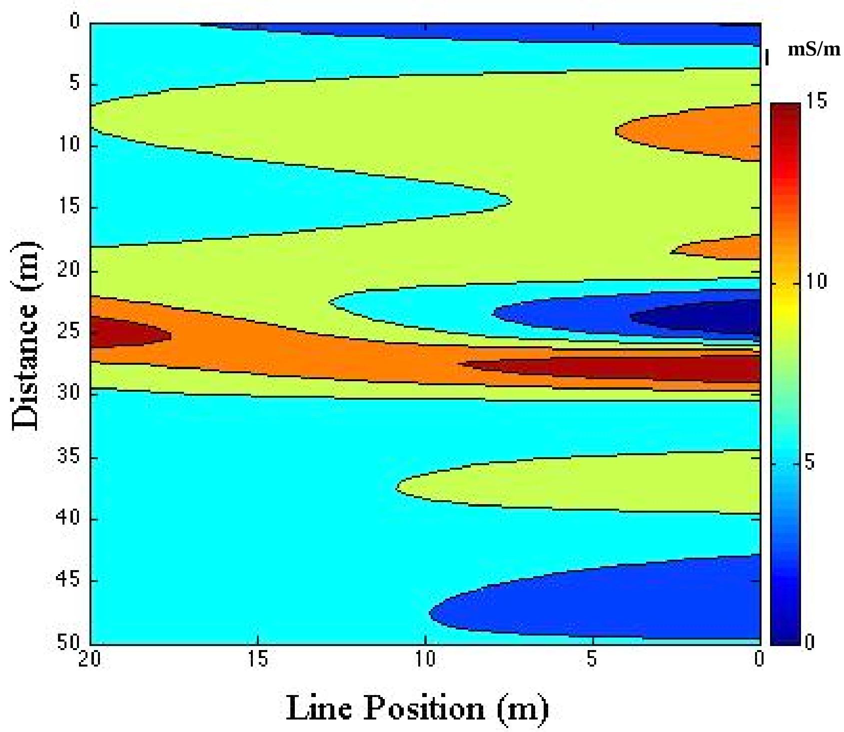

Figure 5.122 Desiccation Cracks - Quad-phase – VCP, Perpendicular to Line

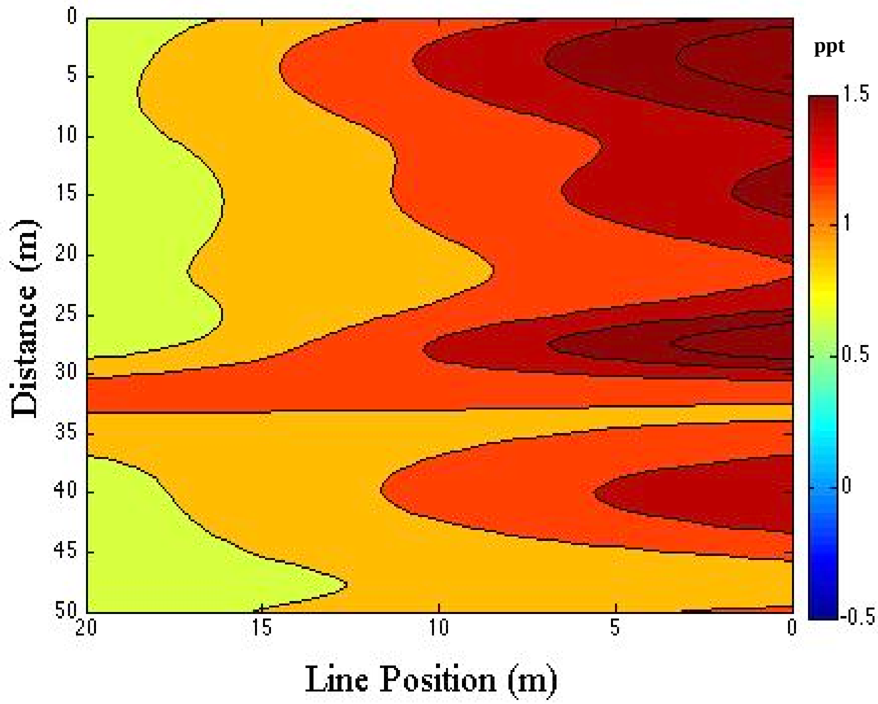

Figure 5.123 Desiccation Cracks: - In-phase – HCP, Perpendicular to Line

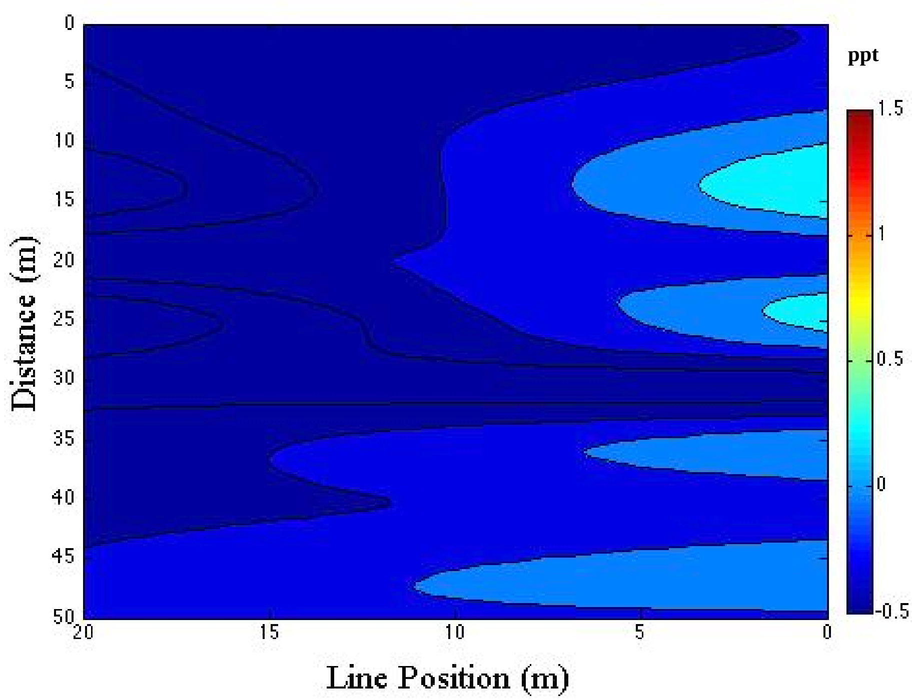

Figure 5.124 Desiccation Cracks: - In-phase – VCP, Perpendicular to Line

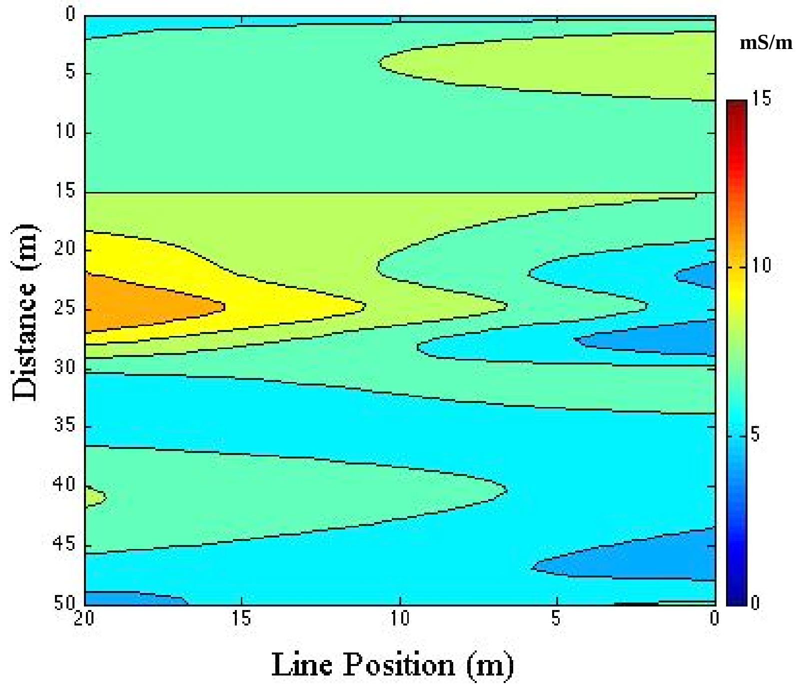

Figure 5.125 Desiccation Cracks: - Quad-phase – HCP, Parallel to Line

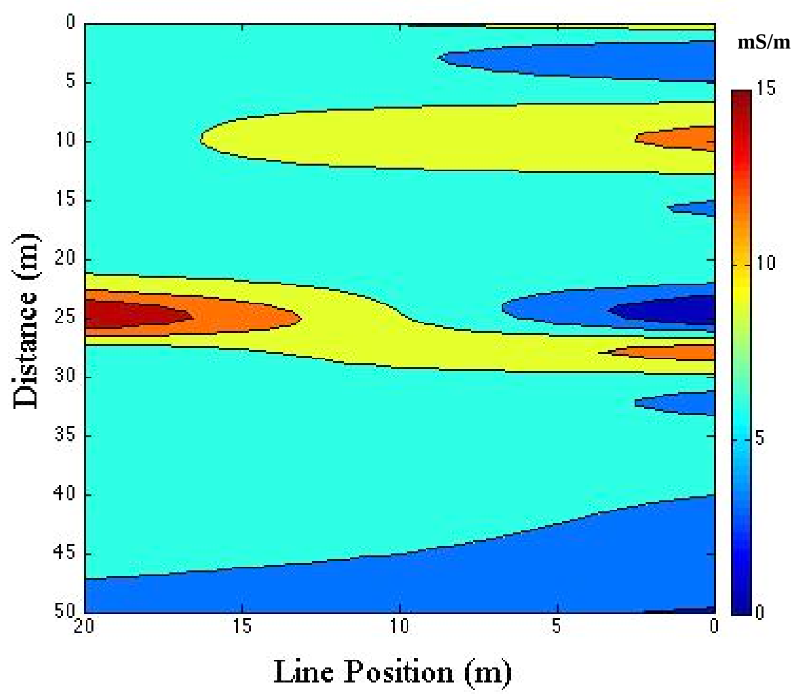

Figure 5.126 Desiccation Cracks: - Quad-phase – VCP, Parallel to Line

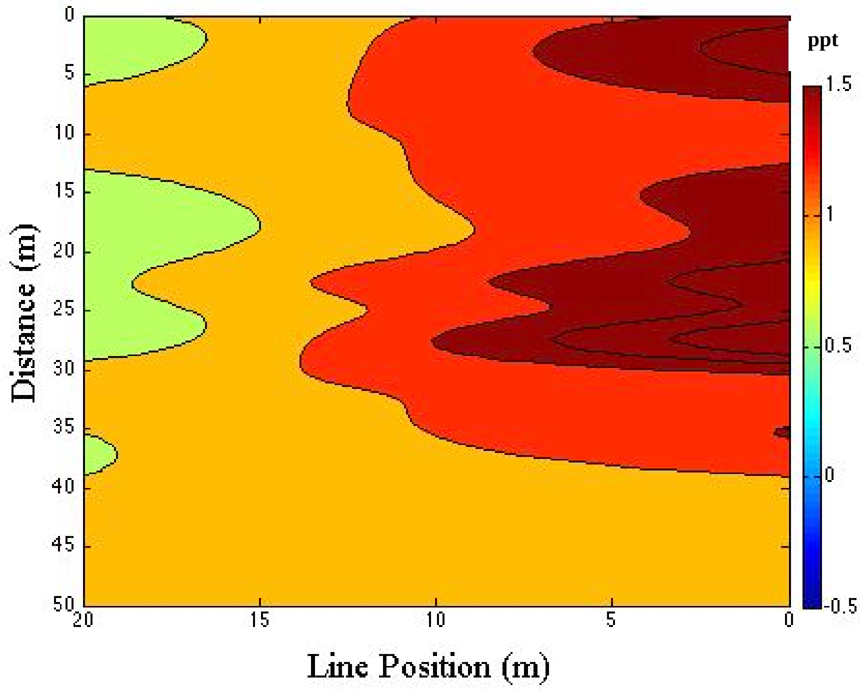

Figure 5.127 Desiccation Cracks: - In-phase – HCP, Parallel to Line

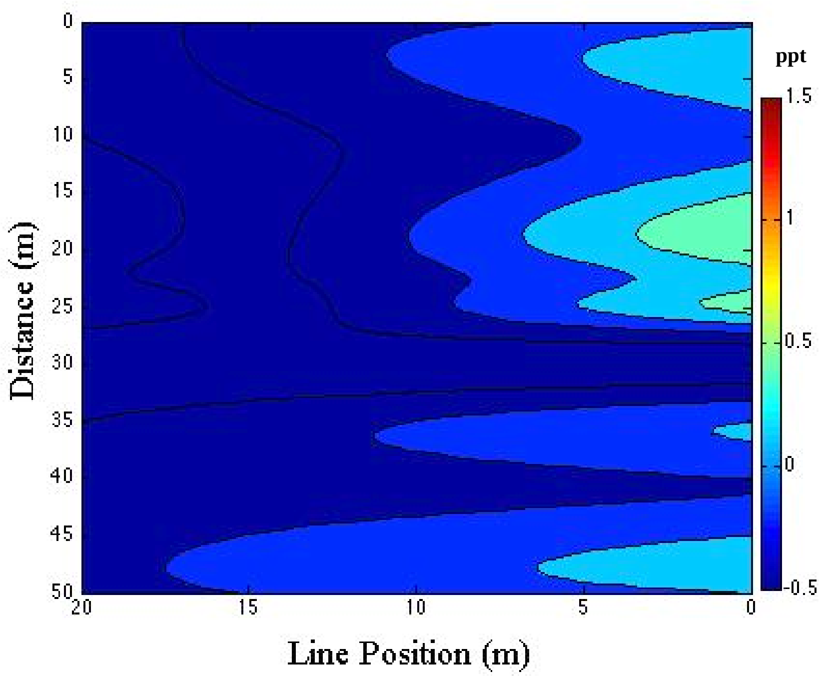

Figure 5.128 Desiccation Cracks: - In-phase – VCP, Parallel to Line

6.0 GROUND PENETRATING RADAR

6.1 Technique

Ground penetrating radar is a similar technique to seismic in that it sends waves into the earth and records reflections. GPR, however, uses radio waves and not sound waves. It has been demonstrated to be a useful technique in many fields and is particularly good for location of features in the top meter to several meters of the earth. There are different frequency antennas which can be used with this technique, the higher the frequency the greater the resolution of the profile, but the shallower the penetration. For more information on the technique and for other applications please refer to Ground-Penetrating Radar for Archaeology, Lawrence B Conyers.

The three systems we took out to the site were the MALA system, the GSSI SIR-2 and the GSSI SIR-10 systems. For information on the MALA system, refer to www.malags.com and for information on the two GSSI systems, refer to www.gssi.com. For all three systems, we used the fixed separation method, with both 500 MHZ and 100 MHZ antennas. After running test lines, it was decided to continue with only the 100 MHZ antenna. This was because we got a relatively decent resolution at the site and we wanted more ground penetration.

6.2 Data Collection

During the two weekends spent at the Willcox site we collected GPR profiles on both Grid 1 and Grid 2 and at the Desiccation cracks. During this time we encountered a number of problems with the data collection equipment.

The profiles along the grids were not all run in the same direction, some East to West and some West to East, since this made the data collection more efficient in the field. This was not a problem in processing the data, since we can reposition the line during processing. The orientation of each profile was recorded and we placed a mark every 5 m along the profile to make horizontal distance location more accurate in the processing.

<u>Day 1</u>

Test lines were run using all three GPR systems across the area near where there were visible fissures, in order to determine what response the fissure gave on the profiles. The MALA system did not work reliably and therefore, the system was not used again during this survey. Both the SIR-10 and the SIR-2 systems gave repeatable data with an anomaly over the fissure.

After running a few test lines over the fissure, a metal coil was buried ~ 0.5m deep to test for velocity. This gave a diffraction event on the 500 MHz antenna record, as shown in Figure 6.21; however the depth calculations on this profile do not correlate well with expected velocities and dielectric constants. There are two reasons why this test was unsuccessful: first, the coil was not buried very deep, which caused its signal to be obscured by the direct signal, and second, the relatively shallow coil also caused the time frame of the signal to be so small that an accurate interpretation was difficult.

Day 2

Prior to running the profiles, the brush was cleared along each profile as best as possible. This was to avoid decoupling of the antennas with the ground.

The SIR-10 system was initially chosen to run the profile lines as it was the system most familiar to the team. It was decided that for the desired depth of penetration, only the 100 MHz antenna would be used. Profiles 1-5 were run and then a repeat on profile 5 was run. Unfortunately, this repeat did not compare well to the initial profile. A third profile was run along profile 5; again there was poor repeatability. The instrument was taken apart in the field and connections between all the boards where checked. No loose connections were found. Since the data were not repeating, it was decided to switch to the SIR 2 system.

All 13 profiles on Grid 1 were run with this system. The speed at which the profile data were collected was kept as constant as possible, with some differences depending on who pulled the antennas and the brush along the profile.

Day3

Having completed the profiles along Grid 1, profiles along Grid 2 were surveyed. Again the SIR-2 system was used, because the SIR-10 system was still not collecting reliable data. Profiles 1 to 13 were run, again recording the orientation of the profile. Profiles 1 and 12 were repeated and these were consistent.

After the Grid 2 was run, it was decided that another depth/velocity test was needed to reliably assess the velocity of the area. A trench was dug and a segment of rebar was hammered into the side at a depth of 0.85 m, so it would be underneath undisturbed soil. There was possibly diffraction on these profiles but it wasn’t very obvious. It was then decided a much larger metal pipe, 2.5 inch diameter, would be buried in the trench. Even with diffractions from the disturbed soil, the pipe was large enough that it showed distinctive and very ringy diffractions. This target was buried at a depth of 0.8m. Two profiles were run along this area and continued along it, so that it crossed the pipe line running from the wells to the power plant. The results of these profiles are discussed in Section 6.31.

Day 4

The SIR-2 was run along the test lines laid out both perpendicular and parallel to the fence and power lines. There is a distinct late reflection seen in the profiles due to the power line. The control board of the SIR-10 system was switched with a spare control board in the field and this instrument became operational again. Five profiles were run under the power line, perpendicular to the fence line. These were at different gains, all repeating the line. These profiles also show a nice reflection hyperbola late record that correlates nicely with the power line; it also is repeated on all five profiles.

After the test lines at site were completed, another site was surveyed, known as the "Desiccation Crack" site, and three profiles were run perpendicular to a road across a suspected desiccation crack. We used the SIR-2 system again to maintain consistency with the data from site one. Again, a repeat of profile 1 was taken to ensure reliability of the data.

6.3 Data Processing

6.31 Depth-Velocity calculations

The second series of velocity tests described in Section 6.2, Day 3, were much more successful. The anomaly produced in these data is more easily determined. When this is combined with the known depth, an average velocity or dielectric constant can be obtained for the area of study. We required this information in order to put a depth scale on the GPR profiles. There is also another method of determining a dielectric constant: hyperbola migration. Using this method, we found a dielectric constant of 27 and an average soil velocity of 0.04 m/ns. This however was not used to interpret the grid profiles because it applied to shallower depths than are of interest in this report. For the interpretation of the data, a dielectric constant of 20 was used. This was obtained by fitting a depth scale to the pipes at 0.85 meters. This can be seen in the images of the processed test profiles, Figures 6.1-6.3.

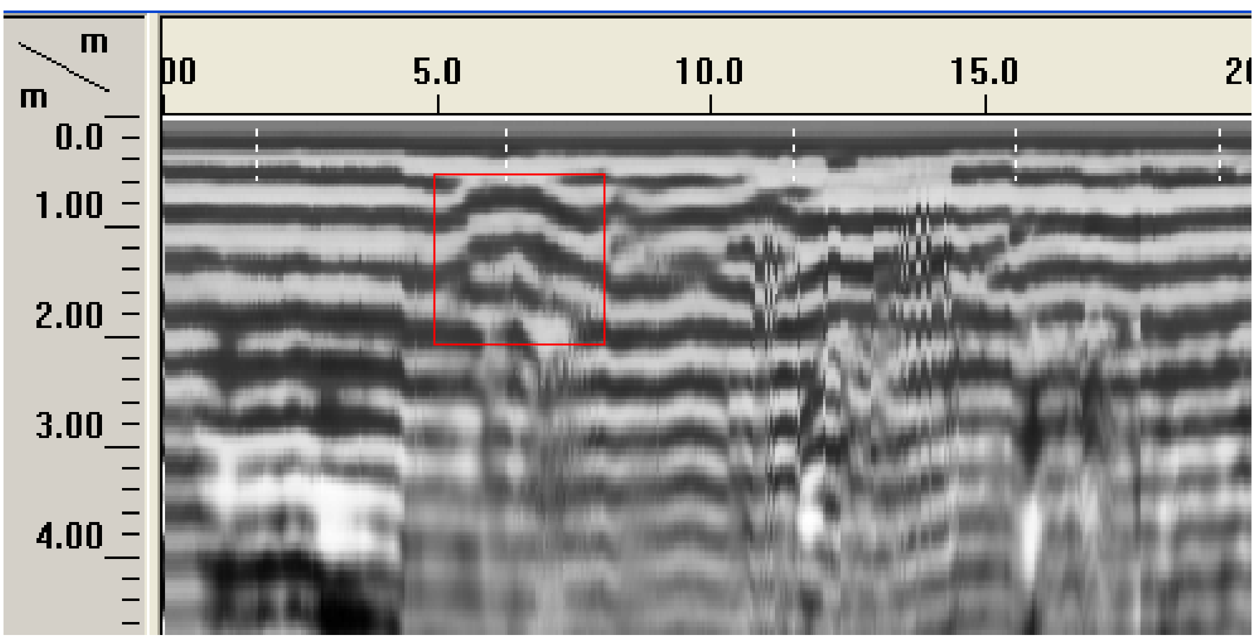

Figure 6.1 Buried iron pipe and pipeline test. The red box is around the signature of the buried iron pipes.

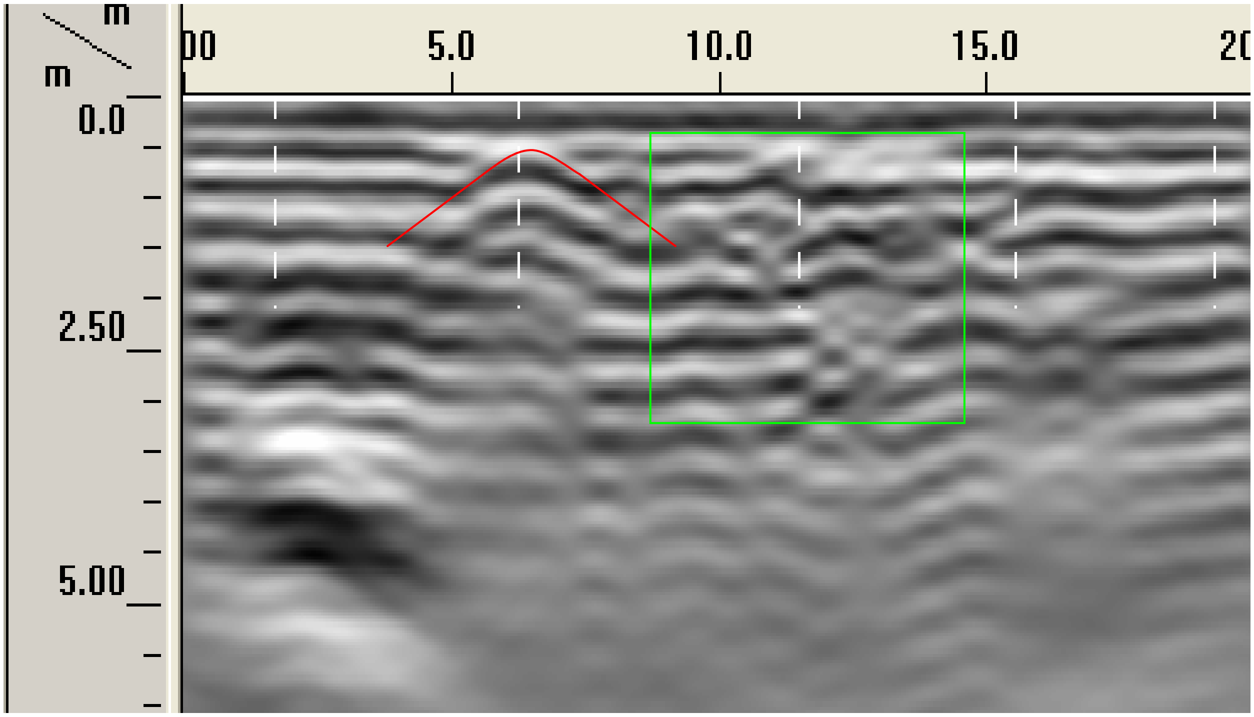

Figure 6.1a Figure 6.12 after using a spatial filter in RADAN. The red hyperbola illustrates an example of how hyperbola matching is used when calculating the dielectric constant and average velocity of a soil. In this case, the red hyperbola marks the iron pipes which were buried on site. The other hyperbolas in the green box are assumed to be the existing pipeline.

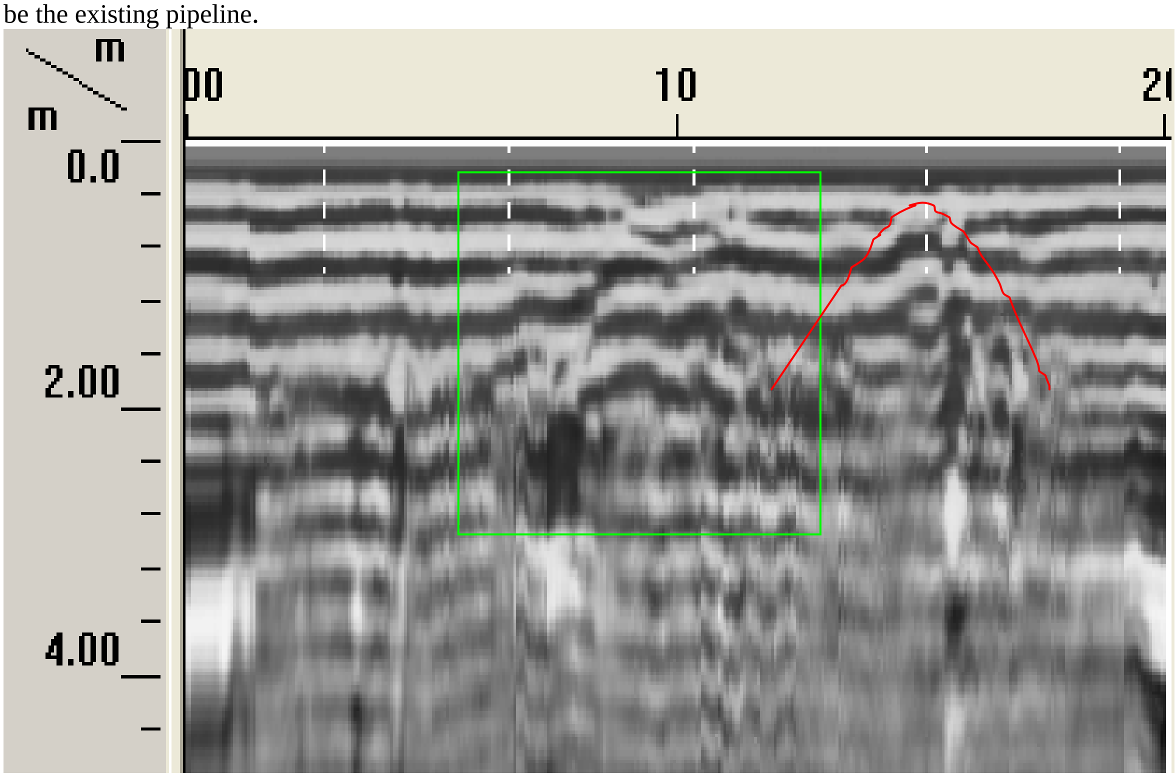

Figure 6.2 Reversed iron pipes and pipeline test. Shows that the SIR-2 system is collecting repeatable data. Green box denotes existing pipeline and red hyperbola shows the buried pipes.

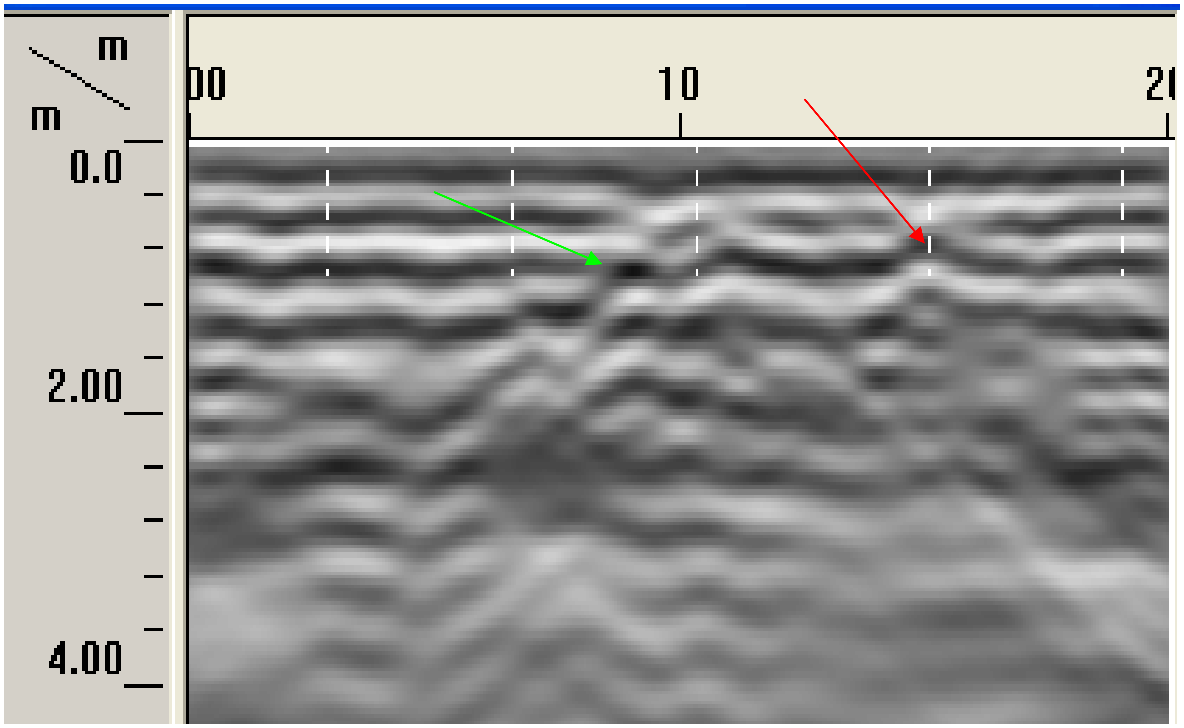

Figure 6.2a Figure 6.13 after a spatial filtering in RADAN. Notice the large anomaly at ten meters, which is the existing pipeline and the smaller one at 15 meters, which are our buried pipes.

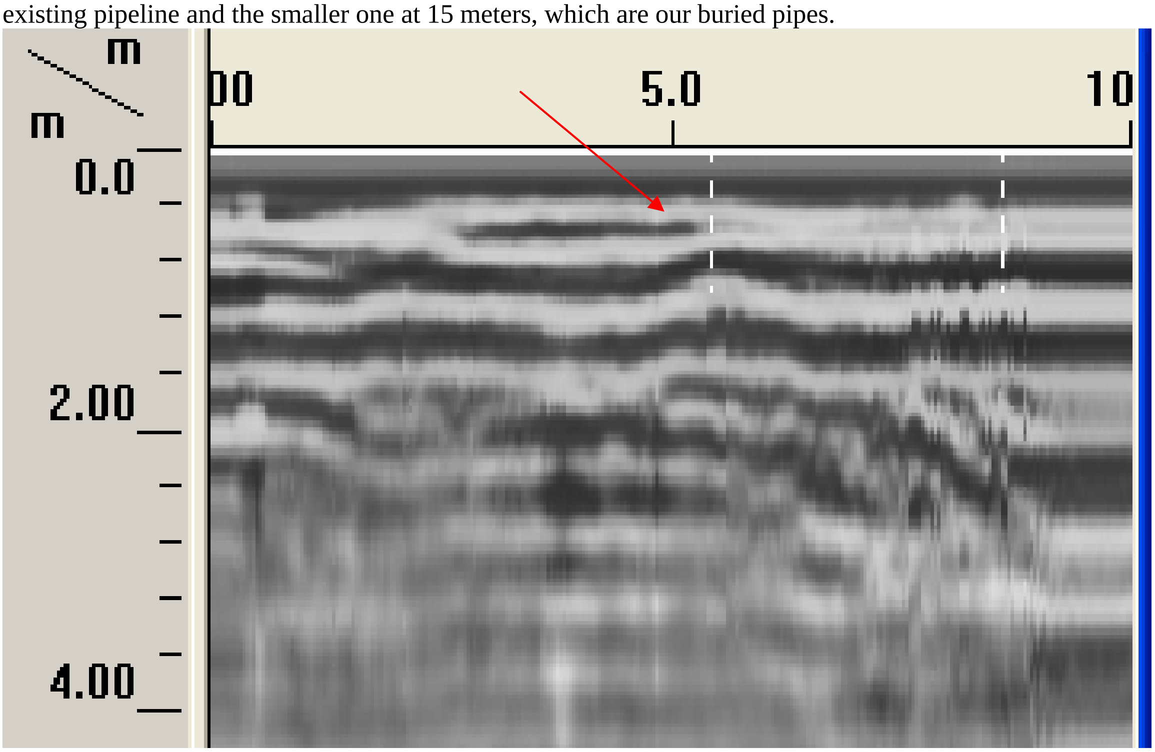

Figure 6.3 10 meter rebar test. The first marker points out where the rebar was located. This image shows that we are picking up the rebar at the correct depth of 0.7 meters.

6.32 2D Processing

The data were processed using GSSI's RADAN v6.6. The first step for every profile was to see if it needed stacking. Then we position-corrected for zero time. Knowing the distance between each mark and the exact number of scans that we had taken over the whole 50m, we were able to reliably calculate distance along each profile. A process called FIR filtering can remove interfering signals. It was used to remove continuous signals for longer than 80 scans - this makes it possible to more easily distinguish the diffractions in areas of interest.

6.33 3D Processing

Further processing with RADAN v6.6 was done using the 3D module part of the program. The first step in creating these 3D sections was to take the previously processed data from Section 6.22 and compile them into one 3D file project. Once this was done, an interpolated 3D image of the data could be viewed and processed with different filters. Unfortunately due to an error in GSSI software, the 3D cube only shows three quarters of usable data. This is due to the fact that the program takes a portion of the 3D display and re-displays it over a quarter of the 3D display.

In attempts to try to correct this error, the original unprocessed 2D data were reprocessed in the same way (minus the FIR filter) and the 3D file was rebuilt several times. Still the error persisted in both data sets for each grid. Having noted this error and recognizing that the data will be invalid for the corrupted quarter of the 3D image, further filtering was done to see if any correlation with the fissure could be seen in the valid sections of the 3D figure.

The resolution of the image was set to 1:8, meaning that several time slices are shown per unit depth along the Z axis. After a background removal filter is applied, which subtracts the average of amplitudes from the whole displayed window, a Root Mean Square filter is applied that will display the RMS of amplitude values. Finally a Median Filter is applied which smoothes the data horizontally.

6.4 Data Description

Due to the error in the 3D processing, only the processed 2D profiles are shown here. The repeatability of the data is evident from Figures 6.14 a & b and 6.26 a & b. The long wavelength diffractions are similar. Furthermore, the subsurface imaging away from the diffractions is repeatable and the diffractions do occur at the same points along the profiles. There are numerous diffractions along each profile, some correlate with approximate locations of the fissure and some do not. Those that do not correlate with the fissure could be associated with plant roots from the vegetation or other subsurface disturbances.

6.5 Interpretation

During interpretation of the 2D profile it was noticed there were two types of significant anomalies identified on the profiles. One was a ringy diffraction with the same wavelength as the background along the profiles and one was a longer wavelength. We suspect that the long-wavelength anomalies are due to a substantial velocity contrast, probably caused by a void. These anomalies are identified on the profiles; the normal wavelength diffraction is identified by a green oval and the long wavelength diffraction is identified by a red box. These were then put into a spreadsheet to see if there was any correlation across the grid.

6.51 Grid 1 Interpretation

There are many more diffraction targets identified in Grid 1, compared with Grid 2. Grid 1 shows evidence of an open fissure near many of the lines, which is around 20 to 25m on each line. Line 13, however, did not show any evidence of a nearby open fissure, yet there is a clear indication of a diffraction event over the projected location of the fissure. As you can see from Figure 6.41a, there is a correlation with the 20-25 m region and a lineation of diffractions identified. However, there are both long and normal wavelength diffractions along this region, meaning there is not a strong correlation with a particular type of anomaly that may be produced by the fissure. Another interesting feature worth noting is the responses on the profiles which are similar. They show two bumps, approximately 1 m apart at the surface, which is then carried down through the record as a ringing response. This may be due to a change in the velocity from the ground cavity as you cross the fissure.

6.52 Grid 2 Interpretation

Grid 2 does not display the large ringing anomalies of Grid 1. It is generally difficult to pick out any large anomalies present in these images, which limits the ability to present a plan display of the GPR anomalies for Grid 2. The most significant results for Grid 2 come within the first three lines, near where the fissure is visible on the surface. Moving one's focus to smaller and less definable anomalies, however, does produce some intriguing results. Images for Grid 2 lines 1-3 and 7-11 all have minor anomalies present within the 20 to 30 meter range (Figures 6.33-6.37). These are different from those seen in Grid 1. They may be cause by thinner subsurface features, which could correlate with a thin fissure, not showing signs of surface erosion. This is interesting, because the underground pipeline is expected to be near lines 5 and 6 and may wipe out any traces of the fissure (see Figure 6.41b for a plot of anomalies present at various locations). There is no real linear correlation in this plot compared with Figure 6.41a.

6.53 Desiccation Crack Interpretation

Upon review of the desiccation crack SIR-2 profiles, it has been concluded that there may be a correlation between anomalies seen in the data and the location of the desiccation crack. The two 50-meter profiles of the desiccation crack display noticeable disturbances within the data where the desiccation crack is expected. The desiccation crack is located about 1 meter south of the center of the road and the center of the lines correlates with the center of the road. This means that on the North to South profile shown in Figure 6.1, the anomaly should be at approximately 25 meters. On the South to North profile, the anomaly should be a little before 25 meters. This is supported in the data, although it is seen that the anomaly appears at about 25 meters in Figure 6.3. It appears that the GPR may be effective for shallow-depth desiccation crack location. An anomaly also shows up in the 20 meter desiccation line at about 7 meters; this is about 3 meters North of where it was expected. This could be explained by the fact that this anomaly is not the desiccation crack and rather some other event, while the crack itself was not seen in the record. Another possibility is that the desiccation crack made an undocumented switch from the South side of the road to the North side. In either case, the 20-meter desiccation profile cannot be used to determine the reliability of GPR in this case.

6.6 Cultural Interference

The repeatability and the effect of cultural interference were also assessed based on a profile taken under a power line and one taken by a fence. There are several SIR-2 and SIR-10 profiles taken on the test line. These all show that the GPR system is performing repeatable data acquisition. They also show that the power line does appear in the record, as a very late arriving long wave hyperbola. This does not have any real effect on the data itself and can be removed using a temporal or spatial filter. From the processed profile, it can be seen that the fence does not negatively effect the collection of subsurface GPR data. Although some of the other techniques seem to show the presence of the fissure around the center of this seismic line, the GPR system does not display a discernable anomaly; however the arrow in Figure 6.4 is pointing to a possible fissure related disturbance within the fence seismic line.

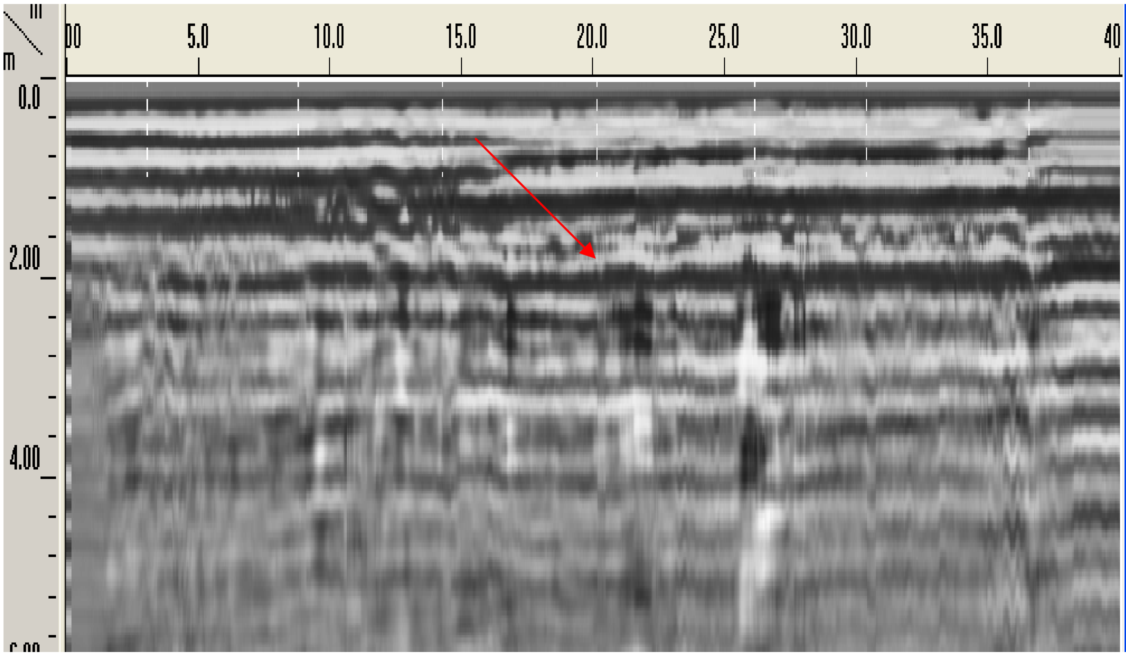

Figure 6.4, Fence seismic line, fissure expected to be around the 20 meter mark. The red arrow points to a long wave diffraction at the 22 meter mark, possibly fissure related.

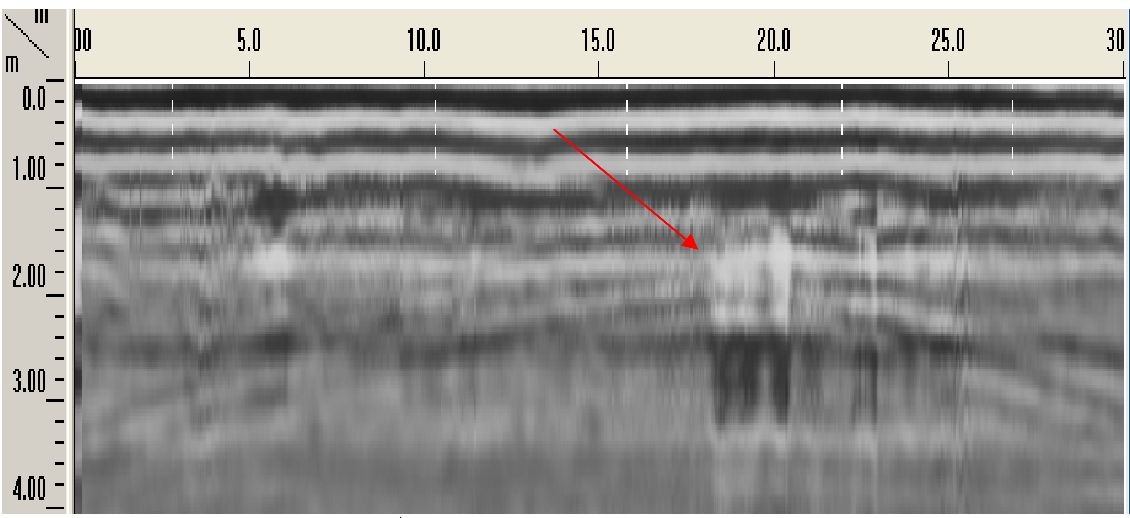

Figure 6.5 SIR-10 power line test, 1st run. Arrow marks meter local of power line.

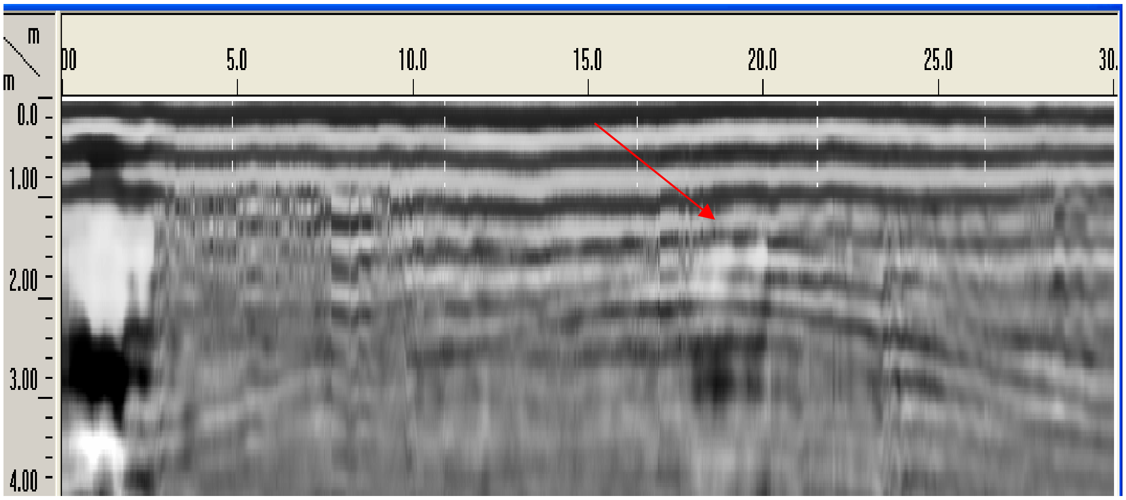

Figure 6.6 SIR-10 power line test, 2nd run. Arrow marks meter local of power line.

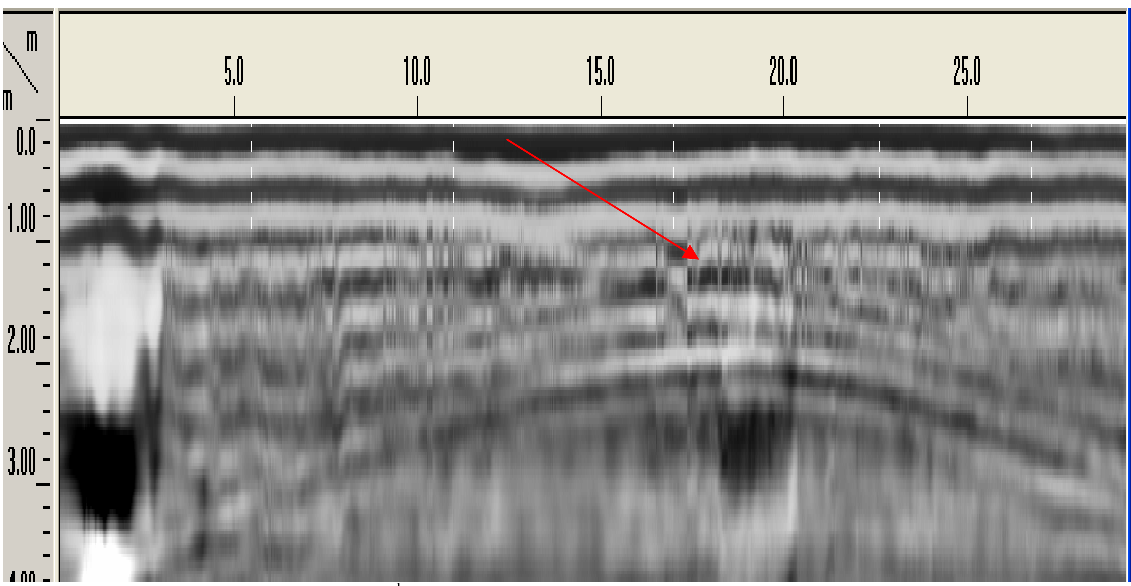

Figure 6.7 SIR-10 power line test 3rd run. Arrow marks meter local of power line.

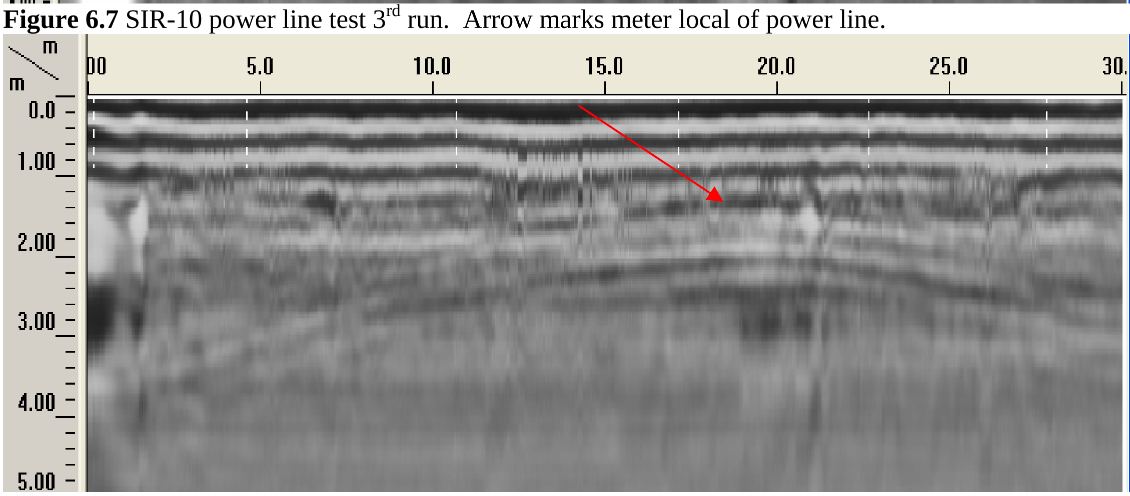

Figure 6.8 SIR-2 power line test. Arrow marks meter local of power line.

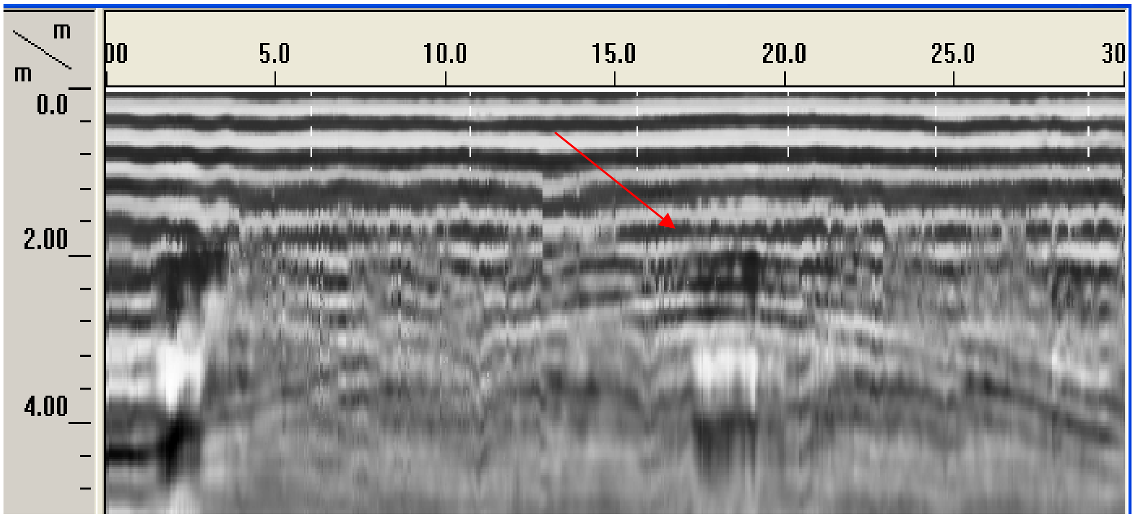

Figure 6.9 SIR-2 power line test. Arrow marks meter local of power line.

6.7 2D Profiles (All collected using SIR-2 and a 100 MHz Antenna.)

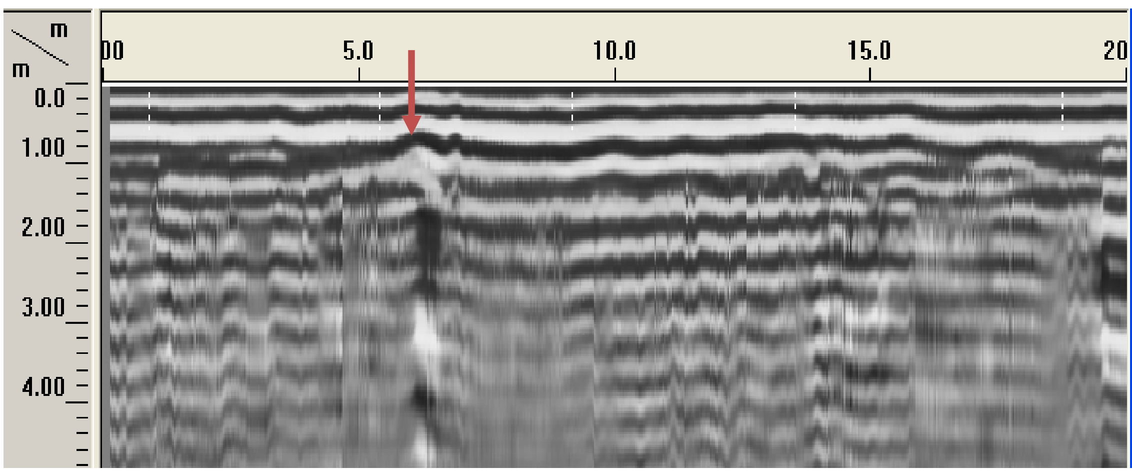

Figure 6.10 desiccation line 1, 20 meters long, north to south scan. Red arrow denotes anomaly

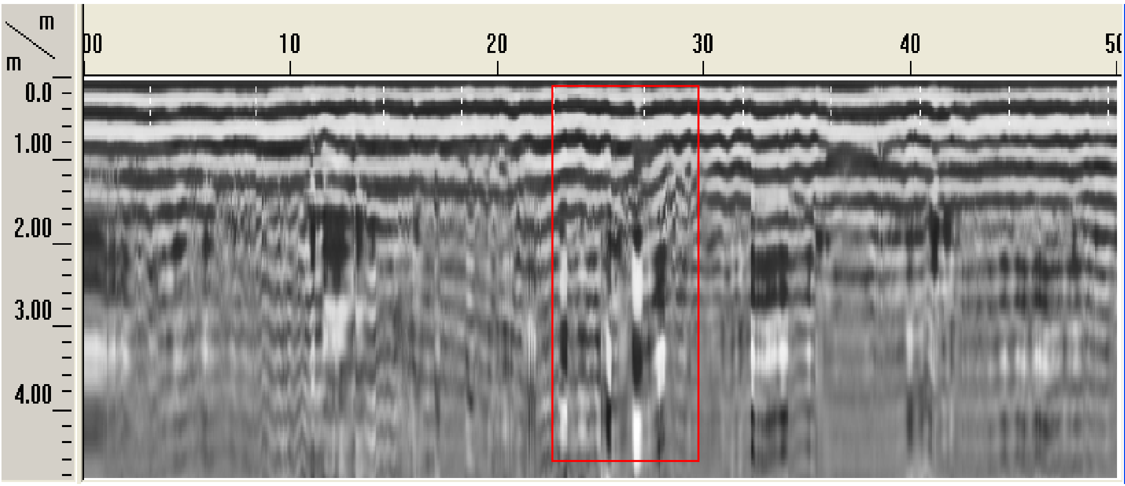

Figure 6.11 desiccation line 2, south to north scan, red box denotes possible disturbance from desiccation crack.

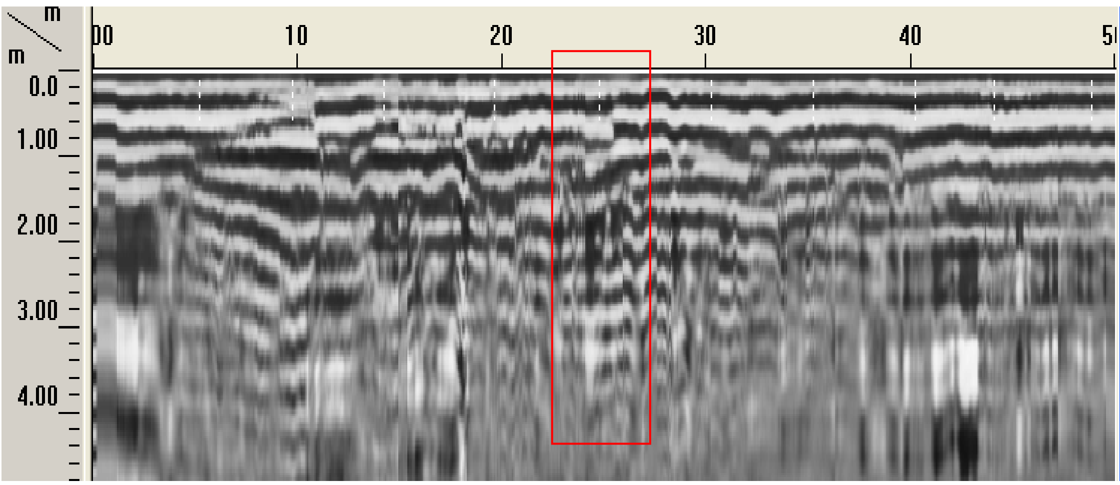

Figure 6.12 desiccation line 3, north to south scan, red box denotes possible disturbance from desiccation crack.

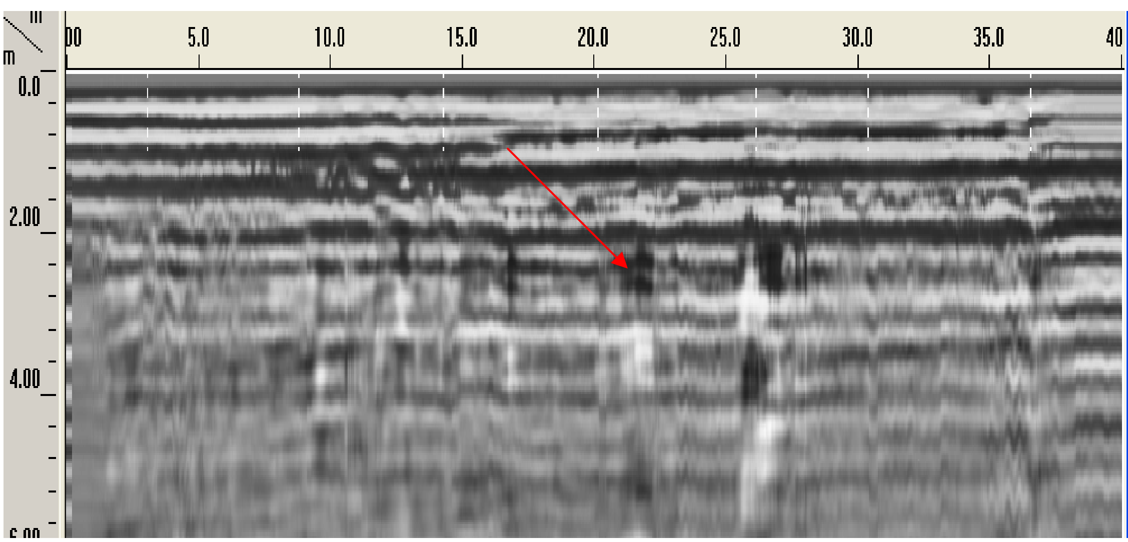

Figure 6.13 Fence seismic line, fissure expected to be around the 20 meter mark. The red arrow points to a long wave diffraction at the 22 meter mark, possibly fissure related.

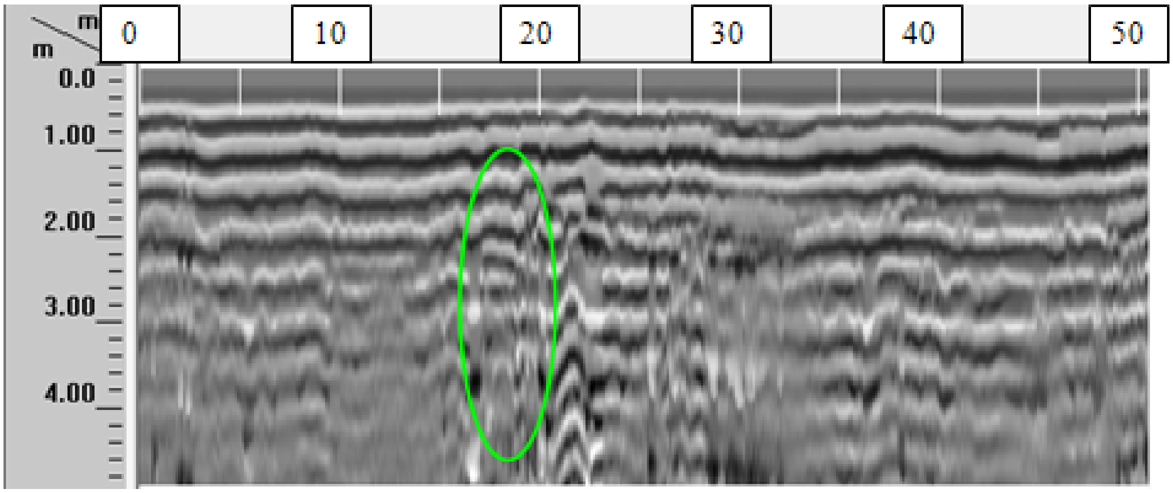

Figure 6.14a GPR profile of grid 1; (line 1 or 0 meter mark) Red box denotes a long wave length anomaly and a green oval denotes a normal wave length anomaly.

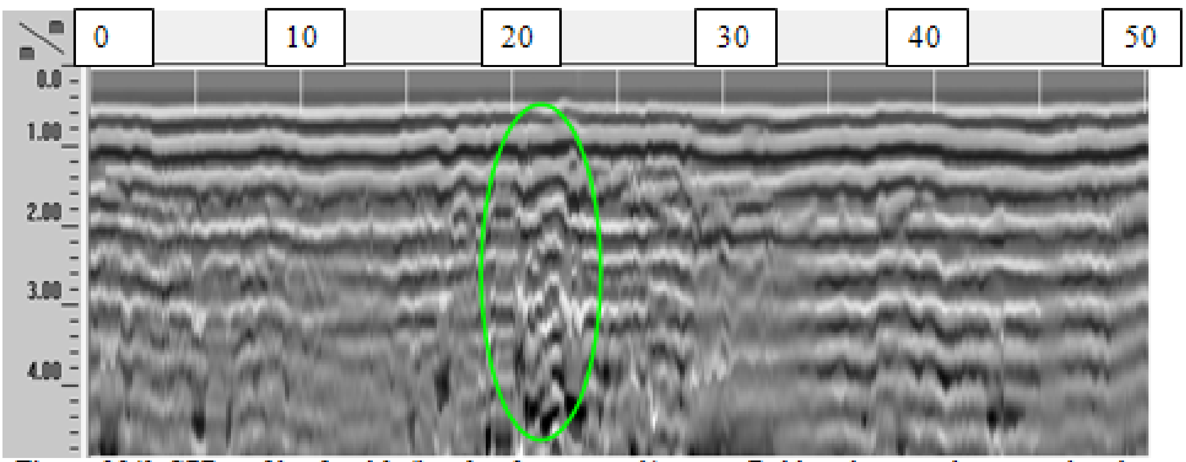

Figure 6.14b GPR profile of grid 1; (line 1 or 0 meter mark) repeat. Red box denotes a long wave length anomaly and a green oval denotes a normal wave length anomaly.

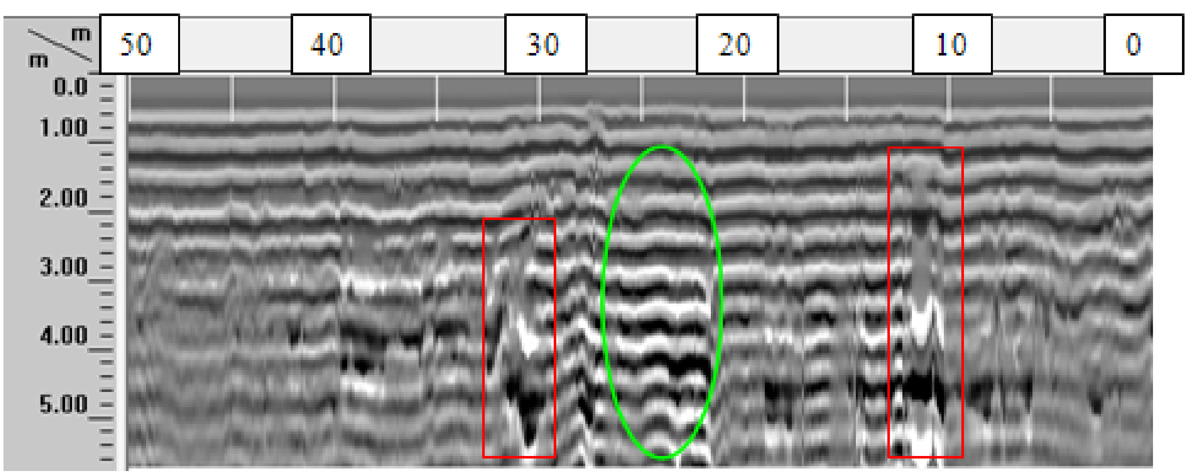

Figure 6.15 GPR profile of grid 1; (line 2or 5 meter mark), Red box denotes a long wave length anomaly and a green oval denotes a normal wave length anomaly.

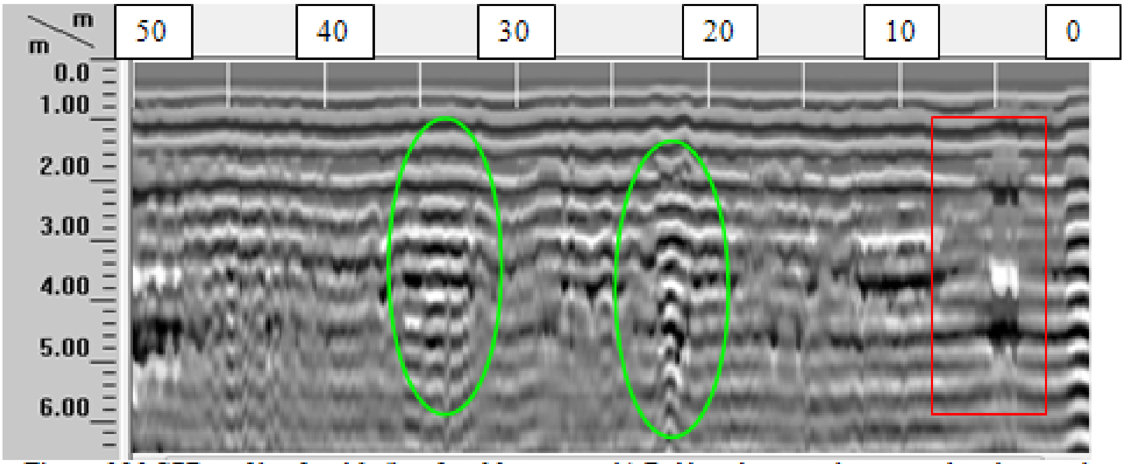

Figure 6.16 GPR profile of grid 1; (line 3 or 10 meter mark) Red box denotes a long wave length anomaly and a green oval denotes a normal wave length anomaly.

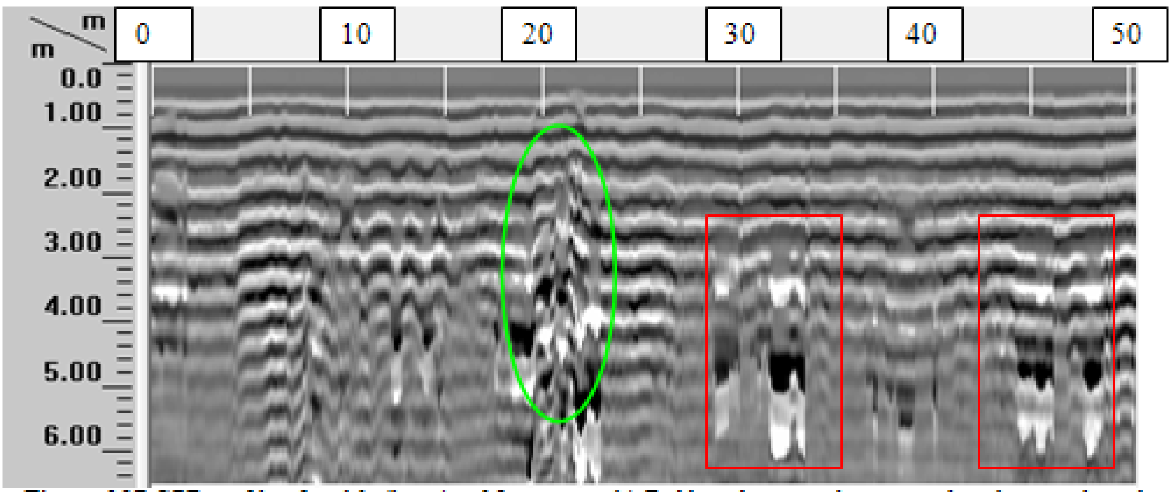

Figure 6.17 GPR profile of grid 1; (line 4 or 15 meter mark) Red box denotes a long wave length anomaly and a green oval denotes a normal wave length anomaly.

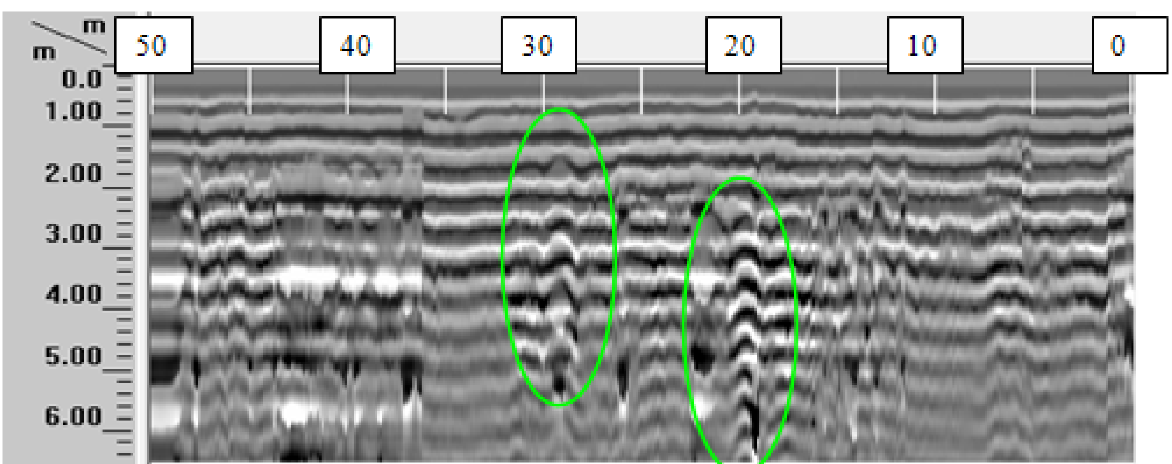

Figure 6.18 GPR profile of grid 1; (line 5 or 20 meter mark) Red box denotes a long wave length anomaly and a green oval denotes a normal wave length anomaly.

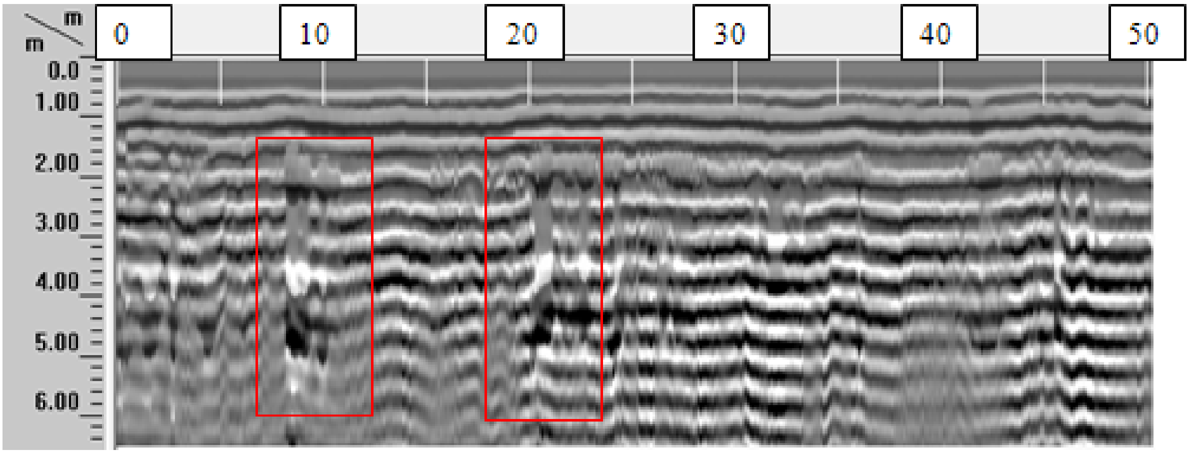

Figure 6.19 GPR profile of grid 1; (line 6 or meter mark 25) Red box denotes a long wave length anomaly and a green oval denotes a normal wave length anomaly.

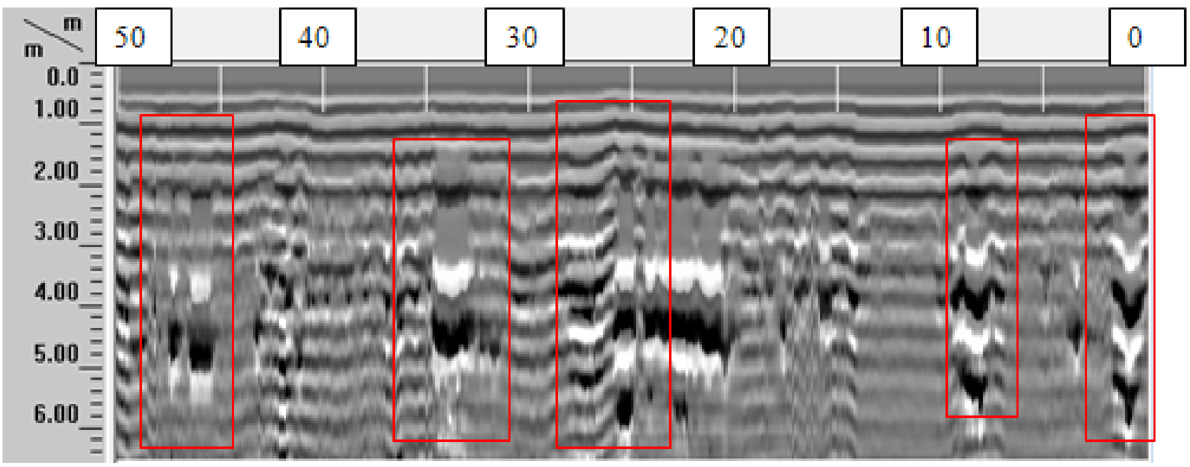

Figure 6.20 GPR profile of grid 1; (line 7 or meter mark 30) Red box denotes a long wave length anomaly and a green oval denotes a normal wave length anomaly.

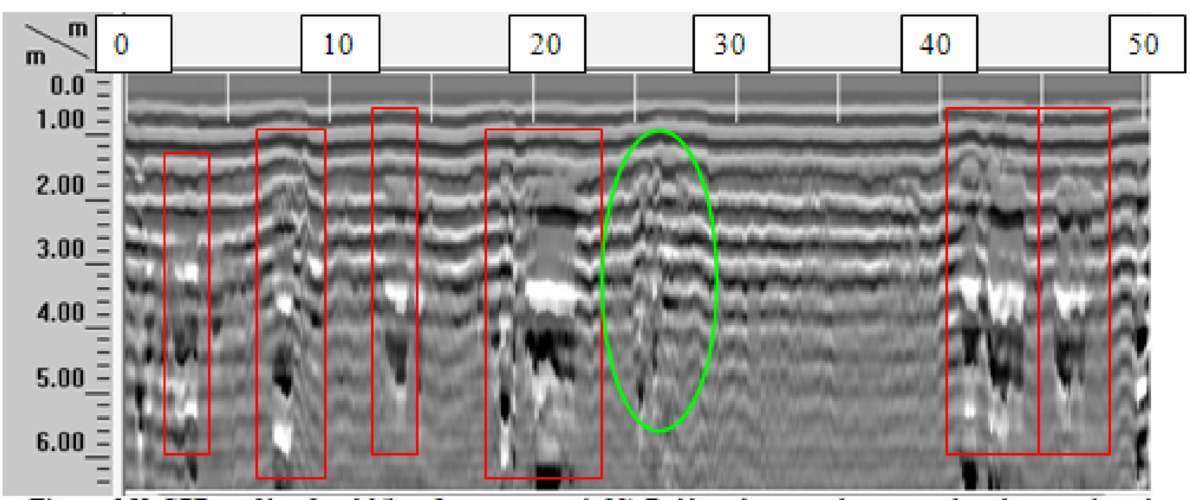

Figure 6.21 GPR profile of grid 1(line 8 or meter mark 35) Red box denotes a long wave length anomaly and a green oval denotes a normal wave length anomaly.

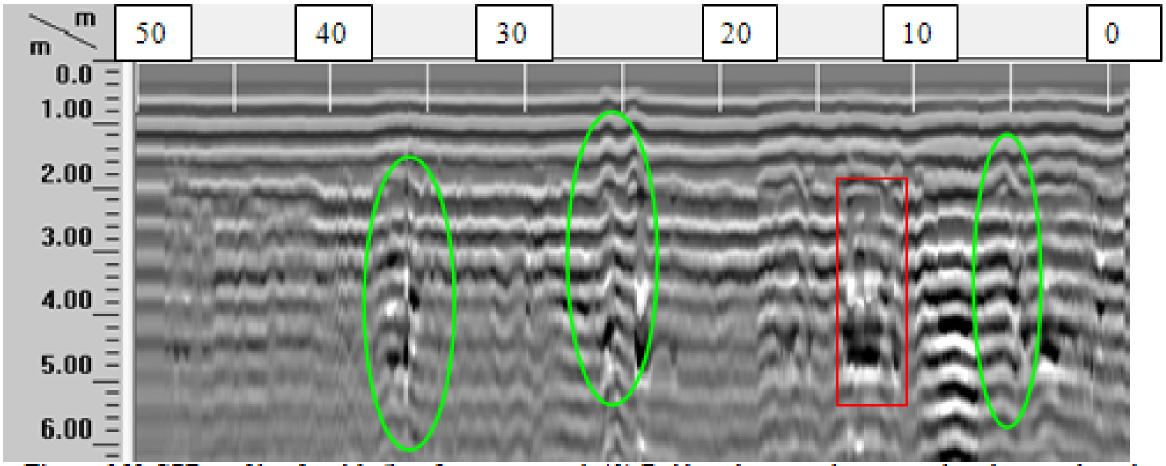

Figure 6.22 GPR profile of grid 1; (line 9 or meter mark 40) Red box denotes a long wave length anomaly and a green oval denotes a normal wave length anomaly.

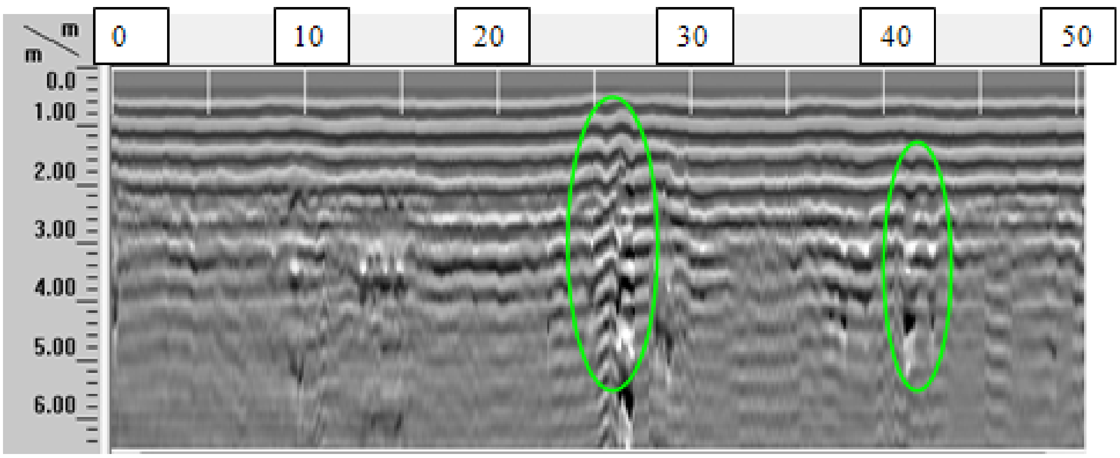

Figure 6.23 GPR profile of grid 1; (line 10 or meter mark 45) Red box denotes a long wave length anomaly and a green oval denotes a normal wave length anomaly.

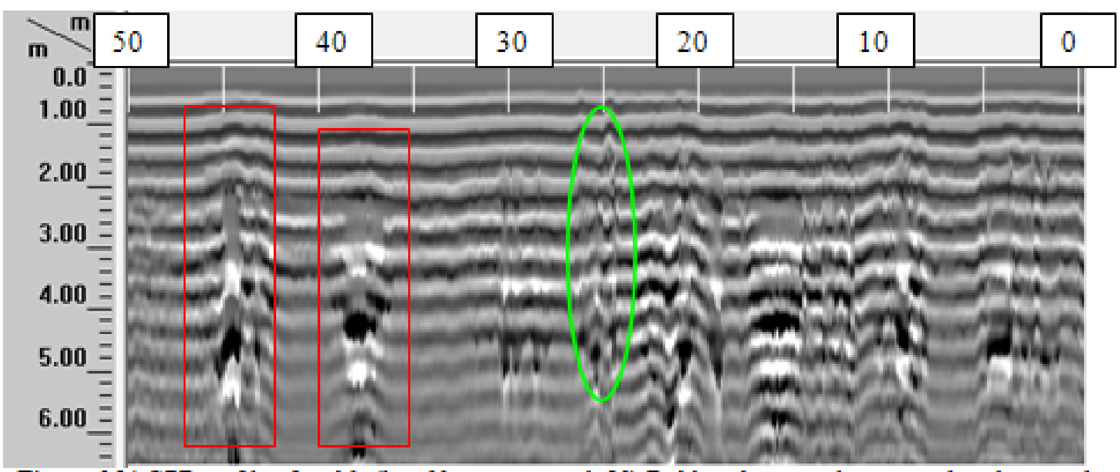

Figure 6.24 GPR profile of grid 1; (line 11 or meter mark 50) Red box denotes a long wave length anomaly and a green oval denotes a normal wave length anomaly.

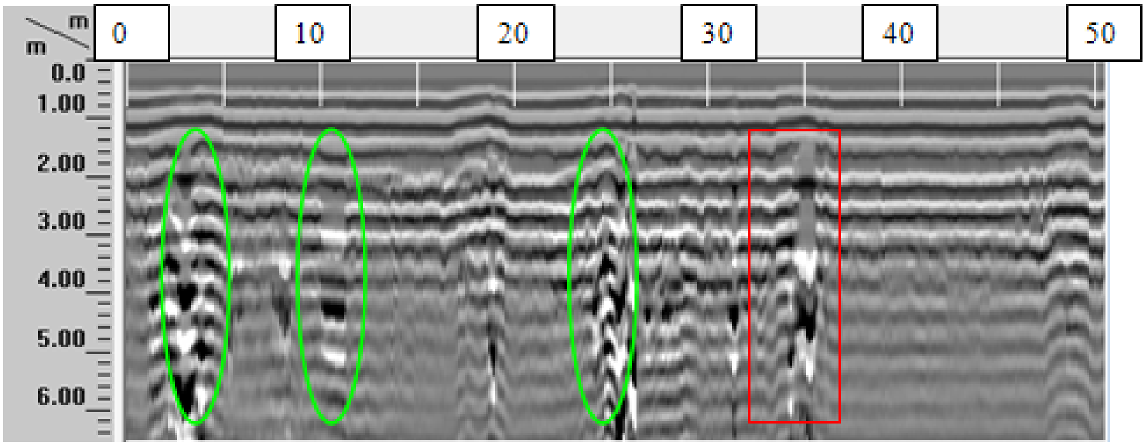

Figure 6.25 GPR profile of grid 1; (line 12 or meter mark 55) Red box denotes a long wave length anomaly and a green oval denotes a normal wave length anomaly.

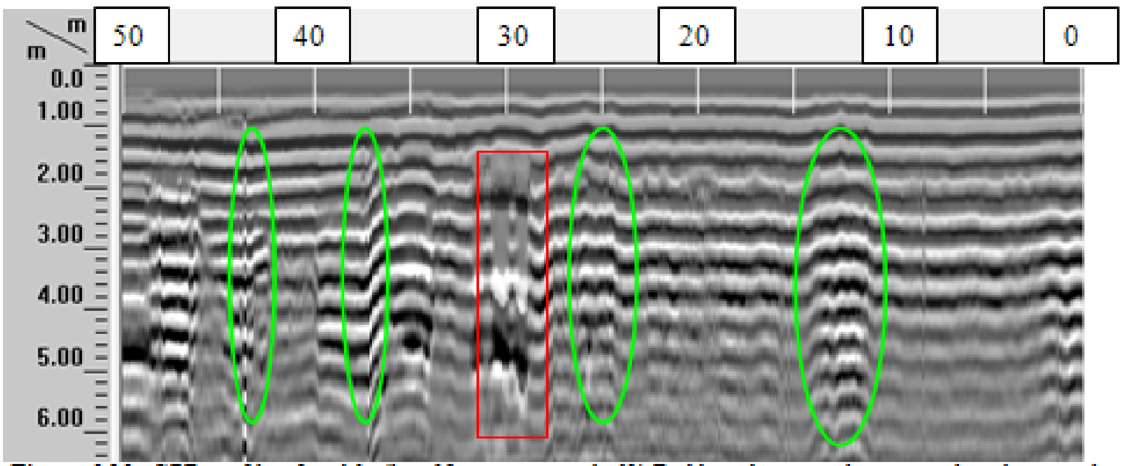

Figure 6.26a GPR profile of grid 1; (line 13 or meter mark 60) Red box denotes a long wave length anomaly and a green oval denotes a normal wave length anomaly.

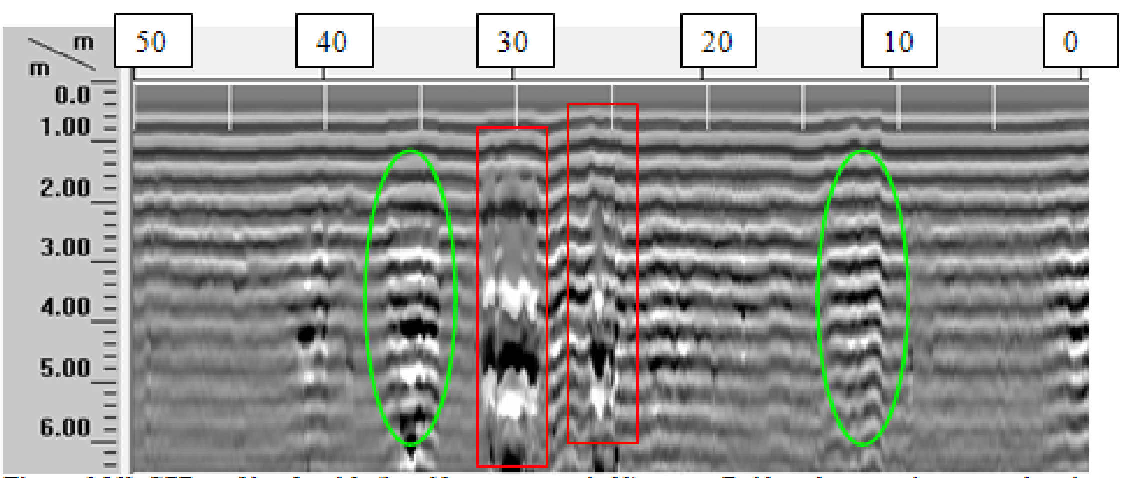

Figure 6.26b GPR profile of grid 1; (line 13 or meter mark 60) repeat. Red box denotes a long wave length anomaly and a green oval denotes a normal wave length anomaly.

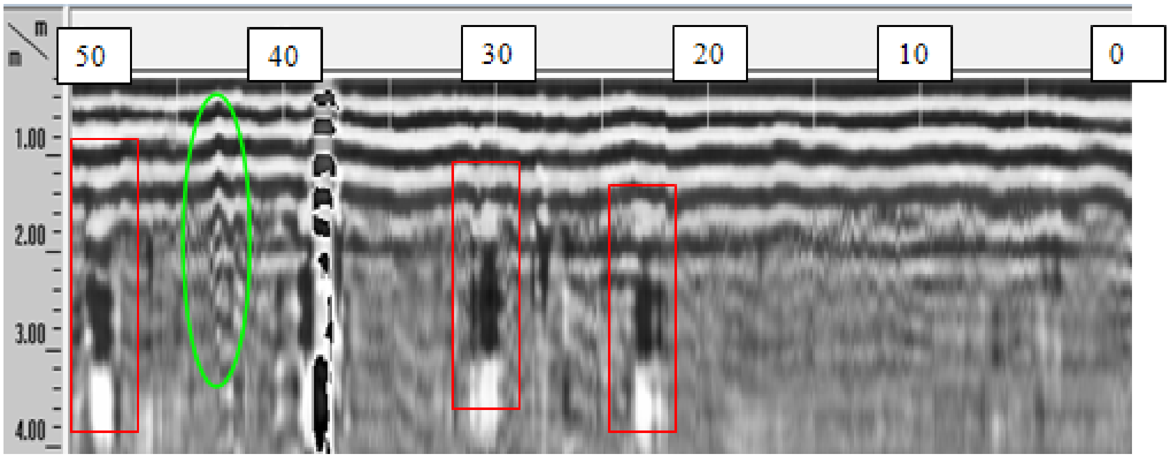

Figure 6.27 GPR profile of grid 2; (line 1 or meter mark 0) Red box denotes a long wave length anomaly and a green oval denotes a normal wave length anomaly. Large ringing anomaly at 40 is a metallic object close to the surface and will be omitted.

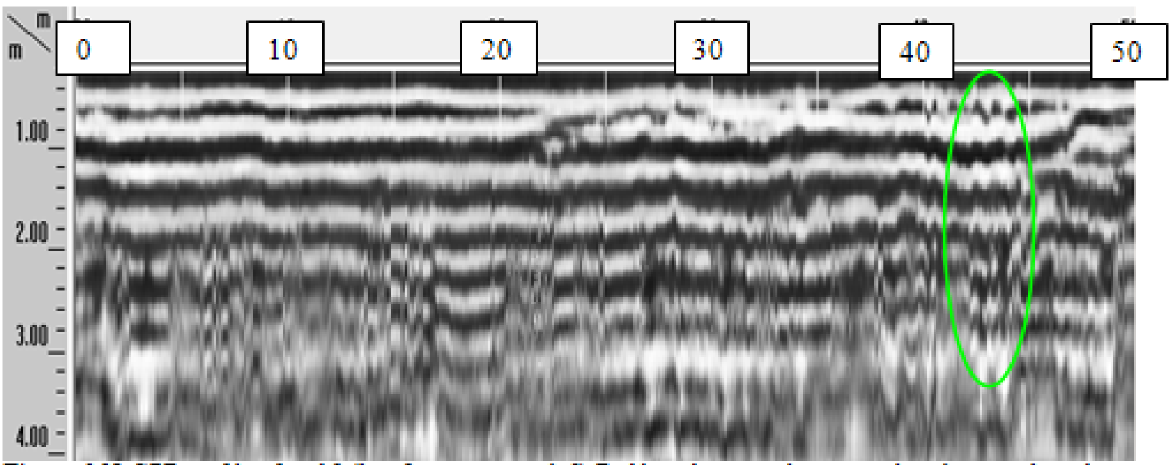

Figure 6.28 GPR profile of grid 2 (line 2 or meter mark 5) Red box denotes a long wave length anomaly and a green oval denotes a normal wave length anomaly.

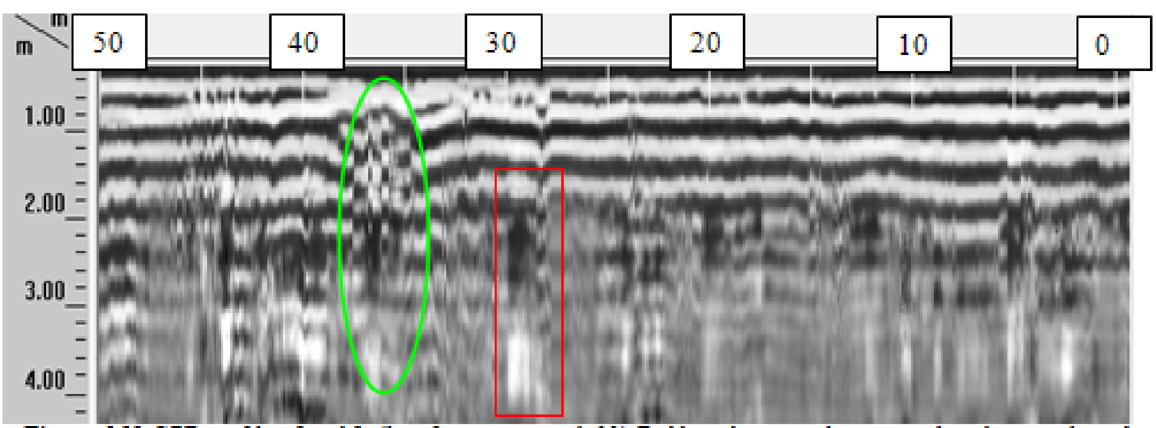

Figure 6.29 GPR profile of grid 2; (line 3 or meter mark 10) Red box denotes a long wave length anomaly and a green oval denotes a normal wave length anomaly.

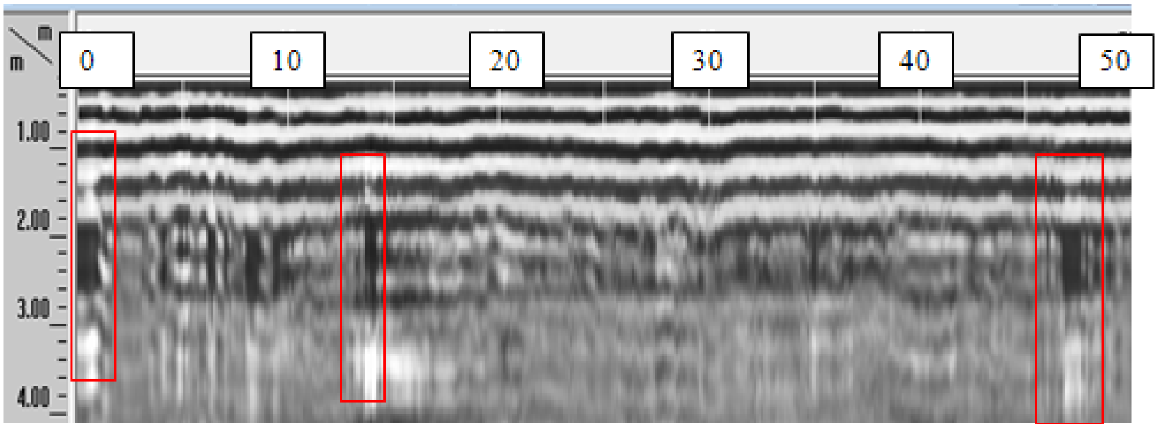

Figure 6.30 GPR profile of grid 2; (line 4 or meter mark 15) Red box denotes a long wave length anomaly and a green oval denotes a normal wave length anomaly.

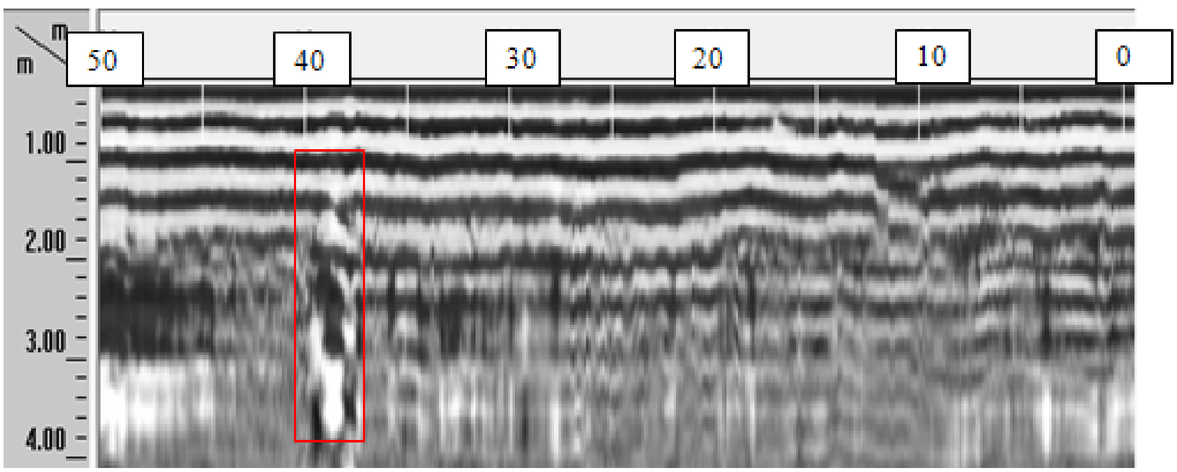

Figure 6.31 GPR profile of grid 2; (line 5 or meter mark 20), Red box denotes a long wave length anomaly and a green oval denotes a normal wave length anomaly.

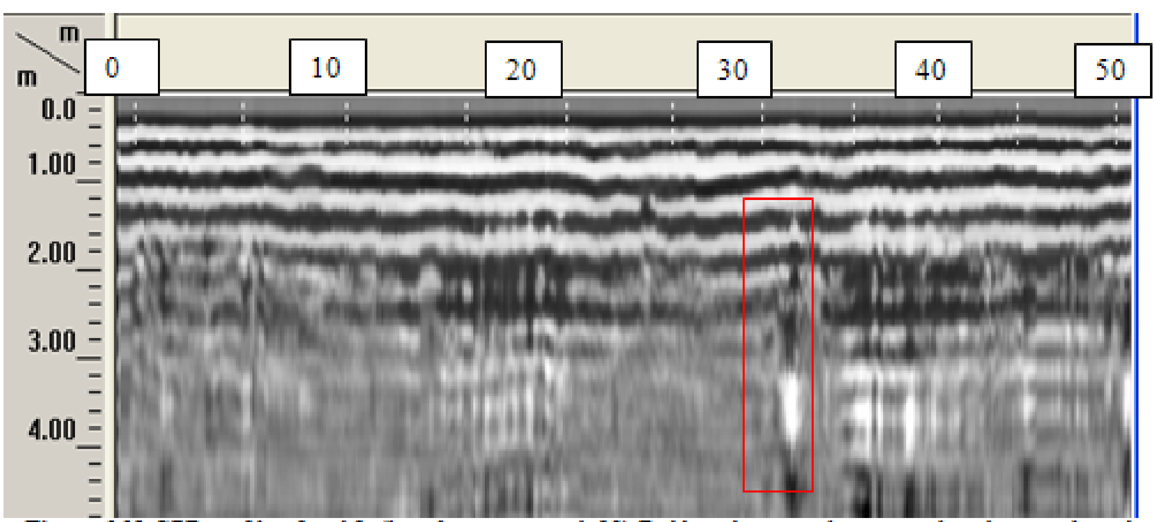

Figure 6.32 GPR profile of grid 2; (line 6 or meter mark 25) Red box denotes a long wave length anomaly and a green oval denotes a normal wave length anomaly.

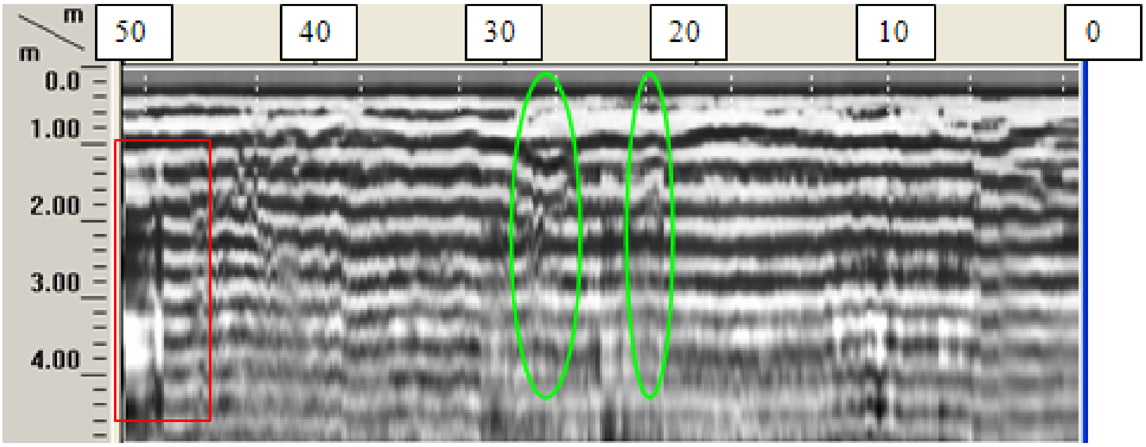

Figure 6.33 GPR profile of grid 2; (line 7 or meter mark 30) Red box denotes a long wave length anomaly and a green oval denotes a normal wave length anomaly.

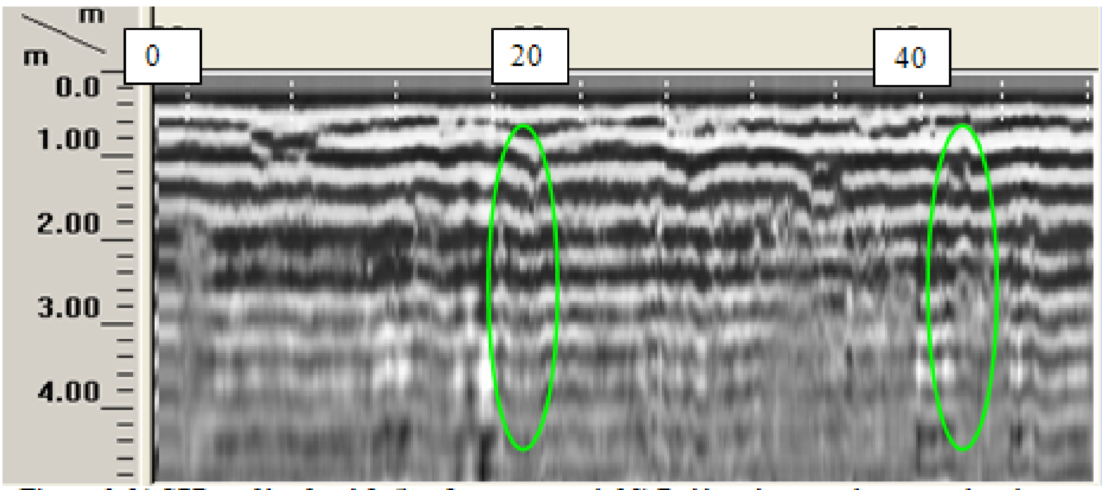

Figure 6. 34 GPR profile of grid 2; (line 8 or meter mark 35) Red box denotes a long wave length anomaly and a green oval denotes a normal wave length anomaly.

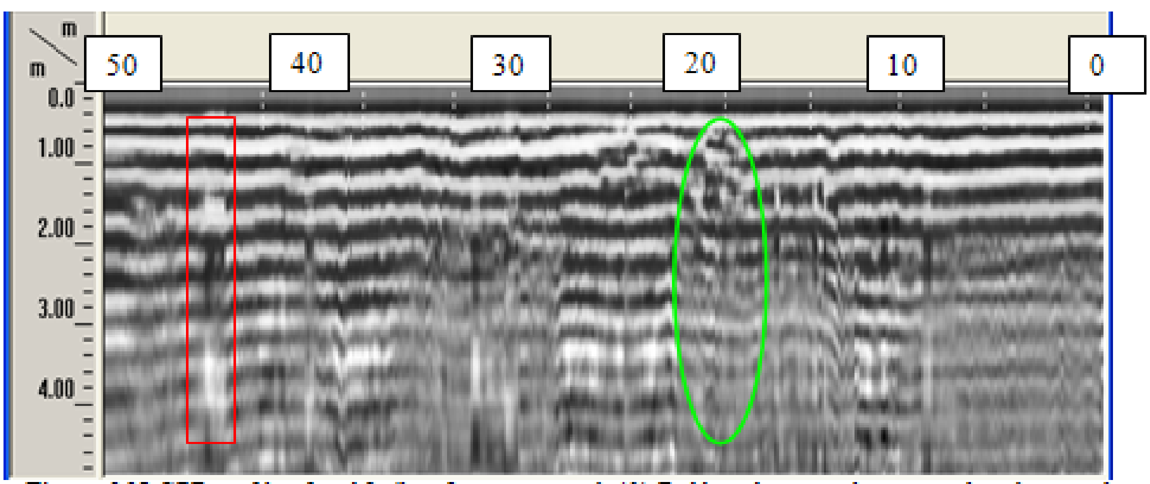

Figure 6.35 GPR profile of grid 2; (line 9 or meter mark 40) Red box denotes a long wave length anomaly and a green oval denotes a normal wave length anomaly.

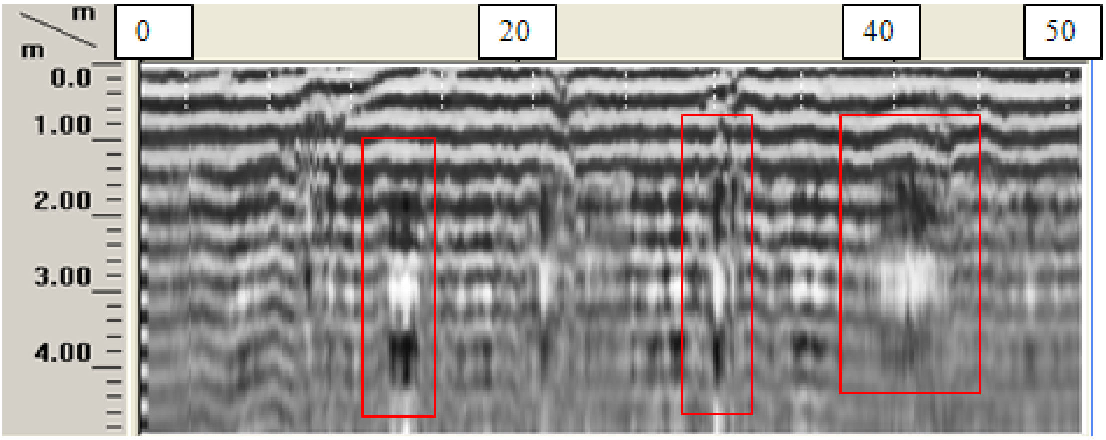

Figure 6.36 GPR profile of grid 2; (line 10 or meter mark 45) Red box denotes a long wave length anomaly and a green oval denotes a normal wave length anomaly.

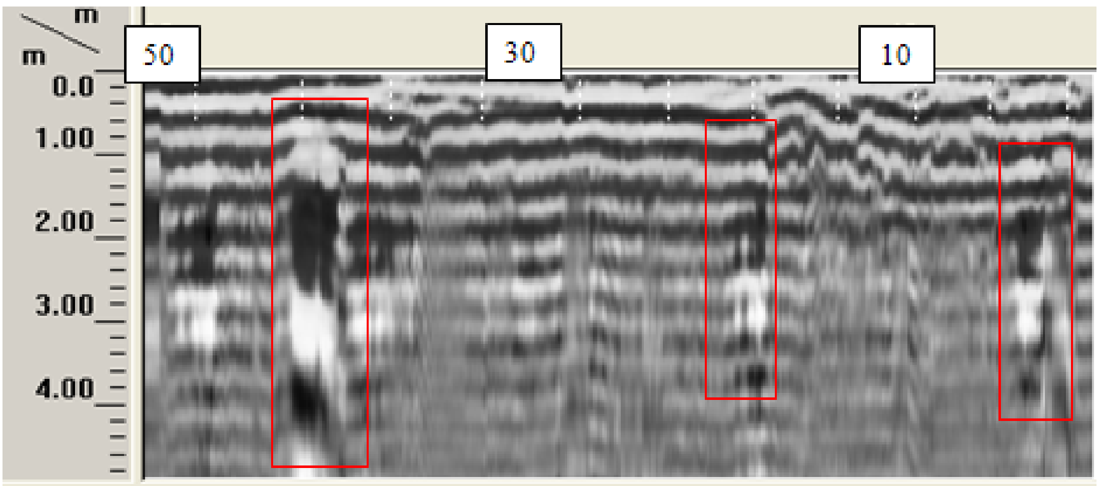

Figure 6.37 GPR profile of grid 2; (line 11 or meter mark 50) Red box denotes a long wave length anomaly and a green oval denotes a normal wave length anomaly.

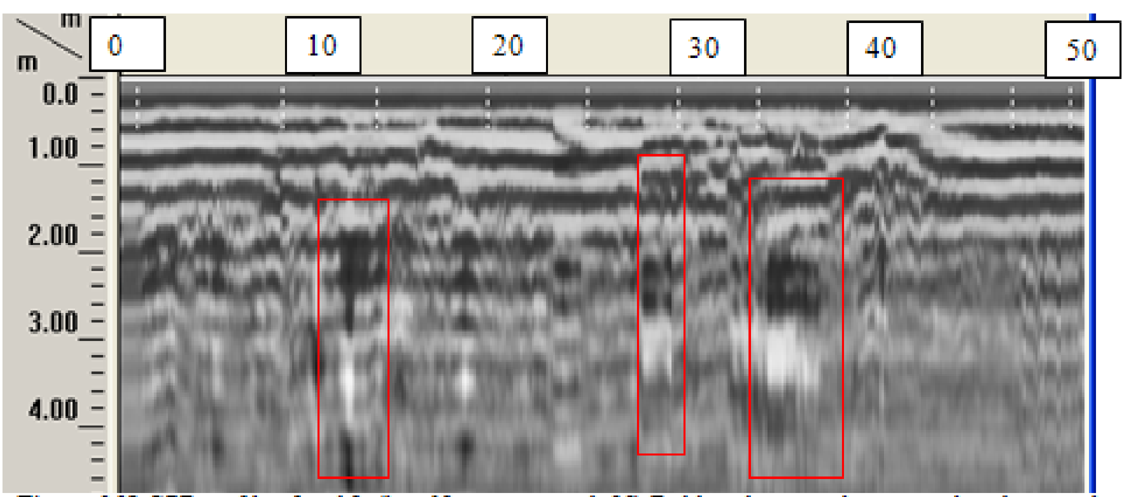

Figure 6.38 GPR profile of grid 2; (line 12 or meter mark 55) Red box denotes a long wave length anomaly and a green oval denotes a normal wave length anomaly.

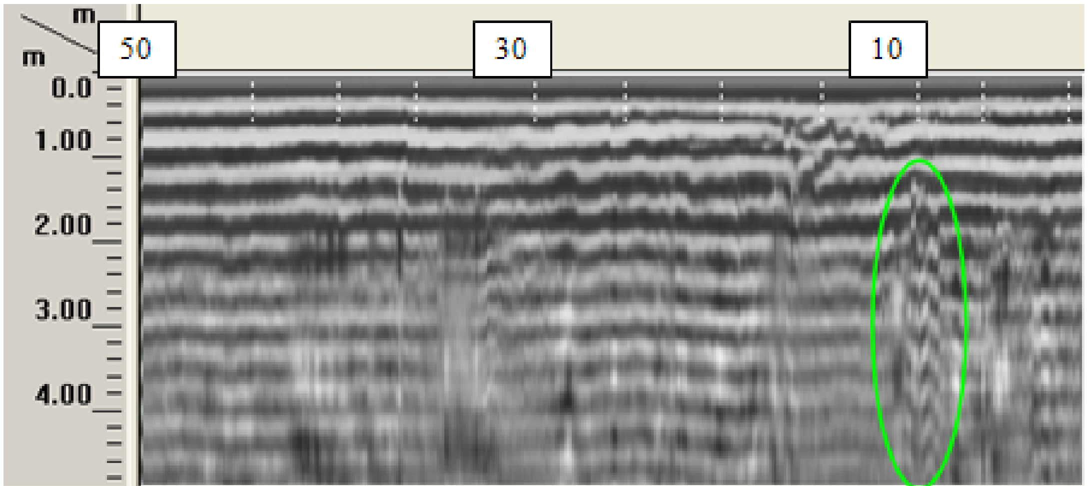

Figure 6.40 GPR profile of grid 2; (line 13 or meter mark 60). Red box denotes a long wave length anomaly and a green oval denotes a normal wave length anomaly.

Grid 1 Plot of Long and Normal wave Anomalies											
Line\m	0	5	10	15	20	25	30	35	40	45	50
1					S						
2			L			S	L				
3								S			
4					L		L			L	
5					S	L	S				
6			L		L						
7	L		L		L	L		L		L	
8			L		L	S				L	
9		S		L		SL		S			
10						LS					
11						S			L	L	
12		S	S			S		L			
13			S			S	L				

Figure 6.41a Plotof grid 1 anomalies. L denotes the occurrence of a long wave length anomaly, while S denotes the occurrence of a normal wave length anomaly.

Grid 2 Plot of Long and Normal wave Anomalies											
Line\m	0	5	10	15	20	25	30	35	40	45	50
1						L	L			S	L
2						S				S	
3							L	S		L	
4	L			L							
5				S					L		
6								L			
7					S			S			L
8					S					S	
9						S					L
10					L			L	L		
11	L				L					L	
12			L								
13			S								

Figure 6.41b Plotof grid 2 anomalies. L denotes the occurrence of a long wave length anomaly, while S denotes the occurrence of a normal wave length anomaly.

7.0 SEISMIC REFRACTION & REFRACTION MICROTREMOR™

7.1 Technique

Two seismic methods, seismic refraction and refraction microtremor™ (ReMi), were combined to assist in detecting seismic anomalies consistent with earth fissures, and evaluation of the subsurface conditions at the earth fissure site. Expanding on a concept presented by Wrege and others (1985), a seismic refraction method to detect and trace earth fissures was initially described by Rucker and Keaton (1998) with a recent update by Rucker and Holmquist (2006). The method has been used to identify and trace earth fissures at multiple sites in Arizona and Nevada. Seismic traces are used to identify the presence or verify the absence of seismic data anomalies consistent with earth fissures. In essence, an earth fissure forms a vertical or near-vertical open crack in the subsurface. Seismic energy cannot propagate across the crack; seismic signals between adjacent geophones lose excessive signal amplitude (severe attenuation) and / or first arrival times are significantly delayed (time offset). The crack does not need significant aperture to impact the seismic signal. A possible earth fissure is located by locating an area of anomalous seismic signal through visual evaluation of the seismic traces in the field. The presence of such anomalies in several data sets for a seismic line, such as in both foreshot and backshot trace sets, is considered an indicator of an earth fissure or similar soil discontinuity. Interpretation of the absence or presence of anomalies consistent with earth fissures is made in the field during the performance of each seismic line. The location of each anomaly interpretation along a seismic line is immediately staked in the field while the geophone cabling is still deployed on the ground. A test trench is later dug across the seismic anomaly location to confirm the qualitative seismic interpretation.

In addition, seismic refraction interpretations provide general subsurface information for geologic and engineering characterization. Results include assessment of subsurface material strengths as a function of compression wave (p-wave) profiles in two dimensions (p-wave velocities laterally and vertically along the seismic line), and subsurface geometry as a function of interface depths at various points along the seismic line. Limitations include interference from noise at or near the site, and the inability to detect a lower velocity horizon underlying a higher velocity horizon (velocity reversal).

The Refraction Microtremor™ (ReMi) seismic method is a variation of multi-channel analysis of surface waves (MASW) that uses surface-wave travel times to characterize subsurface structure up to 100-m depth (Louie, 2001). ReMi provides assessment of subsurface shear wave (s-wave) profiles in one dimension as a vertical profile representing a discrete length of seismic line (typically about 33 or 69 meters on this project). ReMi uses surface waves from ambient site noise as the energy source, and is effective at noisy sites. Although limited to a one-dimensional vertical profile, significant velocity reversals (a lower seismic velocity, less competent zone underlying a higher seismic velocity, more competent zone) can be detected and interpreted. This capability is particularly useful in the desert southwest, where soil profiles tend to include a relatively more competent, cemented horizon overlying a less competent horizon. A benefit of combining seismic refraction and ReMi is that areas of low velocity (such as buried channels and fissures) can be more readily interpreted from surface measurements (Rucker and Fergason, 2006; Rucker and others, 2008). Anomalous attenuation of seismic refraction signals due to a thin high-velocity horizon can also be assessed; such attenuation could otherwise be confused as an earth fissure signature.

The seismograph used in this survey for both seismic refraction and ReMi was a Geometrics 24-channel Smartseis SE-24. Arrays of either 12 or 24 low-frequency 4.5 Hz geophones deployed at 3-meter intervals were used to collect both seismic refraction and ReMi data. Low frequency geophones can be subject to unwanted effects of ‘ground roll’ when collecting seismic refraction data; ground roll noise was not a concern at this site. On the other hand, surface wave energy (which is ‘ground roll’) is the very signal utilized by the ReMi method; 4.5 Hz geophones were ideal for this purpose. For seismic refraction, the sampling rate was set to 62 microseconds with record lengths of 256 milliseconds. A sledgehammer striking a metal plate served as the seismic refraction energy source. Three hammer impacts were typically stacked at each shotpoint for each data set. Shotpoints were positioned at 9-meter intervals along the geophone arrays. The ReMi method uses ambient energy sources, such as ground vibrations from traffic or wind, for the passive energy source. For this survey, the “ambient” noise consisted of one to three people jumping in place beyond the end of the geophone array to create the source signal.

7.2 Location

The current surface seismic survey consisted of two 36-meter (Lines 1 and 2) and one 72-meter (Line 3) seismic arrays, with 3-meter spacing between geophones. In addition, a historic 36-meter seismic array (Line L6) was completed at the desiccation crack site. Each linear array trended roughly east to west. Data were obtained along Seismic Lines 1 and 2 on 3/7/09 and along Seismic Line 3 on 3/28/09. Seismic Line 1, oriented east-west, was situated about 3-meters south of the barbed wire fence, and was centered upon the fissure. Seismic Line 2, oriented along Grid 2 Line 6, was centered at about the 25-meter point on Grid 2 Line 6.

Seismic Line 3, oriented along Grid 2 Line 4, was centered at about the 20-meter point on Grid 2 Line 4. Seismic Lines 2 and 3 were approximately centered about 5 meters north and south, respectively, of a small tree growing on the alignment along a known 16-inch diameter fibreglass water line buried at a depth of several feet. Seismic Lines 1, 2 and 3 were all oriented approximately east to west.

Historic Seismic Line L6, also 36 meters long with 3-meter geophone spacing, was located across the desiccation crack to the south of the ponds along Line 2 in the Desiccation Crack area. Completed on December 13, 2005, this line was oriented south to north and centered on the desiccation crack. Notes on the field traces included "in road west of AEPCO east of wheel-rolled area," "at easternmost ground crack in road," and at the geophone array centerpoint, "@ gnd crack."

7.3 General Interpretation and Analysis of Seismic Anomaly Traces for Earth Fissures

An initial definition and description of seismic anomalies as used in 1994 when the method was developed and applied to earth fissure detecting and tracing in the field is presented in Rucker and Keaton (1998) as follows:

> *Qualitative interpretation of isolated attenuation data is separated into four semi-empirical categories: excellent, good, poor and none. An excellent indication is given by an amplitude ratio in excess of about 4 (12 db) for adjacent geophones and 3 for equidistant geophones, or by cycle skipping… A good indication is given by an amplitude ratio in excess of about 3 for adjacent geophones and 2 (6 db) for equidistant geophones… A poor indication has a lower*

amplitude ratio, which may or may not be due to isolated attenuation… Absence of attenuation results in an interpretation that no fissure is present.

Continuing experience has modified the empirical interpretations somewhat as the field seismic methods have evolved and additional subsurface conditions have been encountered and interpreted, and then verified and evaluated, using test pits and trenches. Improved seismic methods include the use of 5 shotpoints at 9-meter intervals along a 36-meter seismic line (3 meter geophone spacing) and the introduction of surface wave data collection for ReMi as an additional means of empirically evaluating seismic amplitude attenuation. The introduction of 24-channel seismic equipment, still using 9-meter shotpoint intervals and 3-meter geophone spacing, has further improved seismic anomaly detection as less overlap of adjacent seismic lines is required. The inclusion of a distinct lateral reduction in seismic velocity is now also included in the interpretation of a weak to possible seismic anomaly. Additional subsurface conditions include encountering, interpreting and verifying buried (paleo-) stream channels and collecting data across observed surface desiccation cracks typical of areas with giant polygonal desiccation features.

The presence of a velocity reversal condition in the subsurface can generate seismic anomalies that could be confused with earth fissure-type seismic anomalies. Typically, such velocity reversal-induced seismic signal attenuation and apparent cycle skipping can be generated due to subsurface conditions involving a cemented or cohesive horizon overlying a less cemented or uncemented (or cohesionless) horizon. Very rapid attenuation of p-wave refraction signals in thin high-velocity layers, about 5 to 10 db per wavelength when the layer is less than about one-half wavelength in thickness, has been presented in the literature (O'Brien, 1967; Sherwood, 1967). Vertical s-wave profiles and signal attenuation patterns that repeat at the same apparent distance from the shotpoints across multiple shot trends can help to discriminate between a relatively thin cemented horizon and a significant discrete anomaly, including an earth fissure.

Given these considerations, a current definition of seismic anomalies in native ground and embankments, tempered with engineering judgment, may be considered as follows.

Strong seismic anomaly – would typically be an excellent to good (Rucker and Keaton, 1998) seismic signal indication obtained in multiple seismic shot trends (i.e.: fore-shot, forward quarter-shot and back quarter-shot). This interpretation typically indicates the presence of a significant and discrete subsurface anomaly. Such an anomaly in native ground could be an earth fissure, or in an embankment could be a significant crack. An example of a strong seismic anomaly in an embankment is presented in Figure 9 of Rucker and Holmquist (2006).

Weak seismic anomaly – would typically be a poor (Rucker and Keaton, 1998) seismic signal indication obtained in multiple seismic shot trends (i.e.: forward quarter-shot, mid-shot and back-shot). There may be one good (Rucker and Keaton, 1998) seismic shot trend in the group, but the other shot trends do not support a strong seismic anomaly interpretation. A distinct or discrete reduction in lateral seismic velocity at multiple seismic shot trends, perhaps over an apparent lateral distance of perhaps two to three geophones, with or without significant attenuation, can also contribute to the interpretation of a weak seismic anomaly. In native ground, this interpretation more likely indicates the presence of a subsurface anomalous condition that influences seismic velocity, such as a distinct zone of cohesionless material in a geologic setting of cemented materials, rather than a discrete earth fissure-type feature. In an embankment, this interpretation is more likely consistent with a zone of desiccation cracking that is relatively shallow in extent.

Possible seismic anomaly – would typically be less distinct than a weak seismic anomaly, but still expresses sufficient character that it would be imprudent to ignore in an investigation to evaluate the presence or absence of subsurface anomalies.

P-wave interpretations for seismic velocities of horizons and depths of horizon interfaces typically utilize first arrival picks as far as can be determined from each energy point. Under normal conditions, data for a minimum distance of at least 9 to 12 geophones of a 24-geophone array can be picked for each energy point. Attenuation of the seismic signal eventually degrades the signal traces such that usable signals are not expected across an entire 24-geophone array. Multiple energy points along each seismic line provide multiple opportunities to interpret the potential for anomalous signal loss, depths to subsurface interfaces, possible velocity reversals, and laterally variable velocity conditions.

ReMi surface wave signal traces also provide opportunity to evaluate potential anomalous signal attenuation under some conditions. However, anomalous time delays may not be readily discernable or interpretable using this method. ReMi’s s-wave use has not been as extensively tested as p-wave seismic refraction, but may be effective in some conditions.

7.4 Evaluation of Seismic Field Traces

The primary seismic earth fissure interpretation was performed in the field looking at the trace amplitudes and arrival times. Copies of the field traces are reviewed and discussed in the following subsections. Discussion will begin with the earlier seismic traces at the desiccation crack where no seismic anomaly was present. That set of traces is an example of the "null" case, where no seismic anomaly is evident in seismic field traces. Then field traces from the three lines completed in March 2009 are evaluated for possible seismic anomalies consistent with the presence of an earth fissure.

7.4.1 Seismic Traces at Desiccation Crack South of Ponds

Seismic refraction field traces for Seismic Line L6 completed in December 2005 across the desiccation crack are presented in Figures 7.1 and 7.2. The geophone array was deployed with it's centerpoint at the ground crack. The complete set of traces across 12 geophones, 36 meters of seismic array, can be seen in the "FS" trace in Figure 7.1 and the "BS" trace in Figure 7.2. In both the "FS" and "BS" traces, seismic first arrivals are well formed and appear similar in shape. First arrival times can be manually read and selected in a straightforward pattern of increasing time (about 4 to 6 milliseconds additional time for each geophone as distance from the sledgehammer shotpoint increases) across the entire geophone array. Interference from the hammer impact air wave is apparent in the high frequency first arrivals at 2 to 3 geophones closest to each shotpoint; this indicates that the surficial horizon has a p-wave velocity slower than the speed of sound in air. Seismic trace gains (in decibels) increase gradually as the distance from the shotpoint and the receiving geophone increases. The seismic trace patterns visually appear to be mostly unaffected by the presence of an obvious ground crack at the center of the geophone array. Apparently, the crack visible at the ground surface did not extend through the higher p-wave velocity, more competent shallow subsurface horizon. The seismic first arrival signal propagated unimpeded under the crack along this more competent, cemented horizon.

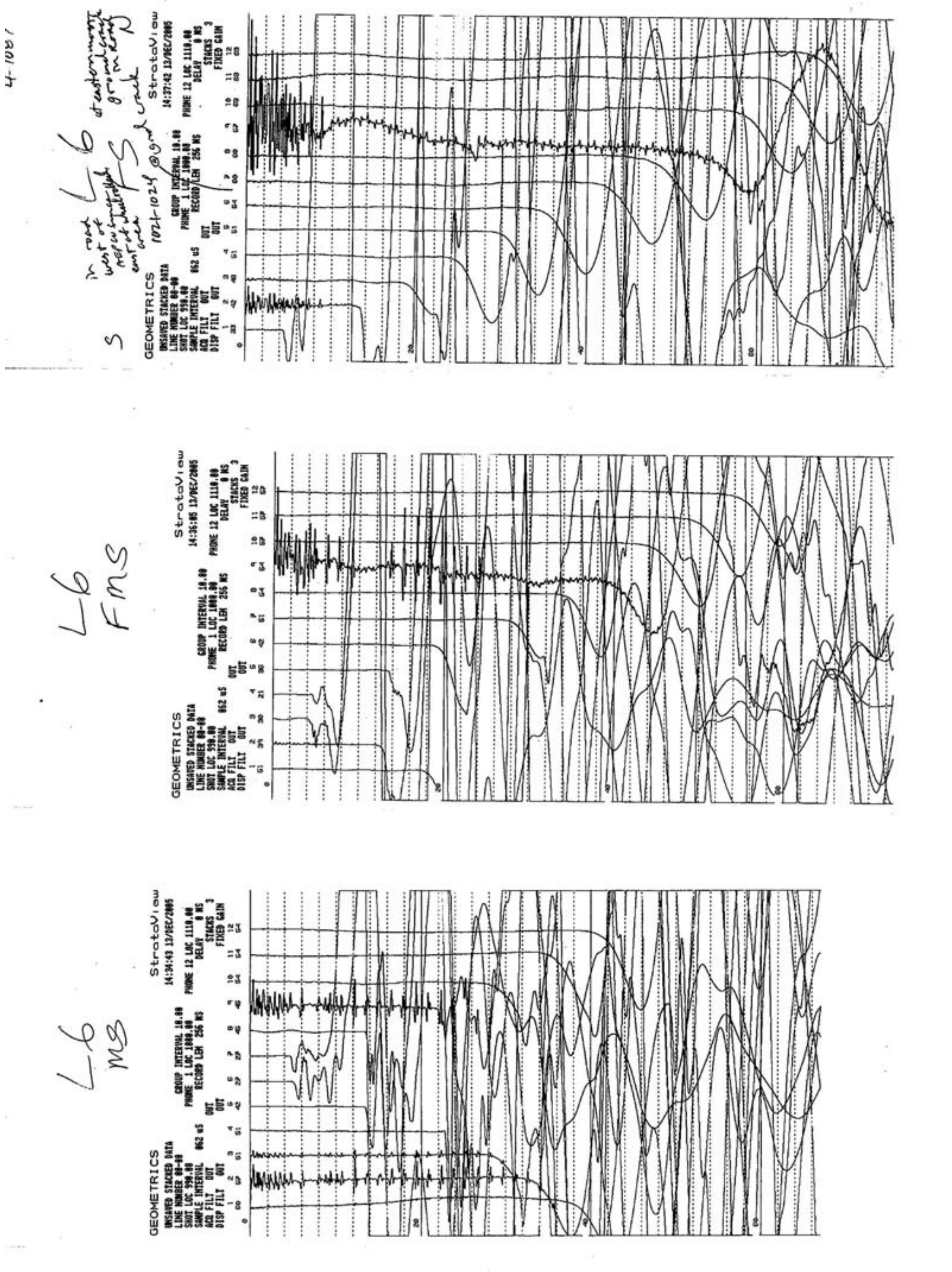

Figure 7.1 Seismic Line across desiccation crack south of ponds.

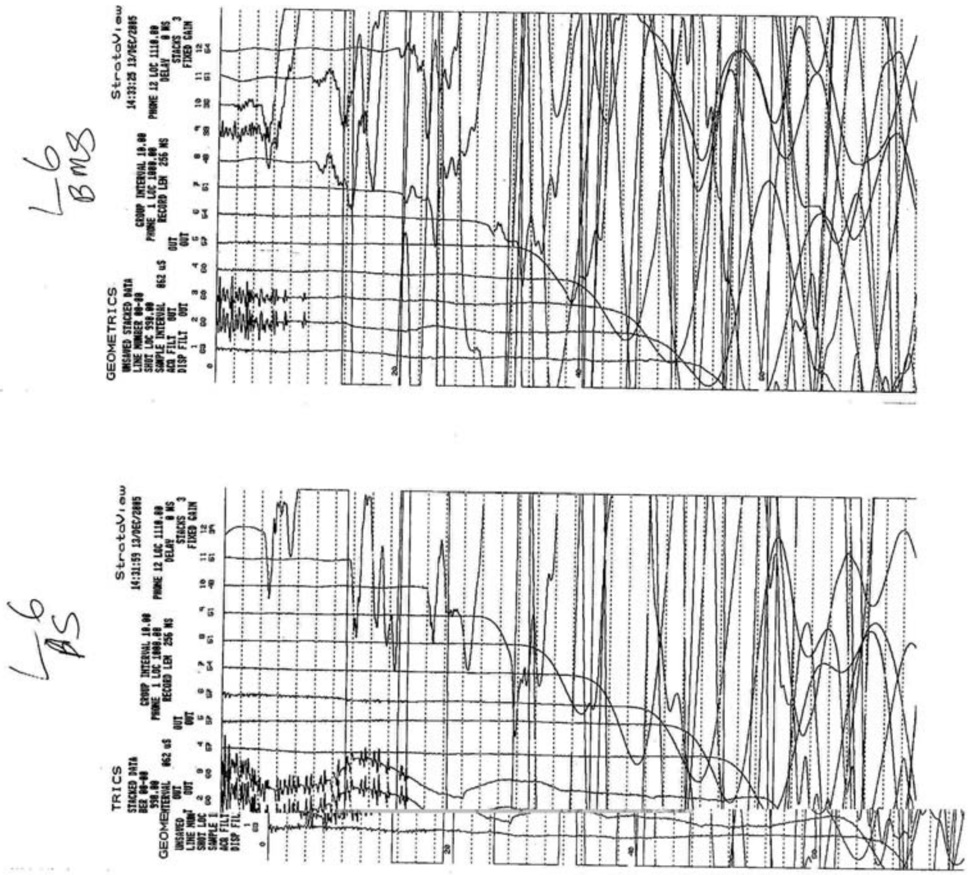

Figure 7.2 Seismic line across desiccation crack south of ponds

Thus, the ground crack was interpreted to be a desiccation crack that extended to only a very shallow to shallow depth, and not an earth fissure. An earth fissure would have a seismic signal-disrupting crack extending through the more competent cemented horizon.

7.4.2 Field Traces at Seismic Line 1

Seismic refraction field traces for Seismic Line 1 completed on March 7, 2009 South of the barbed wire fence between Grids 1 and 2 are presented in Figures 7.3 through 7.5. The geophone array was deployed west to east in an area without surface expression of the earth fissure. The centerpoint was positioned along the projection of the last visible portion of the earth fissure to the South. Figure 7.3 presents traces for the easternmost shotpoint and the next shotpoint 9 meters to the West. From the easternmost shotpoint, well formed first arrival traces are observed for the adjacent geophones 11 through 7. First arrival times can be manually read and selected in a straightforward pattern of increasing time (about 4 to 6 milliseconds additional time for each geophone as distance from the sledgehammer shotpoint increases) across this part of the geophone array. At geophone 6, however, the signal becomes noisy and attenuated, and by geophone 5, the first arrival signal is lost entirely. At the next shotpoint (between geophones 9 and 10), clear first arrival signals can be observed at geophones 8 through 6, to perhaps geophone 5. By geophone 4, the first arrival signal is lost. These traces indicate a strong seismic anomaly consistent with an earth fissure in the general area of geophones 4 to 6.

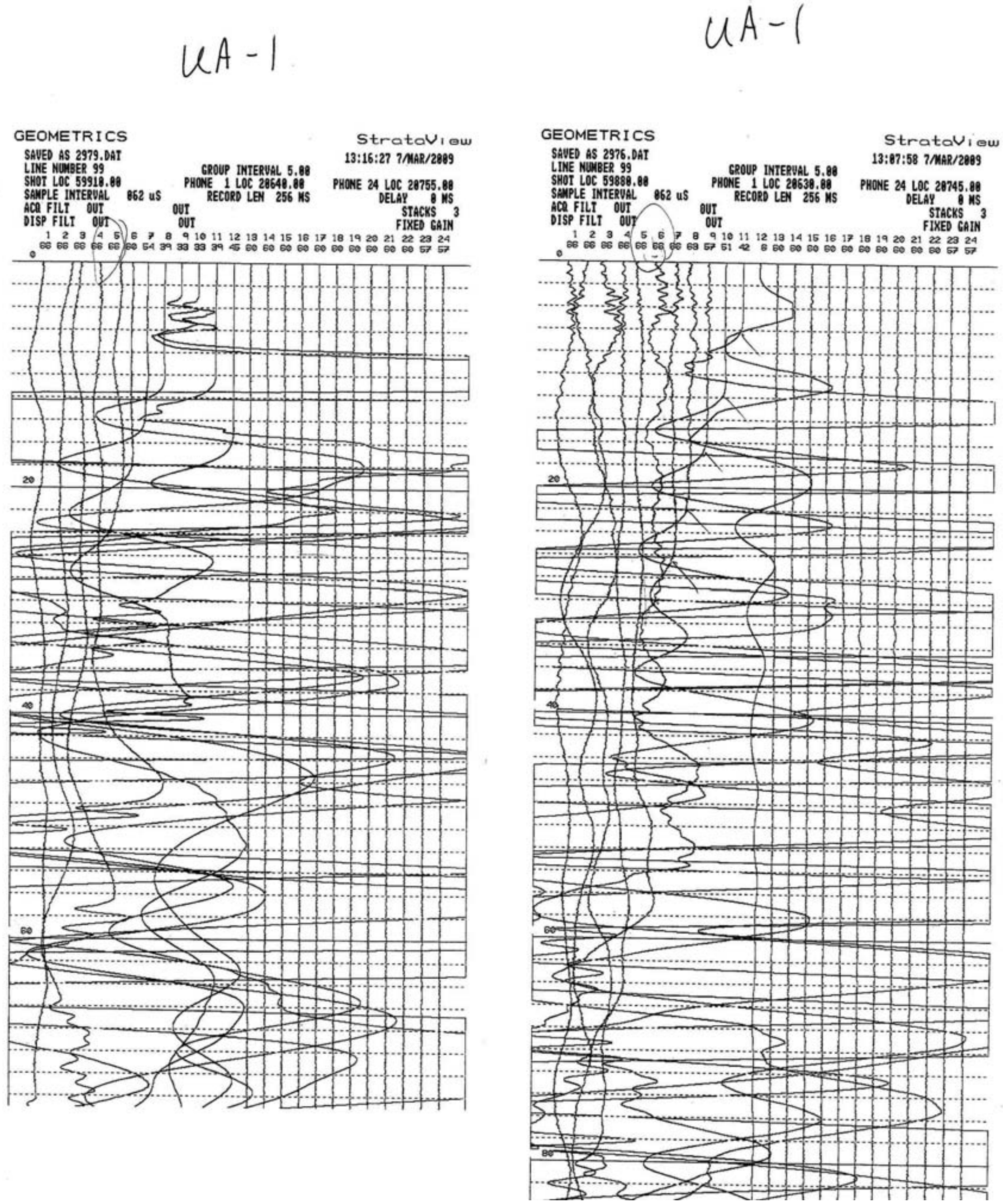

Figure 7.3 Seismic Line 1 traces for easternmmost (right) shotpoint and shotpoint 9 meters West (left).

Figure 7.4 presents traces for the center shotpoint (between geophones 6 and 7) and the next shotpoint 9 meters to the West (between geophones 3 and 4). From the center shotpoint, well formed first arrival traces are observed for the adjacent geophones 7 through 12 to the East. First arrival times can be manually read and selected in a straightforward pattern of increasing time (about 4 to 6 milliseconds additional time for each geophone as distance from the sledgehammer shotpoint increases) across this part of the geophone array; no earth fissure-type seismic anomaly is indicated East of the center shotpoint.

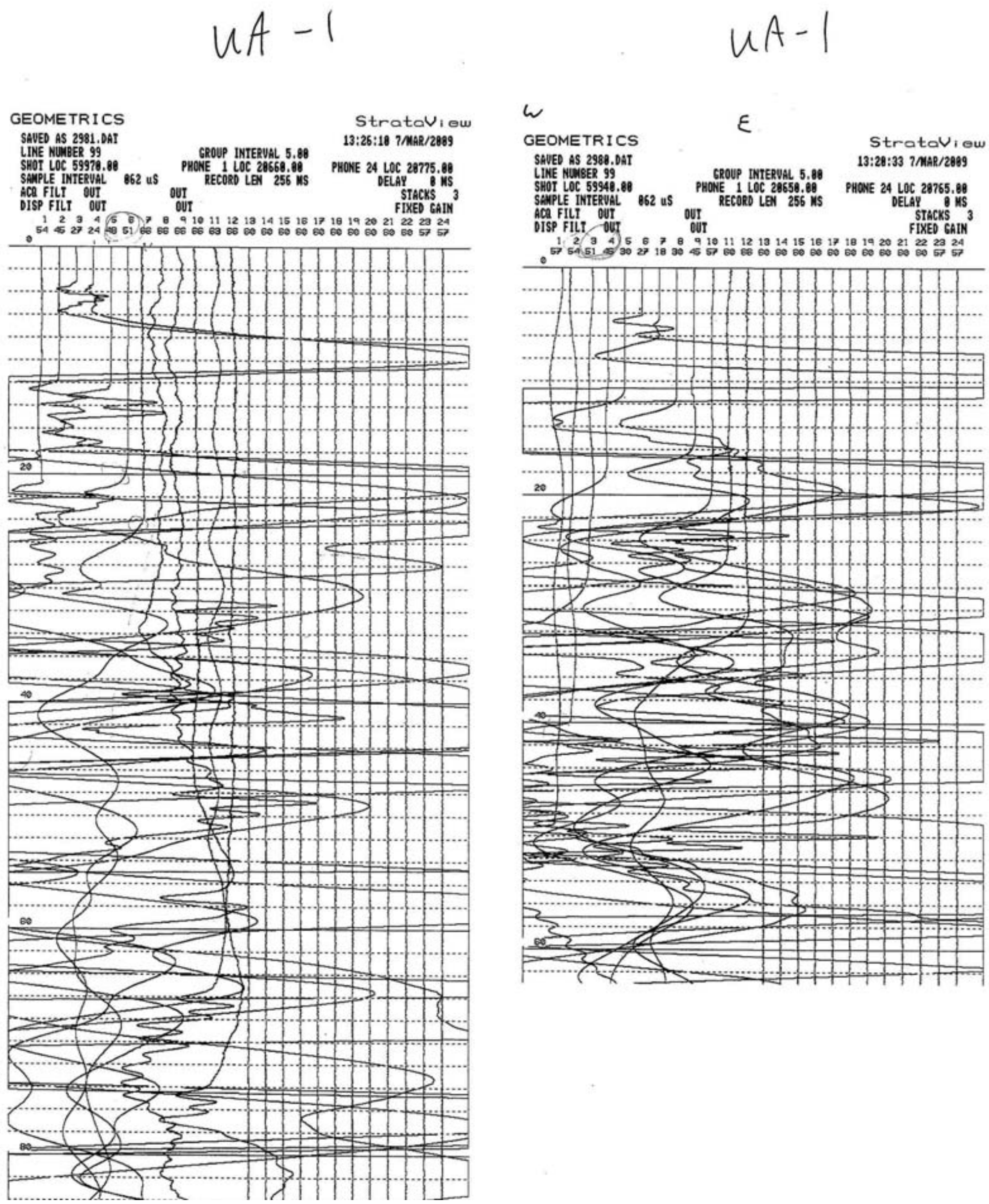

Figure 7.4 Seismic Line 1 traces for center (right) shotpoint and shotpoint 9-meters from West end of line (left).

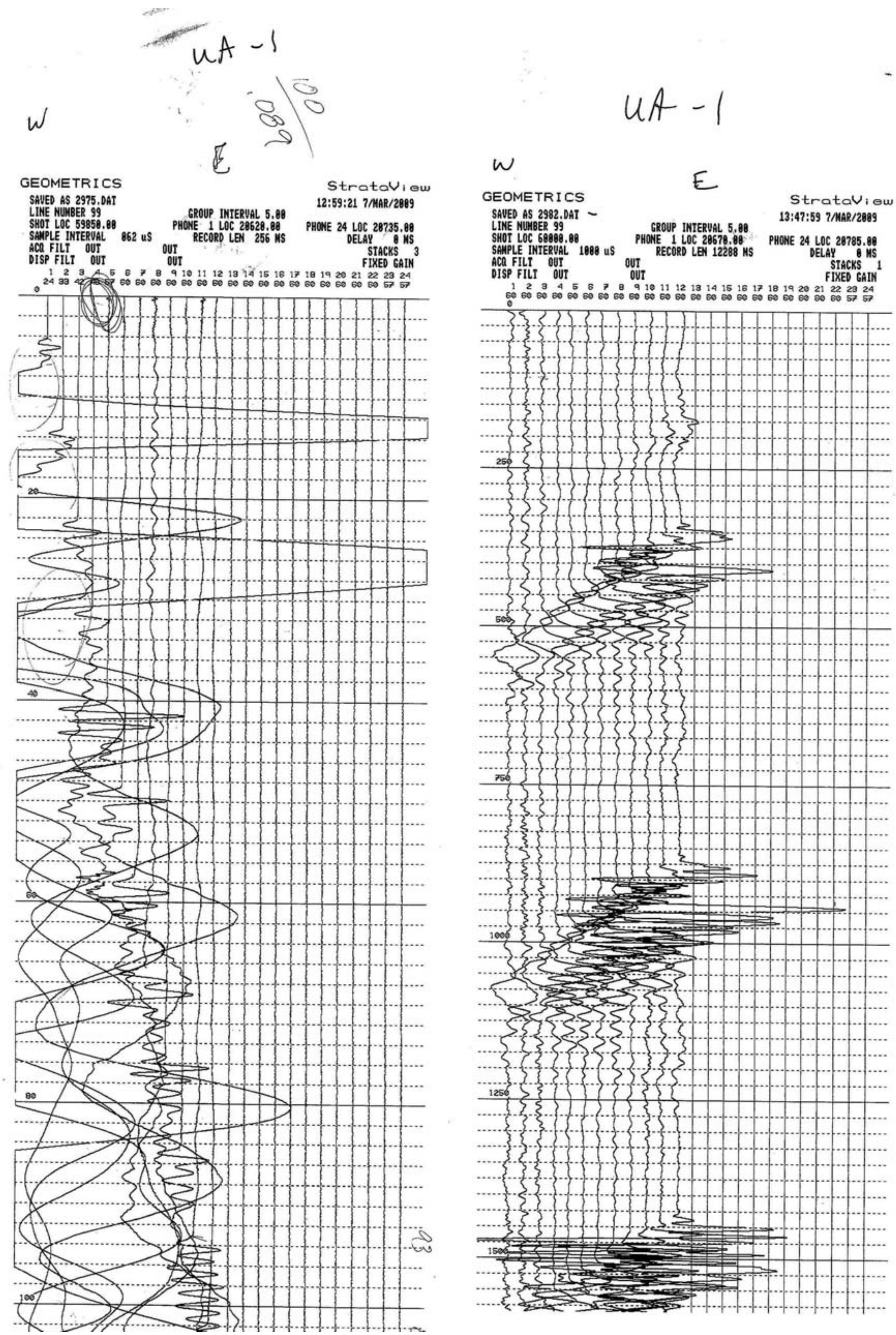

Figure 7.5 Seismic Line 1 westernmost shotpoint traces and example ReMi traces.

To the West at geophones 5 through 3 (Figure 7.4 center shotpoint), well formed first arrivals are present, but the arrival times increase with distance from the shotpoint. By geophone 2, a higher frequency first arrival indicates air wave. Most of the clear first arrivals at the shotpoint between geophones 3 and 4 are air wave, and possible ‘normal’ first arrival signals are present only at geophones 6 and 7. Traces from the westernmost shotpoint shown in Figure 7.5 all show interference from air wave signals, although some following first arrival ground signal can be discerned in the noisy traces. Overall, the traces West of the Seismic Line 1 center indicate disruption of the seismic signal propagation through the western half of the seismic line.

Based on visual evaluation of the seismic refraction traces, a strong seismic anomaly consistent with an earth fissure-type feature is interpreted to be present in the subsurface at about the location of geophone 6.

7.4.3 Field Traces at Seismic Line 2

Seismic refraction field traces for Seismic Line 2 completed on March 7, 2009 along Grid 2 Line 6 are presented in Figures 7.6 through 7.8. The geophone array was deployed West to East in an area without surface expression of the earth fissure. The center point was positioned North of the buried waterline along the projection of the last visible portion of the earth fissure and the small tree at the waterline to the south. Figure 7.6 presents traces for the easternmost shotpoint and the next shotpoint 9 meters to the West. From the easternmost shotpoint, well formed first arrival traces are observed for only the adjacent geophones 12 through 10 in a straightforward pattern of increasing time (about 4 milliseconds additional time for each geophone). At geophone 9, however, the signal becomes attenuated, and by geophone 8, the first arrival signal is lost. At the next shotpoint (between geophones 9 and 10), clear first arrival signals can be observed at geophones 9 through 7. By geophone 6, the first arrival signal is lost. These traces indicate a seismic anomaly at a consistent distance of about 3 geophones from the shotpoint; such a pattern is consistent with rapid attenuation due to a thin high velocity horizon.

Figure 7.7 presents traces for the center shotpoint (between geophones 6 and 7) and the next shotpoint 9 meters to the West (between geophones 3 and 4). From the center shotpoint, well formed first arrival traces are observed for the adjacent geophones 7 through 9 to the East, and then rapid attenuation by geophone 10. To the West at geophones 5 through 3, a higher frequency first arrival indicates air wave before possible well formed signal traces are observed at geophones 2 and 1. Similarly, some traces near the shotpoint between geophones 3 and 4 indicate air wave (geophones 6 through 8) while the other geophones (2 to 1 and 9 through 12) have possible 'normal' first arrival signals. Traces from the westernmost shotpoint shown in Figure 7.8 are well formed only to geophone 3, and then show rapid attenuation and significant time delay.

Based on visual evaluation of the seismic refraction traces, a series of weak or possible seismic anomalies more consistent with a thin higher velocity horizon than an earth fissure-type feature are interpreted to be present across this seismic line.

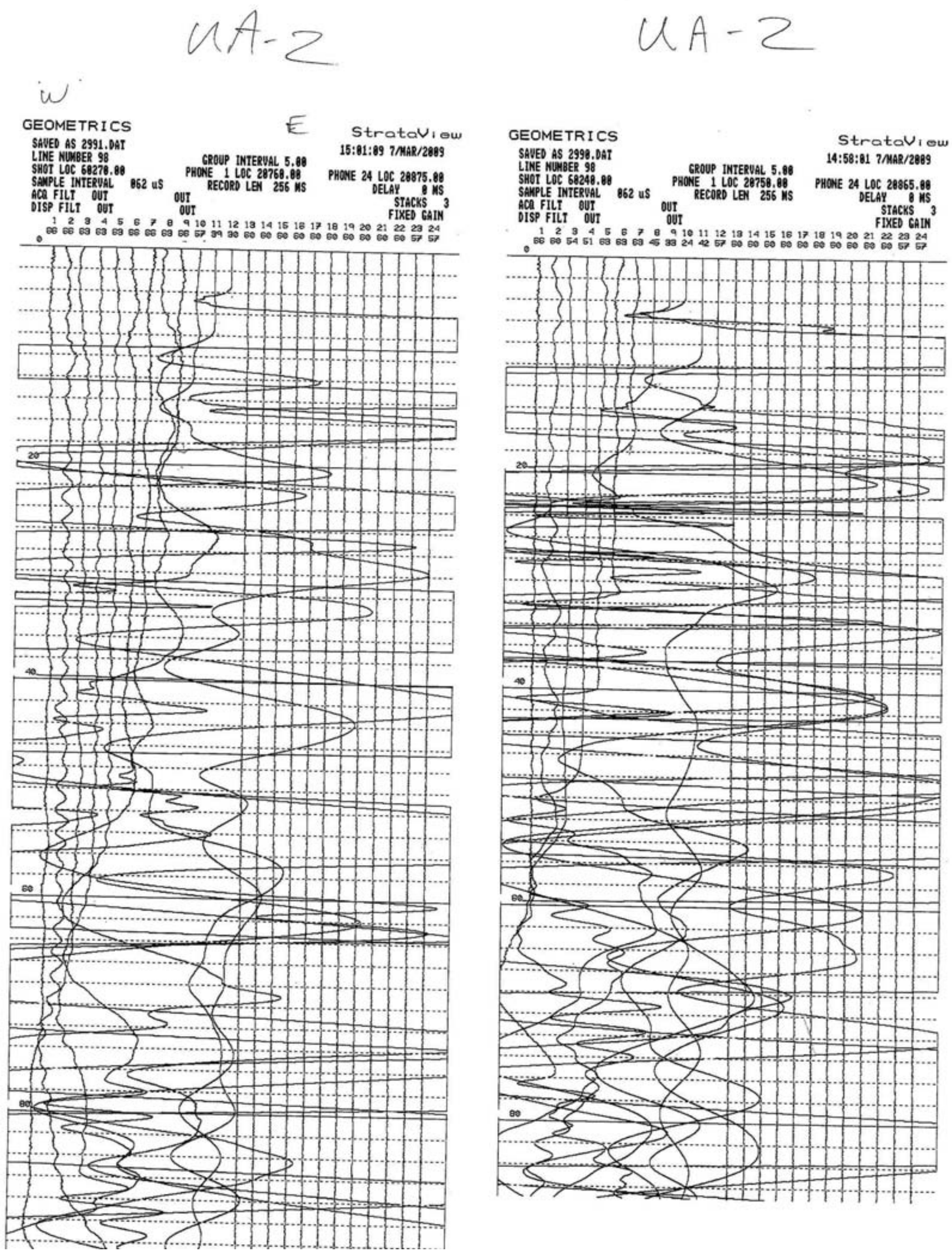

Figure 7.6 Seismic Line 2 traces for easternmmost (left) shotpoint and shotpoint 9 meters West (right).

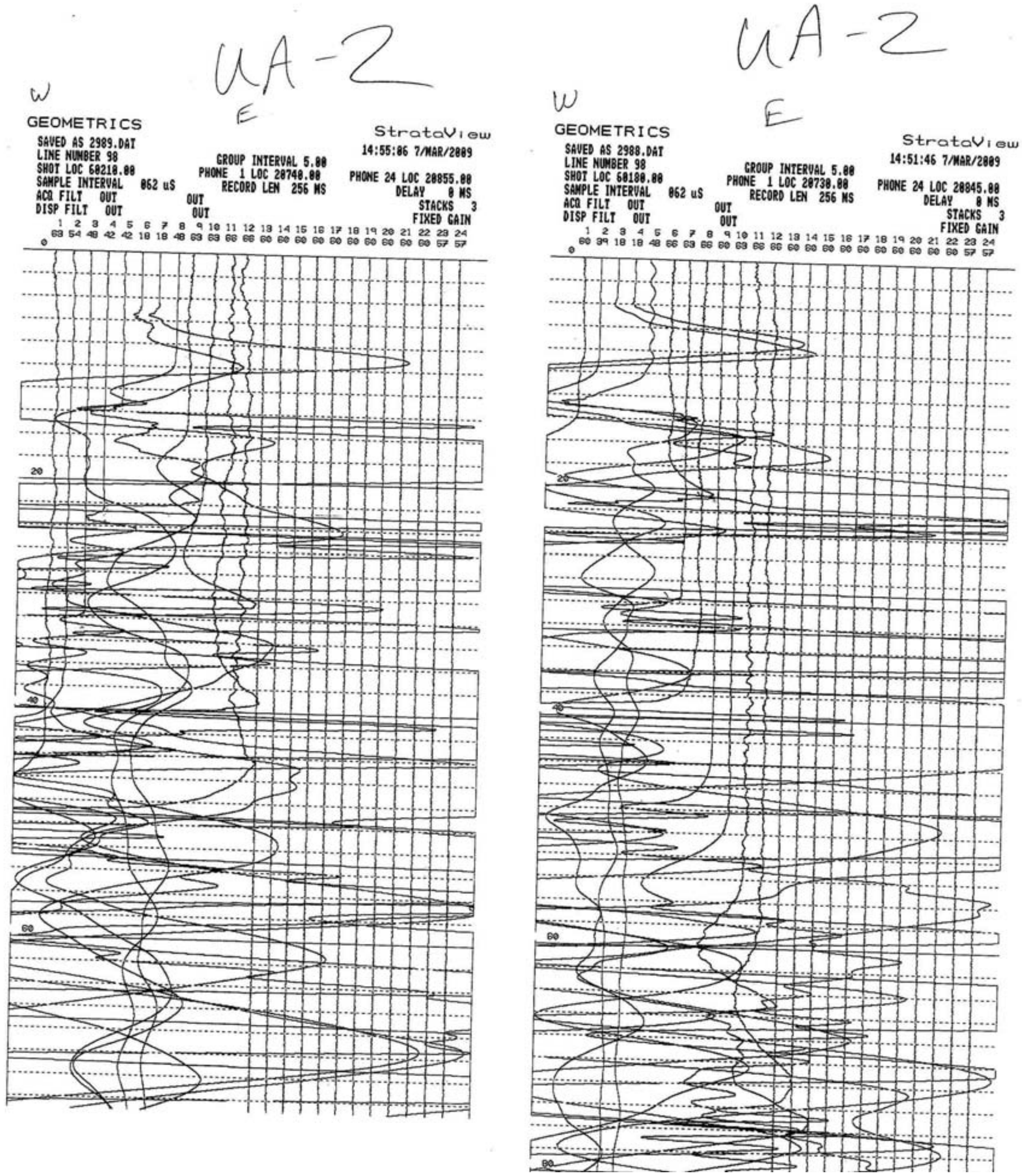

Figure 7.7 Seismic Line 2 traces for center (left) shotpoint and shotpoint 9-meters from West end of line (right).

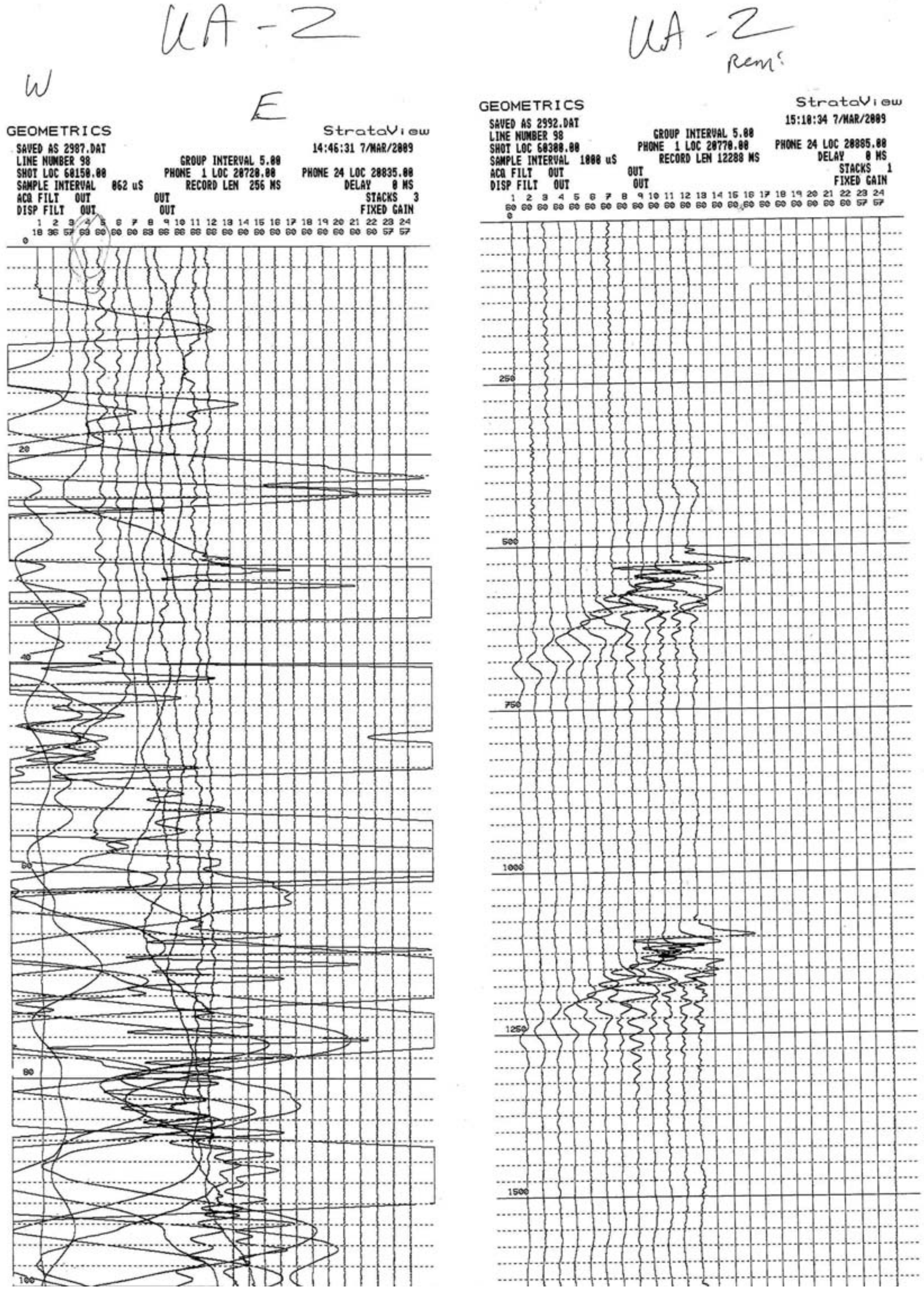

Figure 7.8 Seismic Line 2 westernmost shotpoint traces and example ReMi traces.

7.4.4 Field Traces at Seismic Line 3

Seismic refraction field traces for Seismic Line 3 completed on March 28, 2009 along Grid 2 Line 4 are presented in Figures 7.9 through 7.13. Seismic Line 3 was completed as a 72-meter long 24-geophone array with 9 shotpoints distributed at 9-meter intervals along the array. The geophone array was deployed West to East in an area without surface expression of the earth fissure. The centerpoint was positioned at location Grid 2, Line 4, 20 m, South of the buried waterline along the projection of the last visible portion of the earth fissure to the South and the small tree at the waterline to the North.

Figure 7.9 presents traces for the easternmost shotpoint just east of geophone 24. From the easternmost shotpoint, well formed first arrival traces are observed for the adjacent geophones 24 through 18 in a straightforward pattern of increasing time (about 4 milliseconds additional time for each geophone), with gradual but persistent attenuation evident at geophones to the West. The next two shotpoint traces are presented in Figure 7.10. At the next shotpoint (between geophones 21 and 22), clear first arrival signals can be observed at geophones 23 and 24, but signal traces are of poor quality for geophones to the West. At the shotpoint between geophones 18 and 19, clear first arrival signals in both directions between geophone 24 to about geophone 13. Rapid and possibly anomalous attenuation is evident beginning at about geophone 12 and to the West. Although signal attenuation is not abrupt, the traces in this section of Seismic Line 3 are consistent with a weak seismic anomaly in the vicinity of geophone 12.

Figure 7.11 presents traces for the shotpoints between geophones 15 and 16, and 12 and 13, towards the seismic line center. From the shotpoint between geophones 15 and 16, well formed first arrival traces are observed for the adjacent geophones 16 through 22 to the East and geophones 15 through about 11 or 9 (attenuation increasing) to the West. By geophone 8, the first arrival signal has disappeared, and the new first arrival is subject to a long time delay. A clear seismic anomaly is evident at the seismic line center shotpoint, Geophone 13 through 19 traces are clear and well formed, while geophone traces 11 through 8 indicate air wave, and first arrivals are not evident further to the West. Signal attenuation is abrupt in the vicinity of geophone 12, and is a strong seismic anomaly consistent with an earth fissure-type feature.

Figure 7.12 presents traces for the shotpoints between geophones 9 and 10, and 6 and 7, West of the seismic line center. From the shotpoint between geophones 9 and 10, well formed first arrival traces are observed for the adjacent geophones 9 through about 5 to the West, while air wave dominates geophone traces 11 to 14 to the East. Further geophone traces in both directions have long time delays consistent with thin horizon-type attenuation. From the shotpoint between geophones 6 and 7, well formed first arrival traces are observed for the adjacent geophones 8 through about 10 to 11 to the East. By geophone 12, the first arrival signal has disappeared, and the new first arrival is subject to a long time delay. A strong seismic anomaly is evident in these traces.

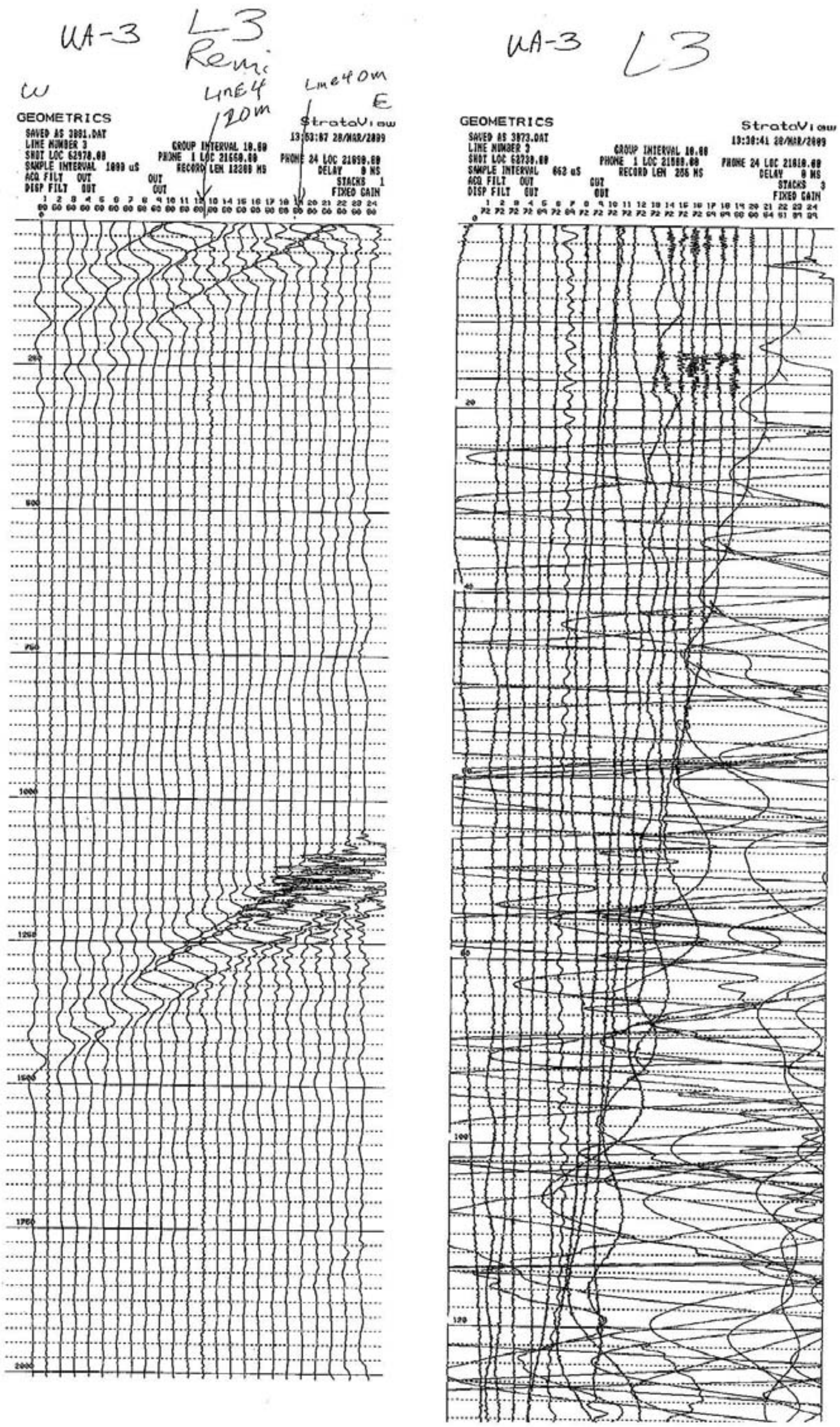

Figure 7.9 Seismic Line 3 easternmost shotpoint traces (right) and example ReMi traces (left).

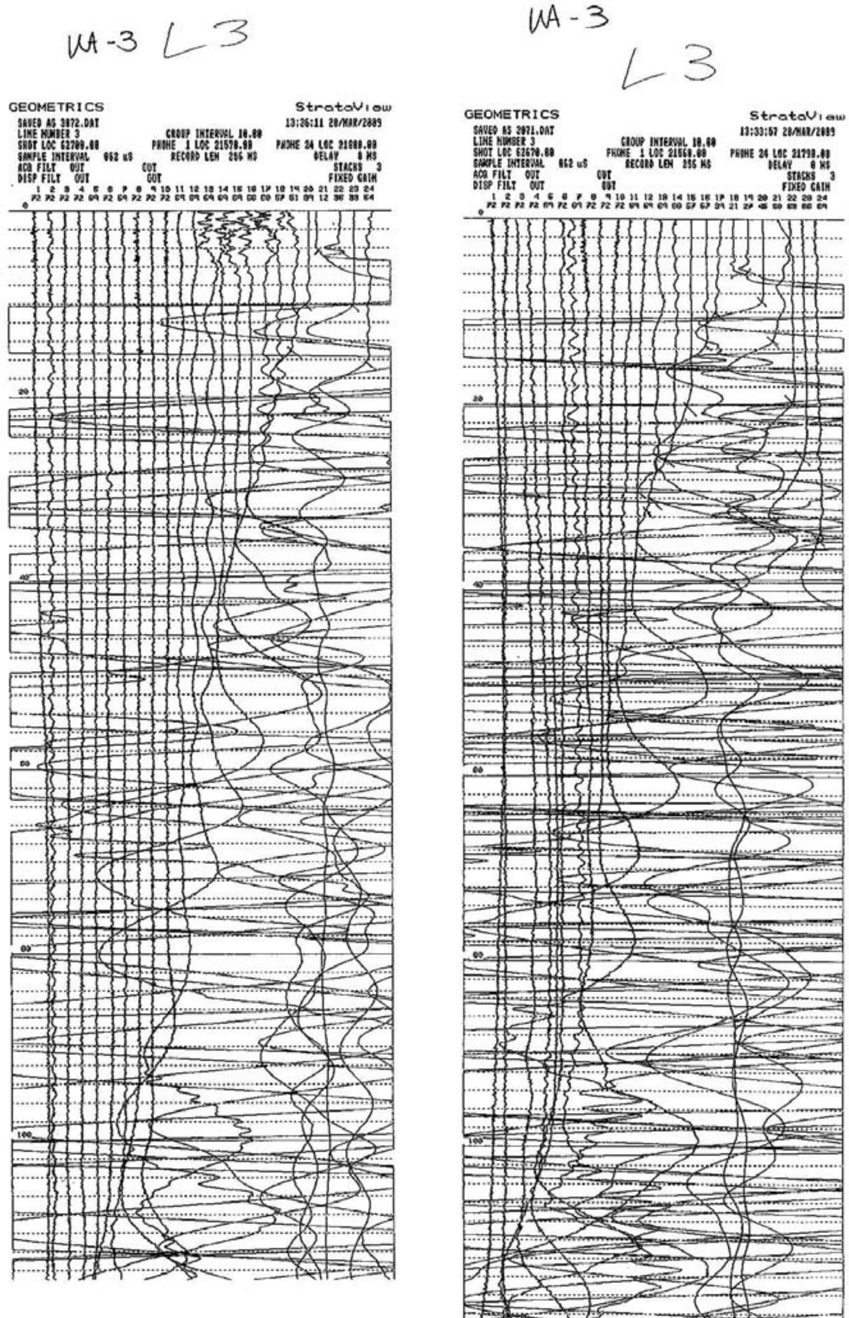

Figure 7.10 Seismic Line 3 shotpoint traces between geophones 21-22 (left) and 18-19 (right).

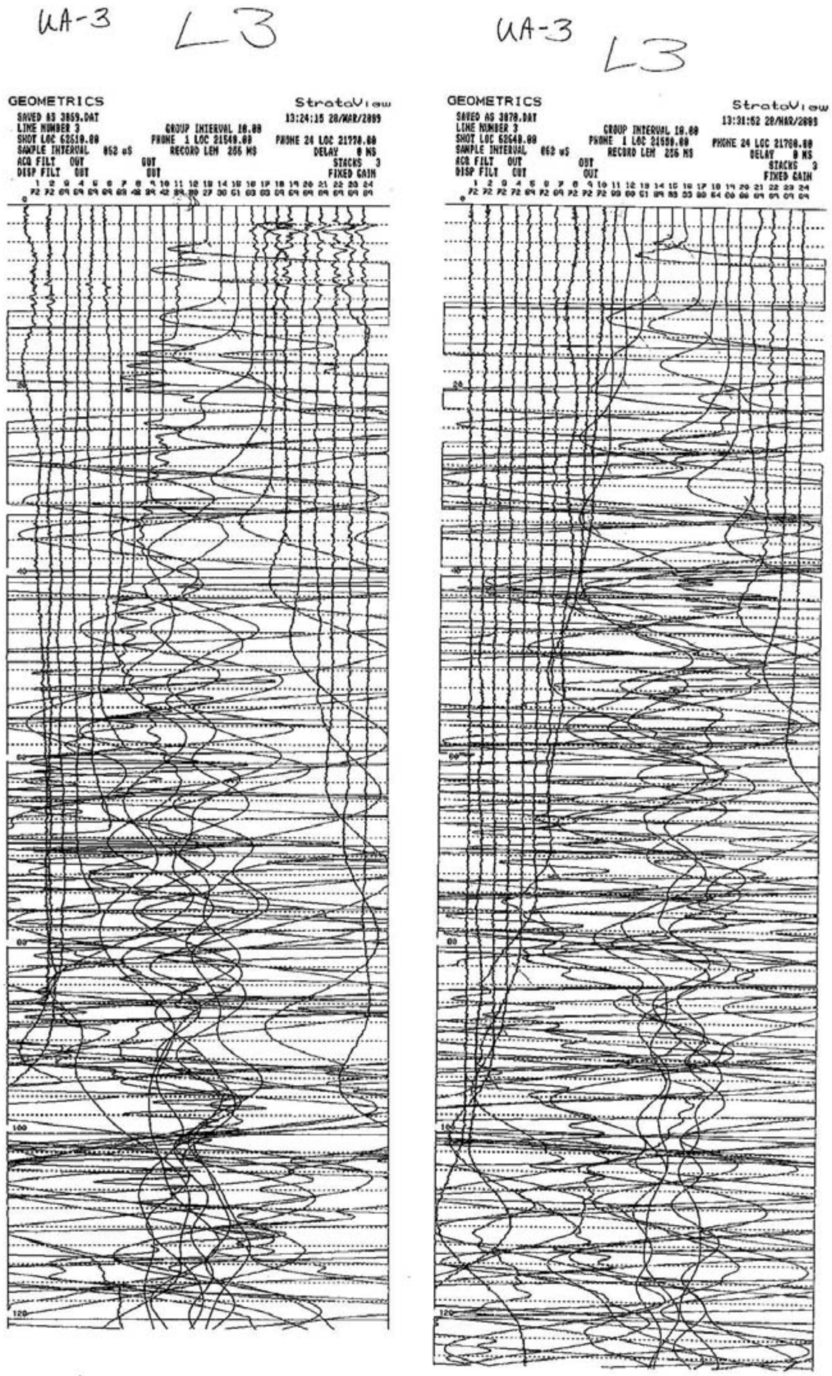

Figure 7.11 Seismic Line 3 shotpoint traces between geophones 15-16 (right) and 12-13 (left).

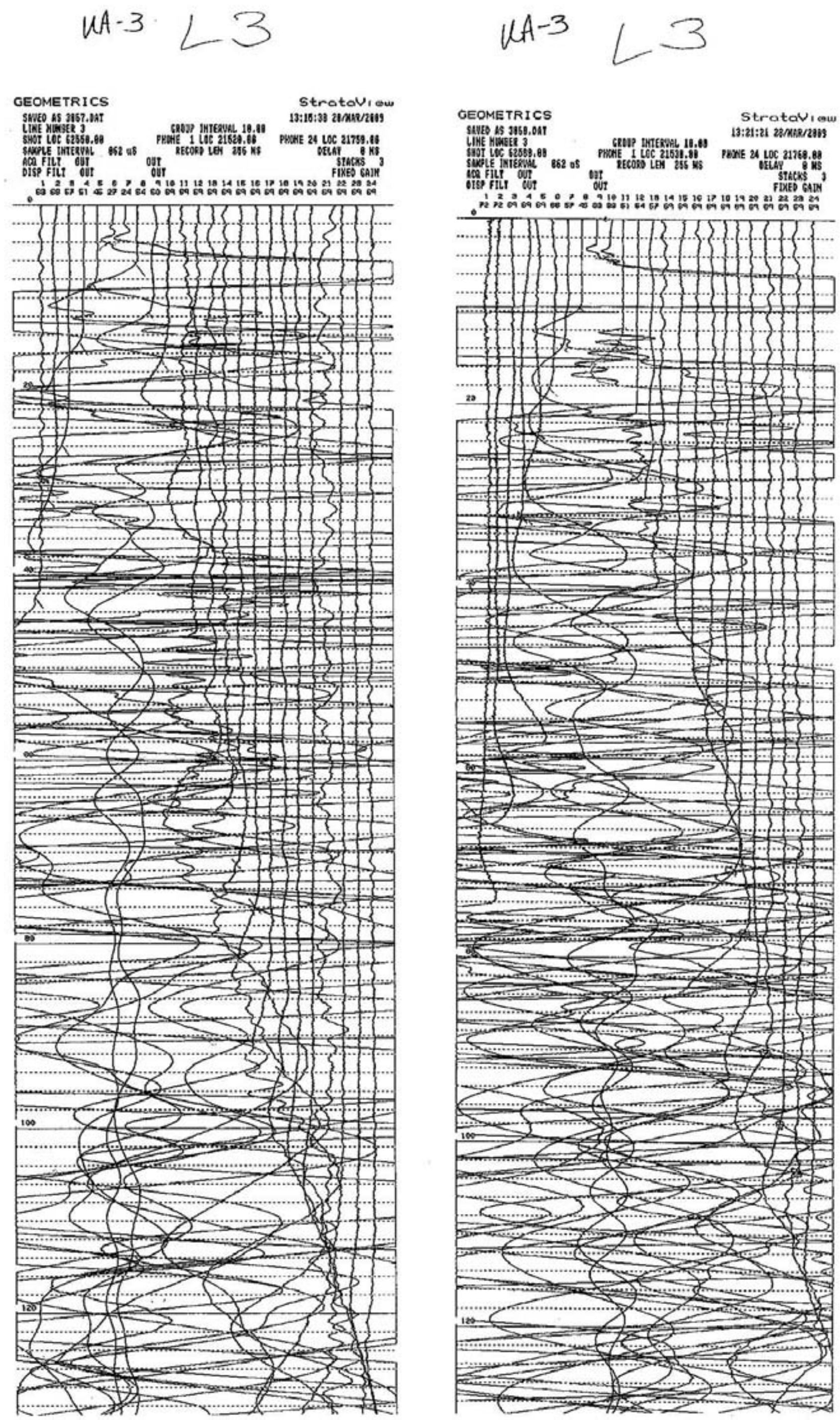

Figure 7.12 Seismic Line 3 shotpoint traces between geophones 9-10 (right) and 6-7 (left).

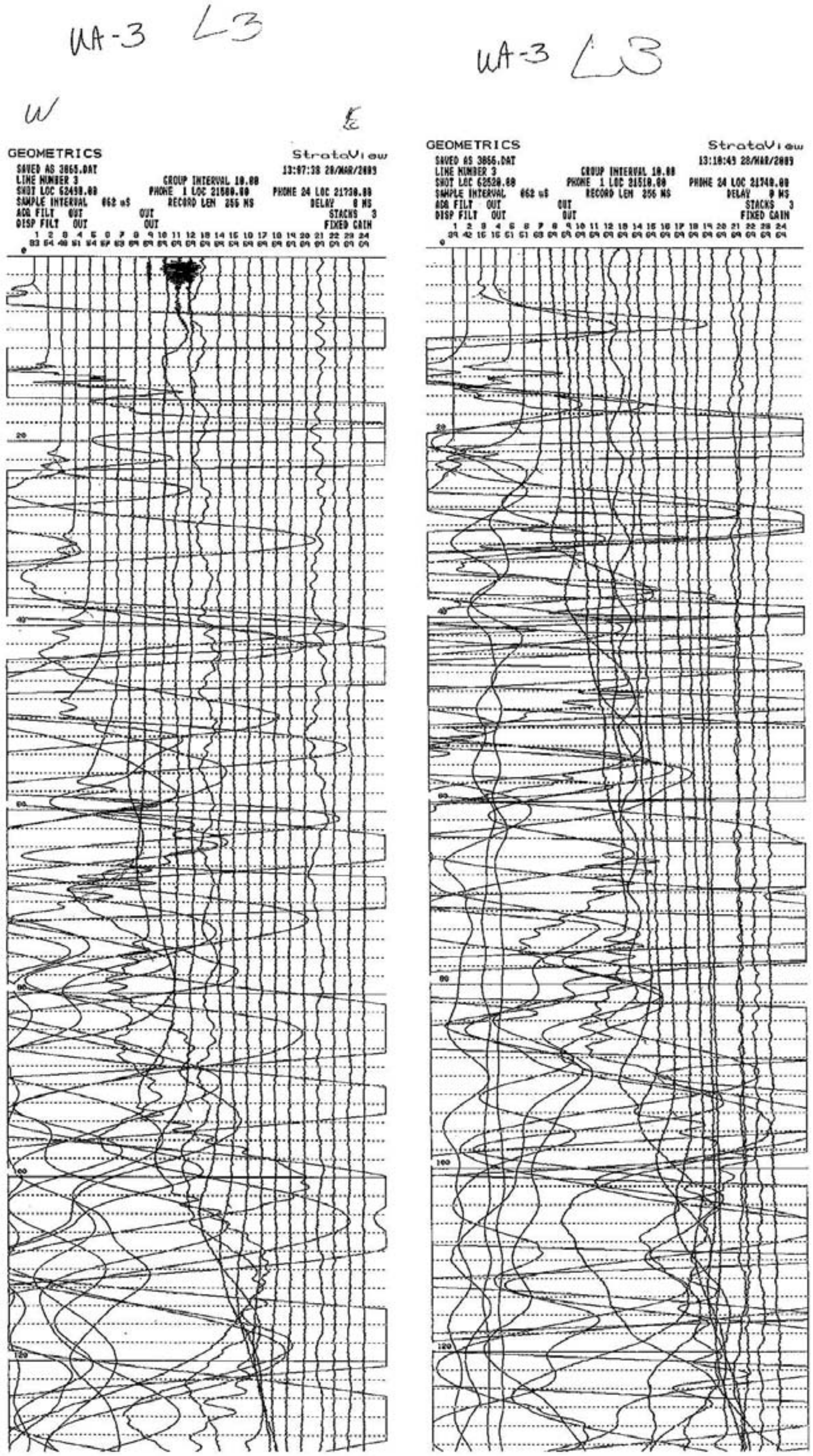

Figure 7.13 Seismic Line 3 shotpoint traces between geophones 3-4 (right) and off of West end of seismic line (left).

Figure 7.13 presents traces for the shotpoints between geophones 3 and 4, and at West end of the seismic line. From the shotpoint between geophones 3 and 4, well formed first arrival traces are observed for the adjacent geophones 6 through about 9 to the east. Further geophone traces to the East have signal loss and long time delays consistent with earth fissure-type attenuation. From the westernmost shotpoint, well formed but attenuating first arrival traces are observed for the adjacent geophones 1 through about 6 or 7. Air wave is superimposed on these traces.

Based on visual evaluation of the seismic refraction traces, a strong seismic anomaly consistent with an earth fissure-type feature is interpreted to be present in the subsurface in the vicinity of geophones 11 to 12.

7.5 Data Processing and Interpretation

Data collected with the assistance of the geophysics class was processed and interpreted by Michael L. Rucker, P.E., Senior Engineer, AMEC Earth & Environmental, Inc. Seismic refraction data interpretation using the intercept time method (ITM), as detailed by Mooney (1973) and implemented on a spreadsheet, was used for analysis. ITM is well suited for simple seismic interpretation in this environment of very shallow subsurface horizons, where seismic velocities typically are laterally variable, and velocity inversions are likely when more than 3 subsurface layers are encountered. The spreadsheet is used to perform the necessary calculations to obtain depths and layer velocities, and print out time-distance plots and depth interpretations. This method is used for interpretations of up to three layers. Interpretations are then edited to produce a final interpreted geologic profile and layer depths.

Interpretation of ReMi data was performed using the SeisOpt ReMi Version 3.0 (2004) software package by Optim, L.L.C., of Reno, Nevada. The software consists of two modules. The ReMiVsSpect module is used to convert the SEG2 files into a spectral energy shear wave frequency versus shear wave velocity presentation for a ReMi seismic setup. The interpreter then selects a dispersion curve consisting of the lower bound of the spectral energy shear wave velocity versus frequency trend, and that dispersion curve is saved to disk. Tracing the lower bound (slowest) of the shear wave velocity at each frequency selects the ambient energy propagating parallel to the geophone array, since energy propagating incident to the array will appear to have a faster propagating velocity. The second module, ReMiDisper, is then invoked. The interpreter models a dispersion curve with multiple layers and s-wave velocities to match the selected dispersion curve from the processed data; an interpreted vertical s-wave profile is thus obtained.

It must be understood that the ReMi interpretation may not result in a unique solution. Results from the seismic refraction interpretation are used to help constrain the shallow portion of the ReMi interpretation to reduce uncertainty in the ReMi interpretation. In turn, the ReMi interpretation provides a means to assess velocity reversal conditions in the subsurface profile that cannot be interpreted using the seismic refraction method.

7.6 Seismic Interpretation Results

Interpretation results, first arrival time-distance plots and Remi interpretation results for Seismic Lines 1, 2 and 3 are presented in Figures 7.14 through 7.23. The seismic refraction and ReMi interpretation concepts and procedures do not directly account for seismic signal amplitudes, and are thus ill-suited to quantify all of the issues addressed in the qualitative evaluation of the seismic traces used to assess the possible presence and location of earth fissure-type features. Thus, these interpretations serve to support and confirm the qualitative, visual interpretations made in the field as described in Section 7.4. Interpretation of a thin higher velocity horizon, and the likelihood of seismic signal attenuation due to it's presence, is an important function of these interpretations.

In general, these interpretations indicate that a very low seismic velocity surficial soil horizon is typically underlain by a weakly cemented (Stage 1+ to 2 cementation as described in Rucker and Fergason, 2006) soil horizon. The cemented horizon, perhaps only a few meters thick, is underlain by a lower seismic velocity, less competent soil horizon that extends to depths of about 15 to 20 meters before a more competent horizon is interpreted. Various seismic anomalies and discontinuities are indicated from the time-distance plots, and are labeled in the seismic refraction interpretations. Test pits or trenches are used to verify seismic anomalies or discontinuity interpretations.

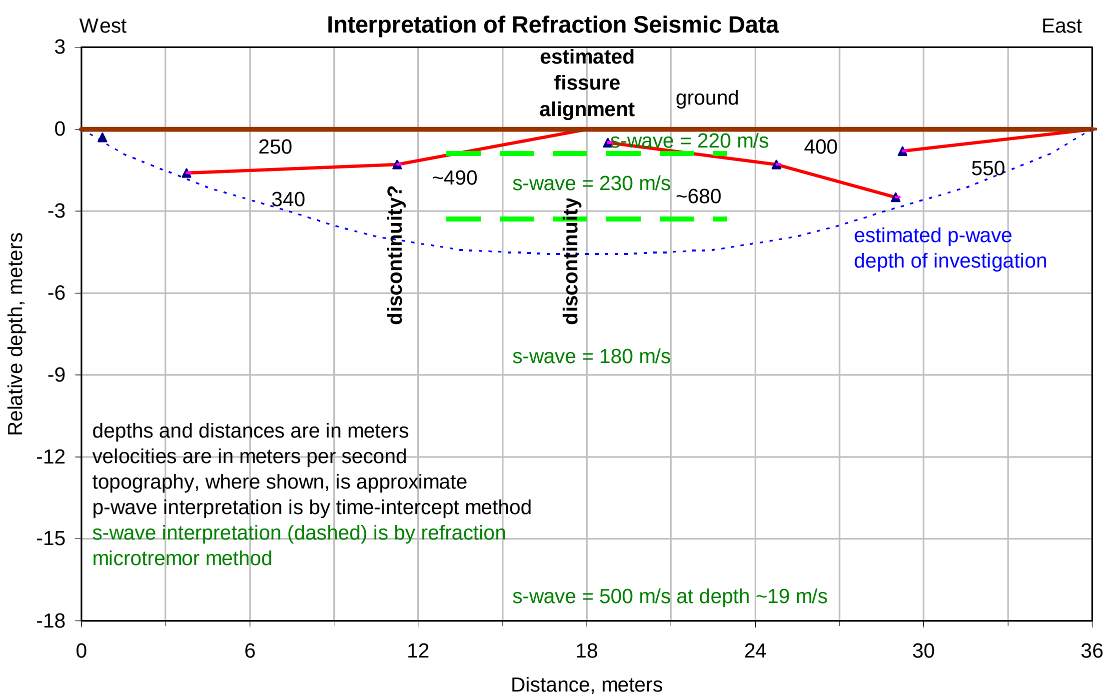

Figure 7.14 Seismic Line 1 seismic refraction and ReMi interpretation results.

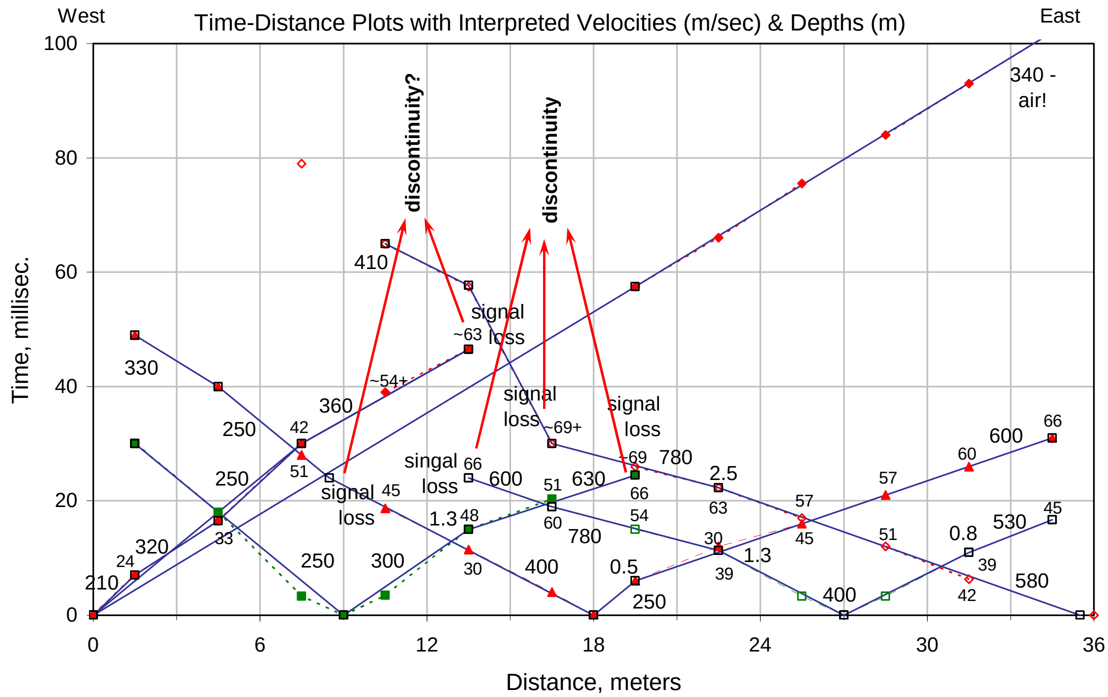

Figure 7.15 Seismic Line 1 seismic refraction first arrival time-distance plots.

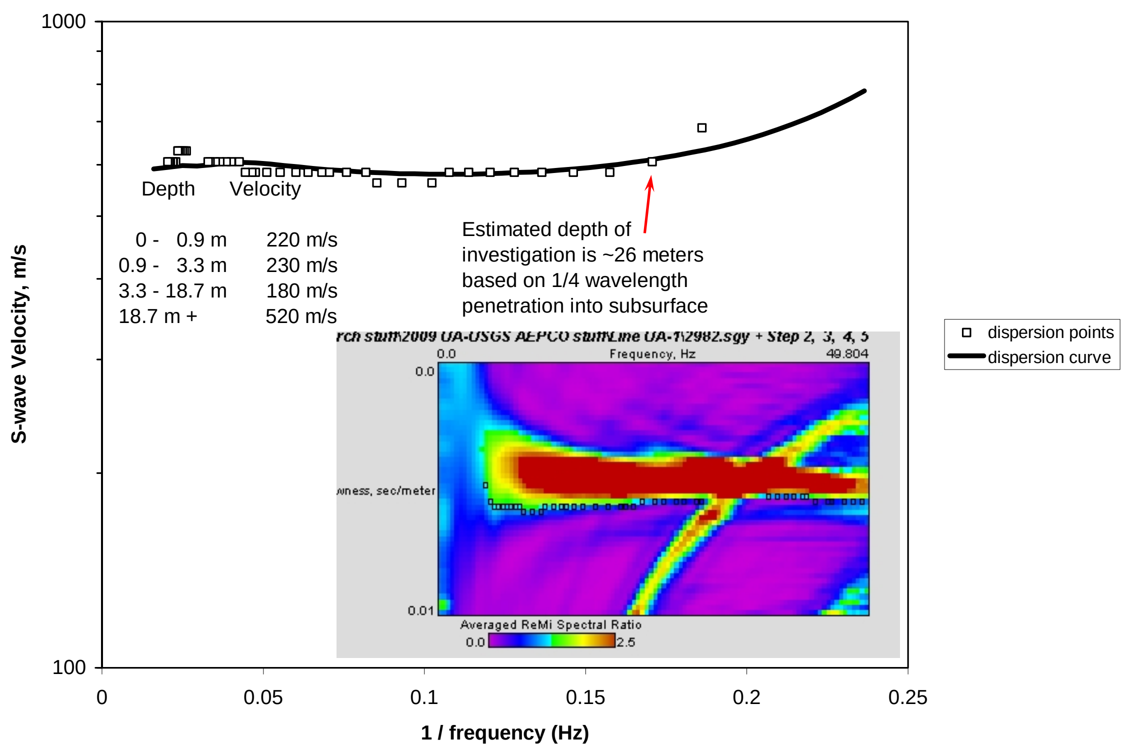

Figure 7.16 Seismic Line 1 ReMi interpretation results.

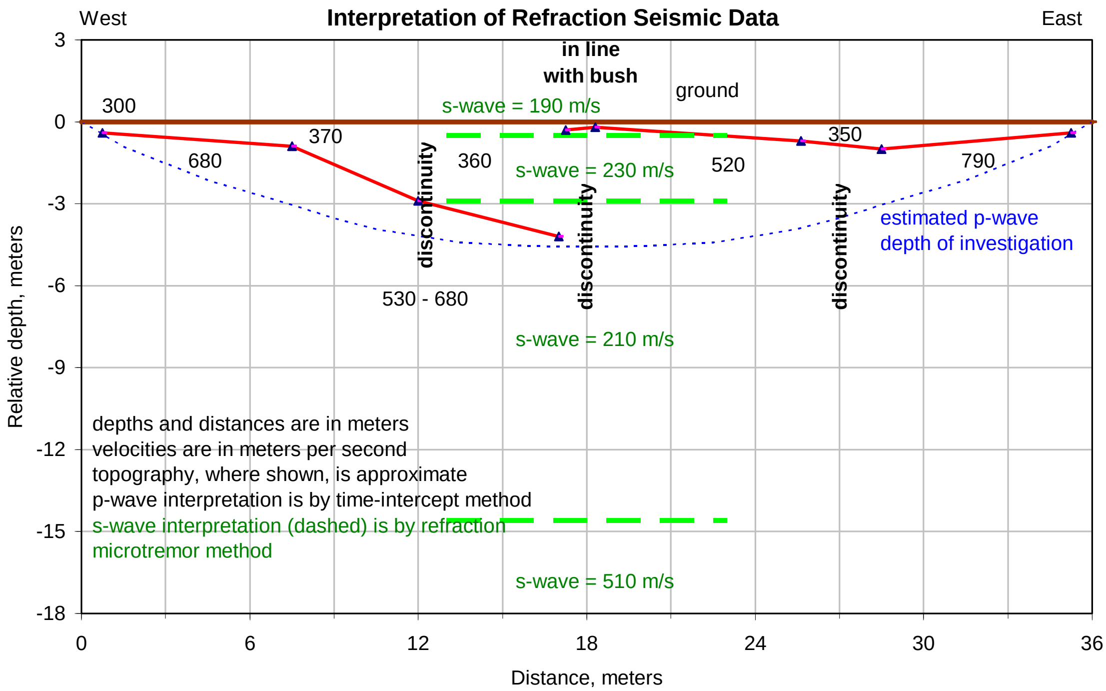

Figure 7.17 Seismic Line 2 seismic refraction and ReMi interpretation results.

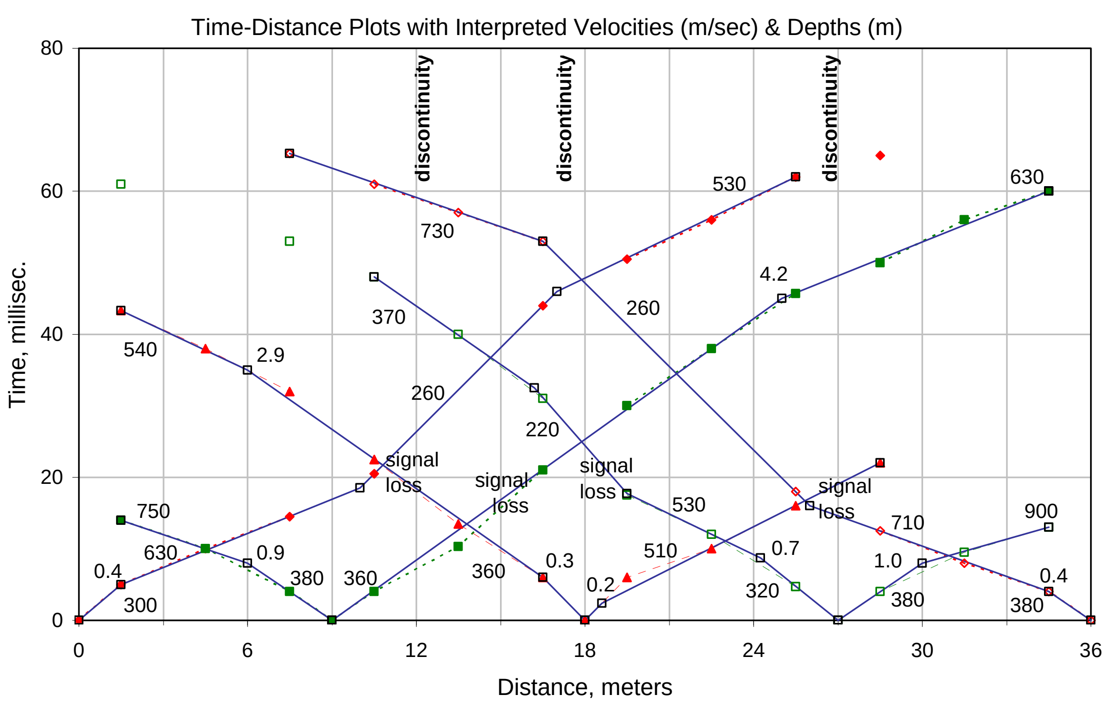

Figure 7.18 Seismic Line 2 seismic refraction first arrival time-distance plots.

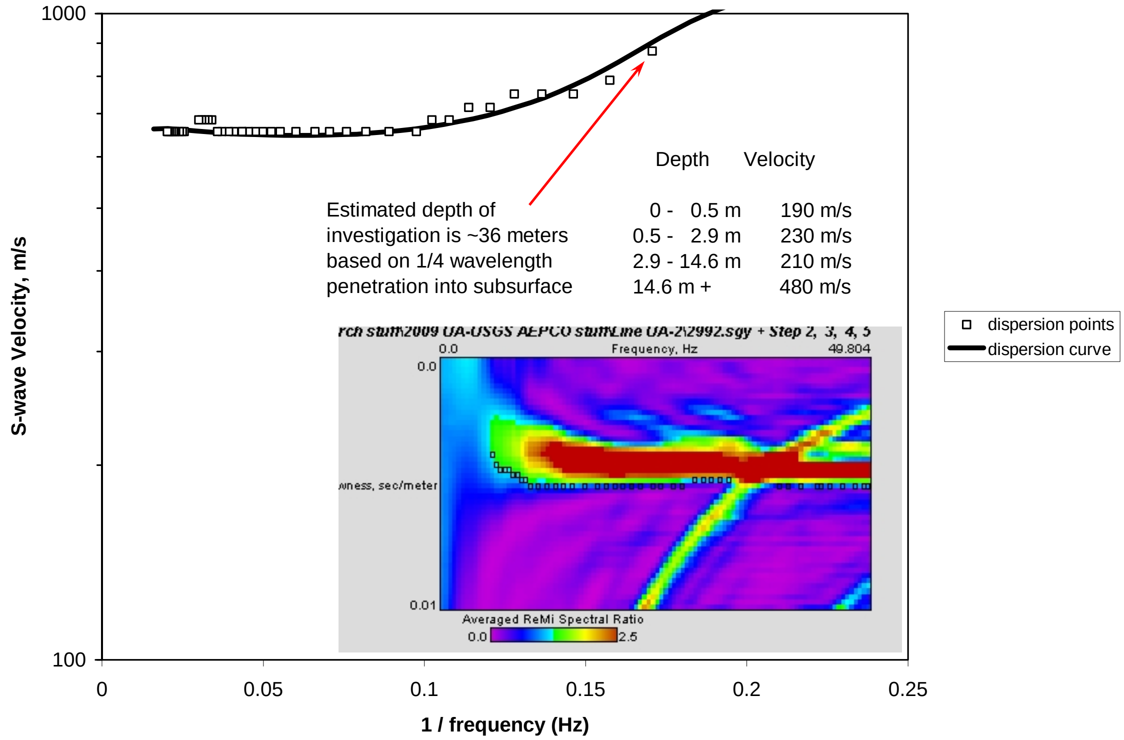

Figure 7.19 Seismic Line 2 ReMi interpretation results.

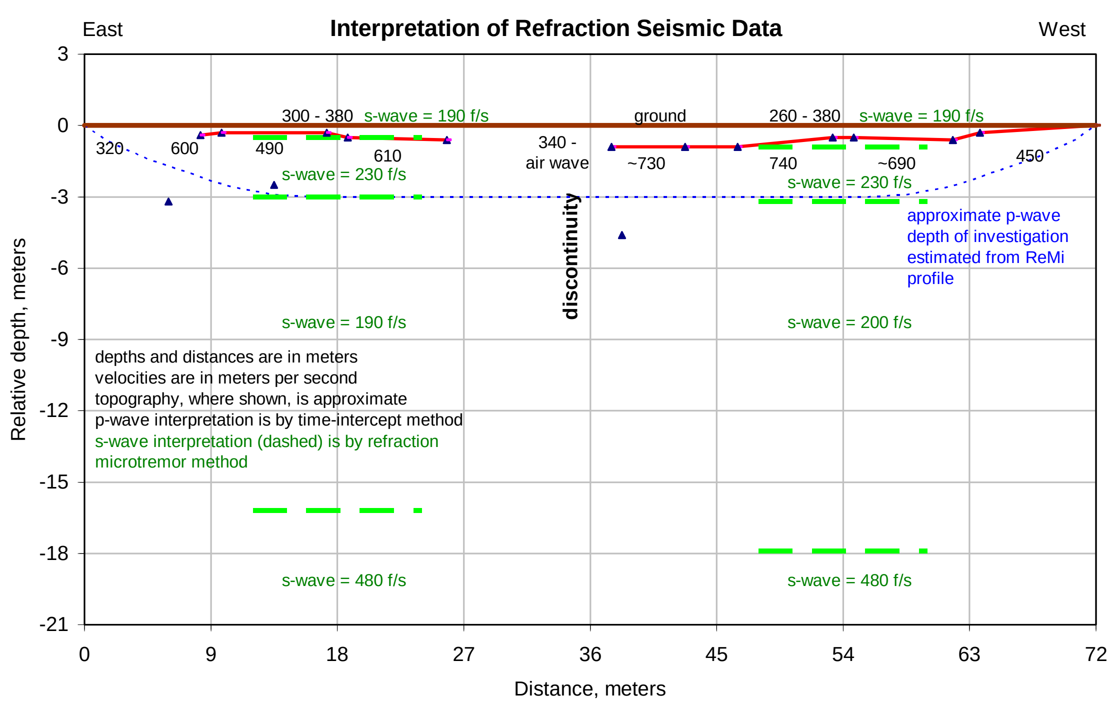

Figure 7.20 Seismic Line 3 seismic refraction and ReMi interpretation results.

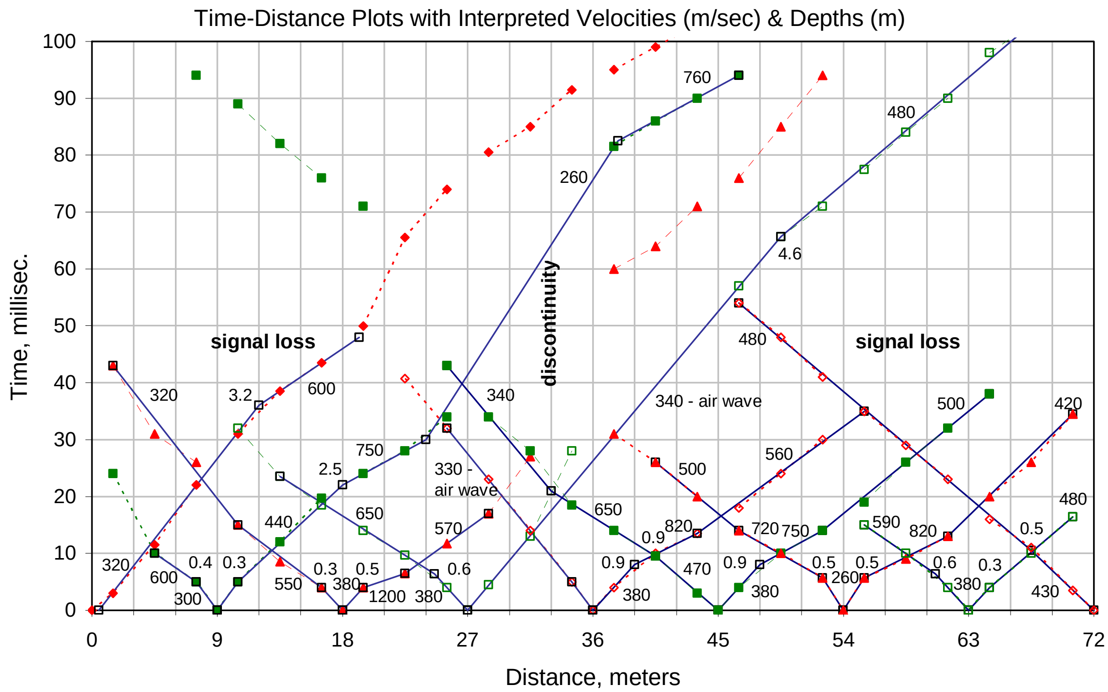

Figure 7.21 Seismic Line 3 seismic refraction first arrival time-distance plots.

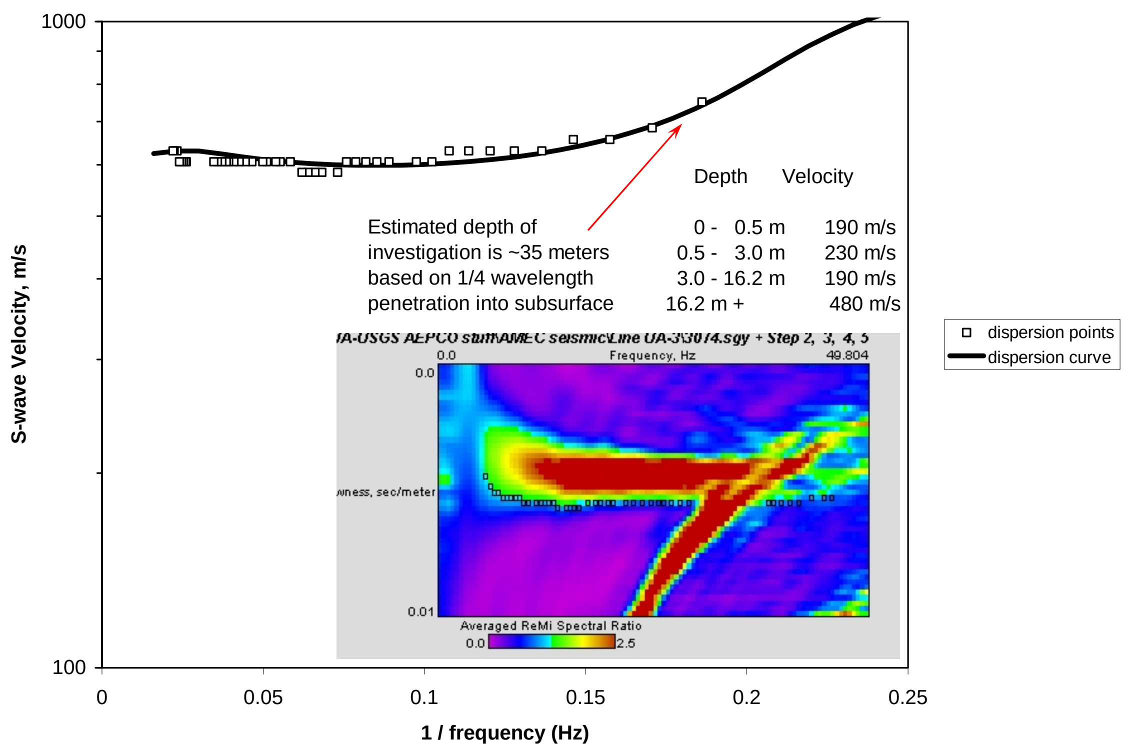

Figure 7.22 Seismic Line 3 (East half) ReMi interpretation results.

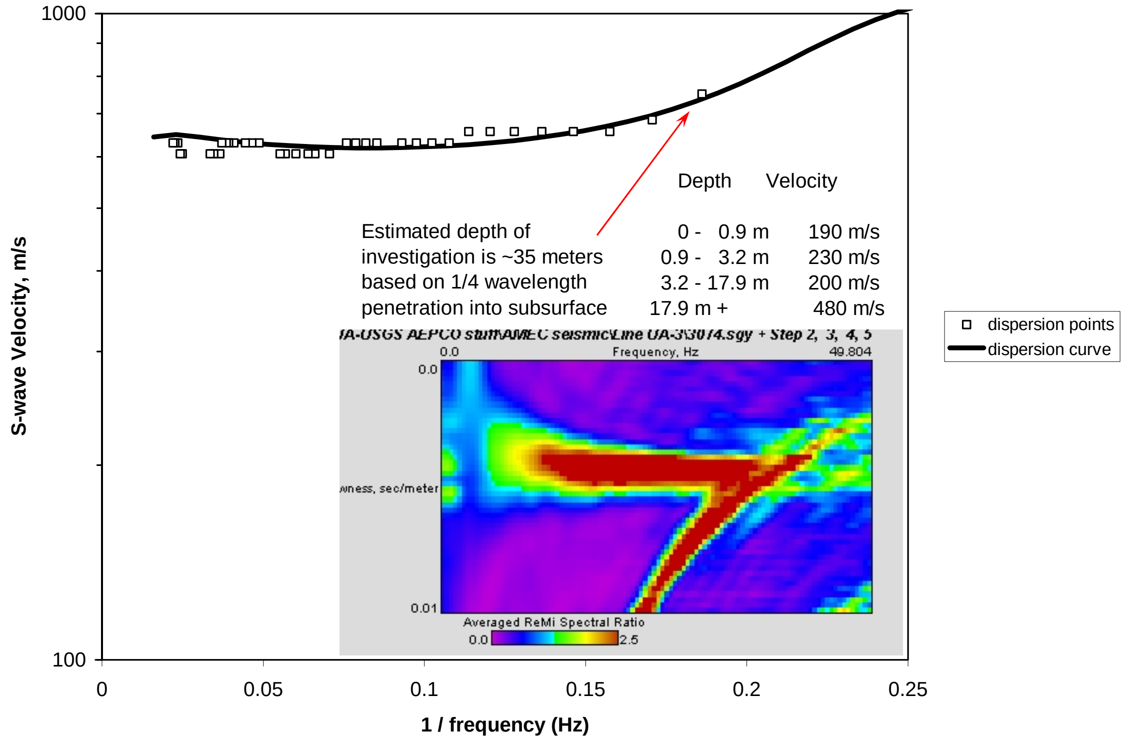

Figure 7.23 Seismic Line 3 (West half) ReMi interpretation results.

8.0 TRENCHING REPORT

A trenching program was carried out to search for the presence of concealed fissures in locations where the geophysical methods have been tested. A total of three trenches were excavated to depths of about 0.9 to 1.2 meters. These trenches were constructed using a Case 580C backhoe, owned by AEPCO and operated by Mr. Jerry Ennis of AEPCO. In two cases (Test Trench 1 and 2), the trenches were positioned in close proximity to ground markers indicating the presence of a seismic refraction anomaly, as staked by AMEC. The third excavation was placed in near proximity to a former LIDAR instrument station, located within Grid 1. Each trench was positioned transverse to the trend of exposed fissures present in the locale, with each trench about 9 to 12 meters long and excavated first with a wide equipment pass to a depth of about 30 cm, followed by the completion of a narrow keyed trench in shallow, smoothed surface. Each trench was then geologically logged by Ralph E. Weeks, RG of GeoSouthwest and subsequently backfilled with the trench spoils. The test trench logs and selected photographs of the earth fissures exposed are attached to this report.

The shallow soil profile encountered in the excavation consisted of a surfical, 15 to 30-cm thick unit (A-1) consisting of slightly moist, soft sandy silt that is uncemented and cohesionless. This unit is underlain by a more cemented, firm to very firm clayed sand whose degree of cementation increases with depth. Units A-2 and A-3, as logged, are very similar, with the exception of the degree of calcareous soil development, with the stage of cementation increasing from Stage I-II to Stage II-II+ with depth.

Physical evidence of earth fissuring was detected in all three trenches, with the features of Trench 2 consisting of a zone of strain, with no definitive earth fissure exposed in the excavation. In contrast the earth fissures present in Trench 1 and 3 were more organized, with segments where the fissuring is expressed as one fracture, with aperture. Descriptions of the earth fissure features observed in each trench are presented on the attached logs 1 through 3.

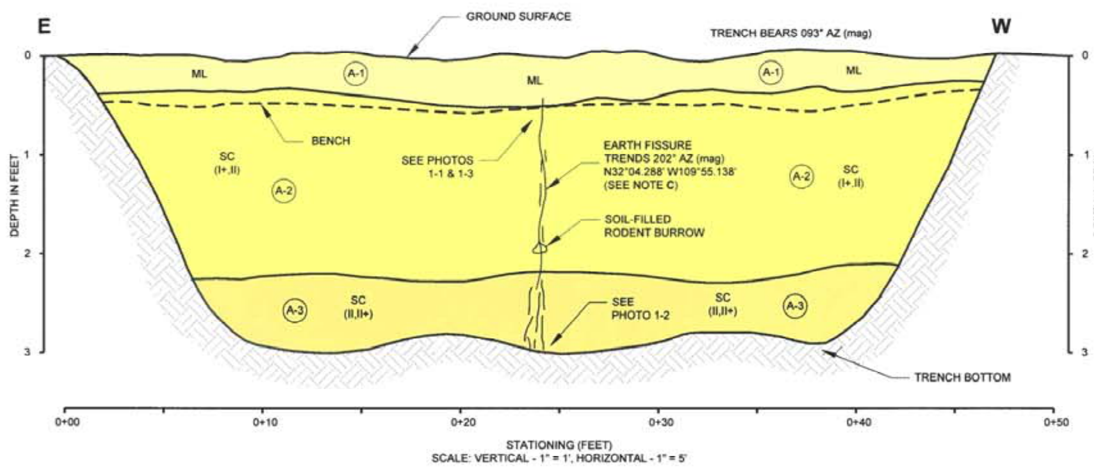

Photograph 1-1

Photograph 1-3

Photograph 1-2

PEDOLOGICAL SOIL CLASSIFICATION		USCS DESIGNATIONS & GEOLOGIC DESCRIPTION
Alluvial Unit A-1 - Holocene note: "A" horizon, but lacking significant organic content, Holocene, likely of original wind blown origin; no observable structure; scattered rootlets, no cementation,slightly cohesive; light brown (7.5YR 6/4)	1	**SANDY SILT (ML)**, trace of fine grained gravel, predominantly fine grained sand, massive, uncemented, nonplastic to very low plasticity, light brown to light reddish-brown, slightly moist, soft
Alluvial Unit A-2 - Late Pleistocene note: "Bk" horizon; Late Pleistocene ?; appears of fluvial origin; some regions with mottled to blocky texture; Stage I+ - II cemenation; nodules common with some filaments; some fine gravel with continuous clasts coatings; light brown (7.5YR 6/4) to white (10yr 8/1)	2	**CLAYEY SAND (SC)**, trace of fine grained, subrounded gravel, crudely bedded, weakly to moderately cemented, low to medium plasticity, light tan to grayish-white, slightly moist, firm to very firm
Alluvial Unit A-3 - Late Pleistocene note: "Bk" horizon; Late Pleistocene ?; appears of fluvial origin; likely same material constituents; as Unit A-2, but with more developed stage of cementation; Stage II - II+ cemenation; carbonate-rich with continuous, persistent white matrix; largely bonded nodules; white (10yr 8/1)	3	**CLAYEY SAND (SC)**, many cemented nodules, massive to crudely bedded, moderately cemented, low to medium plasticity matrix, grayish-white, slightly moist, very firm to hard

KEY

- ALLUVIAL UNIT A-1
- ALLUVIAL UNIT A-2
- ALLUVIAL UNIT A-3
- GEOLOGIC CONTACT
- TRENCH BENCH
- SOIL DISCONTINUITY OR CRACK
- SC (I,II) USCS SOIL CLASSIFICATION WITH STAGE OF CALCIUM CARBONATE CEMENTATION

note: A - nearest surfical evidence (elongated depressions) of earth fissuring located about 24 ft south of trench at bearing of 200° Az (mag)

note: B - marker for geophysical anamoly located 11 ft to the north and normal of test trench alignment

note: C - earth fissure predominantly filled with very soft sandy silt to about 2.5 ft in depth; at 2.5 ft, fissure transitions to diffuse set of vertical fractures in cemented horizon. Near surface fissure is likely eroded to 1 to 1.5 inches; below 2.5 ft, fractures are hairline

JOB NO. 7-117-001096 DESIGN: REW DRAWN: GWH DATE: 5/2009 SCALE: AS SHOWN	LOG OF TEST TRENCH NO. 1 AEPCO Earth Fissure Monitoring Geo Southwest Job No. 09-001	FIGURE 1

amec

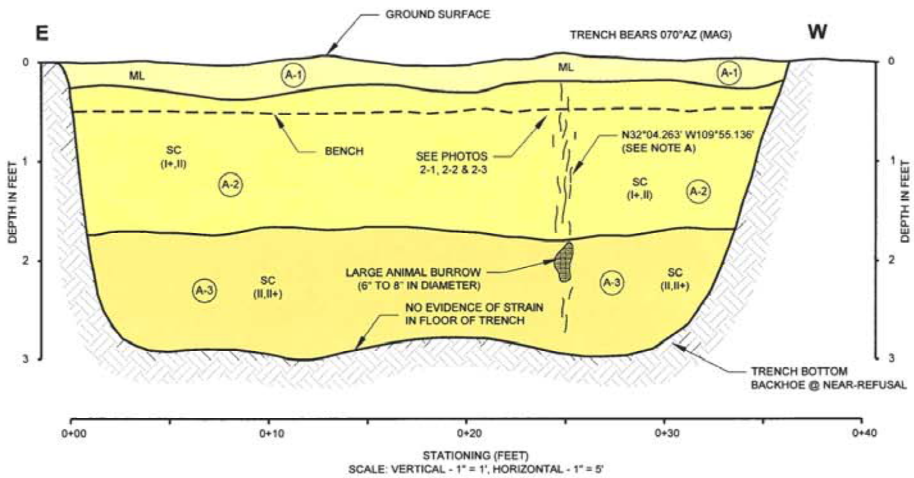

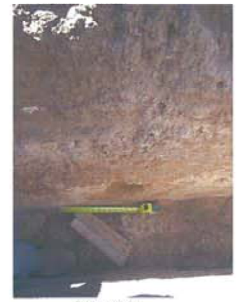

Photograph 2-1

Photograph 2-2

Photograph 2-3

PEDOLOGICAL SOIL CLASSIFICATION		USCS DESIGNATIONS & GEOLOGIC DESCRIPTION
Alluvial Unit A-1 - Holocene note: "A" horizon, but lacking significant organic content; Holocene; likely of original wind blown origin; no observable structure; no cementation; slightly cohesive; light brown (7.5YR 6/4)	1	**SANDY SILT (ML)**, trace of fine grained gravel, predominantly fine grained sand, massive, uncemented, nonplastic to very low plasticity, light brown to light reddish-brown, slightly moist, soft
Alluvial Unit A-2 - Late Pleistocene note: "Bk" horizon; Late Pleistocene ?, appears of fluvial origin; some regions with mottled to blocky texture; Stage I+ - II cemenation; nodules common with some filaments; some fine gravel with continuous clasts coatings; light brown (7.5YR 6/4) to white (10yr 8/1)	2	**CLAYEY SAND (SC)**, trace of fine grained, subrounded gravel, crudely bedded, weakly to moderately cemented, low to medium plasticity, light tan to grayish-white, slightly moist, firm to very firm
Alluvial Unit A-3 - Late Pleistocene note: "Bk" horizon; Late Pleistocene ?; appears of fluvial origin; likely same material constituents; as Unit A-2, but with more developed stage of cementation; Stage II - II+ cemenation, carbonate-rich with continuous, persistent white matrix; largely bonded nodules: white (10yr 8/1)	3	**CLAYEY SAND (SC)**, many cemented nodules, massive to crudely bedded, moderately cemented, low to medium plasticity matrix, grayish-white, slightly moist, very firm to hard

KEY

- ALLUVIAL UNIT A-1
- ALLUVIAL UNIT A-2
- ALLUVIAL UNIT A-3
- GEOLOGIC CONTACT
- TRENCH BENCH
- SOIL DISCONTINUITY OR CRACK
- SC (I,II) USCS SOIL CLASSIFICATION WITH STAGE OF CALCIUM CARBONATE CEMENTATION

note: A - zone of possible strain, no defined earth fissure 14 to 16 inches wide, short fractures with no apertures

note: B - marker for geophysical anamoly located 24 ft to the north and normal of test trench alignment

JOB NO. 7-117-001096	LOG OF TEST TRENCH NO. 2	amec
DESIGN: REW		
DRAWN: GWH		
DATE: 5/2009	AEPCO Earth Fissure Monitoring Geo Southwest Job No. 09-001	FIGURE 2
SCALE: AS SHOWN		

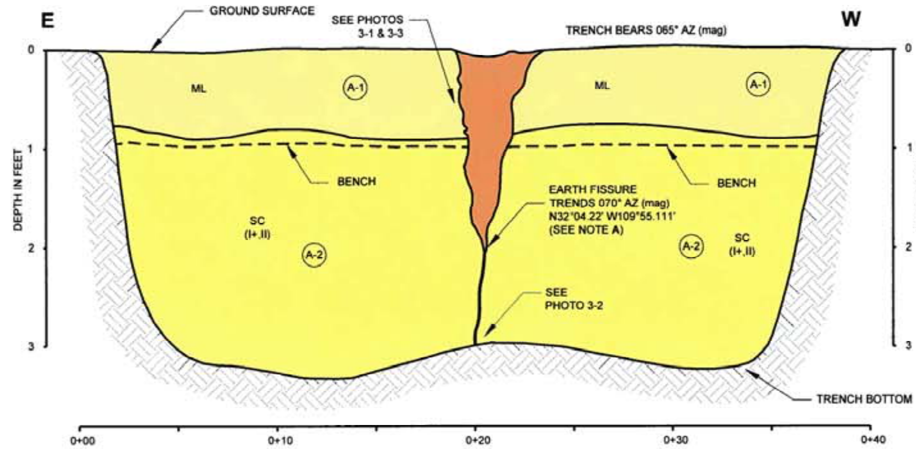

STATIONING (FEET)
SCALE: VERTICAL - 1" = 1', HORIZONTAL - 1" = 5'

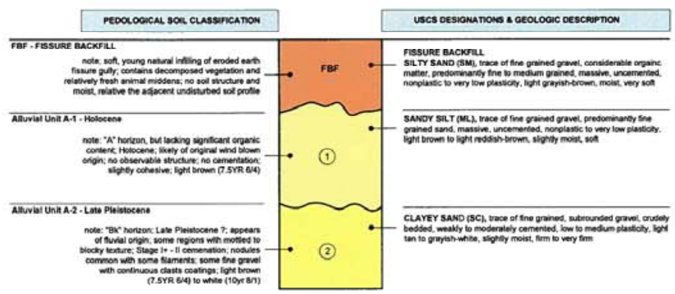

KEY

- FBF - FISSURE BACKFILL
- ALLUVIAL UNIT A-1
- ALLUVIAL UNIT A-2
- GEOLOGIC CONTACT
- TRENCH BENCH
- SOIL DISCONTINUITY OR CRACK
- SC (I,II) USCS SOIL CLASSIFICATION WITH STAGE OF CALCIUM CARBONATE CEMENTATION

Photograph 3-1

Photograph 3-2

Photograph 3-3

note: A - Earth Fissure Description from the surface to a depth of 1.75 ft - eroded fissure (~3 ft wide at surface) filled with recent, unstratified sediments, with multiple burrows and clumps of organic matter; narrows to single fracture at about 2 ft if depth; fissure is completely filled with sediment; appears relatively uneroded across floor of trench; aperture: 5/8"; laterally trench flawteed by elongated surface potholes on each side; continuous fissure present in both trench walls and across trench floor

note: B - no geophysical marker found; located near previous lidar instrument station

JOB NO.	7-117-001096
DESIGN:	REW
DRAWN:	GWH
DATE:	5/2009
SCALE:	AS SHOWN

LOG OF TEST TRENCH NO. 3

AEPCO Earth Fissure Monitoring
Geo Southwest Job No. 09-001

FIGURE 3

amec

9.0 CONCLUSIONS

In order to assess the effectiveness of various geophysical techniques for locating subsidence fissures, geophysical test grids were established in an area of known earth fissuring. Two grids were analyzed West of the AEPCO Apache Generating Station's Waste Disposal Facility, located approximately 30 km southwest of Willcox Arizona.

Through our magnetic surveys it was found that there is a magnetic high that runs the length of Grid 1 at about the 20 to 25 meter mark. This high correlates with the known fissure. In places where the fissure is not visible, there is still a magnetic high. From this we can conclude that there is still a fissure, although buried. For Grid 2 all along the grid there are random highs and lows. The geophysical data do not provide conclusive evidence that a fissure exists in this area. Finally, for the desiccation crack survey, the total field shows a high anomaly running East to West at about the 20-25 meter mark. This may be due to the road only. The postulated desiccation crack location may be too far South to be directly correlated to the magnetic high. Nothing of interest was determined from the magnetic gradient data.

While using the EM31 it was observed on Grid 1 that there is a high for all four orientations of the instrument along the open fissure, as well as near areas where the fissure was not visible at the surface. For Grid 2 there was a high near the open fissure along the southern part of the grid on all four orientations of the instrument. North of the water line there is a low that trends southwest northwest. This is also consistent on all the orientations. For the desiccation crack there was slightly more variation in the four different orientations but there was only a high along the known desiccation crack when the instrument's dipole was oriented vertically. The cultural interference tests showed that a fence has a large influence on the data but the power lines had a limited effect.

EM34 surveys found strong and continuous conductivity anomalies over or near the fissures for Grid 1, especially VCP conductivity. We therefore conclude that this method is useful for mapping subsurface fissures. Over the desiccation crack, it was possible to infer the E-W orientation and location at approximately 25 m. Apparently the fissures have a high response or anomalous response caused by moisture or underground water that causes high conductivity.

It was found through EM38 measurements along Grid 1 that the fissure is seen both in QP and IP measurements at approximately 25 meters. This is seen in all plots, which show anomalies over the fissure. The QP values are large over the fissure. The IP data display a trend over Grid 1 through which values get larger from line 1 to 13. However, it was seen that along line 13 where the fissure is not open at the surface EM38 showed a high where the fissure is suspected to be.

Along Grid 2 it was seen that QP measurements picked up the open fissure but the IP did not. More anomalies were more pronounced over lines 1-4 than lines 12-13. Again, the IP had a similar trend where the values along lines 1-4 were smaller than lines 12 and 13. There are other anomalies that were present in these data sets; however, we do not have a clear idea what could be causing these.

While measuring EM38 data along the desiccation crack there was a clear anomaly in both the QP and IP data sets. This anomalous high can be seen on all graphs at the 25meter mark for the QP and 30 meter mark for IP. We believe that this anomaly may be representative of the desiccation crack.

For GPR, using the 2D processing, we could see a correlation between the diffractions and the location of the fissure along the individual profiles. The 3D processing, however, had a programming error that caused a false repeating pattern in the plots.

The seismic results interpreted from the geologic profiles and layer depths obtained, indicate a strong seismic anomaly consistent with an earth fissure in the general area of geophones 4 to 6 for Seismic Line 1. Based on visual evaluation of the seismic refraction traces, a series of weak or possible seismic anomalies more consistent with a thin higher velocity horizon than an earth fissure-type feature are interpreted to be present across Seismic Line 2. Upon visual evaluation of the seismic refraction traces, a strong seismic anomaly consistent with an earth fissure-type feature is interpreted to be present in the subsurface in the vicinity of geophones 11 to 12 in Seismic Line 3.

Finally, the historic 36-meter seismic array (Line L6) results completed at the desiccation crack site indicate that the seismic trace patterns visually appear to be mostly unaffected by the presence of an obvious ground crack at the center of the geophone array. The ground crack was interpreted to be a desiccation crack that extended to only a very shallow, to shallow depth, and not an earth fissure. An earth fissure would have a seismic signal-disrupting crack extending through the more competent cemented horizon.

For fissure and desiccation crack analysis it was found that many geophysical methods were useful in the areas that are near open fissures, but where there was no obvious sign of the fissure on the surface. The magnetic surveys, EM31, EM34 and EM38 all provided strong correlations with the suspected fissures in Grid 1. GPR had a few problems but with better 3D processing and techniques it appears that it could be reliable for finding fissures and desiccation cracks in similar areas. Seismic studies were promising for fissures but did not appear to pick out the desiccation crack.

10.0 REFERENCES

Anderson, T. W. "Summary of the Southwest Alluvial Basins, Regional Aquifer-System Analysis, south-central Arizona and parts of adjacent states." USGS publication 1995 PP 1406-A (1995).

ADWR, 2009, 5/20/2008 to 5/5/2009 EnviSat InSAR Image, produced by the Arizona Department of Water Resources.

Arizona Electric Power Cooperative Inc. 20 Apr. 2009 <http://www.aepco.coop>.

Arizona Land Subsidence Group, 2007, White Paper - Land Subsidence and Earth Fissures in Arizona, Research and Informational Needs for Effective Risk Management, available at http://www.azgs.az.gov/Resources/CR-07-C_Dec07.pdf

Arizona Water Atlas. Phoenix: Arizona Department of Water Resources (ADWR), 2009.

Callegary, James. "Geologic Framework, Hydraulic Monitoring, and Land-Use Change in the Willcox and Douglas Basins, Southeast Arizona." Introduction to 2009 Willcox Geophysics Survey. University of Arizona, Tucson. 2 Feb. 2009.

Conyers, Lawrence B., 2004, Ground-Penetrating Radar for Archaeology: Rowman & Littlefield Publishers, INC.

Drewes, H., 1980, Tectonic Map of Southeast Arizona, U. S. Geological Survey, Miscellaneous Investigation Series, Map I-1312, Washington, D.C., GPO.

Geonics, Ltd. Mississauga, ON, Canada: available at www.geonics.com.

Geometrics, Inc., San Jose, CA accessed at http://www.geometrics.com/geometrics-products/seismographs/smartseis/

Geophysical Survey Systems, Inc. available at http://www.geophysical.com accessed May 2009.

Greenwood, W J., Kruse, S E., Swarzenski, P W., Meunier, J K., (2004), Mapping Porewater Salinity with Electromagnetic Methods in Shallow Coastal Environments: Tampa Bay, Florida, *Eos Trans. AGU*, *85*(17), Jt. Assem. Suppl., Abstract NS31A-09.

Holzer, T.L., 1980, Earth Fissures and Land Subsidence, Bowie and Willcox Areas, Arizona, USGS, Miscellaneous Field Investigations Map MF-1156, Washington, D.C., GPO.

Kansas Geological Survey accessed at http://www.kgs.ku.edu/software/surfseis/masw.html

Keary, P., Brooks, M., and Hill, I., 2002, An Introduction to Geophysical Exploration: Blackwell Science Ltd., p. 225.

Louie, J., 2001, Faster, better: Shear wave velocity to 100 meters depth from refraction microtremor arrays, Bulletin of the Seismological Society of America, v. 91, no. 2, p. 347-364.

MALÅ Geoscience available at http://www.malags.com accessed May 2009.

Mooney, H.M., 1973, Engineering Seismology Using Refraction Methods, Bison Instruments, Inc., Minneapolis, Minnesota.

O'Brien, P.N.S., 1967, The use of amplitudes in seismic refraction survey, in Musgrave, A.W. (ed), Seismic Refraction Prospecting, Society of Exploration Geophysicists, Tulsa, Oklahoma, 85-118.

Robinson, D. A., Lebron, I., Lesch, S. M., and Shouse, P., 2004, Minimizing Drift in Electrical Conductivity Measurements in High Temperature Environments using the EM38, Soil Science Society of America Journal, v. 68, no. 2, p. 339-345.

Rucker, M.L. and Keaton, J.R., 1996, Three-Dimensional Characterization with Limited Data: An Example from Playa-Lake Basin, Southeast Arizona, Transportation Research Record

No. 1526, Transportation Research Board, National Research Council, National Academy Press, Washington, D.C., p 191-198.

Rucker, Michael L., Micheal D. Greenslade, Ralph E. Weeks, Kenneth C. Fergason, and Bibhuti Panda. Geophysical and Remote Sensing Characterization to Mitigate McMicken Dam. Tech. Tempe: AMEC Earth and Environmental Inc., 2009.

Rucker, M.L., and Fergason, K.C., 2006, Characterizing unsaturated cemented soil profiles for strength, excavatability and erodability using surface seismic methods, Proceedings from the Fourth International Conference on Unsaturated Soils, Carefree, AZ, April 2-6, 2006.

Rucker, M.L. and Keaton, J.R., 1998, Tracing an earth fissure using refraction-seismic methods with physical verification, in Land Subsidence, Case Studies and Current Research, Proceedings of the Joseph F. Poland Symposium on Land Subsidence, ed. J.W. Borchers, Special Publ. No. 8, Association of Engineering Geologists, pp. 207-216.

Rucker, M.L. and Holmquist, O.C., 2006, Surface seismic methods for locating and Tracing earth fissures and other significant discontinuities in cemented unsaturated soils and earthen structures, in Unsaturated Soils, Miller, G.A., Zapata, C.E., Houston, S.L. and Fredlund, D.G., eds, Geotechnical Special Publication No. 147, ASCE, Reston, Va., pp. 601-612.

Rucker, M.L., Greenslade, M.D., Weeks, R.E., Fergason, K.C., and Panda, B., 2008, Geophysical and remote sensing characterization to mitigate McMicken Dam, Proceedings from the ASCE GeoCongress Conference, New Orleans, LA, March 9-12, 2008.

Sherwood, J.W.C., 1967, Refraction along an embedded high-speed layer, in Musgrave, A.W. (ed), Seismic Refraction Prospecting, Society of Exploration Geophysicists, Tulsa, Oklahoma, 138-151.

Tadayon, Saeid. "Arizona Water Use." United States Geological Survey. Univeristy of Arizona, Tucson. 1 May 2009 <http://az.water.usgs.gov/projects/9671-9DW/>.

Towne, Douglas C., and Maureen C. Freark. Ambient Groundwater Quality of the Willcox Basin: A 1999 Baseline Study. Rep. no. 2001-09. Phoenix: Arizona Department of Environmental Quality, 1999.

USGS Publication accessed at http://pubs.usgs.gov/of/2005/1169/chapters/of2005-1169_part2_07_14_Stephenson.pdf

Wrege, B.M., Hasbrouck, W.F. and Schumann, H.H., 1985, Seismic surface-wave attenuation across earth fissures in the alluvium, south-central Arizona, Surface and Borehole Geophysical Methods in Ground Water Investigations, 2nd National Conference and Exposition, National Water Well Association, p. 121-131.